SANDIA REPORT

SAND2006-6964
Unlimited Release
Printed November 2006

Final Report on LDRD Project: Elucidating Performance of Proton-Exchange-Membrane Fuel Cells via Computational Modeling with Experimental Discovery and Validation

Ken S. Chen, Michael A. Hickner, Nathan P. Siegel, David R. Noble, Ugur Pasaogullari, and Chao-Yang Wang

Prepared by
Sandia National Laboratories
Albuquerque, New Mexico 87185 and Livermore, California 94550

Sandia is a multiprogram laboratory operated by Sandia Corporation,
a Lockheed Martin Company, for the United States Department of Energy's
National Nuclear Security Administration under Contract DE-AC04-94AL85000.

Issued by Sandia National Laboratories, operated for the United States Department of Energy by Sandia Corporation.

Available to DOE and DOE contractors from
U.S. Department of Energy
Office of Scientific and Technical Information
P.O. Box 62
Oak Ridge, TN 37831

Telephone: (865) 576-8401
Facsimile: (865) 576-5728
E-Mail: reports@adonis.osti.gov
Online ordering: http://www.osti.gov/bridge

Available to the public from
U.S. Department of Commerce
National Technical Information Service
5285 Port Royal Rd.
Springfield, VA 22161

Telephone: (800) 553-6847
Facsimile: (703) 605-6900
E-Mail: orders@ntis.fedworld.gov
Online order: http://www.ntis.gov/help/ordermethods.asp?loc=7-4-0#online

SAND2006-6964
Unlimited Release
Printed November 2006

Final Report on LDRD Project: Elucidating Performance of Proton-Exchange-Membrane Fuel Cells via Computational Modeling with Experimental Discovery and Validation

Ken S. Chen[1], Michael A. Hickner[2], Nathan P. Siegel[2], and David R. Noble[1]
[1]Engineering Sciences Center
[2]Energy, Infrastructure, & Knowledge Systems Center
Sandia National Laboratories
Albuquerque, NM 87185-0836

Ugur Pasaogullari[*] and Chao-Yang Wang
Electrochemical Engine Center, and
Department of Mechanical and Nuclear Engineering
The Pennsylvania State University
University Park, PA 16802

Abstract

In this report, we document the accomplishments in our Laboratory Directed Research and Development project in which we employed a technical approach of combining experiments with computational modeling and analyses to elucidate the performance of hydrogen-fed proton exchange membrane fuel cells (PEMFCs). In the first part of this report, we document our focused efforts on understanding water transport in and removal from a hydrogen-fed PEMFC. Using a transparent cell, we directly visualized the evolution and growth of liquid-water droplets at the gas diffusion layer (GDL)/gas flow channel (GFC) interface. We further carried out a detailed experimental study to observe, via direct visualization, the formation, growth, and instability of water droplets at the GDL/GFC interface using a specially-designed apparatus, which simulates the cathode operation of a PEMFC. We developed a simplified model, based on our experimental observation and data, for predicting the onset of water-droplet instability at the GDL/GFC interface. Using a state-of-the-art neutron imaging instrument available at NIST (National Institute of Standard and Technology), we probed liquid-water distribution inside an operating PEMFC under a variety of operating conditions and investigated effects of evaporation due to local heating by waste heat on water removal. Moreover, we developed computational models for analyzing the effects of micro-porous layer on net water transport across the membrane and GDL

[*] Current address: Connecticut Global Fuel Cell Center, and Department of Mechanical Engineering, University of Connecticut, Storrs, CT 06269-5233.

anisotropy on the temperature and water distributions in the cathode of a PEMFC. We further developed a two-phase model based on the multiphase mixture formulation for predicting the liquid saturation, pressure drop, and flow maldistribution across the PEMFC cathode channels.

In the second part of this report, we document our efforts on modeling the electrochemical performance of PEMFCs. We developed a constitutive model for predicting proton conductivity in polymer electrolyte membranes and compared model prediction with experimental data obtained in our laboratory and from literature. Moreover, we developed a one-dimensional analytical model for predicting electrochemical performance of an idealized PEMFC with small surface over-potentials. Furthermore, we developed a multi-dimensional computer model, which is based on the finite-element method and a fully-coupled implicit solution scheme via Newton's technique, for simulating the performance of PEMFCs. We demonstrated utility of our finite-element model by comparing the computed current density distribution and overall polarization with those measured using a segmented cell. In the last part of this report, we document an exploratory experimental study on MEA (membrane electrode assembly) degradation.

Acknowledgments

This work was funded by the Laboratory Directed Research and Development (LDRD) program at Sandia National Laboratories. We would like to thank J. Bruce Kelley (6334) and Joel S. Lash (1514) for programmatic support. We would also like to acknowledge the helpful discussions with Chris J. Cornelius (6338) and David Ingersoll (2521) and their participations in the early stage of this work. Thanks also go to Kevin Grossarth (summer student intern) for his assistance on the image analysis of growing droplets, Anne Grillet and Carlton Brooks (both 1512) for use of their feed through goniometer, and Dominic N. McBrayer (student intern) for his assistance in analyzing the neutron images on liquid water distribution in an operating PEM fuel cell. We would like to acknowledge Daniel Hussey, David Jacobson, and Mohammed Arif of the National Institute of Standard and Technology for their assistance and collaboration during the neutron experiments conducted at NIST. Lastly, we are thankful to Harry K. Moffat (1514) and Brian Carnes (1543) for performing peer reviews of this report.

Table of Contents

1. Introduction

The acronym PEM refers to Proton Exchange Membrane or alternatively Polymer Electrolyte Membrane. Though the concept of fuel cells was demonstrated more than 160 years ago by Sir William Robert Grove (an English lawyer turned scientist) and the first generation of PEM fuel cells (PEMFCs) were developed in the early 1960s by General Electric for the Gemini space program, research and development in PEMFCs didn't receive much attention and funding from the federal government (in particular, the US Department of Energy) and industry until 15 – 20 years ago when breakthrough methods for reducing the amount of platinum required for PEMFCs were developed and subsequently improved by Los Alamos National Laboratory (LANL) and others. Notably, Raistrick (1986) of LANL came up with a catalyst-ink technique for fabricating the electrodes. This breakthrough method made it possible to increase the utilization of active catalyst and at the same time to reduce the amount of precious platinum metal needed. Readers who are interested in more detailed accounts of the history of fuel cells in general and PEMFCs in particular are referred to two extensive reviews by Sandstede et al. (2003) and Chen (2003), respectively.

During the last decade, PEMFCs are increasingly emerging as a viable alternative clean power source for automobile and stationary applications. Before PEMFCs can be employed to power automobiles and homes, several key technical challenges must be properly addressed. One technical challenge is elucidating the mechanisms underlying water transport in and removal from PEMFCs. On the one hand, sufficient water is needed in the polymer electrolyte membrane or PEM to maintain sufficiently high proton conductivity. On the other hand, too much liquid water present in the cathode can cause "flooding" (that is, pore space is filled with excessive liquid water) and hinder the transport of the oxygen reactant from the gas flow channel (GFC) to the three-phase reaction sites. Another challenge is fundamentally understanding effects of non-uniform and anisotropic properties of the gas diffusion layer (GDL) on fuel cell performance. GDLs used in PEMFCs are made from carbon paper or carbon cloth, which is characterized by its fibrous microstructure that gives rise to non-uniform and anisotropic transport properties. The use of a Teflon coating to treat the surfaces of large GDL pores so as to render them hydrophobic (thus improving oxygen transport through the GDL) further worsens the non-uniform transport properties in GDLs. Yet another challenge is elucidating MEA (membrane electrode assembly) degradation and failure mechanisms. Under practical operating conditions, fuel cell components, particularly those of the MEA, degrade chemically and physically over time – this is the issue of durability. Other challenges include reducing costs of materials (platinum-containing catalyst, membrane, and bi-polar plate) and of manufacturing. Readers who are interested in more comprehensive discussions on the current status and future challenges in PEMFC research and development are referred to the review articles, respectively, by Gasteiger and Mathias (2003), Adler (2005), and Du et al. (2006).

Figure 1.1 shows a schematic of a single-cell PEMFC with straight channels – this is a three-dimensional view. A sectional (i.e., 2D view) cartoon of a single-cell PEMFC is depicted in Figure 1.2. In practice, serpentine design is often employed to create the active area that is needed to deliver the desired rates of electrochemical reactions. As shown in Figures 1.1 and 1.2, the basic unit of a PEMFC consists of seven components: anode GFC, anode GDL, anode catalyst layer (CL), membrane layer or simply membrane, cathode CL, cathode GDL, and cathode GFC – clearly, this basic unit is symmetric with respect to the membrane layer. Moreover, the electrochemical heart or engine of the basic unit is the membrane electrode assembly or MEA, which is comprised of the anode CL, membrane, and cathode CL. Thus, the basic unit of a PEMFC is made up of the anode GFC, anode GDL, MEA, cathode GDL, and cathode GFC.

As can be seen in Figures 1.1 and 1.2, gaseous hydrogen (which is usually humidified in order to provide water for hydrating the membrane) is pumped into a PEMFC's anode GFC (on the left of Figures 1.1 and 1.2). As the hydrogen-water gas mixture is forced to flow down the anode GFC by a hydrodynamic pressure gradient (the back pressure, i.e. pressure at the outlet, is normally set to create the desired pressure gradient), H_2 flows (driven by pressure gradient) and diffuses (driven by concentration gradient) through the porous anode GDL and into the porous anode CL. Simultaneously, highly humidified air is pumped into the cathode GFC (on the right of Figures 1.1 and 1.2). Similar to what happen in the anode side, as the air-water gas mixture is forced to flow down the cathode GFC, O_2 flows and diffuses through the cathode GDL and into the cathode CL.

To reach the three-phase (gas/electrolyte/electrode) interfaces, the fuel H_2 and reactant O_2 are transported in the gas phase occupying GDL/CL pores whereas protons are transported in form of the hydronium ion H_3O^+ through the electrolyte phase (which is usually made of a perfluorosulfonic acid polymer such as Nafion) and electrons are conducted via the electrode phase (i.e., platinum-covered carbon supports). When reaching the respective three-phase interfaces, H_2 is oxidized in the hydrogen oxidation reaction (HOR) to generate protons and electrons whereas O_2 is reduced in the oxygen reduction reaction (ORR) in which electrons and protons are consumed and H_2O is produced. The protons generated in the anode and consumed in the cathode are transported through the Nafion membrane via diffusion and electro-migration, driven by the electrolyte-potential gradient. Connecting the anode and cathode electrode phases at the respective current connectors via conductive metal wires and through the external load completes the electric circuit for the PEMFC. Besides H_2O, waste heat is generated in the PEMFC due to the inefficiency in converting chemical energy to electricity. By comparison, a relatively minor amount of heat is produced from the exothermic ORR.

To elucidate the performance of PEMFCs, we employed an approach of combining experiments and computational modeling/analysis in the present work. Typically, we first performed discovery experiments to probe the relevant key phenomena. We then developed the physical, mathematical, and numerical models to simulate the observed phenomena. We carried out further experiments to obtain data for model validation. Lastly, we compared experimental data with model predictions.

This report is organized as follows. In Chapter 2, we describe our experimental efforts in 1) directly visualizing the evolution and growth of liquid-water droplets at the GDL/GFC interface of an operating PEMFC using a transparent cell, and 2) observing, via direct optical visualization, the formation, growth, and instability of liquid water droplets at the GDL/GFC interface of a simulated PEMFC cathode by employing a specially-designed apparatus. In Chapter 3, we present the development of a simplified model for predicting the onset of water droplet instability at the GDL/GFC interface and compare measured and computed droplet instability diagrams. In Chapter 4, we document our efforts in probing liquid water distribution inside an operating PEMFC using a state-of-the-art neutron imaging instrument available at NIST (National Institute of Standard and Technology) and analyzing the effect of evaporation due to local heating by waste heat on water removal. In Chapter 5, we present a mathematical model for describing transport in the multi-layered hydrophobic gas diffusion media (GDM) and apply the model to analyze the effect of micro-porous layer on liquid water transport in a PEMFC. In Chapter 6, we describe a multi-dimensional model for predicting the two-phase transport of heat and water and employ the model to study the effects of GDL anisotropy on the temperature and water distributions in the cathode of a PEMFC. In Chapter 7, we present a two-phase model based on the multiphase mixture formulation for predicting the liquid saturation, pressure drop, and flow maldistribution across the PEMFC cathode channels. In Chapter 8, we report a new constitutive model for predicting proton conductivity as a function of water content in the polymer electrolyte membrane. In Chapter 9, we present 1) a one-dimensional analytical model for predicting performance of an idealized PEMFC in which surface over-potentials are relatively small, and 2) a multi-dimensional computer model for simulating performance of PEMFCs – this model is based on the finite-element method and a fully-coupled implicit solution scheme via Newton's technique. In Chapter 10, we document an exploratory experimental study on MEA degradation. Lastly, in Chapter 11 we summarize findings in our LDRD project and point out directions for future research. A list of refereed and proceeding publications is also provided as an appendix at the end of this report.

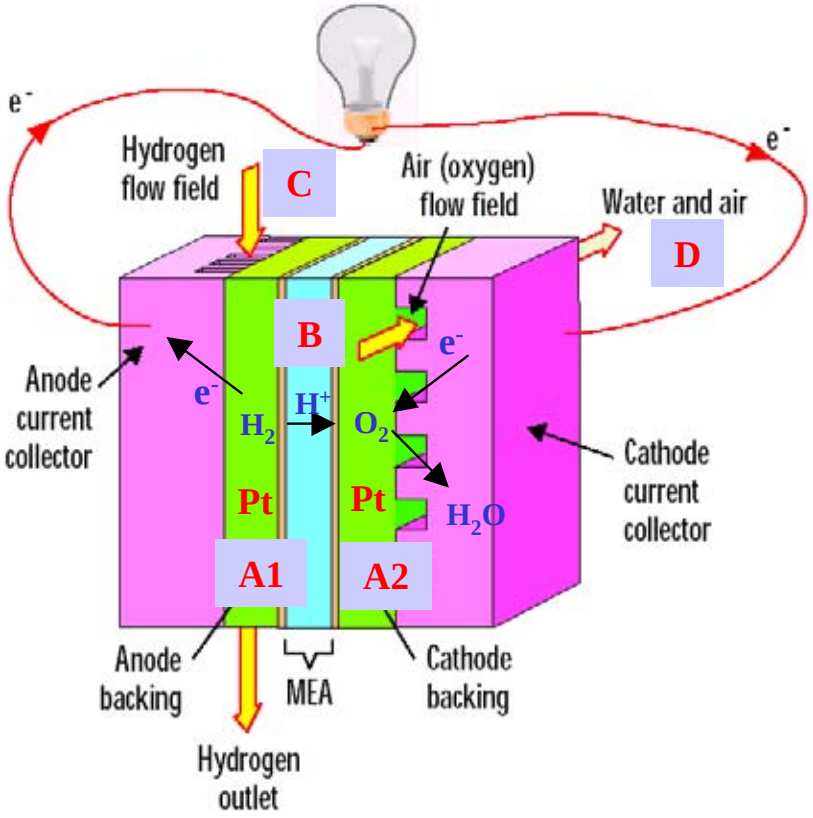

Figure 1.1. Schematic of a single-cell PEM fuel cell with straight channels (3D view)

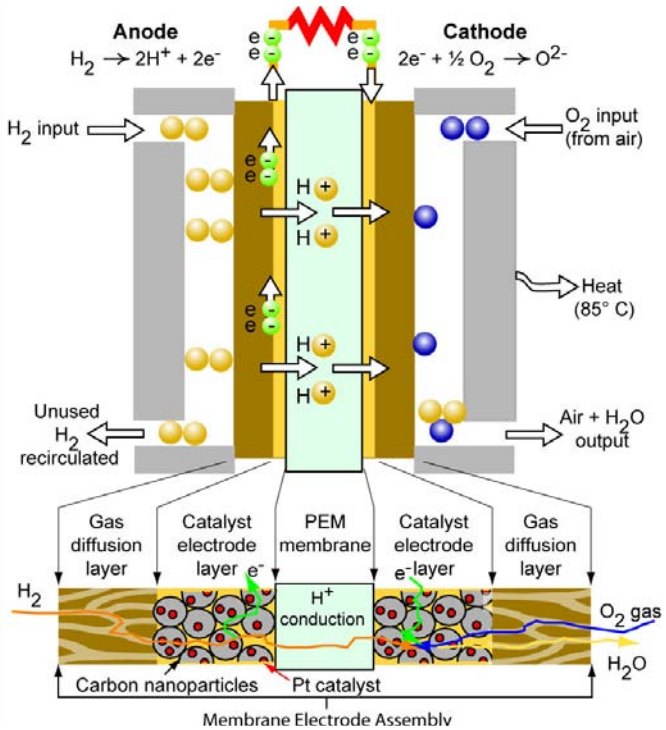

Figure 1.2. Sectional cartoon of a single-cell PEM fuel cell (Jacobson et al. 2003)

2. Direct Visualization of Liquid Water Droplet Formation, Growth, and Instability at the Gas Diffusion Layer/Gas Flow Channel Interface[†]

2.1. Introduction

The presence of liquid water droplets has been observed by previous researchers in the cathodes of operating PEM fuel cells (Tuber et al. 2003, Yang et al. 2004, Wilkinson and Vanderleeden 2003). Liquid water can cause "flooding" in the cathode GDL and GFC by blocking oxygen transport to the reaction sites. Flooding is detrimental because it decreases the performance of the fuel cell at desirably high current densities, and the presence of excessive liquid water may impact the durability of the fuel cell over long periods of operation. Effective liquid water removal from the fuel cell is a key determinant in minimizing massive mass transport losses that accompany liquid water flooding.

Water molecules are generated by the oxygen reduction reaction or ORR in the cathode catalyst layer of a PEM fuel cell or simply PEMFC. Flooding can occur in the catalyst layer itself, in the adjacent GDL, or in the GFC by the formation of droplets that partially block the channel. In the most extreme cases, "slugs" of liquid water can block the entire channel. If liquid water at the GDL/GFC interface can be removed effectively as small droplets, the detrimental effects of channel blockages by excessive water build-up could be mitigated.

Using a transparent cell similar to that employed by Yang et al. (2004) as shown in Figure 2.1, we were able to directly visualize in our PEMFC laboratory the evolution and growth of liquid water droplets at the GDL/GFC interface in the cathode of an operating PEMFC. Figure 2.2a shows a sample image of two liquid water droplets forming on the GDL surface (i.e., at the GDL/GFC interface) at the cathode side of a PEMFC, recorded using a digital video camera with a microscope attachment. Figure 2.2b displays a sample image of a single water droplet forming near the hydrophilic GDL side wall. Figure 2.2c shows more sample images of water droplets forming at the GDL/GFC interface. These images obtained using a transparent fuel cell confirm that there are indeed water droplets formed in fuel cells and these scoping experiments help identify the operational conditions under which droplets are present. However, the view of the GDL in the transparent fuel cell where droplets were observed perpendicular to the GDL did not yield quantitative information on the droplet shape and height, which is critical for determining their behavior. To visualize the shape and height of deformed droplets in the gas flow of a PEMFC cathode, a specially-designed apparatus was built to simulate the formation and growth of liquid water droplets at the GDL/GFC interface as detailed in Section 2.2 below.

[†] Portion of this chapter has been published in a proceeding paper: M. A. Hickner and K. S. Chen, "Experimental studies of liquid water droplet growth and instability at the gas diffusion layer/gas flow channel interface", in *ASME Proceedings of FUELCELL2005*, paper # 74118 (2005).

We have chosen to study the behavior of liquid water droplets at the GDL/GFC interface as a first step to elucidating liquid water removal in PEMFCs, which consists of three sub-processes: 1) transport from the catalyst layer to the GDL/GFC interface via capillary action; 2) removal at the GDL/GFC interface via shearing by flowing gas or evaporation; and 3) transport through the GFC in form of films, droplets and/or vapor. The growth and detachment of water droplets are influenced by two factors: the operating conditions of the fuel cell and the physical and chemical material characteristics of the GDL surface (e.g. in terms of the hydrophilic/hydrophobic properties). In this study, we measured the stability of water droplets on Toray paper GDL surfaces (one Teflon treated and one untreated), which were subject to shearing by air flowing in a channel under different mean-flow velocities and channel lengths. As shown by Chen et al. (2005), the static contact angle (θ_s) and contact angle hysteresis (the difference between advancing and receding contact angles, i.e., θ_A-θ_R), are both important parameters in determining the force required to move a droplet across a surface. From the droplet stability measurements, an instability diagram could be constructed from which the conditions for unstable droplets could be assessed. It is desirable to operate the fuel cell under such conditions that droplets become unstable and can be removed instantaneously from the GDL/GFC interface so as to prevent blockage of pathways for oxygen transport to the three-phase reaction sites.

Contact angle hysteresis on surfaces is generally measured using the conventional Wilhelmy plate, sessile drop, or tilting plate methods (Johnson et al. 1965, Adamson 1990, Lander et al. 1993). However, none of these experimental techniques is applicable to determine contact angle hysteresis during droplet growth, deformation, and detachment in a fuel cell cathode. In this work, an experimental technique, which simulates the actual shearing of liquid droplets by an air flow as would be encountered in a PEMFC, was developed to determine liquid water droplet instability on the surface of GDL materials.

Three material factors affect contact angle hysteresis of a given solid surface: physical roughness (or surface topology), chemical roughness (inhomogeneous surface energy), and average chemical surface energy (usually expressed in terms of a static contact angle). These factors play distinct roles in the continuity and pinning of the contact lines and thus the contact angle hysteresis of a droplet. Öner and McCarthy (2000) investigated the contact angle hysteresis of a variety of micro-patterned surface topographies and argued that the structure of the three-phase contact line is important to the dynamic wettability of a surface. They assert that a “screen” promotes the formation of a continuous contact line that will pin during advancing or receding of the contact line, while an island type of surface morphology promotes a discontinuous contact line which will not pin. Possible schematics of screen and island structures and their possible contact lines are shown in Figure 2.3.

In their experimental investigations, Öner and McCarthy determined that randomly arrayed surface features (on the order of 5 to 30 μm) in the x, y, and z dimensions could have lower contact angle hysteresis than regularly spaced features with constant heights (Öner and MaCarthy 2000). Chen et al. (1999) investigated the surface chemical factors that contribute to contact angle hysteresis. They were able to show that attaching monolayers of siloxane/hydrocarbon oligomers to silicon surfaces greatly reduced the contact angle hysteresis of water (θ_A/θ_R = 106°/105°), methyliodide (θ_A/θ_R = 70°/64°), and hexadecane (θ_A/θ_R = 30°/26°). These monolayer treatments produced surfaces that were extremely chemically uniform. Chemical roughness embodied by patches of hydrophilic and hydrophobic material (such as those that may exist in GDLs) could pin the contact line and cause an increase in contact angle hysteresis. Investigations of contact angle hysteresis on idealized surfaces help determine the factors that contribute to hysteresis on less well-characterized GDL surfaces.

2.2. Experimental

Contact angle hysteresis measurements of growing water droplets on GDL surfaces were performed. The experimental setup mimics the process in the fuel cell cathode where liquid water is generated in the catalyst layer, is transported through the GDL, and finally appears as water droplets at the GDL/GFC interface where they are deformed by the cathode air flow in the GFC. Because of the difficulty in generating droplets in a small channel (with characteristic dimensions on the order of 1 mm X 1 mm, as in the GFC of a PEMFC, a slot geometry was utilized where the channel width was much greater (2 cm) than the height (2 mm). This geometry approximates a slit. Figure 2.4 shows a schematic of the experimental apparatus for generating water droplets in a channel on the GDL surface whereas Figure 2.5 displays a schematic diagram of a PEMFC cathode with membrane, catalyst layer, GDL and GFC. The latter depicts water transport from the catalyst layer to flow channel and simultaneous oxygen transport from flow channel to the catalyst layer.

The GDL samples were mounted on plastic microscope cover slips with cyanoacrylate adhesive gel. A hole (diameter approximately 2.2 mm) in the cover slip allows water to contact the underside of the GDL. Water was delivered by a computer-controlled capillary syringe to the back side of the GDL at a rate of approximately 0.3 $\mu L/min$ or $5 \cdot 10^{-6}$ cm^3/s. At room temperature (25°C), the density of water is 0.997 g/cm^3; accordingly, the molar flow rate of water is $0.277 \cdot 10^{-6}$ *moles/s*. To generate this amount of water from the oxygen reduction reaction, a molar rate of oxygen of $0.1385 \cdot 10^{-6}$ *moles/s* is required. Using the cross-sectional area of the pre-drilled, water-supplied hole (0.038 cm^2) as the electrode area and from Faraday's law, we compute the corresponding current density to be 1.4 A/cm^2 ($i = \frac{4Fr_{o_2}}{A}$ with F =

96487 *C/mole*, r_{o_2} = 0.1385·10^{-6} *moles/s*, and A = 0.038 *cm*^{2}), which is a reasonably high current density for PEMFC operations where one could expect liquid water formation to occur. The water penetrated through the GDL and droplets were allowed to form naturally on the top-side of the GDL. A close-up of the sample geometry and droplet formation is shown in Figure 2.4b.

Even though water was introduced to a large area of GDL undersurface, water droplets tended to form only in certain, repeatable locations. Humidified air was forced through the channel with controlled flowrate and images of the deformed droplets were recorded at one-second intervals with a high magnification CCD camera. The images were then analyzed for droplet height (h) and advancing and receding contact angles (θ_A and θ_R respectively) as shown in Figure 2.6. The dimensionless droplet height ($\hat{H}$) is the height of the droplet (h) divided by the height of the channel (H) and the contact angle hysteresis is the difference of the advancing and receding contact angles, θ_A-θ_R. The droplet height and contact angle hysteresis data were used to create droplet stability diagrams (dimensionless droplet height versus contact angle hysteresis) as detailed in Section 2.3 (i.e., the Results and Discussion section) below, from which droplet instability could be assessed.

2.3. Results and Discussion

A series of images of a growing liquid water droplet at times 0, 20, 40, 65, and 90 seconds are shown in Figure 2.7. In this investigation we were concerned with the onset of droplet instability at which the droplet detaches from the surface or begins to spread across the surface forming a water film. The contact angle hysteresis and droplet height data were used to construct droplet stability diagrams as shown in Figure 2.8. The open shapes represent the observable states of the droplets in this experiment and the dotted line represents the “upper-bound” of the droplet stability. Above and to the left of this line there are no observable droplets because they have become unstable and detached or spread across the GDL surface. In general, as the droplet grows in height, a larger contact angle hysteresis is required to support the resulting viscous drag applied to the larger droplet by the flowing air. Initially, small droplets with little contact angle hysteresis are formed. As a droplet grows, the contact angle hysteresis increases, and this process of increasing height and resulting increasing contact angle hysteresis proceeds until the contact angle hysteresis of the material is exceeded and the droplet detaches, or the droplet spreads across the surface. There is scatter in the data below the upper bound of droplet stability due to smaller droplets sometimes having large contact angle hysteresis. These droplets usually grew in height without much increase in contact angle hysteresis until they reached in the stability limit (i.e., at the onset of instability) and then the contact angle hysteresis increased.

Three different parameters were explored experimentally: air flow velocity, channel length, and static contact angle. Experiments were carried out at air flow velocities of 200 and 400 cm/s on 30 weight % Teflon treated Toray carbon paper GDLs (θ_s = 140°) with growing droplets. Multiple runs under each set of conditions were executed in order to establish a "stability window" for the droplets. The experimentally measured droplet stability diagrams for 200 cm/s and 400 cm/s air flow velocities are shown in Figure 2.9. Larger contact angle hysteresis was measured for 400 cm/s for a given droplet height. This result is entirely predictable because the larger air flow velocity exerts more drag force on the droplet and causes it to deform to a greater extent.

The effect of channel length on the droplet stability diagram for a constant air flow velocity of 200 cm/s is shown in Figure 2.10. This result demonstrates the distinct advantage of longer gas flow channel lengths in fuel cells which create larger pressure drops for a given flow velocity which results in a larger instability window (see a more detailed discussion in Chapter 3). A smaller stability window is desirable because the droplets do not occupy as much of the channel (smaller droplet height) for a given contact angle hysteresis. This is important in an operating fuel cell because the droplets can block the gas flow channels and cause those channels to shut down or form water slugs that must be expelled by large pressure gradients.

Static contact angle (θ_s) on the GDL surface also affects droplet stability. On GDL materials, increased surface static contact angles can be achieved by impregnating the carbon paper substrate with Teflon or other hydrophobic polymers. A liquid water droplet on two GDLs, one Teflon treated (30 wt %) with θ_s = 140° and one untreated with θ_s = 120°, is shown in Figure 2.11, highlighting the effect of surface treatment on static contact angle. Droplet stability was examined on the two GDL materials in 4 cm channels with air flow velocities of 200 cm/s. The stability diagram for each GDL is shown in Figure 2.12. The measured droplet stability diagrams show that the Teflon treated GDL with increased surface static contact angles (highly hydrophobic) have smaller droplet stability windows that those GDLs with less hydrophobic static surface contact angles. This means that droplet removal from the fuel cell is enhanced on GDLs where the surface is treated to produce larger static contact angles. There are no data points above about 0.9 dimensionless channel heights, because the droplets tended to be slightly attracted to the upper surface of the slot and made contact with the upper plane when they grew to within 0.1 mm of the upper surface.

Droplets in high velocity air flows up to 2000 cm/s were observed at the GDL/GFC interface. At these high velocities, only small droplets were observed and they tended to spread rapidly because of their high contact angle hysteresis values as shown in Figure 2.13. The observation of quickly spreading droplets in high velocity shear flows is not a desirable attribute of GDL surfaces that were studied in this work. It

would be more desirable for GDL surfaces to support very little contact angle hysteresis which would promote droplet detachment and removal instead of spreading.

2.4. Summary and Concluding Remarks

Liquid water droplet stability on GDL surfaces can be affected by the material properties of the GDL surface, and GFC geometry and flow conditions. The effects of channel length, air flow velocity, and surface static contact angle on droplet stability were investigated in this study. It was observed that droplets become more unstable due to longer channel lengths, higher air flow velocities, and increased static contact angle. Droplet visualization experiments confirm that droplet detachment from the GDL in an air shear flow is highly unlikely due to the large contact angle hysteresis values for water droplets on GDL surfaces. In this experimental investigation, we were able to identify some of the key variables that influence droplet stability in this application. In the next chapter, we document our effort to correlate these experimental observations using a simplified model.

Large drops in high velocity fields tend to spread across the surface of the GDL rather than detaching. This observation has serious consequences for water removal from the fuel cell. Consequently, liquid water removal must be by other mechanisms such as annular water flow on the channel walls or evaporation. Current GDL materials are such that they can support large contact angle hysteresis values (over 60° in some cases), which leads to spreading droplets rather than droplet detachment. The ultimate goal is to not only characterize and accurately model the droplet growth and removal phenomenon in fuel cell gas flow channels, but also be able to guide GDL material design by elucidating the fundamental mechanisms of liquid water transport and removal in PEMFC systems. It is clear from this experimental study that liquid water droplets at the GDL/GFC interface are difficult to remove by the air flow in the channel due to the high contact angle hysteresis of the GDL materials. As a result, the channel must become partially or completely plugged before liquid water is expelled from the system. By reducing the physical roughness or chemically treating the GDL surface, liquid water droplet removal may be enhanced thereby reducing flooding in the channel and plugged channels.

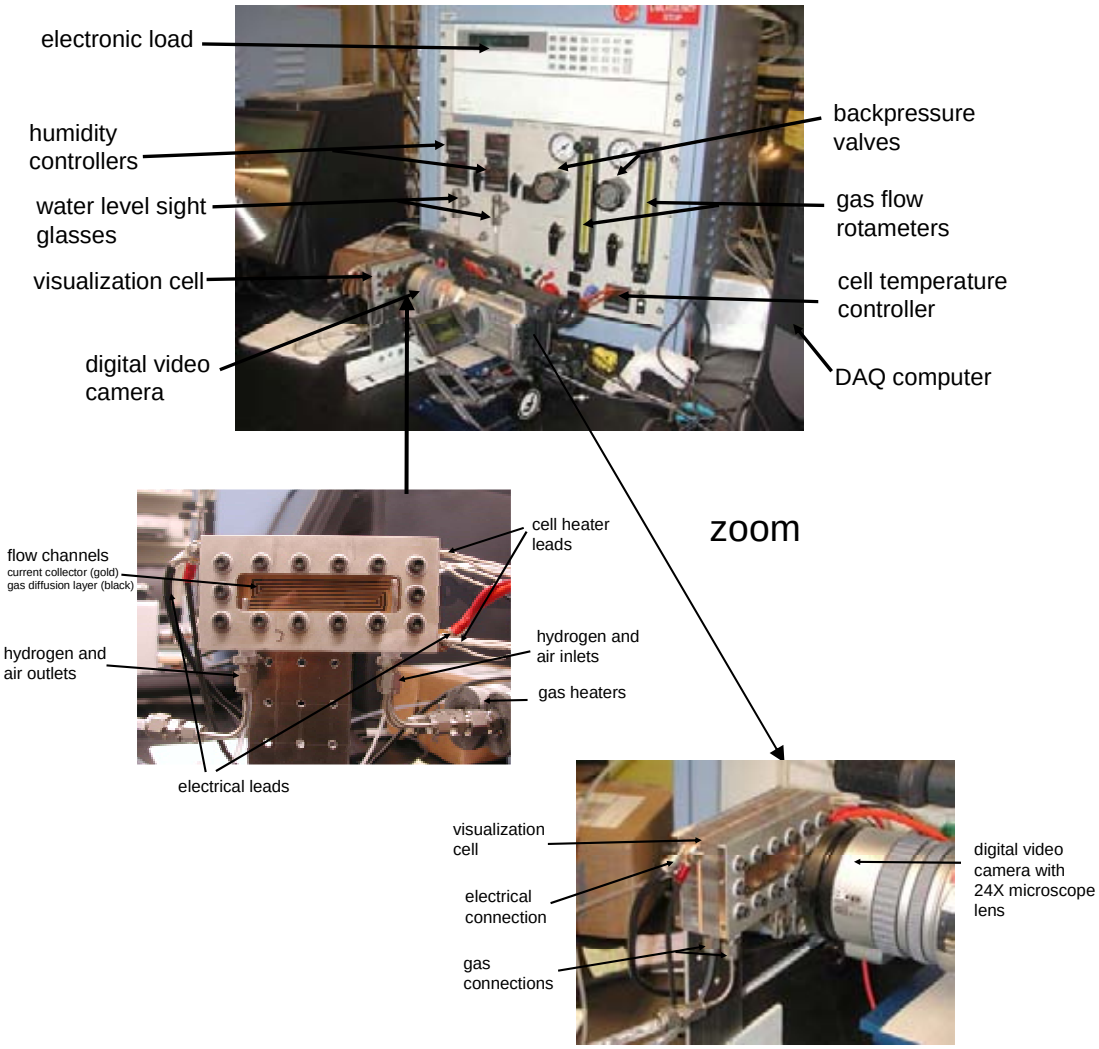

Figure 2.1. Specially-designed, transparent, fuel cell direct-visualization apparatus

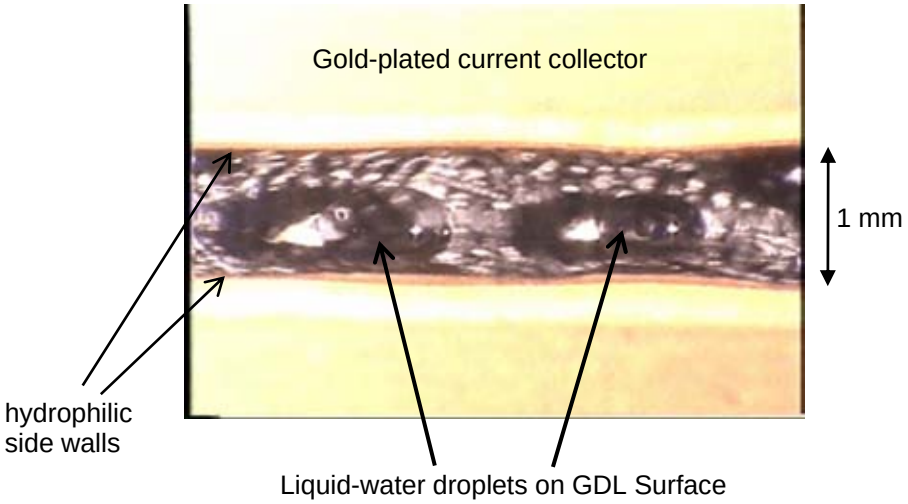

Figure 2.2a. Sample image of two water droplets forming at the GDL/GFC interface

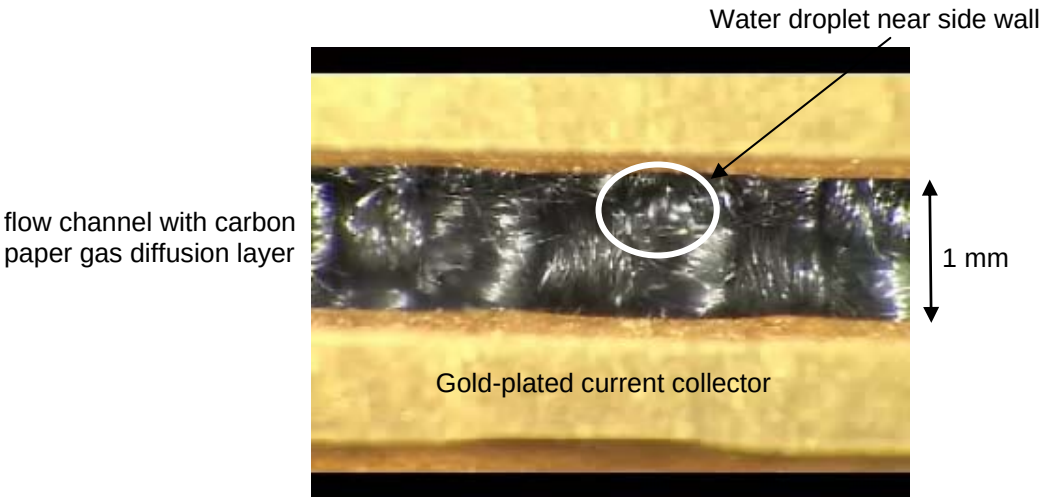

Figure 2.2b. Sample image of a water droplet forming near the hydrophilic GDL side wall

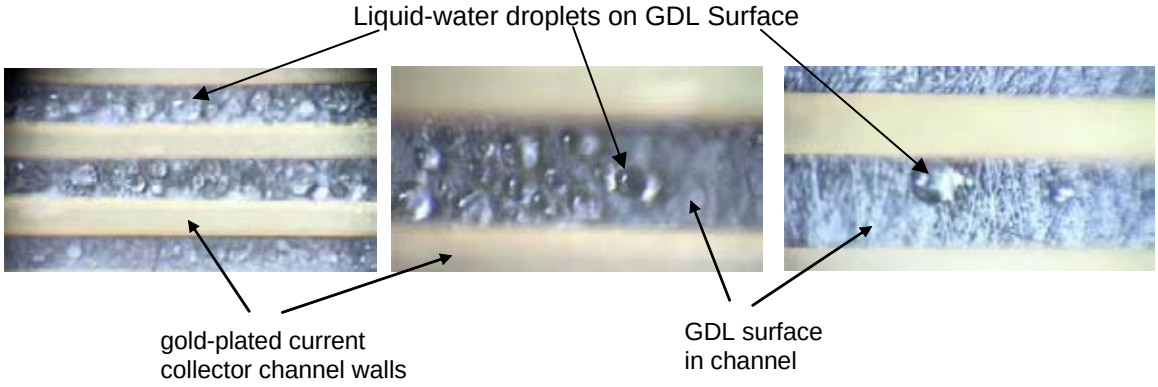

Figure 2.2c. More sample images of water droplets forming at the GDL/GFC interface

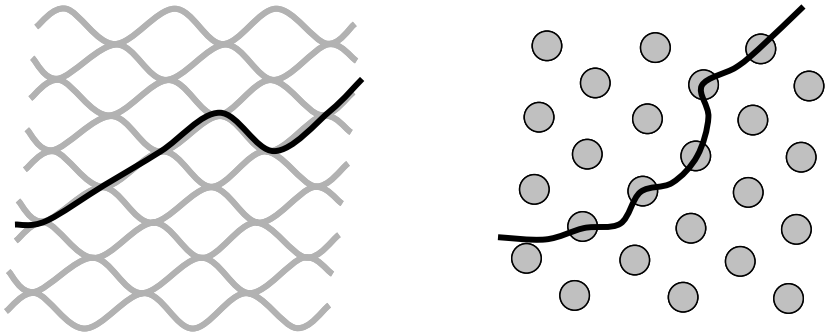

Figure 2.3. Screen (a) and island (b) surface structures and possible contact lines (re-drawn from Oner and McCarthy 2000).

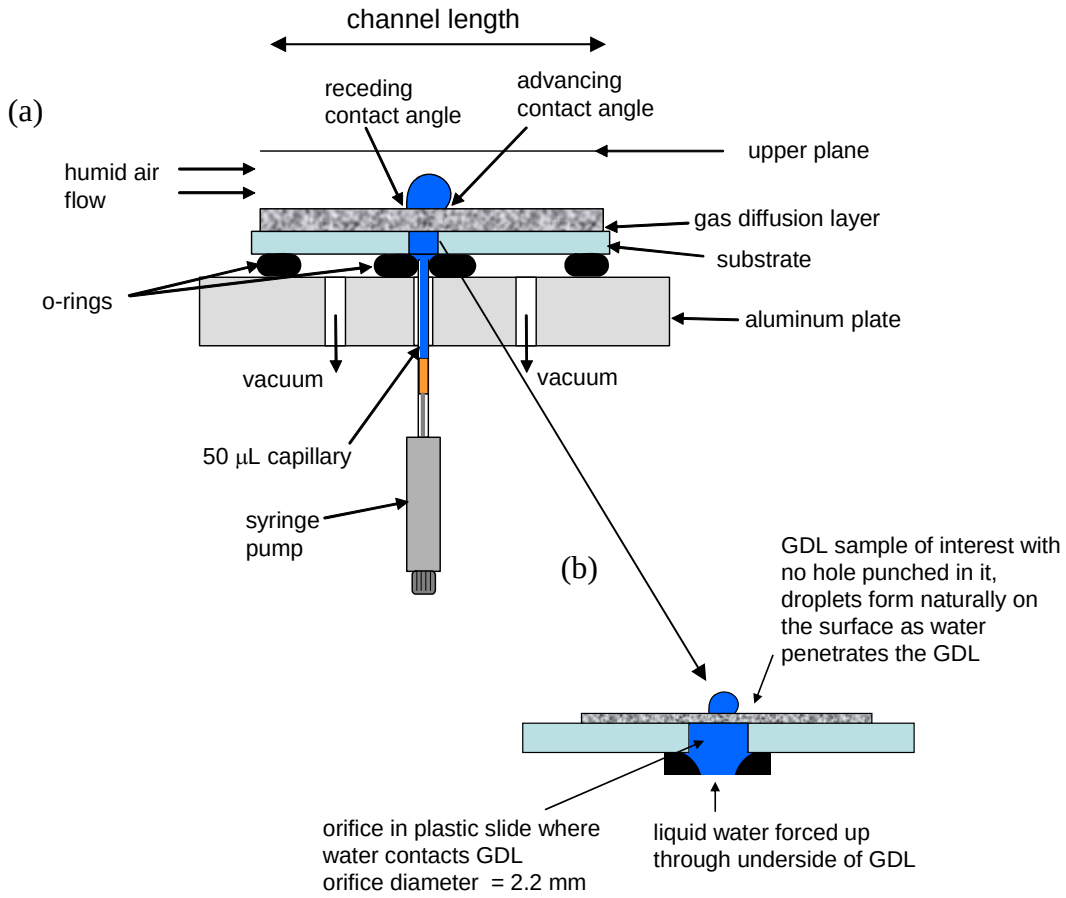

Figure 2.4. Schematic of the experimental apparatus for generating liquid water droplets in a channel on the GDL surface; (a) overall view of apparatus geometry, (b) close-up view of droplet emergence from GDL surface.

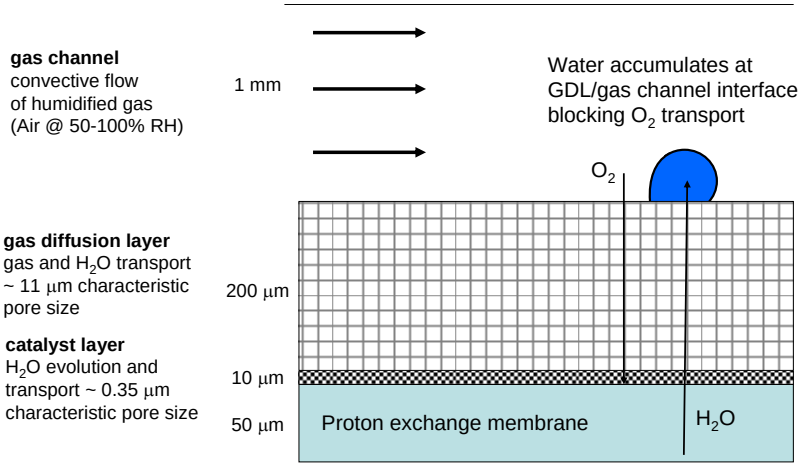

Figure 2.5. Schematic diagram of a PEMFC cathode with membrane, catalyst layer, GDL and GFC. Water transport from catalyst layer to flow channel and oxygen transport from flow channel to catalyst layer are depicted.

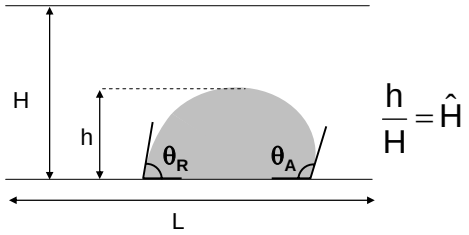

Figure 2.6. Advancing and receding contact angles, and droplet and channel heights.

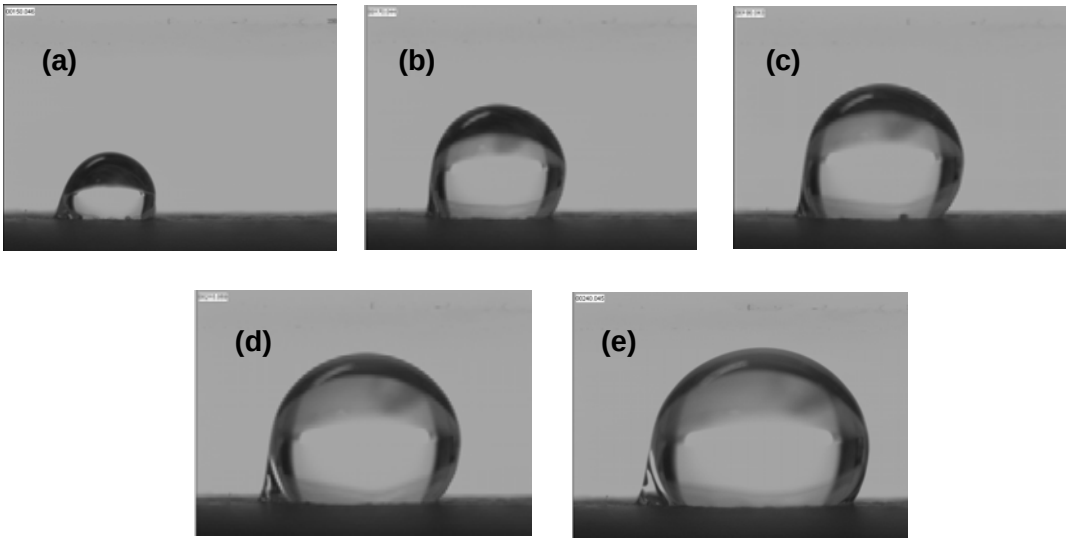

Figure 2.7. Images of water droplets sheared by air flowing at 750 cm/s: (a) t = 0 s, $\hat{H}$ = 0.29, (θ_A-θ_R) = 32°; (b) t = 20 s, $\hat{H}$ = 0.50, (θ_A-θ_R) = 45°; (c) t = 40 s, $\hat{H}$ = 0.59, (θ_A-θ_R) = 61°; (d) t = 65 s, $\hat{H}$ = 0.65, (θ_A-θ_R) = 63°; (e) t = 90 s, $\hat{H}$ = 0.68, (θ_A-θ_R) = 66°.

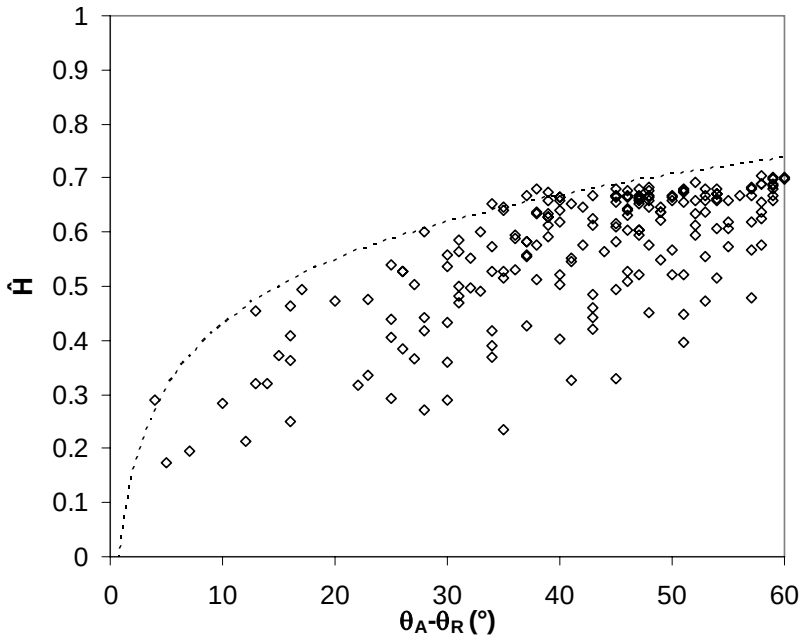

Figure 2.8. Droplet instability diagram for an air flow velocity of 800 cm/s, L = 7 cm and θ_s = 140°; (◊) experimental data points, (---) upper bound of experimental data.

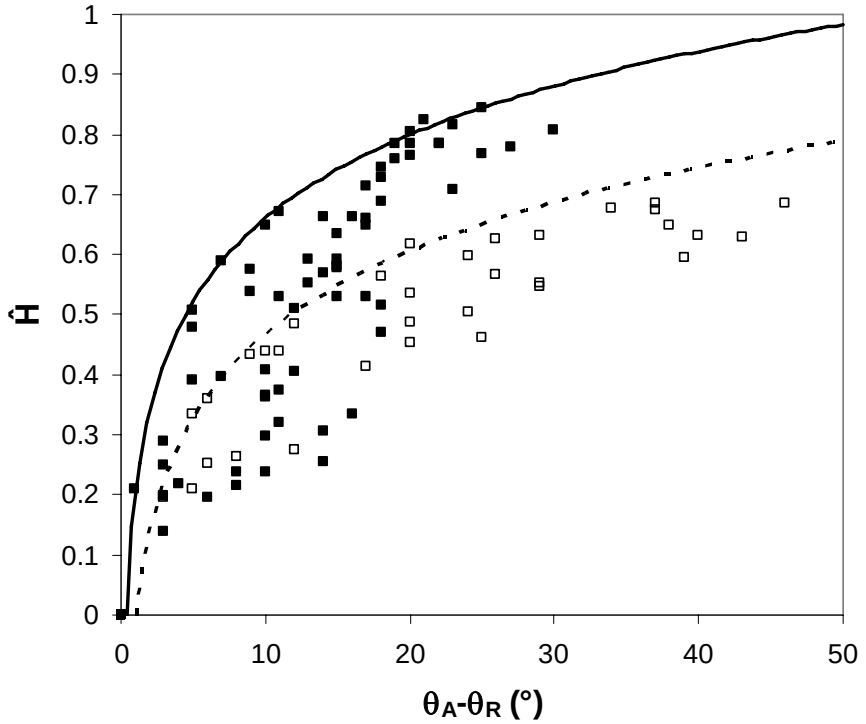

Figure 2.9. Droplet instability diagram for L = 14 cm and θ_s = 140°; (▪) experimental data for <v> = 200 cm/s and (−) upper bound, (▫) experimental data for <v> = 400 cm/s and (---) upper bound.

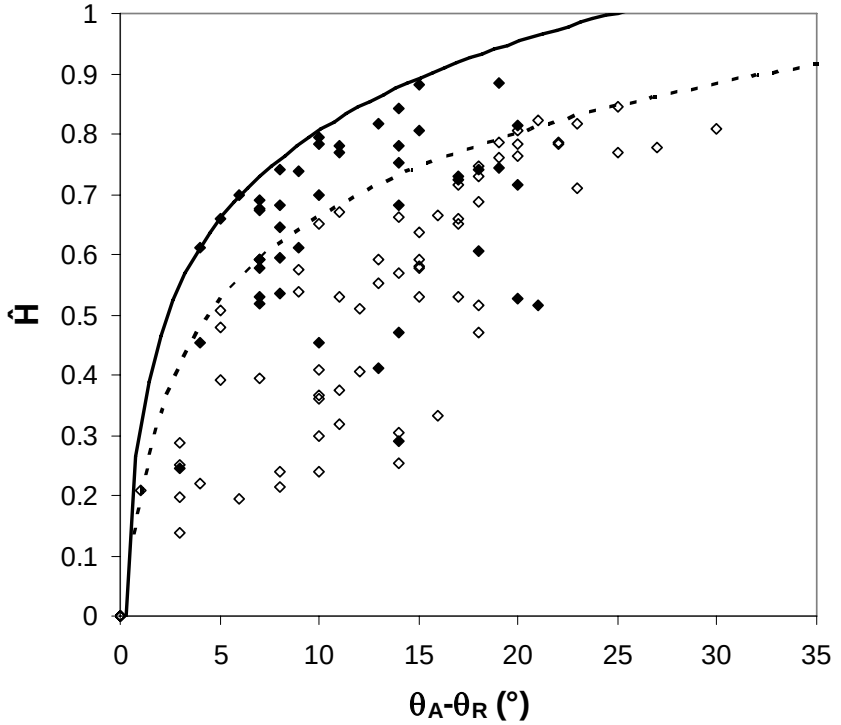

Figure 2.10. Droplet instability diagram for θ_s = 140°, <v> = 200 cm/s; (♦) experimental data for L = 4 cm and (−) upper bound, (◊) experimental data for L = 14 cm and (---) upper bound.

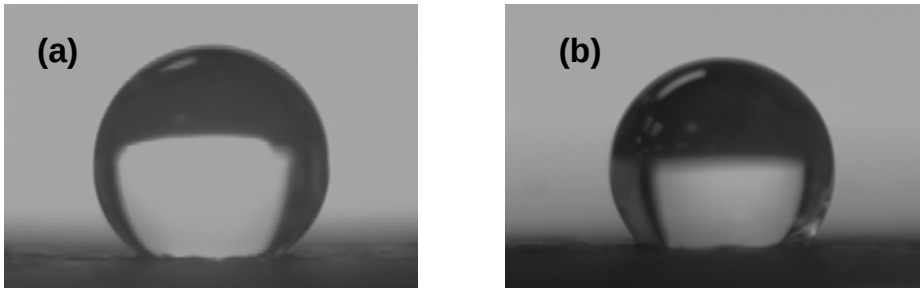

Figure 2.11. Static surface contact angles for Teflon treated and untreated Toray paper GLDs, 1 mm droplet height: (a) 30 wt % Teflon treated Toray paper GDL, θs = 140°; (b) untreated Toray paper GDL, θs = 120°.

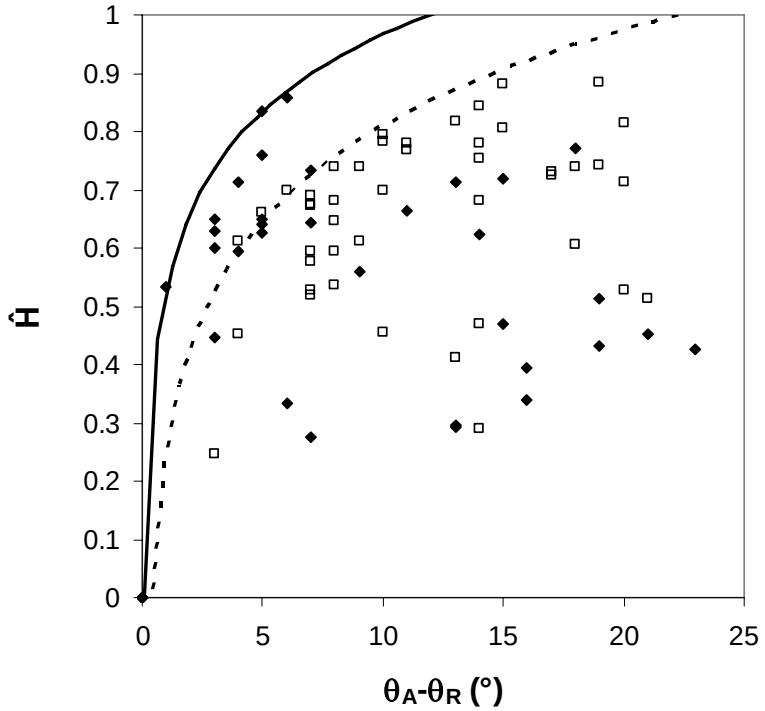

Figure 2.12. Droplet instability diagram for L = 4 cm, <v> = 200 cm/s; (♦) experimental data for θ_s = 120° and (−) upper bound, (▫) experimental data for θ_s = 140° and (---) upper bound.

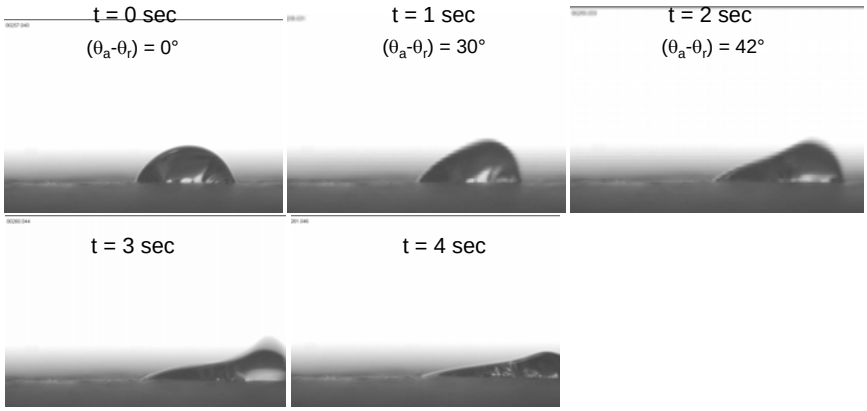

Figure 2.13. Water droplet spreading in 2000 cm/s air flow velocity.

3. Predicting the Onset of Water Droplet Instability at the Gas Diffusion Layer/Gas Flow Channel Interface[‡]

3.1. Introduction

As alluded to in Chapter 2, three distinct phenomena of liquid water transport occur in a PEMFC: 1) liquid water transport by capillary action within the gas diffusion layer from the catalyst layer (in which water is produced in the oxygen reduction reaction) to the GDL/GFC interface; 2) liquid water removal by flowing gas shearing and/or evaporation from the liquid-water/gas interfaces; and 3) liquid water transport within the gas flow channels. Analyzing liquid water removal from the GDL/GFC interface is the subject matter of this chapter.

Recently, water management and cathode flooding in PEMFCs have received much attention in the literature due to their importance. An extensive review article by Wang (2004) on fundamental models for fuel cell engineering provides a timely review on the subject of liquid water transport in PEMFCs. Several numerical studies employing the macroscopic two-phase transport approach in modeling liquid water transport in PEMFCs by various research groups have been reported (e.g., He et al. 2000, Wang et al. 2001, Natarajan and Nguyen 2001, 2003; You and Liu 2002, Berning and Djilali 2003, Mazumder and Cole 2003, Siegel et al. 2004; Pasaogullari and Wang 2004, 2005); all these studies focus on the liquid water transport through the cathode GDL, but do not investigate the key phenomenon of liquid water removal at the cathode GDL/GFC interface (i.e., how the liquid water gets off the GDL/GFC interface and enters into the GFC). To the authors' knowledge, no modeling work on analyzing liquid water removal at the cathode GDL/GFC interface has been reported in the open literature at the time when this work was carried out.

There have been relatively few experimental studies that aim at elucidating water transport, and in particular liquid water transport, in PEMFCs. Mench et al. (2003) employed gas chromatography in measuring the in-situ flow channel water vapor distribution with full humidification in an operating fuel cell flow field. Tuber et al. (2003) visualized water accumulation in a PEMFC by using a fuel cell with transparent walls. They recorded images of water formed inside the cathode gas flow channels under fuel cell operation with a digital camera. They found that significant drops in current density were correlated with their visual observation of liquid water in the flow channel. Satija et al. (2004) reported images of water formation and distribution in an operating PEM fuel cell obtained by the in-situ neutron imaging technique. Their work focused on exploring the experimental method of neutron imaging (as a tool to perform in-situ non-destructive analysis on an operating PEMFC) rather than on elucidating the liquid

[‡] Portion of this chapter has been published in a journal paper: K. S. Chen, M. A. Hickner, and D. R. Noble, "Simplified models for predicting the onset of liquid water droplet instability at the gas diffusion layer/gas flow

water transport phenomena. More recently, Yang et al. (2004) reported direct visualization of liquid water transport in a PEMFC made of transparent walls and under automotive conditions (0.82 A/cm^2, 70° C, and 2 atm). They provided experimental evidence and empirical data on the mechanics of liquid water transport: from droplet emergence on the GDL/GFC interface, to droplet growth and departure, and to two-phase flow in the GFC. More specifically, they presented images of the water droplet distribution in the GFC and the dynamic process of water droplets growing, coalescing, and being broken up to form a liquid film on the hydrophilic sidewalls.

Though no modeling work applicable to water droplet removal at the cathode GDL/GFC interfaces as in PEMFCs has been reported in the literature at the time when this work was carried out, the subject of displacing liquid droplets from solid surfaces is a fundamental problem of fluid mechanics and has attracted considerable interests due to their important applications in chemical process technologies such as coating-flow manufacturing processes and enhanced oil recovery (see, e.g., Dussan V. and Chow 1983, Dussan V. 1985, 1987; Dimitrakopoulos and Higdon 1997, 1998, 2001). The first two studies by Dussan V. and co-workers, which consider only small drops with small contact angles and employ analytical techniques (made possible by using lubrication theory and asymptotic analysis) for solving the resultant governing equations, focused on the influence of gravity in dislodging the drops from non-horizontal surfaces. They found that the contact angle hysteresis (which is defined as the difference between the advancing contact angle and the receding contact angle, $\theta_a - \theta_r$) is the single most important characteristic of the system. The third study by Dussan V. evaluated the ability of the creeping motion of the surrounding fluid to remove the drops by sweeping them across the solid surface. More recently, Dimitrakopoulos and Higdon (1997, 1998, 2001) employed the spectral finite element method to numerically investigate the displacement or stability of fluid droplets from solid surfaces in shear and viscous pressure driven flows with vanishing Reynolds number (that is, creeping flows in which Stokes equations apply). They determined the optimal droplet shape and contact line position that allows the highest flow rate for which the droplet can adhere to the surface. They separately examined the effects of the viscosity ratio between the fluids, the capillary number, the plate separation, and the contact angle hysteresis. Whereas Dussan V.'s asymptotic analyses are limited to small drops with small contact angles (which means strongly hydrophilic solid surfaces), Dimitrakopoulos and Higdon's numerical studies are applicable only to creeping flows with vanishing Reynolds numbers (which are suitable for analyzing processes in which inertia effect can be neglected, e.g., coating-flow manufacturing processes). Consequently, neither Dussan V.'s asymptotic theory nor Dimitrakopoulos and Higdon's boundary-element models can be employed to analyze the process of liquid water removal from the GDL/GFC

channel interface", *Int. J. Energy Research*, **29**, p. 1113 – 1132 (2005).

interface, in which the Reynolds number is on the order of hundreds or higher and the solid surface is hydrophobic (that is, $\theta_a > 90°$). Thus, new models are needed.

The present work focuses on elucidating the instability leading to the removal of water droplets at the GDL/GFC interface when subject to shearing by the pressure gradient driven gas flow. The objective of the present work was to develop simplified models that can be employed to predict the behavior of water droplets for given channel geometry, flow condition, and hydrophilic/hydrophobic nature of the GDL/GFC interface. Predictions computed from the simplified spherical-droplet model were then compared against experimental data. To assess its validity, predictions computed from the simplified cylindrical-droplet model were compared with results from two-dimensional finite element simulations of flow above cylindrical droplets. Comparison between full flow analysis and simplified model prediction for spherical droplets requires three-dimensional finite-element simulation – such time-intensive computational undertaking has not been carried out in the present work and awaits future efforts.

3.2. Simplified Models

3.2.1. Spherical droplet

Figure 3.1 shows a control volume (cross section along the flow direction) enclosing the spherical water droplet growing at the interface between the gas diffusion layer (GDL) and the gas flow channel (GFC). Macroscopic force balance along the channel-flow direction (i.e., *z*-direction as shown in Figure 3.1) within the control volume that encloses the spherical droplet yields

$$(p_0' - p_L')2Bl + l^2 \tau_{xz}{}^w + f_{\mu,d} = 0 \qquad (3.1),$$

where p_0' and p_L' are the flowing gas pressure immediately upstream and downstream of the water droplet, respectively; $2B$ is the height of the flow channel; l is the maximum distance between upstream droplet surface and downstream droplet surface; $l^2 \tau_{xz}{}^w$ represents the shear stress exerted by the flowing gas on the top wall in an area of l^2 (which is the area projected by the droplet); $f_{\mu,d}$ is the viscous drag exerted on the water droplet by the flowing gas. By approximating the flow channel between the top wall surface and the droplet surface as that between two parallel plates with height $2b$, and taking flow to be fully developed and laminar and the flowing fluid to be Newtonian, the top-wall shear stress per unit area, $\tau_{xz}{}^w$, can be estimated as follows (see, e.g. Bird et al. 2002, p. 63):

$$\tau_{xz}{}^w = \frac{(p_0' - p_L')}{l}(-b) \qquad (3.2).$$

Substituting Equation (3.2) into Equation (3.1) yields an approximation for the viscous drag on the droplet surface:

$$-f_{\mu,d} = (p_0' - p_L')(2B - b)l \tag{3.3}$$

It is interesting to check the limit when the droplet completely blocks the channel, that is, at $b = 0$ and $l = 2B$:

$$-f_{\mu,d,\max} = (p_0' - p_L')(2B)^2 = (p_0' - p_L')4B^2 \tag{3.4}$$

indicating that the shear stress on the top wall surface vanishes and the drag on the droplet achieves its maximum value, as expected. By taking the flowing gas to be a Newtonian fluid, the flow to be fully developed and laminar in a narrow slit (velocity profiles for such flows are well documented, see e. g., Bird et al. 2002), the pressure drop across the droplet, $(p_0' - p_L')$, can be related to the overall pressure drop, average velocity, viscosity, and channel height:

$$(p_0' - p_L') = (p_0 - p_L) - (L - l)\frac{3\mu U}{B^2} \tag{3.5}$$

and

$$(p_0' - p_L') = \frac{3\mu U'}{b^2} l \tag{3.6}$$

where p_0 and p_L are the flowing gas pressure at the entrance and exit of the channel, respectively, L is the length of the flow channel, μ is the flowing-gas viscosity, U is the average velocity along flow direction in the upstream and downstream regions, and U' is the average velocity along flow direction in the region directly above the droplet. From mass balance,

$$U' = \frac{B}{b}U \tag{3.7}$$

Substituting Equation (3.7) in Equation (3.6), solving for U' in terms of $(p_0' - p_L')$, and then substituting the resultant in Equation (3.5) gives

$$(p_0' - p_L') = (p_0 - p_L)\frac{l}{l + (L - l)\left(\frac{b}{B}\right)^3} \tag{3.8}$$

Combining Equations (3.3) and (3.8) yields an approximate viscous drag on the droplet surface in terms of the overall pressure drop and droplet size:

$$-f_{\mu,d} = (p_0 - p_L)\frac{l^2(2B-b)}{l+(L-l)\left(\frac{b}{B}\right)^3} \tag{3.9}$$

From Figure 3.1, the height of the minimum flow passage between the top wall surface and the droplet surface is related to the channel height, droplet radius (r), and advancing contact angle (θ_a) by

$$2b = 2B - r\cos\theta_a \quad \text{or} \quad b = B - \frac{r}{2}\cos\theta_a \tag{3.10}$$

Upon substituting Equation (3.10), Equation (3.9) becomes

$$-f_{\mu,d} = \frac{(p_0 - p_L)B(\frac{l}{L})^2 L(1+\widehat{H})}{(1-\widehat{H})^3 + \frac{l}{L}[1-(1-\widehat{H})^3]}, \tag{3.11}$$

where

$$\widehat{H} = \frac{r(1-\cos\theta_a)}{2B} \tag{3.12}$$

is the dimensionless droplet height based on the channel height with θ_a varying from 0° to 180°. When the droplet grows to be sufficiently large and with $\theta_a \geq 90^o$, $l = 2r$ as shown in Figure 3.1, Equation (3.11) can be simplified to

$$-f_{\mu,d} = \frac{(p_0 - p_L)}{L}\frac{16B^3}{(1-\cos\theta_a)}\frac{(1+\widehat{H})\widehat{H}^2}{(1-\cos\theta_a)(1-\widehat{H})^3 + \frac{4B}{L}\widehat{H}[1-(1-\widehat{H})^3]} \tag{3.13}$$

or, in terms of average velocity in the upstream and downstream regions away from the droplet, the approximate viscous drag exerted on the droplet is given by

$$-f_{\mu,d} = \frac{48\mu UB}{(1-\cos\theta_a)}\frac{(1+\widehat{H})\widehat{H}^2}{(1-\cos\theta_a)(1-\widehat{H})^3 + \frac{4B}{L}\widehat{H}[1-(1-\widehat{H})^3]} \tag{3.14}$$

The total surface tension force, $f_{\gamma,d}$, which tends to hold the droplet in place, is given by

$$f_{\gamma,d} = \pi(r\sin\theta_a)\gamma\cos(180-\theta_a) + \pi(r\sin\theta_a)\gamma\cos\theta_r \tag{3.15}$$

where the first and second terms on the right side represent the surface-tension forces acting on the advancing and receding contact lines, respectively; $r\sin\theta_a$ denotes the droplet's wetted radius; θ_a and θ_r refer to the advancing and receding contact angles, respectively; and γ is the surface tension of liquid water (more accurately, γ denotes the surface-tension force per unit length acting on the liquid-water/air

interface). Making use of trigonometric relations and the fact that $r = 2B\widehat{H}/(1-\cos\theta_a)$, Equation (3.15) can be re-written as

$$f_{\gamma,d} = \frac{4\pi B\widehat{H}\sin\theta_a}{1-\cos\theta_a}\gamma\sin\frac{1}{2}(\theta_a+\theta_r)\sin\frac{1}{2}(\theta_a-\theta_r) = \frac{4\pi B\widehat{H}\sin\theta_a}{1-\cos\theta_a}\gamma\left[(\sin\theta_a)y\sqrt{1-y^2}-(\cos\theta_a)y^2\right] \quad (3.16)$$

where $y = \sin\frac{1}{2}(\theta_a-\theta_r)$. At the onset of droplet instability, the surface tension force and the viscous drag (which tends to shear the droplet along the GDL/GFC interface) balance each other:

$$f_{\gamma,d} + f_{\mu,d} = 0 \quad \text{or} \quad -f_{\mu,d} = f_{\gamma,d} \quad (3.17).$$

Substituting Equations (3.14) and (3.16) into Equation (3.17) and approximating the advancing contact angle by the static contact angle (θ_s) result in a nonlinear equation relating the critical droplet height to contact angle hysteresis, ($\theta_a-\theta_r$), at the onset of instability:

$$y\sqrt{1-y^2}-(\cot\theta_s)y^2 - \frac{12\mu U}{\pi\gamma\sin^2\theta_s}\frac{\widehat{H}(1+\widehat{H})}{(1-\cos\theta_s)(1-\widehat{H})^3+\frac{4B}{L}\widehat{H}[1-(1-\widehat{H})^3]} = 0 \quad (3.18),$$

where $0<\theta_s<180°$. Equation (3.18) can be conveniently solved for y using Newton's method with $\widehat{H}$ varying from 0 to 1. Once y is computed, then the contact angle hysteresis can be determined from $(\theta_a-\theta_r) = 2\sin^{-1}(y)$.

3.2.2. Cylindrical droplet

Macroscopic force balance within a control volume that encloses a cylindrical droplet having a length (normal to the flow direction or into the page) of unity yields an equation similar to Equation (3.3) for a spherical droplet:

$$-f_{\mu,d,cylindrical} = (p_0'-p_L')(2B-b) \quad (3.19).$$

Following the steps in section 3.2.1 in deriving the viscous drag for a spherical droplet (that is, expressing the local pressure drop, $p_0'-p_L'$, in terms of the overall pressure drop, p_0-p_L, and the minimum flow passage height, b, in terms of the dimensionless droplet height, $\widehat{H}$), the following equation relating viscous drag exerted on the cylindrical droplet with a length of unity by the flowing gas is obtained:

$$-f_{\mu,d,cylindrical} = \frac{(p_0 - p_L)}{L} 4B^2 \frac{(1+\widehat{H})\widehat{H}}{(1-\cos\theta_a)(1-\widehat{H})^3 + \frac{4B}{L}\widehat{H}[1-(1-\widehat{H})^3]} \quad (3.20).$$

In terms of average velocity in the upstream and downstream regions, this equation becomes

$$-f_{\mu,d,cylindrical} = 12\mu U \frac{(1+\widehat{H})\widehat{H}}{(1-\cos\theta_a)(1-\widehat{H})^3 + \frac{4B}{L}\widehat{H}[1-(1-\widehat{H})^3]} \quad (3.21).$$

The total surface-tension force acting on the contact lines of a cylindrical droplet with a length (normal to flow direction or into the page) of unity is given by

$$f_{\gamma,d} = \gamma\cos(180-\theta_a) + \gamma\cos\theta_r = 2\gamma\sin\frac{1}{2}(\theta_a+\theta_r)\sin\frac{1}{2}(\theta_a-\theta_r)$$
$$= 2\gamma[(\sin\theta_a)y\sqrt{1-y^2} - (\cos\theta_a)y^2] \quad (3.22).$$

Equating Equations (3.21) and (3.22) yields an equation relating the critical height of a cylindrical droplet to the contact angle hysteresis at the onset of instability:

$$y\sqrt{1-y^2} - (\cot\theta_s)y^2 - \frac{6\mu U}{\gamma\sin\theta_s}\frac{\widehat{H}(1+\widehat{H})}{(1-\cos\theta_s)(1-\widehat{H})^3 + \frac{4B}{L}\widehat{H}[1-(1-\widehat{H})^3]} = 0 \quad (3.23),$$

where $y = \sin\frac{1}{2}(\theta_a - \theta_r)$ as in Equations (3.16) and (3.18). In arriving at Equation (3.23), the advancing contact angle (θ_a) was approximated by the static contact angle (θ_s) as was done in deriving Equation (3.18).

3.3. Two-Dimensional Flow Simulation

To assess the validity of the simplified cylindrical-droplet model, two-dimensional analyses via finite element simulations are carried out, and results from the finite-element simulations of flow over cylindrical droplets are then compared with predictions computed by the simplified cylindrical-droplet model. Taking the flowing gas and liquid water inside the droplet to be incompressible Newtonian fluids, velocities and hydrodynamic pressures in the GFC and inside the droplet are governed by the steady Navier-Stokes equation system that accounts for momentum and mass conservation:

$$\mathrm{Re}\,\mathbf{u}\cdot\nabla\mathbf{u} - \nabla\cdot\mathbf{T} = 0 \quad \text{where} \quad \mathbf{T} = -p\mathbf{I} + \mu[\nabla\mathbf{u} + (\nabla\mathbf{u})^T] \quad (3.24),$$

$$\nabla\cdot\mathbf{u} = 0 \quad (3.25),$$

where $\mathrm{Re} = \frac{\rho UB}{\mu}$ is the Reynolds number with ρ and μ being fluid density and viscosity, respectively, U being the mean velocity in regions away from the droplet, and B being the half channel height as defined in section 3.2. In Equation (3.24), the gravity term has been dropped because the effect of gravity in the present problem is negligible. The position of the liquid water/flow gas interface (i.e., the shape of the droplet) is determined by the traction boundary condition, or force balance, at the liquid/gas interface:

$$\mathbf{n} \cdot \mathbf{T}_g = \mathbf{n} \cdot \mathbf{T}_l + 2\gamma\kappa\mathbf{n} \tag{3.26},$$

where subscripts g and l denote gas and liquid phases, respectively; **n** is the unit vector normal to the liquid/gas interface with **n** pointing into the gas phase; κ is the local curvature along the liquid/gas interface; and γ is surface tension of water. The other boundary condition at the liquid/gas interface is the requirement that the velocities be continuous at the interface. The Navier-Stokes equation system (Equations (3.24) and (3.25)) as well as pseudo-solid mesh-motion equations that employ an arbitrary Lagrangian Eulerian (ALE) formulation are solved using the finite-element method and a fully coupled implicit solution scheme via Newton's technique. The ALE formulation and its applications to free-surface flows are detailed by Sackinger et al. (1995), whereas the fully coupled implicit solution scheme via Newton's technique is documented by Schunk et al. (1997).

The boundary conditions for the water droplet on the GDL surface are such that the contact lines are pinned but the angles of contact at both the advancing and receding contact lines are not specified; instead, they are part of the solution to Equations 3.24 – 3.26.

3.4. Results and Discussion

3.4.1. Necessary conditions for preventing droplets from lodging in the flow channel

By considering the extreme scenarios in which droplets grow to the full channel height and using the simplified models developed in section 3.2, necessary conditions for preventing droplets from lodging in the flow channel were developed and are presented in this section.

3.4.1.1. Spherical droplets

When the droplet grows to the full channel height, i.e. when $\widehat{H} = 1$, Equation (3.14) with $\widehat{H} = 1$ yields

$$-f_{\mu,d,\max} = \frac{24\mu UL}{(1-\cos\theta_a)} \tag{3.27}.$$

Similarly, Equation (3.16) with $\widehat{H} = 1$ yields

$$f_{\gamma,d,\max} = \frac{4\pi B \sin\theta_s}{1-\cos\theta_s}\gamma \sin\frac{1}{2}(\theta_a+\theta_r)\sin\frac{1}{2}(\theta_a-\theta_r) \tag{3.28}$$

To prevent droplets from lodging in the flow channel, it is necessary that the viscous drag exerted on the droplet be greater than the surface-tension force acting on the droplet's contact lines, i.e.

$$-f_{\mu,d,\max} > f_{\gamma,d,\max} \tag{3.29}$$

Substituting Equations (3.27) and (3.28) into (3.29) yields a necessary condition for preventing spherical droplets from lodging in the flow channel:

$$\frac{L}{2B}\frac{\mu U}{\gamma} > \frac{\pi}{12}\sin\theta_s \sin\frac{1}{2}(\theta_a+\theta_r)\sin\frac{1}{2}(\theta_a-\theta_r) \tag{3.30}$$

Since $\sin\theta_s \sin\frac{1}{2}(\theta_a+\theta_r)\sin\frac{1}{2}(\theta_a-\theta_r) < 1$ and $\sin\frac{1}{2}(\theta_a+\theta_r) < 1$, Equation (3.30) can be further simplified to

$$\frac{L}{2B}\frac{\mu U}{\gamma} > \frac{\pi}{12} > \frac{\pi}{12}\sin\theta_s \sin\frac{1}{2}(\theta_a-\theta_r) > \frac{\pi}{12}\sin\theta_s \sin\frac{1}{2}(\theta_a+\theta_r)\sin\frac{1}{2}(\theta_a-\theta_r) \tag{3.31}$$

Equation (3.31) states simply that if the product of channel length-to-height aspect ratio by the capillary number is greater than $\pi/12$, then spherical droplets can be prevented from lodging in the flow channel. Some design rules can be readily developed from Equation (3.31). Regardless wetting properties or characteristics at the GDL/GFC interface, water droplet removal can be enhanced by increasing the aspect ratio of channel length to channel height or by increasing the flowing-gas average velocity in the flow channel. The aspect ratio of channel length to channel height can be increased by either lengthening the channel or reducing channel height. Since the gas flow channel is usually a square duct, reducing the channel height implies reducing the channel width also. This design rule of increasing the channel aspect ratio may in part explain the serpentine flow channel design widely employed in practice and perhaps also the trend toward reducing channel width/height. It should be pointed out that the discussion presented above applies to the situation in which only a single droplet emerges from the GDL/GFC interface at any given time. In a real-world operating PEMFC, multiple water droplets may emerge simultaneously from the GDL/GFC interface along the flow-channel – this scenario may change the pressure gradients exerting on droplets downstream and thus affect their instabilities. Moreover, lengthening flow channel while maintaining a constant pressure gradient (or mean velocity) requires raising the pressure drop across the

entire channel. With fixed channel geometry and flow conditions, droplet removal can be improved by making the GDL/GFC interface more hydrophobic or reducing contact angle hysteresis.

3.4.1.2. Cylindrical droplets

Similarly, a necessary condition for preventing cylindrical droplets from lodging in flow channels was developed from Equations (3.21) and (3.22) with $\widehat{H} = 1$:

$$\frac{L}{2B}\frac{\mu U}{\gamma} > \frac{1}{6} > \frac{1}{6}\sin\frac{1}{2}(\theta_a + \theta_r)\sin\frac{1}{2}(\theta_a - \theta_r) \qquad (3.32).$$

Equation (3.32) states simply that if the product of channel length-to-height aspect ratio by the capillary number is greater than 1/6, then cylindrical droplets can be prevented from lodging in the flow channel. Since $\pi/12 > 1/6$, it is clear from comparing Equations (3.31) and (3.32) that it is easier to prevent cylindrical droplets from lodging in the flow channel as compared with spherical ones.

3.4.2. Predicted instability windows for partially grown droplets – base-case studies

For partially grown spherical droplets (i.e., $\widehat{H} < 1$), Equation (3.18) was solved numerically using Newton's method to obtain the dimensionless droplet height ($\widehat{H}$) as a function of contact angle hysteresis ($\theta_a - \theta_r$) at the onset of instability so that the droplet-instability windows could be constructed. For partially grown cylindrical droplets, Equation (3.23) was solved to obtain the critical values of $\widehat{H}$ and ($\theta_a - \theta_r$) for constructing the droplet-instability windows. Figure 3.2 shows a pair of droplet-instability windows, respectively for spherical and cylindrical droplets, computed by the simplified models in a base-case study. Parameters for the base-case study are: $2B$ = 0.1 cm, L = 5 cm, U = 500 cm/s, μ = 0.0002087 poise (or g cm^{-1} s^{-1}), γ = 62.5 dyne/cm, and θ_s = 110°. Here, the viscosity and surface tension values correspond to that of air and that of liquid water at 80° C, respectively. The value of static contact angle chosen is typical of GDLs used in PEFCs. The values of channel height and mean velocity of flowing gas used are also typical of PEFC operations. Since density of air at 80° C is about 0.001 g/cm^3, the Reynolds number with parameter values in the base case is around 240. As can be easily seen in Figure 3.2, the instability window for a spherical droplet is narrower than that for a cylindrical droplet – this means that a spherical droplet is more stable and thus more difficult to be removed from the GDL/GFC interface than a cylindrical one – similar conclusion is also reached in Section 3.4.1 for fully grown droplets. This can be explained in terms of the ratio of surface area to wetted length. For convenience, let's consider a spherical droplet with the wetting line situated at the equator (such that its surface area is $2\pi r^2$ and its wetted length is $2\pi r$ with r being the droplet radius) and a cylindrical droplet

with the wetting line also located at the equator (such that its surface area is πrL and its wetted length is 2L with r being the radius and L being the length of the droplet, respectively). For such a cylindrical droplet, the surface-area-to-wetted-length ratio is $(\pi/2)r$ whereas it is r for a such spherical droplet. That is, the surface-area-to-wetted-length ratio for a cylindrical droplet is $(\pi/2)$ times of that for a spherical droplet. Consequently, a cylindrical droplet is less stable and can be removed more easily as compared with a spherical droplet. Again, in Section 3.4.1, similar conclusion is also drawn for fully grown droplets.

The effect of channel length on spherical-droplet instability is displayed in Figure 3.3. Here, the channel length is varied from 3.5 cm to 14 cm with the other parameters being the same as in the base case. Figure 3.3 clearly shows that lengthening the GFC while holding the other parameters fixed enlarges the instability window. It should be pointed out that lengthening flow channel while maintaining a constant pressure gradient (or mean velocity) requires raising the pressure drop across the entire channel as indicated by the inset of Figure 3.3 in which pressure drop over the droplet is plotted as a function of flow channel length. Figure 3.4 shows the effect of mean gas flow velocity on spherical-droplet instability. Plainly, increasing the mean gas flow velocity (which requires higher pressure drop across the GFC) with the other parameters fixed enlarges the instability window as is expected intuitively. Lastly, Figure 3.5 displays the effect of the static contact angle of the GDL/GFC interface (which depends on its hydrophilic/hydrophobic nature). As can be seen from the figure, increasing the static contact angle (which means making the GDL/GFC interface more hydrophobic) enlarges the instability window and thus enhances droplet removal.

3.4.3. Comparison between computed and measured droplet instability windows

The contact angle hysteresis ($\theta_a - \theta_r$) and dimensionless droplet height ($\hat{H}$) were measured for each image as detailed in Chapter 2 (see, Figures 2.6 and 2.7). Using these data, droplet-instability windows were constructed as presented in the following. Figure 3.6 shows comparisons of computed and measured instability windows for spherical droplets at two different mean air flow velocities. Relevant parameters are: $2B$ = 0.2 cm, L = 4 cm, μ = 0.000184 poise (or g cm^{-1} s^{-1}), γ = 72 dyne/cm, and θ_s = 140°. Here, the viscosity and surface tension values correspond to that of air and that of liquid water at 25° C, respectively. In Figure 3.6, filled and unfilled squares represent observable states of droplets, respectively, at 200 cm/s and 400 cm/s of mean air-flow velocity. Multiple runs under each set of conditions were made to record the observable states shown in Figure 3.6. As can be seen from Figure 3.6, the computed droplet-instability windows agree with experimental observation reasonably well – better agreement is achieved at 200 cm/s than at 400 cm/s. As can also be seen from Figure 3.6, increasing the mean gas-flow velocity enlarges the droplet-instability window and thus enhances droplet removal – a qualitative trend

indicated by both the computed predictions and experimental observations. Figure 3.7 shows another comparison between computed and observed instability windows of spherical droplets for two channel lengths: 4 cm and 14 cm; mean air-flow velocity was set at 200 cm/s, and other parameters are the same as that in Figure 3.6. Again, reasonably good agreements between model prediction and experimental observation were obtained, and the computed and observed instability windows indicate that lengthening the GFC enhances droplet removal. Yet another comparison between computed and observed instability windows of spherical droplets are presented in Figure 3.8 for two different types of GDLs: untreated Toray carbon paper ($\theta_s = 120°$) and Teflon-treated Toray carbon paper ($\theta_s = 140°$); channel length was set to 4 cm, and other parameters are the same as that in Figure 3.7. As can be seen from Figure 3.8, making the GDL/GFC interface more hydrophobic (that is, increasing the static contact angle) enlarges the droplet-instability window and thus enhances droplet removal. Lastly, Figure 3.9 shows comparison of computed and measured instability window of spherical droplets at relatively high air-flow velocity of 800 cm/s. The computed droplet heights at the onset of instability is consistently higher than the experimentally observed values as the contact-angle hysteresis is increased from 0° to 60°, which results in a narrower computed droplet-instability window than the observed one. This discrepancy seems to confirm what is shown in Figure 3.6 – the agreement between computed and observed onset of instability worsens with increasing air-flow velocity. That the simplified model under-estimates drag on the droplet (because it over-estimates drag on the top wall surface due to approximating the flow channel between the top wall surface and the droplet surface as that between two parallel plates with the narrowest passage, *2b*, as the height) is most likely responsible for this discrepancy; and apparently, this discrepancy worsens as air flow velocity is increased.

3.4.4. Two-dimensional flow analysis & comparison with simplified model for cylindrical droplets

To assess the validity of the simplified cylindrical-droplet model, detailed two-dimensional finite-element simulations were performed of air flow over a cylindrical water droplet confined in a channel. Figure 3.10 shows computed streamlines in a particular case. Parameters for this case are the same as those for the base case in section 3.4.2 (i.e., channel height of 1 mm, mean air-flow velocity of 500 cm/s, air viscosity of 0.0002087 poise, air density of 0.001 g/cm^3, and water surface tension of 62.5 dyne/cm). Figure 3.11 shows the critical droplet height as a function of contact angle hysteresis at the onset of instability computed by the finite-element simulations for cylindrical droplets. Also plotted are the predictions computed by the simplified cylindrical-droplet model. The effect of channel length is explored by simulating two channel lengths, 5 mm and 15 mm. In practical PEFC operations, much longer channels are employed. The computational cost of simulating realistically sized channels is prohibitive, however. The effect of inertia in the flow is also explored. The Reynolds number is approximately 240 using the

channel height as the characteristic length as computed in section 3.4.2. However, by neglecting the inertial terms in the Navier-Stokes equations, creeping flow is simulated. This shows the deformation that the drop would experience if the Reynolds number were zero.

Figure 3.11 shows that the simplified cylindrical-droplet model successfully predicts the droplet deformation as the droplet grows in the channel. Quantitatively, the simplified model overpredicts the stability of the droplet. This indicates that the simplified model under-estimates the shear force or drag on the droplet (due to over-estimation of the shear force on the top-wall surface as alluded to previously in Section 3.4.3). By comparing the effect of neglecting inertia in the simulations, it becomes apparent that a great deal of this discrepancy is due to the effect of inertia in the flow. The difference between the simplified model and finite-element simulations at vanishing Reynolds number (in this case, the first term on the left hand side of Equation 3.24 drops out) is less than half the difference between the model and simulations at Re = 240. Simplified models that incorporate inertial effects are currently under development and will be presented elsewhere. By comparing the finite-element simulations with the 5 mm and 15 mm channels, it is apparent that these inertial effects become even more important as the length of the channel is increased.

3.5. Conclusions

Simplified models were developed for predicting the onset of instability leading to removal of water droplets at the gas diffusion layer (GDL)/gas flow channel (GFC) interface as in polymer electrolyte fuel cells (PEFCs). Droplet-instability windows computed by the simplified spherical-droplet model compare reasonably well with the observed ones constructed from visualization experiments using a simulated PEFC cathode. The discrepancy that exists between simplified model prediction and experimental observation worsens as the mean gas flow velocity increases. The simplified model prediction was also compared with two-dimensional flow analyses via finite element simulations for cylindrical droplets. Whereas the simplified model was found to successfully predict the qualitative droplet instability trend, agreement between the simplified model and finite-element simulations at high Reynolds number is not as good as that at low Reynolds number. This is attributed to the simplified model under-estimating the drag on the droplets due to the geometry approximation. Necessary conditions derived using the simplified models suggest that fully grown droplets can be prevented from lodging in the flow channel when the product of the channel length-to-height aspect ratio by the capillary number (i.e., $\frac{L}{2B}\frac{\mu U}{\gamma}$) is greater than $\pi/12$ for spherical droplets or larger than 1/6 for cylindrical droplets. Lastly, simplified model predictions computed for partially grown droplets indicate that increasing flow-channel length or mean gas-flow velocity, decreasing channel height or contact angle hysteresis, or making the GDL/GFC interface more

hydrophobic all result in enhancing removal of partially grown droplets. It should be noted that the present work applies to the situation in which only a single droplet emerges from the GDL/GFC interface at any given time. The scenario in which multiple water droplets may emerge simultaneously from the GDL/GFC interface along the flow channel awaits future analyses.

Nomenclature

B = half height of the flow channel (cm)

b = half height of the minimum channel flow passage (cm)

$f_{\mu,d}$ = viscous drag exerted on droplet surface by flowing gas (dyne)

$f_{\gamma,d}$ = total surface tension force acting on advancing and receding contact lines (dyne)

$\hat{H}$ = dimensionless droplet height based on channel height ($\equiv \frac{r(1-\cos\theta_a)}{2B}$)

L = flow channel length (cm)

l = maximum distance between upstream and downstream droplet surfaces (cm)

p = hydrodynamic pressure of flowing gas (dyne/cm^2)

p_0 = flow-gas pressure at the entrance of the gas flow channel (dyne/cm^2)

p_0' = flow-gas pressure immediately upstream of water droplet (dyne/cm^2)

p_L = flow-gas pressure at the exit of the gas flow channel (dyne/cm^2)

p_L' = flow-gas pressure immediately downstream of water droplet (dyne/cm^2)

r = water droplet radius (cm)

Re = Reynolds number ($\equiv \frac{\rho UB}{\mu}$)

$\mathbf{T}$ = viscous stress tensor

U = average velocity along flow direction in upstream and downstream regions (cm/s)

U' = average velocity along flow direction in the region directly above droplet (cm/s)

$\mathbf{u}$ = velocity vector of flowing gas

$y = \sin\frac{1}{2}(\theta_a - \theta_r)$

Greek letters

γ = surface tension of water (dyne/cm)

κ = local curvature along the liquid/gas interface

μ = viscosity of flowing gas (poise or g cm^{-1} s^{-1})

θ_a = advancing contact angle (°)

θ_r = receding contact angle (°)

θ_s = static contact angle (°)

ρ = density of flowing gas (g/cm^3)

τ_{xz}^{w} = wall shear stress per unit area ($dyne/cm^2$)

Subscript

d = droplet

g = gas phase

l = liquid phase

L = downstream

0 = upstream

γ = surface tension

μ = viscous

Superscript

w = wall

$'$ = droplet region

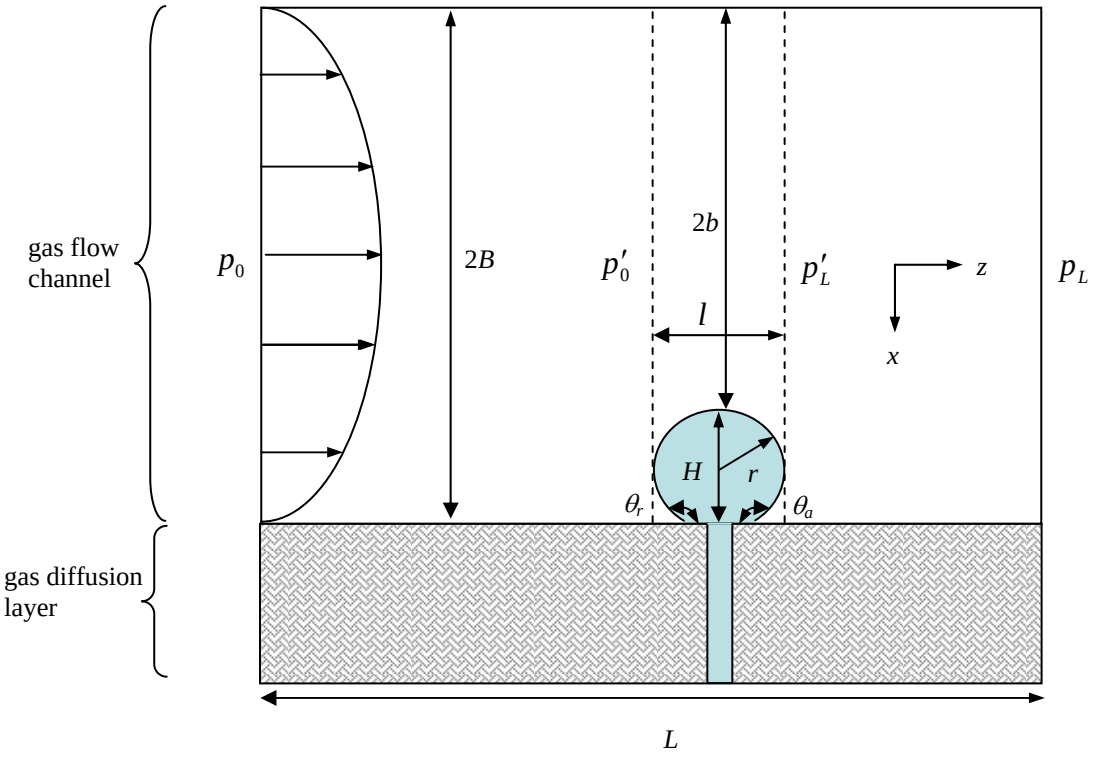

Figure 3.1. Control volume enclosing the liquid-water droplet

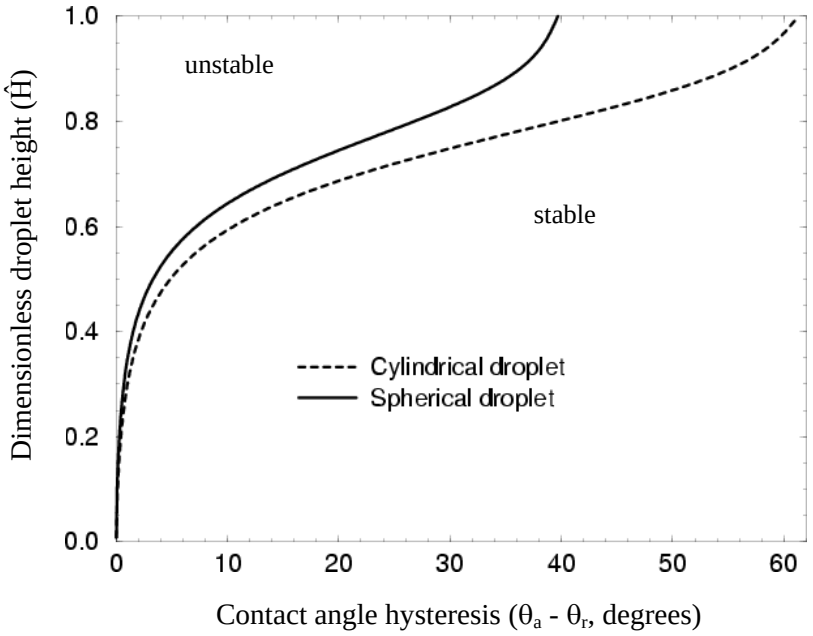

Figure 3.2. Droplet-instability diagram computed by the simplified models: spherical droplet vs. cylindrical droplets.

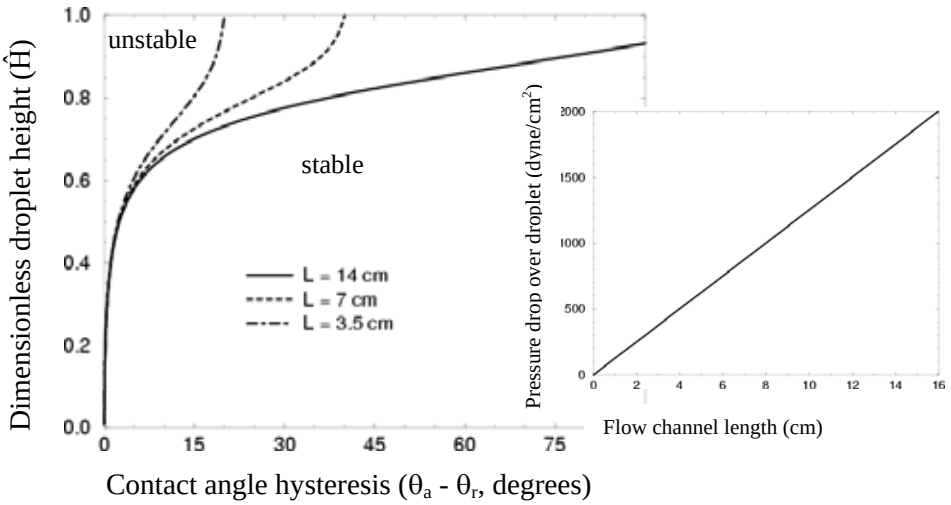

Figure 3.3. Computed effect of channel length on spherical droplet instability.

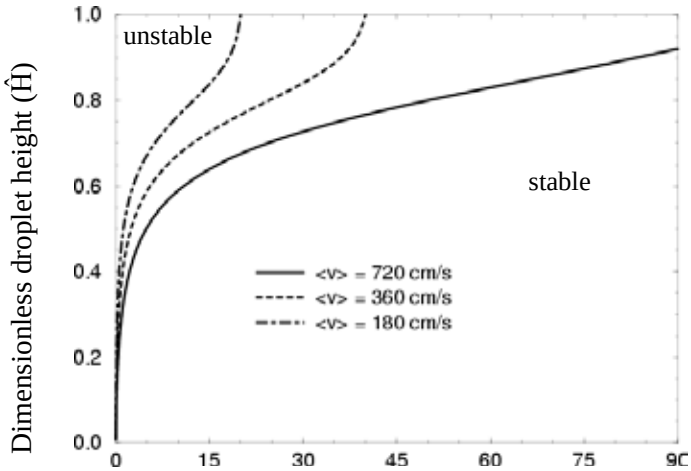

Figure 3.4. Computed effect of mean flow velocity on spherical droplet instability.

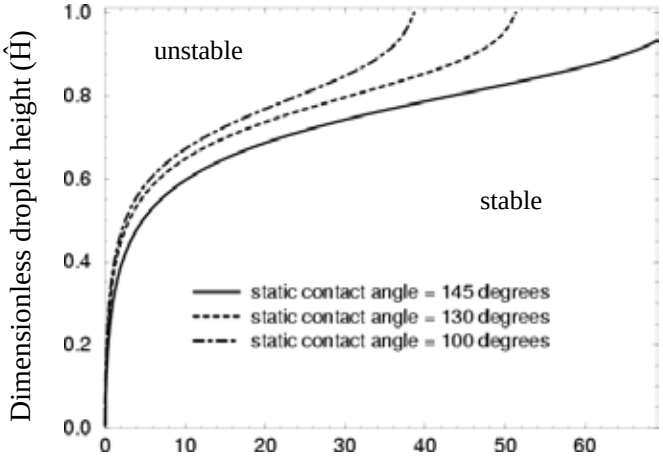

Figure 3.5. Computed effect of static contact angle on spherical droplet instability.

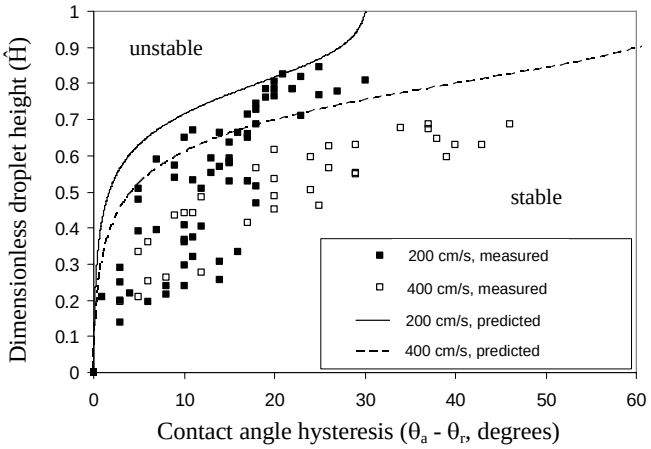

Figure 3.6. Comparison of computed & measured droplet instability diagrams: effect of air-flow velocity.

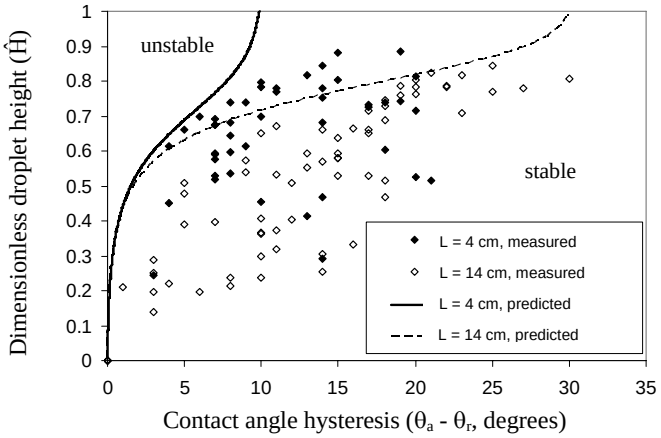

Figure 3.7. Comparison of computed and measured droplet instability diagrams: effect of channel length.

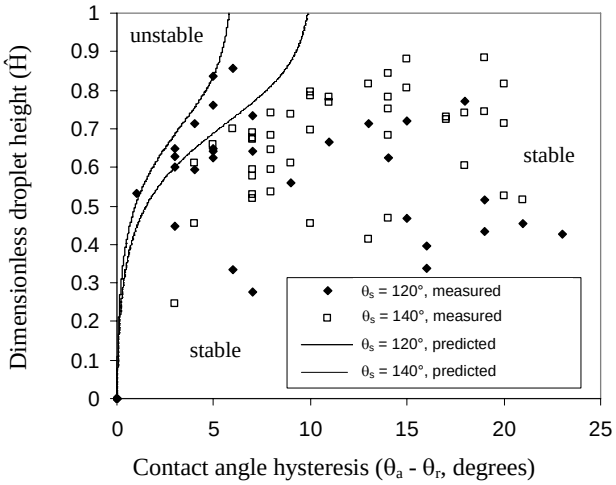

Figure 3.8. Comparison of computed & measured instability diagrams: effect of GDL surface treatment.

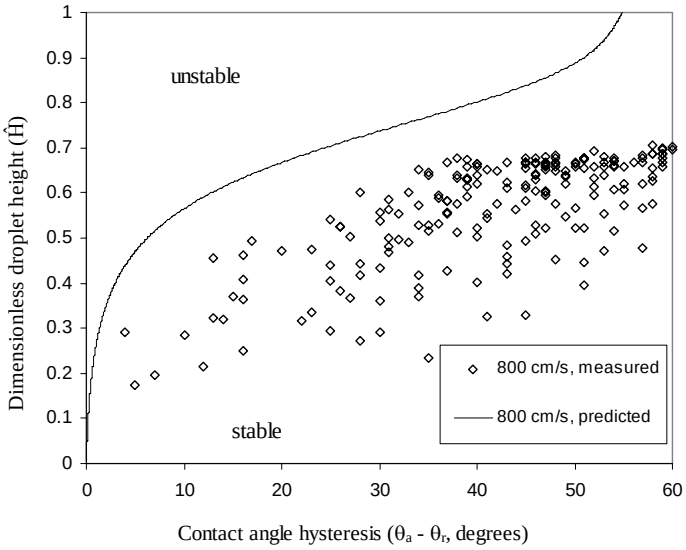

Figure 3.9. Comparison of computed and measured droplet instability diagrams: high air-flow velocity.

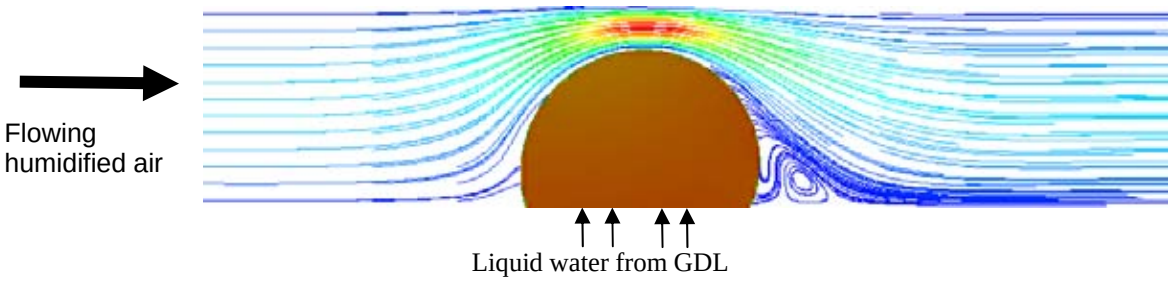

Figure 3.10. Finite element simulation of air flow over a cylindrical water droplet.

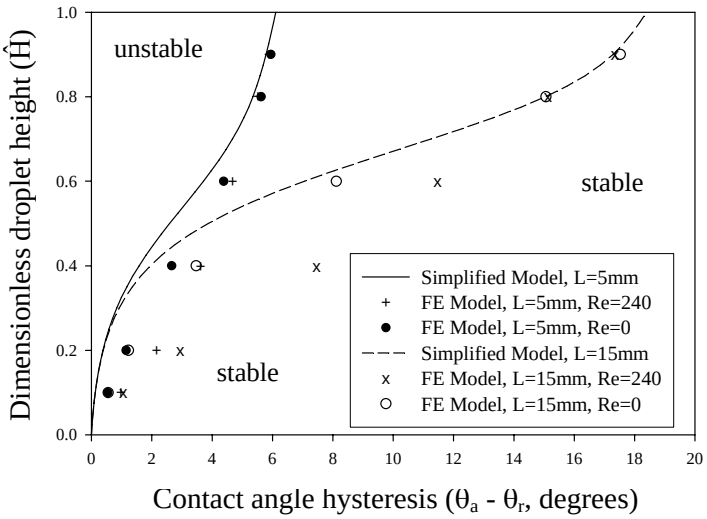

Figure 3.11. Comparison of simplified and full model predictions for a cylindrical liquid-water droplet.

4. Imaging Liquid Water Distribution inside an Operating PEM Fuel Cell Using Neutron Radiography[§]

4.1. Introduction

This chapter describes our work using neutron radiography to image the liquid water content in an operating PEMFC under both steady-state and dynamic conditions. Our objective was to provide evidence on the presence of liquid water in a PEMFC and determine how the total liquid water content and liquid water distribution depend on operating conditions. A key feature of this work is our attempt to link the water content in an operating PEMFC with the heat generated by the cell primarily within the cathode catalyst layer. The data contained in this chapter was primarily gathered during a week of experiments we carried out at NIST (National Institute of Science and Technology) in April, 2006.

Neutron radiography's utility in studying water distribution in PEMFCs was demonstrated seven years ago by Bellows et al. (1999). Since that time, the team at NIST and their collaborators supported with funding from the US Department of Energy's HFCIT program have built a world-class fuel cell radiography instrument that can be used for detailed studies of liquid water transport in fuel cell systems. There is much talk of "flooding" in PEMFCs, but there exists little detailed information on exactly what phenomena constitute flooding. In the catalyst layer liquid water could plug the pores, thus slowing reactant diffusion to the catalyst site. There could also be pore flooding in the micro-porous layer or macro-porous GDL, cutting off the pathways for gas transport to the catalytic layer. Finally, GFC flooding may exist where droplets of liquid water on the GDL surface decrease the area for gas transport into the GDL. While the neutron radiography technique employed in most of our studies cannot distinguish between water in the different planes of the fuel cell, catalyst layer versus GDL versus gas flow channel, the data collected using this technique is useful in determining quantitatively how much liquid water exists in an operating PEMFC and its distribution under a variety of operating conditions.

4.2. Experimental

The imaging instrumentation, experimental fuel cell setup, and data analysis used in this work was similar to that reported previously (Hickner et al. 2006). Co-flow anode and cathode, 4-pass serpentine flow fields were used in 50 cm^2 fuel cell hardware (Fuel Cell Technologies, Albuquerque, NM). Experiments were conducted under both stoichiometric control (gas flow adjusted relative to current production) and constant flow on the cathode at all current densities with the back pressure on the cell maintained at 50 *kPa* on both anode and cathode regardless of flow rate. The anode flow rate was maintained at 1500 *std*.

[§] This chapter was based on a proceeding paper accepted for publication: M. A. Hickner, N. P. Siegel, K. S. Chen, D. S. Hussey, D. L. Jacobson, and M. Arif, "Neutron imaging studies of water and heat transfer in PEM fuel cells", accepted for publication in the 2006 Fuel Cell Seminar Conference Proceeding (2006).

cm³/min for all tests and both anode and cathode inlet gas streams were humidified to 100% relative humidity at the inlet temperature and pressure. Membrane electrode assemblies consisted of Ion Power (New Castle, DE) catalyst coated membranes with Nafion 112 membrane (Dupont, Wilmington, DE) and catalyst loadings of 0.3 *mg Pt/cm²* on both anode and cathode. GDLs were carbon fiber paper and integral micro-porous layers with a total thickness of about 220 *microns*. All quantitative measurements and images were processed using a dry reference image. In the results presented below, false-color radiographs are shown with darker colors (black, gray, and blue) representing low water thicknesses and light colors (light blue, yellow, red) representing regions of higher water thicknesses. The grayscale and colorized images are shown in Figure 4.1. All images in this chapter were colored with the same scale as shown in Figure 4.2.

4.3. Analytical

Many of the trends observed in the neutron radiography data related to water content and water distribution are thought to be related to evaporative water removal driven by excess heat production, called local heating, within the cell. Two separate models of the cell were constructed to explain some of the observed results. One of the models, allowing for the prediction of the maximum water content of the cell as a function of current density, is a simplification of the model described in this section and is presented in full in Hickner et al. (2006). Both models consist of a water mass balance applied to the cathode gas stream including liquid water input contribution due to electrochemical production. The model described in this section, was designed to predict the distribution of the liquid water within the cell as a function of current density. The basis of the cathode gas stream water mass balance is the specific humidity which is defined as follows:

$$\omega = \frac{MW_{H_2O}}{MW_{Air}} \cdot \frac{P_v}{P_{tot} - P_v} \tag{4.1}$$

where P_v and P_{tot} are the vapor pressure and total pressure, respectively, MW_{H2O} is the molar mass of water, and MW_{air} is the molar mass of air. The maximum water-carrying capacity of an air stream at given temperature and pressure can be determined by replacing the vapor pressure terms in Equation 4.1 with the temperature-dependent saturation pressure expressed as:

$$Log_{10} P_{sat} = 1.4454E^{-7}T^3 - 9.1837E^{-5}T^2 + 0.02953T - 2.1794 \tag{4.2}$$

$$\omega_{\max} = \frac{MW_{H_2O}}{MW_{Air}} \cdot \frac{P_{sat}}{P_{tot} - P_{sat}} \tag{4.3}$$

where P_{sat} is the saturation pressure in bar, T is the liquid temperature is Celcius, and ω_{max} is the maximum water carrying capacity. The first step in using the model is to discritize the solution domain into volumes along the flow direction. The flow field discretization is shown in Figure 4.3.

A water mass balance is performed on the gas flow in each discrete volume – the result of which is a change in the specific humidity of the gas stream. The rate of liquid water entering a given volume is calculated based on the operating current density and the area of the discrete volume and is expressed as:

$$\dot{m}_{liq} = \frac{I \cdot A_{DV}}{2F} \tag{4.4}$$

where I is the cell current density, A_{DV} is the area of the discrete volume in the plane of the fuel cell active area, and F is Faraday's constant. The rate of water vapor entering the first volume in the solution domain is a function of the mass flow rate of the air, which is typically a function of current density and the specific humidity, and is expressed as:

$$\dot{m}_{v1} = \dot{m}_{air} \cdot \omega(T_1, P_1) \tag{4.5}$$

where $\dot{m}_{v1}$ is the water-vapor mass flow rate, $\dot{m}_{air}$ is the dry-air mass flow rate, and $\omega(T_1, P_1)$ is the specific humidity at the cell inlet pressure and humidity bottle temperature. The amount of water vapor leaving the volume, and entering successive volumes, is the sum of the vapor entering and the liquid water produced within the volume. The specific humidity at the exit of a volume can then be calculated and is expressed as:

$$\omega(T_2, P_2) = \frac{\dot{m}_{v1} + \dot{m}_{liq}}{\dot{m}_{air}} \tag{4.6}$$

A volume is said to be saturated if the specific humidity at the volume exit is greater than the maximum specific humidity (maximum local water-carrying capacity) which is calculated with Equation 4.4 using the local pressure at the exit of the volume and the temperature at the outlet of the fuel cell. If this condition is not true, the volume is assumed to be dry and capable of removing all liquid water produced in the gas phase. The analysis is repeated down the channel until a saturation condition is reached, at which point liquid water is assumed to be present.

The phenomenon of decreasing liquid water content with increasing current density can be explained by considering the heat production of the cell. As the current density of the cell increases, the voltage drops, thus rendering the cell less efficient. The heat production of the cell is given by (Larminie and Dicks, 2003):

$$Q_{cell} = (V_{HHV} - V_{cell})J \tag{4.7}$$

where V_{HHV} is the energy content of hydrogen based on its higher heating value (1.48V) and J is the total cell current.

An energy balance to account for the degree of local heat production was neglected as it has been shown in a previous analysis (Hickner et al. 2006) that sufficient thermal energy exists within the fuel cell to satisfy the energy input needed to saturate the cathode gas stream as its temperature rises. The other assumptions included in the model are listed as follows:

a) Water production is uniform across the cell (equal in each discrete volume).
b) The inlet gas stream is humidified to 100% relative humidity at the humidification bottle control temperature.
c) The gas temperature entering Volume 1 (greater than the humidification bottle temperature) is equal to the fuel cell exit gas temperature measured during neutron imaging. This assumption requires that heat transfer to the gas be much quicker than the mass transfer of water vapor (humidification). This assumption effectively results in an instantaneous drop of inlet relative humidity below 100% at the inlet of the cell and defines, along with the local pressure, the maximum water-carrying capacity of the gas stream.
d) Pressure drop is linear along the flow field length.
e) The mass of air flow is reduced by oxygen consumption due to the oxygen reduction reaction at the cathode.
f) All of the liquid water in the cell is on the cathode.
g) The gas stream will continue to pick up water until saturation is reached, at which point liquid water will be produced and appear in the neutron radiographs.
h) Liquid water advection is neglected. Only evaporative removal of water is considered.
i) Liquid water crossover from the anode is neglected.

The output of the model is simply the location within the flowfield at which point liquid water first appears.

4.4. Results and Discussion

Neutron radiographs were taken at different points on the polarization curve to measure the amount of water present at a given current density at steady state. Equilibration times before imaging were about 30 *minutes* and the image data was averaged over 8 *minutes*. A series of radiographs of the active area of the cell are shown in Figure 4.2. The conditions were 80°C cell temperature and a gas flow equal to double the stoichiometric requirement (a stoichiometric flow ratio of 2 or simply a stoic of 2) at each current

density (0.1 A/cm^2 flow at open circuit). The polarization curve and water content are plotted in Figure 4.4. As the current density is increased, the water content sharply increases at first from open circuit to 0.10 A/cm^2, which is noticeable from the neutron radiographs shown in Figure 4.2. The water content of the cell increases slightly from 0.10 to 0.25 A/cm^2 and then begins a steady decline as the cell is operated at higher current densities. At 1.5 A/cm^2, near the limiting current for this cell, the liquid water content is nearly the same as that at open circuit.

As the cell voltage drops and the current density increases, it produces more heat, thus raising the temperature of the inlet gas feeds and causing evaporation of the product water until the gas feeds become saturated at the higher temperature. The vapor pressure of water plays a large role in determining the water content profile of the cell with increasing current density. At lower temperatures, a small rise in temperature does not increase the water carrying capacity of the gas greatly. However, at higher temperatures, even a small rise in gas temperature allows the gas to uptake much more water. This effect is illustrated in Figure 4.5, where the change in specific humidity is plotted for a 4°C temperature rise from 40°C and 80°C. The figure clearly shows that the water carrying capacity of the gas (expressed as specific humidity) for this small temperature rise is a strong function of the bulk temperature. This has ramifications for the water content of fuel cells and how the liquid water of the cell depends on both current density, which is tied to the temperature increase of the cell, and the bulk temperature of the cell.

Shown in Figure 4.6 are two plots: polarization curves for bulk cell temperatures of 40°C, 60°C, and 80°C, and the total cell liquid water content at each of the points on the polarization curves. The polarization curves at each temperature are similar, so the heat production at each temperature is not vastly different. The limiting current of the 40°C cell was just above 1 A/cm^2, while the limiting current at 60°C and 80°C was greater than 1.5 A/cm^2. The water contents of the 40°C and 60°C cells are similar with increasing current density. In both cases the peak in water content is at 0.75 A/cm^2, which is further out on the polarization curve than the peak in water content at 80°C.

The small difference in liquid water content of the cell between 40°C and 60°C can be expected from the information in Figure 4.5, where a small change in temperature at either condition does not greatly affect the water-carrying capacity of the gas. Above 60°C, however, the water vapor pressure starts to rise more rapidly with temperature and the liquid water content of the cell becomes more sensitive to the bulk cell temperature. At the highest current densities for the 60°C case, there is an increase in liquid water content. This is an indication of liquid water flooding although the water content of the cell is not as high as the peak water content at 0.75 A/cm^2. In this case, the gas streams are becoming saturated so the extra

water production must be in the liquid phase. Increasing the bulk cell temperature to 80°C raises the water carrying capacity of the gas and eliminates flooding at the higher current densities.

Neutron radiographs of cells operating at 40, 60, and 80°C at 1 A/cm^2 and a stoichiometric flow ratio of 2 on the cathode are shown in Figure 4.7. The total liquid water content is the same as in Figure 4.6 for each case, but the striking difference in these micrographs is the water content distribution. The water contents in the 40°C and 60°C cases are relatively uniform from inlet (upper left) to outlet (lower right) with what appear to be a few more liquid water slugs, which appear as the lighter regions, in the 40°C case than in the 60°C case. This could be a result of increased surface tension at lower temperatures or there may be more redistribution of water due to the higher vapor pressure at 60°C. At 80°C, a darker, dry region is visible in the upper part of the cell. In this region, there is appreciable local current density as shown by Mench et al. (2003), but the only water entering this part of the cell is from the fully humidified gas inlets. Local heating within the cell causes the temperature of the gas stream near the inlet to rise, effectively increasing its water carrying capacity (specific humidity) and allowing it to pick up liquid water. In addition, the inlet gases are humidified at the inlet pressure of the cell, so as the pressure of the gas drops as it moves down the flow channel, the gas is able to pick up more water by evaporation. Looking back on Figure 4.2, it is clear that the dry region at the inlet of the cell depends on the current density and thus the waste heat production of the cell. This unequal distribution of water across the cell may result in more rapid aging due to unequal material stresses and uneven heating of the cell caused by accompanying current density distributions.

Many of the two dimensional neutron radiography images show a relatively dry region beginning at the inlet of the fuel cell and extending some distance into the flow field along the direction of gas flow. The overall length of this dry region appears to increase with current density. As current density increases, so does the amount of heat generated within the fuel cell as well as, in most cases, the temperature of the gas stream. The increase in temperature coupled with increased heat production allows additional liquid water to be removed from the cell by evaporation via the local heating mechanism. The simple mass balance model described in Section 4.3 and based on the assumption of water removal from the cell by local heating was constructed so as to explain the observed inlet dry out of operating PEMFCs.

Figure 4.8 shows neutron radiographs for the cell operating at 60°C and a stoichiometric flow ratio of 2.0 at three different current densities. Each radiograph in Figure 4.8 has an overlay that indicates the predicted dry out length from the model. The model output is in close agreement with the experimental results indicating that, at least for these conditions, the inlet dry out is likely due to enhanced evaporation caused by local cell heating. By just taking into account the state of the cathode feed, and the temperature rise in the cell, the dry region of the radiographs is well reproduced with this simple model.

The model is also able to predict the drying trend at both 40°C and 80°C as shown in Figure 4.9, although the agreement with the experimental data at 80°C is not as good as that at 60°C. This is likely caused by error associated with the exit gas temperature measurement. The water uptake capacity of a gas at 80°C is far more sensitive to temperature change and any error in the outlet temperature measurement induces a large change in the model prediction.

The model begins to lose accuracy as the gas flow velocity is increased from a stoichiometric flow ratio of 2 to a stoichiometric flow ratio of 6 as shown in Figure 4.10. A striping effect is noticeable as the gas velocity is increased where liquid water begins to accumulate before the channel bends. To investigate the role of liquid water droplet shearing (advective effects) in water removal from a PEMFC, radiographs were taken at 60°C with varying cathode stoichiometric flow ratios of 2, 4, and 6. Figure 4.11 shows the liquid water content of the cells as a function of current density and stoichiometric flow ratio (which is essentially gas flow velocity since the stoichiometric flow ratio is proportional to the gas flow velocity).

Liquid water content decreases as stoichiometry increases. Shown in Figure 4.12 are the polarization curves and liquid water content for the cases with stoichiometric flow ratios of 2, 4, and 6, respectively. The performance of the cell increases somewhat as the stoichiometric flow ratio is raised, especially between 4 and 6 and likely due to a gas pressure increase, however, the water content decreases in all cases. It is interesting to note that the major performance difference occurs in the mass transport regions in the polarization curves having stoichiometric flow ratios of 2 and 4. However, there is not a huge difference in water content between the two cases at high current densities. Additionally, the water content is the lowest of all in the case with a stoichiometric flow ratio of 6, but the performance is not greatly improved when the stoichiometric flow ratio exceeds 4. This shows that liquid water and droplet shearing does play a role in determining the performance of a PEMFC, but there are clearly other effects that matter, such as oxygen diffusion through the GDL.

Many of the neutron radiographs show a non-uniform water distribution wherein liquid water appears to accumulate prior to a bend in the flow field. The amount of liquid water following the bend is significantly less than preceding it. The cause of this non-uniformity is at least partly due to the manner in which the images were averaged; meaning that a large amount of water present within the bend for even a short time would cause an overall increase in the amount of water seen in the steady state averaged image. Generally, liquid droplets grow at the GDL/GFC interface until they reach a certain size at which point they are sheared off and carried out of the fuel cell by the gas stream. As a slug of droplets travels along the flow field it appears to slow down just prior to and within a bend in the flow field. Thus, the residence time of liquid water being advected from the cell is greater upstream of and within the bends in the flow field than downstream, which would appear as an increased amount of water content in the

steady state averaged images. The mechanism behind the slowing of the liquid water droplets near the bends in the flowfield is not yet known, but is likely a result of a change in the character of the gas flow. The gas flow transitions from fully developed laminar flow within the straight sections of the flow field upstream of the bends, to an impinging flow within the bends, and then to a developing flow as it exits the bends. Transitions such as these would affect the manner by which liquid droplets are transported by the gas stream.

4.5. Summary and Conclusions

The liquid water distribution inside an operating PEM fuel cell under various operating conditions was probed using neutron radiography. It was found that the liquid water content of a fuel cell is a product of the competing effects of electrochemical water production and evaporative water removal driven by local cell heating. Although more water is produced by the cell at higher current densities, the cell is less efficient and produces much more waste heat which increases the temperature of the gas flow causing additional water to evaporate and be removed from the cell. This effect is more pronounced at higher bulk cell temperatures where the water carrying capacity of the gas flow increases significantly for relatively small increases in temperature. This behavior is evident in the experimental data where, at 80°C, the maximum liquid water content was observed at 0.25 A/cm^2 while the peak in water content at 40°C and 60°C was observed at 0.75 A/cm^2. Liquid water flooding does not occur until the water production of the cell exceeds the ability of the gas phase to uptake additional water in the vapor phase. Our data indicates that no liquid water flooding exists at 80°C, and is only mild at 40 and 60°C until the limiting current is reached.

A simple model treating water removal mainly via evaporation due to local heating was developed to explain the observed inlet dry out in an operating PEMFC. Agreement between model prediction and experimental observation is fairly good when the flow velocity is moderate (an inlet stoichiometric flow ratio of 2 – 4) but gets poor when the flow velocity is increased from moderate to high (an inlet stoichiometric flow ratio of 6). This is due to the fact that the model neglects water removal via droplet shearing – when the flow velocity is low or moderate, the assumption of water removal mainly via evaporation is valid; but when the flow velocity is sufficiently high, water removal via droplet shearing can be appreciable and thus can not be neglected. The incorporation of water removal via droplet shearing into our simple model is an area for further development.

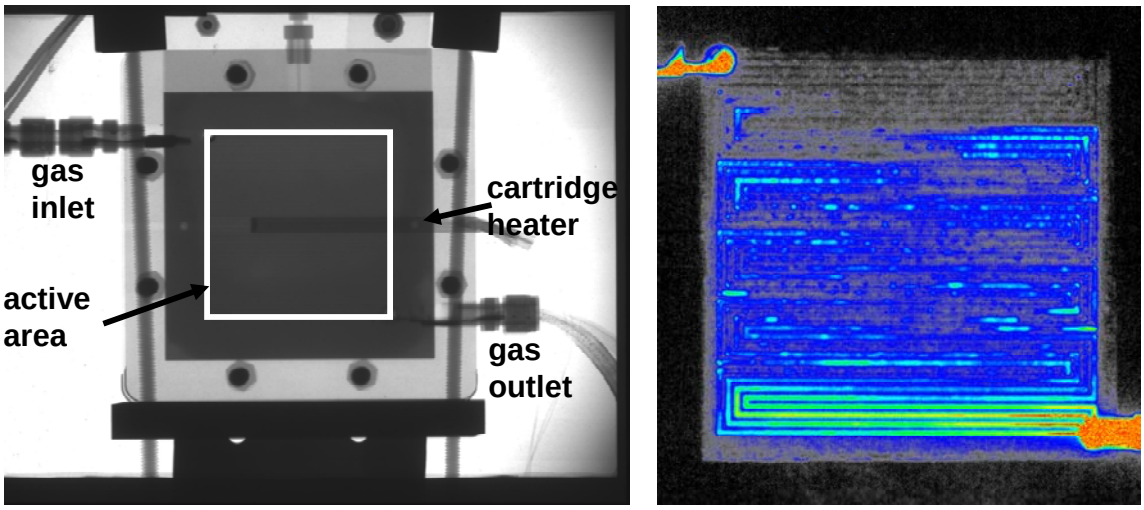

Figure 4.1. Neutron radiographs of a 50-cm^2 PEM fuel cell showing (a) the cell construction, gas ports, and active area in white, and (b) a colorized image showing water content in the active area. Red, orange, and green colors corresponds to maximum water content, and blue and black correspond to minimum water content as indicated in the color bars in Figure 4.2 below.

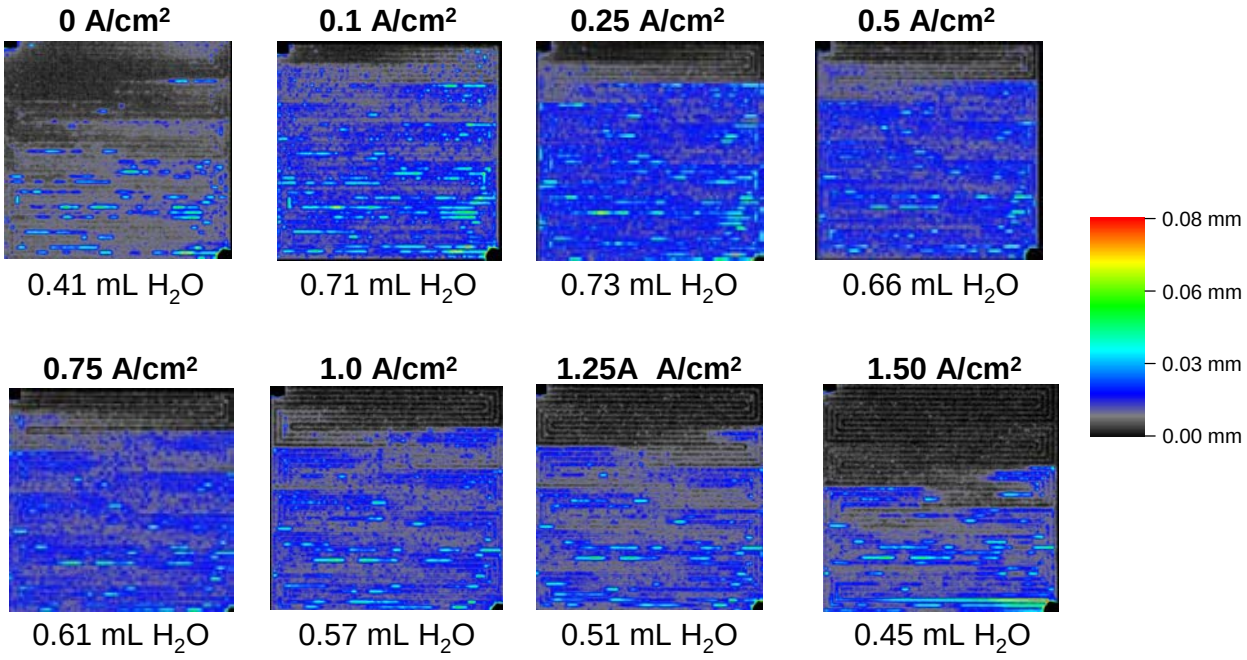

Figure 4.2. Effect of current density on liquid water distribution inside the active area – neutron radiographs of a 50cm^2 PEM fuel cell operating at 80°C and a stoichiometric flow ratio of 2. Both gas inlets are in the upper left of the images and both gas outlets are in the lower left of the images. Gravity is oriented down in the images.

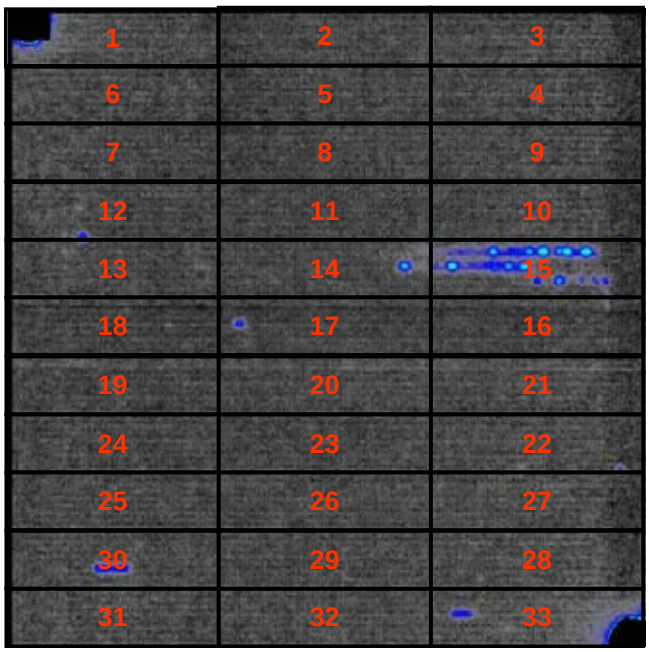

Figure 4.3. Flow field discretization for a 50 cm^2 PEMFC. The flow field is a quad-pass serpentine.

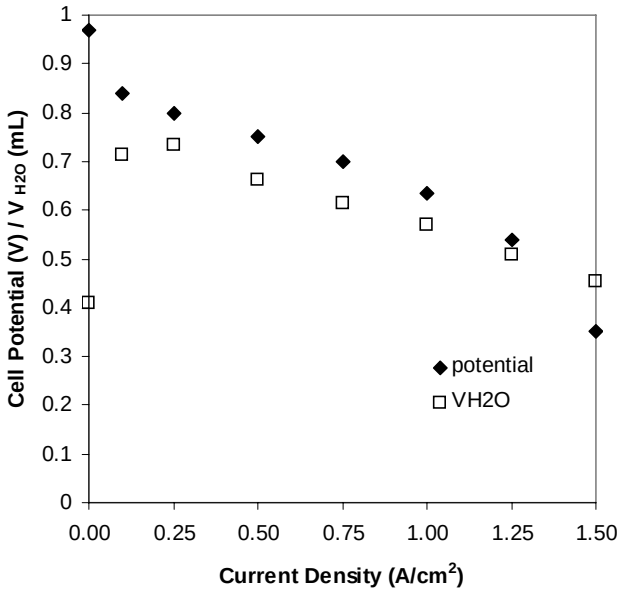

Figure 4.4. Polarization curve and water content for 80C and a stoichiometric flow ratio of 2.

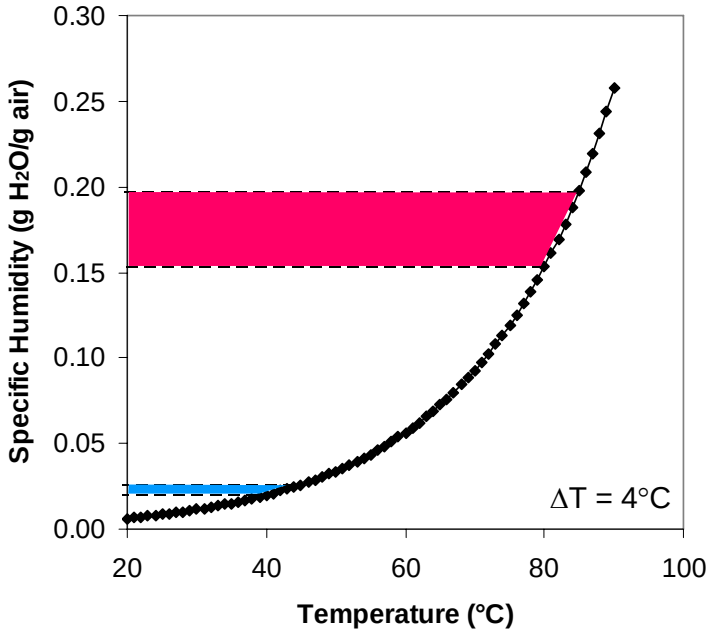

Figure 4.5. Specific humidity as a function of temperature, which shows the change in specific humidity for a 4°C temperature rise at 40°C and 80°C, respectively.

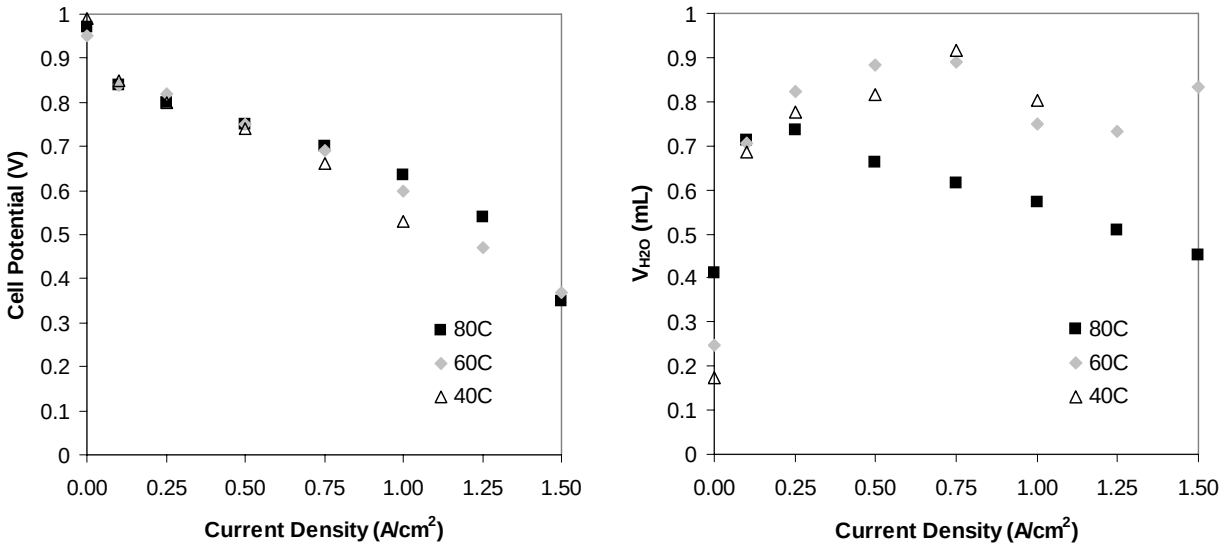

(a) (b)

Figure 4.6. Polarization curves and water content for 40°C, 60°C, and 80°C with a stoichiometric flow ratio of 2: (a) polarization curve; (b) water content.

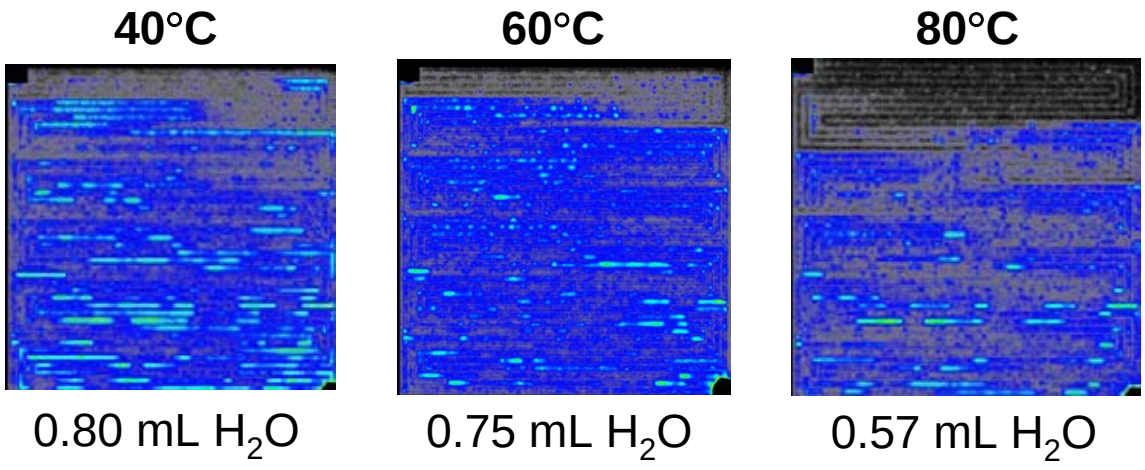

Figure 4.7. Effect of operating temperature on liquid water distribution inside the active area – total liquid water contents and distributions at cell temperatures of 40°C, 60°C & 80°C under a current density of 1 A/cm^2 with 2 stoichiometric flow ratio of 2.

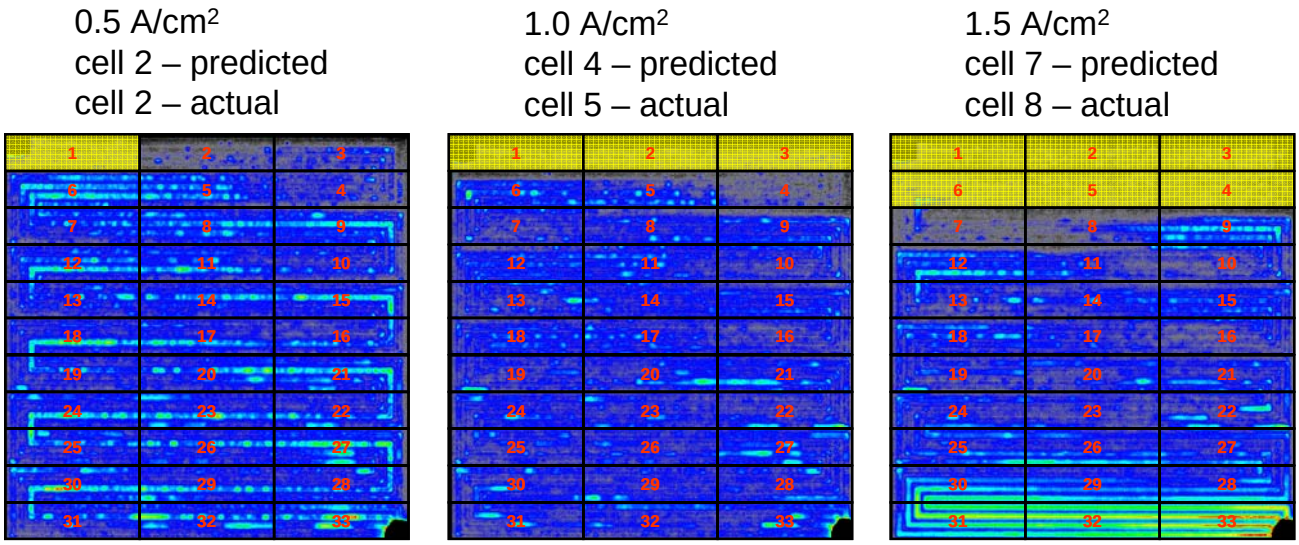

Figure 4.8. Neutron radiographs and predicted dry out at 60°C and 0.5 A/cm^2, 1.0 A/cm^2, 1.5 A/cm^2 with a stoichiometric flow ratio of 2.

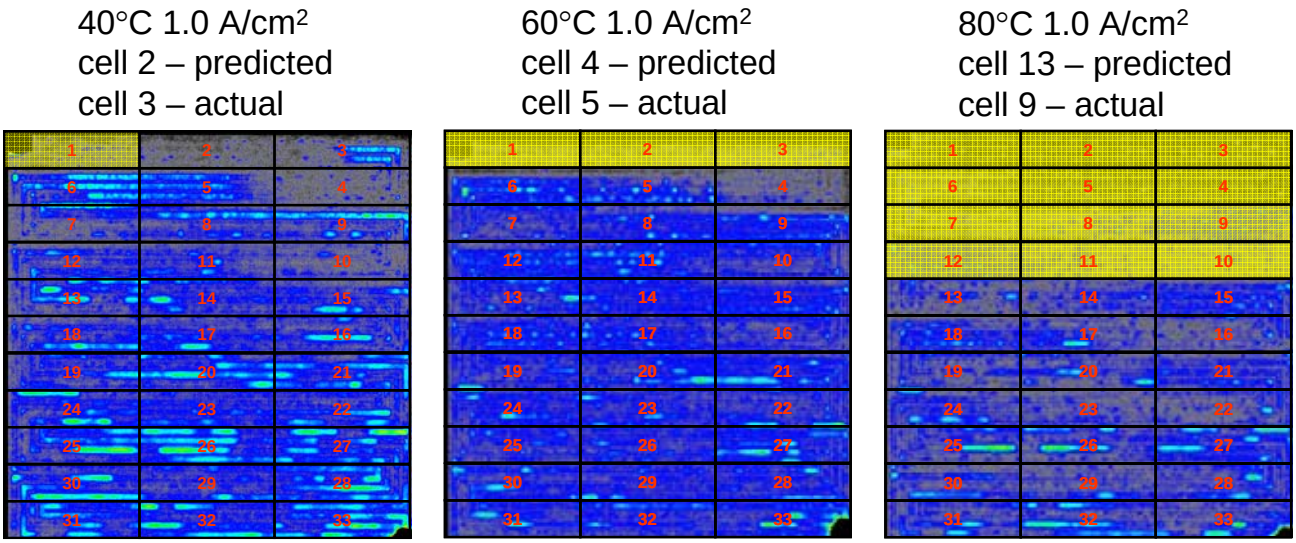

Figure 4.9. Neutron radiographs and predicted dry out at 1.0 A/cm^2 with a stoichiometric flow ratio of 2 at 40°C, 60°C and 80°C.

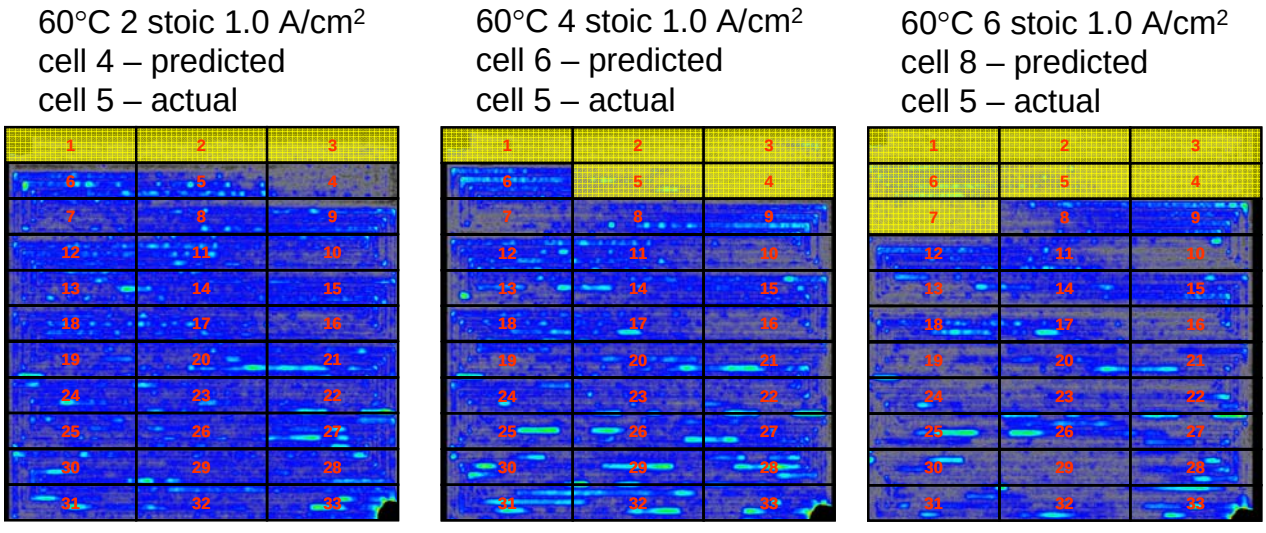

Figure 4.10. Neutron radiographs and predicted dry out at 1.0 A/cm^2 and 60°C with stoichiometric flow ratios of 2, 4, and 6, respectively.

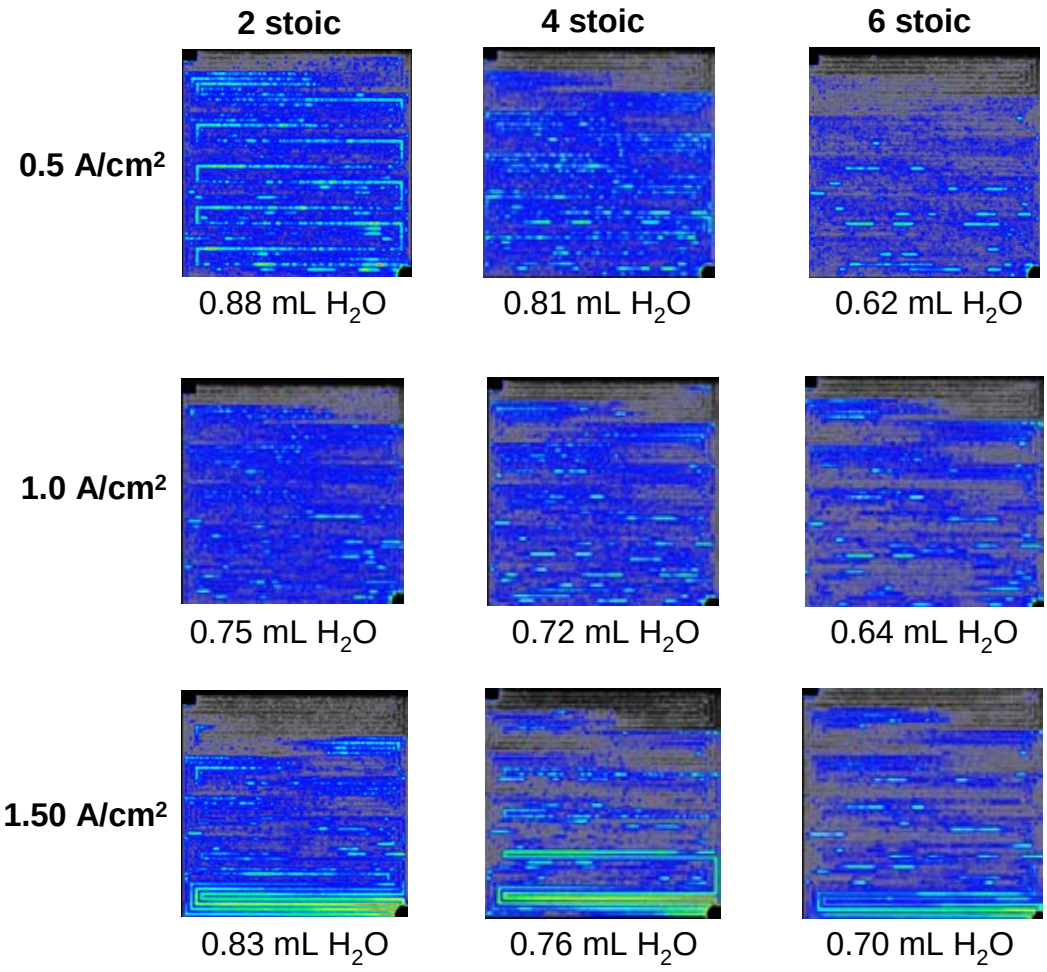

Figure 4.11. Neutron radiographs of a PEMFC operating at 60°C as a function of current density and stoichiometric flow ratio.

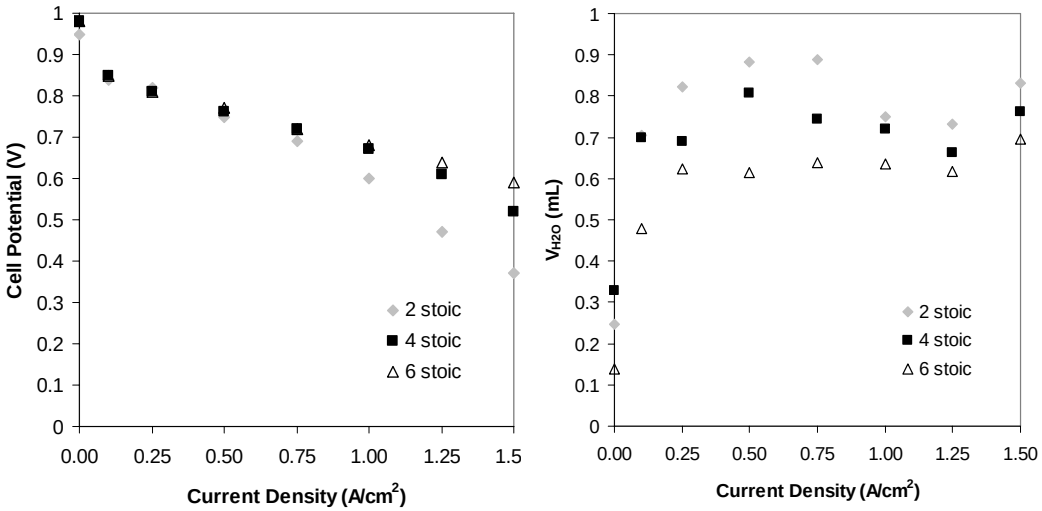

(a) (b)

Figure 4.12. Polarization curves and water content for cases with stoichiometric flow ratios of 2, 4, and 6, respectively, and at 60°C.

5. Modeling Effects of Micro-Porous Layer on Net Water Transport in a PEM Fuel Cell[**]

5.1. Introduction

A main limitation in PEMFC performance results from the transport of reactants from the channel to the catalyst layer, referred to as the mass transport limitation. This limitation is further amplified by the presence of liquid water, which blocks some of the open pores in the gas diffusion media (GDM) and thus reduces the available paths for the transport of reactant species. This phenomenon, commonly referred to as flooding, is more severe in the cathode due to the fact that the slower oxygen reduction reaction (ORR) is more susceptible to the negative impact caused by flooding. Recently, a bi-layer GDM, consisting of a coarse gas diffusion layer (GDL) and a finer micro-porous layer (MPL) has been employed by practitioners to reduce flooding in the porous cathode and to enhance water management in PEMFCs by increasing the back-flow tendency of liquid water across the membrane towards the anode. It has been shown that highly hydrophobic MPLs usually exhibit better performance (Wilson et al. 1995, Hara et al. 1996, Passalacqua et al. 1998, Paganin et al. 1996, Qi and Kaufman 2002, Kong et al. 2002, Jordan et al. 2000, Jannsen and Overvelde 2001, Passalacqua et al. 2001, Giorgi et al. 1998, Cabasso et al. 1998, Lee et al. 1998, Voss et al. 1995). Although the exact mechanisms are yet to be fully elucidated, the performance enhancement is usually associated with better water management capabilities of MPLs. In phosphoric acid fuel cells, Hara *et al.* (1996) wetproofed the GDL using a fluorinated polyethylene film, which has much smaller pore size than commonly used polytetrafluoroethylene (PTFE) particles. It was found that this additional layer, which is similar to the MPL in PEFCs, improved oxygen reduction by reducing the flooding. Passalacqua *et al.* (1998) also showed that introducing a hydrophobic layer between the carbon paper and the catalyst layer improves cell performance. The thin hydrophobic layer of about 2 mg/cm^2 of carbon (Vulcan XC-72), containing 40% of PTFE, substantially improved cell performance both in air and pure oxygen operation, by reducing the ohmic losses and increasing the limiting current density. Therefore, it was concluded that this thin hydrophobic layer is useful both in reducing cathode flooding and improving membrane humidification. Paganin *et al.* (1996) found that the effect of the MPL thickness is more dominant than the PTFE content in improvement of polarization characteristics. Their experiments with pure oxygen, however, suggested that the performance improvement is largely due to decreased ohmic losses. Qi and Kaufman (2002) discovered that MPLs reduced the performance differences among the different GDLs, and attributed this effect to improved water management. They have shown that MPLs are extremely useful, particularly when the GDL is

[**]Portion of this chapter has been published in a journal paper: U. Pasaogullari, C.-Y. Wang, and K. S. Chen, "Two-phase transport in polymer electrolyte fuel cells with bi-layer cathode gas diffusion media", J. Electrochem. Soc., 152, P. A1574 – A1582 (2005).

prone to flooding. They observed that the MPL not only raised the limiting current density, but also improved membrane humidification and hence reduced ohmic losses. They also analyzed the effect of PTFE content of MPL on cell performance, and concluded that although the performances are very similar, the 45% PTFE content sub-layer performed worst, while the 35% sub-layer performed best, suggesting that there is an optimum for MPL hydrophobicity. They also noted that MPLs might improve the contact with the catalyst layer, thereby decreasing the contact losses. Kong *et al.* (2002) found that adding pore formers to coatings applied on the GDL surface improves cell performance. They attributed the performance improvement to the fact that larger pores in MPL accumulate liquid water while the smaller pores remain free of liquid water, resulting in more effective transport of both gaseous oxygen and liquid water. Like Jordan et al. (2000), they also concluded that the pore size range on the order of a micrometer exhibited better performance than larger or smaller pores. It is likely due to a trade-off between water management and oxygen transport that with smaller pores water management is improved (though the oxygen diffusion is hindered) whereas with the larger pores the GDL becomes more prone to flooding.

It is evident from the experimental studies cited above that MPLs improve PEFC performance in several aspects. Two main causes of performance improvement are 1) enhancement of water management by improved humidification of the membrane at the anode side, hence decreasing the ohmic losses, and 2) reduced flooding in the cathode, hence improved oxygen diffusion.

Although several studies exist on modeling of two-phase transport in PEFCs, only a few have discussed the effects of the MPL on water management and two-phase transport. Nam and Kaviany (2003) have modeled the two-phase transport in multi-layered cathode GDM using the unsaturated flow theory (UFT), which assumes a constant gas-phase pressure throughout, and which therefore neglects the gas flow counter to the liquid flow. They have optimized the MPL properties according to the total liquid water in the cathode GDM, and concluded that there exists an optimal MPL thickness and porosity. In contrast, Pasaogullari and Wang (2003, 2004a) elucidated the MPL effect using a full two-phase model, *i.e.* multiphase mixture formulation commonly known as M^2 model, in which the constant gas-phase pressure assumption is relaxed, thereby accounting for the gas flow in counter direction to the capillarity-induced liquid flow. Their results indicated for the first time that the build-up in liquid pressure in the cathode due to the presence of an MPL creates a hydraulic pressure differential to drive water flow back to the anode. This water back-flow can be controlled by pore size and MPL wettability, following the capillary flow theory developed by Pasaogullari and Wang (2004b). In addition, the study of Pasaogullari and Wang revealed a capillarity-driven enhancement of oxygen transport once the two-phase zone is formed. This new enhancement mechanism is, however, suppressed by the increase in the diffusion resistance, yielding

an overall reduction in the oxygen transport capability in most cases of flooding. Weber and Newman (2003) also mentioned the positive role played by MPL, which is to promote back-flow through the membrane by improving humidification of the membrane as well as the anode catalyst layer and by reducing the overall ohmic losses, hence improving PEFC performance. Reviews of other aspects of water transport in PEFCs are available in Weber and Newman (2004) and Wang (2004).

The aim of the present work is to develop a two-phase transport model based on the M^2 model for the entire polymer electrolyte membrane (PEM)-anode/cathode GDM assembly, and to analyze the liquid water transport in PEFCs with MPLs. Effects of MPL pore structure and wetting characteristics are also analyzed. Particularly, the effects of MPL properties on the net water transport rate across the membrane (a combined effect of electro-osmotic drag, back-diffusion and hydraulic permeation) are analyzed. Net water transport across the membrane can only be analyzed with a model considering both anode and cathode as well as the membrane, an important feature that cannot be captured by half cell models (such as those in previous works (Nam and Kaviany 2003; Pasaogullari and Wang 2003 & 2004a).

This chapter is organized as follows. A mathematical model for transport in the multi-layered GDM and PEM is first presented based on the theory of liquid water flow in hydrophobic gas diffusion layers as put forth by Pasaogullari and Wang (2004). Then, liquid water transport in PEMFC with MPL is compared with the conventional PEMFC configuration without MPL and the effects of MPL properties are examined.

5.2. Mathematical Model

The present study focuses on liquid water transport in porous anode and cathode gas diffusion media and across the membrane. The cell is considered to be isothermal for simplicity. The gas channels are excluded from the modeling domain by designating the boundary conditions at the GDL/channel interfaces. Furthermore, catalyst layers are taken to be infinitely thin interfaces and the anode hydrogen oxidation reaction (HOR) and cathode ORR are assumed to take place at the PEM-anode GDL and PEM-cathode GDM interfaces, respectively.

Under these assumptions, the modeling domain is defined to include the porous anode GDL, PEM and cathode GDM, consisting of MPL and GDL, as shown in Figure 5.1, along with the associated transport processes. Although the present model is developed in one dimension (i.e. in the through-plane direction), it can be readily implemented in a multi-dimensional computational fuel-cell dynamics (CFCD) model with the channel and catalyst layer incorporated, as illustrated by Pasaogullari and Wang (2003, 20044c).

5.2.1. Two-phase water transport in gas diffusion media

In this study, the M^2 model is employed to describe the two-phase transport processes in porous media. The M^2 model is an exact reformulation of the classical two-phase, two-fluid model into a single equation (see, e.g., Wang and Cheng 1997, Wang et al 2001). Unlike the unsaturated flow theory or UFT (see, Wang and Cheng 1997), which was utilized in some of the earlier two-phase PEFC models (e.g., Nam and Kaviany 2003, Pasaogullari and Wang 2003, He et al. 2000, Natarajan and Nguyen 2001), the M^2 formulation does not require a constant gas-phase pressure assumption across the porous medium, hence it also accounts for the gas flow counter to the capillarity-driven liquid flow. Interested readers are referred to Wang and Cheng (1997) for details of the M^2 model and its applications to a number of multiphase transport problems in porous media.

Mass conservation in steady-state for the two-phase mixture as given by the M^2 formulation is:

$$\frac{d\left(\rho\vec{u}\right)}{dx} = 0 \tag{5.1}$$

where $\vec{u}$ is the superficial mixture velocity based on the total volume of the porous medium and ρ is the mixture density and given as (Wang and Cheng 1997):

$$\rho = \rho_l \cdot s + \rho_g \cdot \left(1 - s\right) \tag{5.2}$$

Here, *s* and (1-s) represent the fractions of the open pore space occupied by the liquid and gas phases, respectively. When Equation 5.1 is integrated along the GDM thickness, we have:

$$\rho\vec{u} = \vec{j}_m \tag{5.3}$$

Here, $\vec{j}_m$ indicates the total mass flux through the porous media in both phases, and corresponding expressions for each individual layers are given in Table 5.1.

The steady-state, one-dimensional species conservation equation of the M^2 formulation, when written in terms of molar concentrations is (Pasaogullari and Wang 2004):

$$\frac{d}{dx}\left(\gamma_c^i \vec{u} C^i\right) = \frac{d}{dx}\left(D_g^{i,eff}\frac{d}{dx}C_g^i\right) - \frac{d}{dx}\left[\left(\frac{\mathrm{mf}_l^i}{M^i} - \frac{C_g^i}{\rho_g}\right)\vec{j}_l\right] \tag{5.4}$$

where the advection correction factor, γ_c is given by:

$$\gamma_c^i = \begin{cases} \dfrac{\rho}{C^{\mathrm{H_2O}}}\left(\dfrac{\lambda_l}{M^{\mathrm{H_2O}}} + \lambda_g \dfrac{C_g^{\mathrm{H_2O}}}{\rho_g}\right) & \text{for water} \\ \dfrac{\rho\lambda_g}{\rho(1-s)} & \text{for other species} \end{cases} \tag{5.5}$$

In Equation 5.4, C^i denotes the total molar concentration of species *i* in liquid and gas phases, and is defined as:

$$C^i = (1-s)C_g^i + sC_l^i \tag{5.6}$$

The gas diffusion coefficient, $D_g^{i,eff}$ is corrected for tortuosity and reduction in the open pore space due to presence of liquid water via the Bruggeman correlation (Meredith and Tobias 1962), *e.g.:*

$$D_g^{i,eff} = \left[\varepsilon(1-s)\right]^{1.5} D_g^i \tag{5.7}$$

Note that Equation 5.4 strongly resembles the single-phase species conservation except for the last term which describes the capillary transport of species. This equation reduces to its counter-part of single-phase species equation when liquid saturation, *s* approaches zero or unity. Note that, unlike the UFT approximation, the capillary transport term also accounts for the variation in gas-phase pressure through the porous media, hence the gas flow in the counter direction to the capillarity-induced liquid flow is considered. Due to the small length scales involved in PEMFCs, the effect of gravity is negligible and hence the liquid flux, $\vec{j}_l$ is given by:

$$\vec{j}_l = \frac{\lambda_l \lambda_g}{\nu} K \nabla p_c \tag{5.8}$$

where λ_l and λ_g are relative mobilities of gas and liquid phases, respectively:

$$\lambda_k = \frac{k_{rk}/\nu_k}{\sum_k k_{rk}/\nu_k} \tag{5.9}$$

and ν is the kinematic viscosity of the two-phase mixture:

$$\nu = \left[\sum_k \frac{k_{rk}}{\nu_k}\right]^{-1} \tag{5.10}$$

Here, we assume that the GDL and MPL are isotropic and homogeneous porous media, and the relative permeabilities of individual phases are assumed to be proportional to the cube of individual phase

saturations, *i.e.*:

$$k_{rk} = s_k^{\,3} \tag{5.11}$$

The capillary pressure is the difference between the pressures of wetting and non-wetting phases:

$$p_c = p_g - p_l \tag{5.12}$$

In this work, we relate the capillary pressure to individual phase saturations via a Leverette function, *J(s)* (see, e.g., Wang and Cheng 1997):

$$p_c = \sigma \cos(\theta_c)\left(\frac{\varepsilon}{K}\right)^{1/2} J(s) \tag{5.13}$$

where *J(s)* is the Leverette function, and given as (see, e.g., Pasaogullari and Wang 2004a, 2004b):

$$J(s) = \begin{cases} 1.417(1-s) - 2.120(1-s)^2 + 1.263(1-s)^3 & \text{if } \theta_c < 90° \\ 1.417s - 2.120s^2 + 1.263s^3 & \text{if } \theta_c > 90° \end{cases} \tag{5.14}$$

Note that for a hydrophilic media, the wetting phase is the liquid phase, therefore the Leverette function is expressed in terms of gas-phase saturation, whereas in hydrophobic media, the gas phase becomes the wetting phase and therefore the liquid-phase saturation is used. Contact angle, θ_c of the GDL is dependent upon hydrophilic ($0^o < \theta_c < 90^o$) or hydrophobic ($90^o < \theta_c < 180^o$) nature of the GDM and varies with the Teflon content. Here, the surface tension σ for liquid water-air system is taken as 0.0625 N/m at 80ºC.

Mass fraction of water in liquid phase (mf_l^i) is unity, since solubility of other species in liquid phase is assumed to be zero. Therefore, integration of Equation 5.4 for water species across the GDM thickness yields to:

$$\gamma_c^{\mathrm{H_2O}} \vec{u} C^{\mathrm{H_2O}} - D_g^{\mathrm{H_2O},eff} \nabla C_g^{\mathrm{H_2O}} + \left(\frac{1}{M^{\mathrm{H_2O}}} - \frac{C_g^{\mathrm{H_2O}}}{\rho_g}\right)\vec{j}_l = \vec{j}_w \tag{5.15}$$

Here, $C_g^{\mathrm{H_2O}}$ is the molar concentration of water in the gas phase and is equal to saturation concentration of water (*i.e.* P_{sat}/R_uT) if the gas is fully saturated with water vapor. $\vec{j}_w$ represents the net molar flux of water through individual layers of the cell and has the units of [mol·m^{-2}·s^{-1}]. For each individual layer, $\vec{j}_w$ is a function of local current density through the production and net water transport across the membrane, α. Here, the net water transport coefficient across the membrane is defined as the net number of water molecules transported across the membrane per proton, such that:

$$j_m^{\mathrm{H_2O}} = \alpha \frac{\mathrm{I}}{\mathrm{F}} \tag{5.16}$$

The corresponding expressions for the net water flux for each component of the cell is given in Table 5.1.

The liquid saturation is expressed in terms of the total water concentration via the following relation:

$$s = \frac{C^{\mathrm{H_2O}} - C_{sat}^{\mathrm{H_2O}}}{C_l^{\mathrm{H_2O}} - C_{sat}^{\mathrm{H_2O}}} \qquad \text{where } C_l^{\mathrm{H_2O}} = \frac{\rho_l}{M^{\mathrm{H_2O}}} \tag{5.17}$$

Once the liquid saturation, *s* is obtained, the individual phase velocities are obtained using the following relations.

$$\rho_l \vec{u}_l = \vec{j}_l + \lambda_l \rho \vec{u} \tag{5.18}$$

$$\rho_g \vec{u}_g = -\vec{j}_l + \lambda_g \rho \vec{u} \tag{5.19}$$

Then the phase pressure drops can be obtained using Darcy's law for each individual phase *k*:

$$\nabla p_k = -\frac{\mu_k}{k_{rk} K} \vec{u}_k \tag{5.20}$$

5.2.2. Water transport across the membrane

In this study, we consider the water transport across the membrane by permeation driven by the hydraulic pressure gradient, by diffusion due to water concentration gradient across the membrane and by electro-osmotic drag due to proton flux. These three modes of water transport, namely hydraulic permeation, diffusion and electro-osmotic drag, are described with the following equation.

$$\frac{d}{dx}\left(-\rho_l \frac{K_m}{\mu_l M^{\mathrm{H_2O}}} \frac{d}{dx} p_l \right) = \frac{d}{dx}\left(D_m^{\mathrm{H_2O}} \frac{d}{dx} C_m^{\mathrm{H_2O}} \right) - \frac{d}{dx}\left(n_d \frac{\mathrm{I}}{\mathrm{F}} \right) \tag{5.21}$$

where the membrane water concentration, $C_m^{\mathrm{H_2O}}$ is:

$$C_m^{\mathrm{H_2O}} = \lambda \frac{\rho_{dry}}{EW} \tag{5.22}$$

Here, λ is the number of water molecules per sulfonate group in the membrane and referred to as the water content of the membrane. The thermodynamic equilibrium of the membrane water content with the surrounding medium is described by the water uptake curve. Zawodzinski *et. al.* (1993) measured the water uptake for Nafion® membranes, concluding that the water content of the membrane is around 16 when it is in equilibrium with liquid water at 80ºC, and the relation between the water content of the

membrane and the surrounding medium water activity, a ($P_g^{H_2O} / P_{sat}$), is given by the water uptake curve when the membrane is humidified with water vapor. Here, we use a 3rd order polynomial curve fit to Zawodzinski *et. al.*'s data to calculate membrane water content when the membrane is in equilibrium with water vapor:

$$\lambda = 1.4089 + 11.263a - 18.768a^2 + 16.209a^3 \quad \text{for } a \le 1 \tag{5.23}$$

In Equation 5.21, K_m, $D_m^{H_2O}$ and n_d denote membrane hydraulic permeability, water diffusivity and electro-osmotic drag coefficient, respectively. When integrated along the membrane thickness in steady-state, Equation 5.21 becomes:

$$-\rho_l \frac{K_m}{\mu_l M^{H_2O}} \frac{d}{dx} p_l - D_m^{H_2O} \frac{d}{dx} C_m^{H_2O} + n_d \frac{\mathrm{I}}{\mathrm{F}} = \vec{j}_w \tag{5.24}$$

The reported values in the literature for hydraulic permeability of membrane show a large variation, namely between $1.8 \cdot 10^{-18}$ m^2 (Bernardi and Verbrugge 1992) and $2 \cdot 10^{-20}$ m^2 (Meier and Eigenberger 2004), for Nafion® based membranes humidified with liquid water. In this work, we use the data from Meier and Eigenberger (2004), which is $2 \cdot 10^{-20}$ m^2 for a membrane fully humidified with liquid water at 80ºC (*i.e.* λ =16).

Here, the diffusivity of water in the membrane is taken from Motupally *et. al.* (2000) and is given as:

$$D_m^w = \begin{cases} 3.1 \cdot 10^{-7} \lambda \left(e^{0.28\lambda} - 1 \right) e^{-2346/T} & 0 < \lambda \le 3 \\ 4.17 \cdot 10^{-8} \lambda \left(1 + 161 e^{-\lambda} \right) e^{-2346/T} & 3 \le \lambda \le 17 \end{cases} \quad [\mathrm{m}^2/\mathrm{s}] \tag{5.25}$$

It is known that the electro-osmotic drag of water is linearly proportional to the number of protons transported across the membrane, and this proportionality constant is called "electro-osmotic drag coefficient" and known to be a function of water content of the membrane (Springer et al. 1991, Zawodzinski et al. 1995). Springer et al. used a linear dependence of electro-osmotic drag on water content ($2.5\lambda/22$) whereas Zawodzinski et. al. have shown that the electro-osmotic drag coefficient is around 2.5 when the membrane is humidified with liquid water and around unity when humidified with water vapor. That is,

$$n_d = \begin{cases} 1 & \lambda \le 10.1129 \quad (\text{Vapor equilibriated}) \\ 2.5 & \lambda = 16 \quad (\text{Liquid equilibriated}) \end{cases} \tag{5.26}$$

5.3. Boundary Conditions

In our one-dimensional modeling domain ranging from the anode GDL to cathode GDL, the boundary conditions are only required at two GDL/channel interfaces. For a flooded GDL, this boundary condition depends on the size, shape and number of the liquid droplets covering the GDL surface, and is thus a function of such parameters as the channel gas velocity and GDL surface wettability. However, in this work we assume that in both anode and cathode, the GDL surface facing the gas channel is free of liquid water. Although this assumption is an approximation, it is quite valid for high channel gas velocities and/or carbon cloth GDL, according to a recent visualization study (Yang et al. 2004). Therefore, liquid water is assumed to evaporate at the GDL surface and the water vapor is transported from the GDL to the gas channel by convective mass transfer.

$$C^{\mathrm{H_2O}}\Big|_{\mathrm{ACh-AGDL}} = C^{\mathrm{H_2O}}_{ACh} - \frac{\alpha}{h_m}\frac{\mathrm{I}}{\mathrm{F}} \tag{5.27}$$

$$C^{\mathrm{H_2O}}\Big|_{\mathrm{CCh-CGDL}} = C^{\mathrm{H_2O}}_{CCh} + \frac{1}{h_m}\left(\alpha + \frac{1}{2}\right)\frac{\mathrm{I}}{\mathrm{F}} \tag{5.28}$$

The convective mass transfer coefficient, h_m, is calculated by the heat/mass transfer analogy as outlined by Pasaogullari and Wang (2004b) and Wang et al. (2001):

$$h_m = \mathrm{Nu}_{\mathrm{D}}\frac{\mathrm{Sc}}{\mathrm{Pr}}\frac{\cdot D^i}{d_h} \tag{5.29}$$

where D^i is the diffusion coefficient of species i, and d_h is the hydraulic diameter of the gas channel.

5.4. Numerical Procedure

The present model is solved separately in three different regions, namely anode GDL, PEM and cathode GDM, simultaneously. As seen in Table 5.1, the water fluxes across these layers are functions of the net water transport coefficient, α, which is initially unknown. Therefore, an iterative procedure is used to determine $\tilde{\alpha}$. An initial guess is provided for α and this guess is improved in consecutive iterations using bisection method until phase pressures and water content of the membrane converge to the same value at the interfaces. A relative error margin of 10^{-7} is set for convergence criteria, which requires around 25 iterations to obtain α accurate up to 7 digits. The resulting governing equations of water transport are non-linear 1st order ordinary differential equations, which are solved using a 4th-order adaptive-step Runge-Kutta method.

5.5. Results and Discussion

5.5.1. Effects of MPL

In this section, we compare water distribution and flow across the PEFC in two different configurations in order to investigate the effect of MPL. The first configuration is a conventional PEMFC without MPL. The properties of the materials for this configuration are given in Table 5.2. In the other configuration, an MPL with baseline properties as given in Table 5.2 is added to the cathode GDL, resulting in a bi-layer cathode GDM. Here, the total cathode GDM thickness is kept constant at 300 μm, with or without MPL. Both the anode and cathode GDL properties are selected to represent carbon paper (Toray-TGPH-120), as given in Table 5.2.

In Figure 5.2, the variation in the net water transport coefficient with the current density is given for two membrane thicknesses, Nafion 111 (25.4 μm) and Nafion 112 (50.8 μm). When, α (as defined in Equation 5.16) is positive, the electro-osmotic drag of water is larger than hydraulic permeation and back-diffusion of water across the membrane, hence the net water transport across the membrane is towards the cathode.

When an MPL is added to the cathode GDM, it is seen that water transport towards the anode is significantly increased, particularly at lower current densities. Due to its smaller pore size and higher hydrophobicity, the MPL has much larger capillary pressure and hence increases the liquid pressure on the cathode side of the membrane. Here, the permeability of the MPL is calculated from the following expression given by Rumpf and Gutte (Kaviany 1999) for packed beds with a narrow range of size distribution:

$$K = \frac{\varepsilon^{5.5}}{5.6} d^2 \tag{5.30}$$

where d is the average pore diameter. For an MPL having an average pore size of 0.25 μm and a porosity of 0.5, this expression gives a permeability of $0.25 \cdot 10^{-15}$ m^2, compared to $8.7 \cdot 10^{-12}$ m^2 for a carbon-paper GDL. This smaller permeability causes much higher liquid pressure gradient across the cathode GDM as shown in Figure 5.3a, which in turn increases the hydraulic pressure differential across the membrane and hence the water flux across the membrane due to permeation. The higher water permeation flux from the cathode to the anode consequently lowers the net water transport coefficient through the membrane. At higher current densities, the electro-osmotic drag dominates over the enhanced hydraulic permeation; therefore, the effect of MPL is not as significant as at low current densities.

It is evident from Figure 5.2 that the net water transport coefficient increases with increasing membrane

thickness. This is because the electro-osmotic drag does not depend on the membrane thickness, while both the back-diffusion and hydraulic permeation are inversely proportional to the membrane thickness.

Figure 5.3a shows the liquid pressure profiles across the cathode GDM, where the gas pressure in cathode channel is 1.5 atm. It is seen that the increase in liquid pressure across the GDM without MPL is very small, thus not providing sufficient pressure gradient across the membrane to enhance water transport by permeation from the cathode to the anode. However, with the baseline-case MPL, the pressure differential increases by more than 80 kPa at a current density of 1.5 A/cm^2.

In Figure 5.3b, the liquid saturation profiles across the cathode GDM are shown. It is seen that the maximum liquid saturation is less than 10%, which does not introduce severe effects of flooding, due to the boundary condition utilized here (0% liquid saturation at the GDL-channel interface). It is seen that with a single-layer GDL, the liquid saturation is a continuous profile from the cathode channel-GDL interface to the cathode GDL-catalyst layer interface. However, for the bi-layer GDM with MPL, there is a discontinuity at the GDL-MPL interface, due to the disparity in the porous and wetting characteristics of MPL and GDL. This discontinuity is best explained by an illustration of capillary pressure vs. liquid saturation for both GDL and MPL, as shown in Figure 5.4. Since both gas and liquid phase pressures are continuous across the interface; the capillary pressure is also continuous, thus leading to:

$$\cos\left(\theta_c^{\,\mathrm{GDL}}\right)\left(\frac{\varepsilon^{\mathrm{GDL}}}{K^{\mathrm{GDL}}}\right)^{1/2} J\left(s_{\mathrm{int}}^{\mathrm{GDL}}\right) = \cos\left(\theta_c^{\,\mathrm{MPL}}\right)\left(\frac{\varepsilon^{\mathrm{MPL}}}{K^{\mathrm{MPL}}}\right)^{1/2} J\left(s_{\mathrm{int}}^{\mathrm{MPL}}\right) \tag{5.31}$$

Due to its larger permeability, under the same capillary pressure, the liquid saturation is much higher for coarse GDL than for MPL, hence, at the interface the MPL has much lower saturation than GDL. However, again due to smaller permeability, increase in the liquid saturation is much faster across the MPL, and in some cases (such as those shown in Figure 5.3b) the liquid saturation value at the cathode GDM-catalyst layer interface may exceed the single-layer value. In more realistic cases, where the liquid saturation value at the GDL-channel interface is not equal to zero, as in Figure 5.5, the MPL has an additional advantage of reducing the liquid saturation at the cathode GDM-catalyst layer interface.

In Figures 5.6aa and 5.6b, the hydraulic pressure differential across the membrane is plotted against the distance along the membrane thickness for Nafion 111 and Nafion 112 membranes, respectively. It is seen that the hydraulic pressure differential across the MPL can be increased as high as 80 kPa by MPL, improving the permeation of water from cathode to anode. When the net water transport coefficient is positive, the anode loses water and the anode water concentration remains lower than the saturation value even when the anode inlet gas is fully humidified. Consequently, the anode side of the membrane is in equilibrium with water vapor. On the other hand, since the cathode side is flooded, the membrane is in

equilibrium with liquid water on the cathode side. Note that, there is water transport across the membrane via permeation (due to the hydraulic pressure differential) only where the membrane is in equilibrium with liquid water with a corresponding water content, λ of 16. Furthermore, the water content is uniform in the membrane region hydrated with liquid water, thus water diffusion in membrane only occurs in regions which have a gradient in water content. This leads to a water content profile with discontinuous slopes across the membrane as shown in Figure 5.7, once there is liquid water on the cathode side of the membrane and the anode side is under humidified.

In Figure 5.7, it is seen that the region of the membrane that is in equilibrium with liquid water (λ=16) is extended by using MPL, increasing overall water content of the membrane for both membrane thicknesses. However, it is seen that in the thinner membrane (e.g. Nafion 111), a relatively larger portion of the membrane is in equilibrium with liquid water, so the average water content of the thinner membrane is higher. It is also seen that with the increasing current density, this liquid water equilibrated region becomes smaller.

It is observed that a bi-layer cathode GDM consisting of an MPL and a coarse GDL result in water transport characteristics similar to those achieved by adjusting the operating conditions, such as higher cathode and lower anode pressures. Particularly, operating with pressure differentials has been shown to significantly improve the performance (Jannsen and Overvelde 2001), particularly due to improvement of membrane water content, as provided by MPL. In all these cases, an increased pressure differential across the membrane ensues, which enhances the back-flux (*i.e.* towards the anode) of water.

5.5.2. Effect of MPL thickness

In this section, we analyze the effects of the MPL thickness on water transport and distribution. The parameters used for this case are the same as those in Table 5.2, except that the thicknesses of the MPL and GDL are varied in order to keep the total thickness of the cathode GDM to 300 μm. As seen in Figure 5.8, the net water transport coefficient is a strong function of MPL thickness, particularly at lower current densities. As the MPL thickness increases, the net water transport coefficient curve shifts downwards, indicating that the water flux towards the anode is increasing. With increasing MPL thickness, the resistance to liquid water flow in the cathode increases – this causes the fraction of water flowing through the membrane toward the anode to increase, resulting in a decrease in the cathode water flux. The inset of Figure 5.8 shows the change of net water transport coefficient with the MPL thickness at several current densities. It is seen that the dependence of net water transport coefficient on the MPL thickness is much stronger at lower current densities, largely due to weaker electro-osmotic drag. At higher current densities, the electro-osmotic drag dominates over the hydraulic permeation, and the effect of the MPL thickness decreases.

The liquid pressure profiles for different MPL thicknesses at a current density of 1.5 A/cm^2 are shown in Figure 5.9. As discussed above, due to smaller permeability of MPL, there is a larger increase in liquid pressure in the MPL; hence, with increasing MPL thickness, the liquid water pressure at the cathode side of the membrane increases. This causes a higher hydraulic pressure differential across the membrane, resulting in the increased water flux towards the anode.

5.5.3. Effect of MPL pore size

Figure 5.10 shows the net water transport coefficient across the membrane for several mean pore sizes of MPL. Here, the properties of the MPL except for the mean pore size are taken from the baseline-case, which are given in Table 5.2. The net water transport curve shifts downwards with decreasing mean pore size, indicating increasing water flux towards the anode. The capillary pressure and hence the liquid water pressure in the MPL increases with decreasing pore size. Further, the MPL permeability decreases with decreasing pore size (see Equation 5.30), which increases resistance to water flow towards the cathode channel. Therefore, water tends to flow in the path which has smaller resistance, increasing the flow rate towards the anode. The MPL pore size effect is much more visible at lower current densities, in which the back-flux of water dominates over the electro-osmotic drag. As the current density increases, the electro-osmotic drag of water across the membrane becomes larger, diminishing the effect of MPL. As seen in the inset of Figure 5.10, the mean pore size of MPL is not very effective at higher current densities.

It is evident that smaller MPL pore size increases the tendency of liquid water flow towards the anode. However, a design with the smallest pore size may not be optimal since the gas phase transport will be hampered with decreasing pore sizes. Therefore, the optimal MPL pore size should be governed by the competing effects of water transport and oxygen diffusion, and both have to be considered in optimizing the MPL structure.

5.5.4. Effect of MPL porosity

Figure 5.11 shows the net water transport coefficient with respect to current density for different MPL porosities. As seen in Figure 5.11, the MPL porosity is also quite effective in controlling the water transport in a PEMFC. With decreasing MPL porosity, resistance to the liquid water flow in the cathode increases, which results in increased water flux towards the anode, as indicated by lowering of the net water transport coefficient shown in Figure 5.11. The inset of Figure 5.11 shows the change in the net water transport with MPL porosity at different current densities. It is clearly seen that the effect of MPL porosity is more dominant at lower current densities, since electro-osmotic drag is not dominant at these current densities. This behavior shows a similarity to the effect of MPL pore size, which determines the absolute permeability.

5.5.5. Effect of MPL wettability

As with the porosity and the pore size, the wetting characteristics of the MPL also affect the water transport in PEMFCs. Capillarity is directly linked to wettability of the porous materials. In this work, we characterize the MPL wettability by an average contact angle, and we analyze the effect of this average contact angle. Figure 5.12 shows the net water transport coefficient for different MPL contact angles. It is seen that as the MPL contact angle increases (*i.e.* more hydrophobic), permeation of water across the membrane towards the anode due to hydraulic pressure differential is enhanced, resulting in a lower net water transport coefficient. As shown in the inset of the same figure, the slope of the curve gets decreases with increasing current density, as electro-osmotic drag is more effective in higher current densities. It is evident from Equation 5.12 that the capillary pressure is a linear function of $\cos(\theta_c)$. When the MPL is less hydrophobic (*i.e.* lower contact angle), the liquid pressure build-up in the MPL is smaller, resulting in a smaller liquid pressure at the cathode side of the membrane. Consequently, the water flux towards the anode is smaller. Also note that, with increasing MPL contact angle, the capillary transport of liquid water across the MPL is facilitated; therefore the liquid saturation rise across the MPL is reduced.

In the analysis of the effect of MPL wettability, we have not accounted for the fact that the mean pore size also varies with MPL wettability. Because the PTFE and carbon particles in the MPL differ significantly in size; the mean pore size of the MPL also depends on the PTFE content, hence wettability. This effect has to be considered for more accurate analysis and optimization of MPL. However, in general it can be said that the MPL provides better water management capabilities with higher hydrophobicity.

5.6. Conclusions

A one-dimensional, two-phase model has been developed for bi-layer GDMs and membrane of a PEFC, and the effects of the MPL and its properties on water transport are analyzed. The following conclusions can be drawn from this study:

a) Bi-layer cathode GDM provides better water management capability, particularly by increasing the tendency of water flow towards the anode. This effect is a consequence of the hydraulic pressure build-up due to strong capillary pressure in MPL and the increased resistance to liquid water removal from the cathode. This, in turn establishes a higher pressure differential across the membrane, promoting the transport of water from cathode to anode by permeation.

b) The reduced water flux toward the cathode decreases cathode flooding; therefore, it improves the cell performance by relaxing the mass transfer limitations. Furthermore, a discontinuity in the liquid saturation profile at the MPL and GDL interface arises due to their differing micro-porous and wetting

characteristics. This discontinuity further reduces the flooding in the cathode catalyst layer-MPL interface, particularly when saturation levels at the GDL-channel interface are high.

c) It is seen that the water flux towards the anode is enhanced with smaller pore size, larger thickness and hydrophobicity, and lower porosity of the MPL.

Although we have not considered an MPL in the anode GDM, it is expected that the effect of the anode MPL may not be significant unless the anode is as severely flooded as the cathode.

The gas phase transport and electron transport are also affected by the MPL pore structure and wetting characteristics so they need to be accounted for in the MPL optimization. Work is underway to analyze these effects to further optimize the MPL pore structure and its wetting characteristics.

List of Symbols

C^i Molar concentration of species *i* [mol/m^3]

d Pore diameter of MPL [μm]

d_h Hydraulic diameter of the channel [m]

D^i Diffusion coefficient of species *i* [m^2/s]

EW Equivalent weight of membrane [1.1 kg/mol for Nafion® 11-]

F Faraday's constant [96487 C/mol]

h_m Convective mass transfer coefficient [m/s]

I Current density [A/m^2]

$\vec{j}_k$ Mass flux of phase *k* [kg/m^2·s]

K Absolute permeability [m^2]

k_{rk} Relative permeability of phase *k*

M^i Molecular weight of species *i* [kg/mol]

p Pressure [Pa]

s Liquid saturation

$\vec{u}$ Velocity [m/s]

Subscripts

c capillary

g gas

int interface

l liquid

m membrane

sat saturation

Superscripts

GDL Gas diffusion layer

MPL Micro-porous layer

H_2O water species

O_2 oxygen species

Greek Letters

α Net water transport coefficient

δ Thickness

ε Bulk porosity

γ_c Advection coefficient

λ Water content of membrane ($\#H_2O/\#SO_3H$)

λ_k Relative mobility of phase *k*

μ Dynamic viscosity, [Pa.s]

ν Kinematic viscosity, [m^2/s]

ρ Density [kg/m^3]

ρ_{dry} Dry density of membrane [kg/m^3]

σ Surface tension [N/m]

θ_c Contact angle, [^{o}]

Table 5.1 Mass and water flux for individual layers of a PEMFC

	Mass Flux, j_m (Equation 3)	**Water Flux, j_w** (Equations 15 & 24)
Anode GDL	$\frac{\mathrm{I}}{\mathrm{F}}\left(\frac{M^{\mathrm{H_2}}}{2}+\alpha M^{\mathrm{H_2O}}\right)$	$\frac{\mathrm{I}}{\mathrm{F}}\alpha$
Membrane	N/A	$\frac{\mathrm{I}}{\mathrm{F}}\alpha$
Cathode GDL/MPL	$\frac{\mathrm{I}}{\mathrm{F}}\left(-\frac{M^{\mathrm{O_2}}}{4}+\left(\alpha+\frac{1}{2}\right)M^{\mathrm{H_2O}}\right)$	$\frac{\mathrm{I}}{\mathrm{F}}\left(\alpha+\frac{1}{2}\right)$

Table 5.2 Material properties, transport parameters and operating conditions

Parameter	**Value**
Transport parameters	
Surface tension, σ (Incropera and DeWitt 1996)	0.0625 N/m
Anode gas kinematic viscosity, $\nu_{g,a}$ (Incropera and DeWitt 1996)	1.11×10^{-5} m^2/s
Cathode gas kinematic viscosity, $\nu_{g,c}$ (Incropera and DeWitt 1996)	1.76×10^{-5} m^2/s
Liquid kinematic viscosity, ν_l (Incropera and DeWitt 1996)	3.52×10^{-7} m^2/s
Liquid density, ρ_l (Incropera and DeWitt 1996)	974.85 kg/m^3
Water vapor diffusivity in anode @ 1.5 atm, 353.15 K, $D_{g,a}^{\mathrm{H_2O}}$	$1.273\cdot10^{-4}$m^2/s
Water vapor diffusivity in cathode @ 1.5 atm, 353.15 K $D_{g,c}^{\mathrm{H_2O}}$	$2.625\cdot10^{-5}$m^2/s
Prandtl number in anode, Pr_a	0.650
Prandtl number in cathode, Pr_c	0.739
Schmidt number in anode, Sc_a	0.261
Schmidt number in cathode, Sc_c	0.532
Hydraulic diameter of channel, d_h	1.0 mm
Nusselt number, Nu_D (Incropera and DeWitt 1996)	3.61
Material properties *(Typical values)*	
GDL absolute permeability, K_{GDL} (Toray TGPH-120) (Williams et al. 2004)	8.69×10^{-12} m^2
GDL porosity, ε_{GDL} (Williams et al. 2004)	0.75
GDL contact angle, θ_c (Wet-proofed)	110º
Anode GDL thickness, δ_{AGDL}	300 μm
Total cathode gas diffusion media thickness, δ_C	300 μm
Membrane thickness (Nafion® 111), δ_{mem}	25.4 μm
Membrane hydraulic permeability, K_{mem} (at λ=16) (Meier & Eigenberger 2004)	2×10^{-20} m^2
Baseline-case MPL properties	
Thickness, δ_{MPL}	30 μm
Porosity, ε_{MPL}	0.5
Average pore size, d_{MPL}	250 nm
Absolute permeability, K_{MPL}	2.47×10^{-16} m^2
Contact angle, $(\theta_c)_{MPL}$	120º
Operating Conditions	
Cell temperature, T	353.15 K
Anode channel pressure, p_A	1.5 atm
Cathode channel pressure, p_C	1.5 atm
Anode channel humidity	100%
Cathode channel humidity	100%

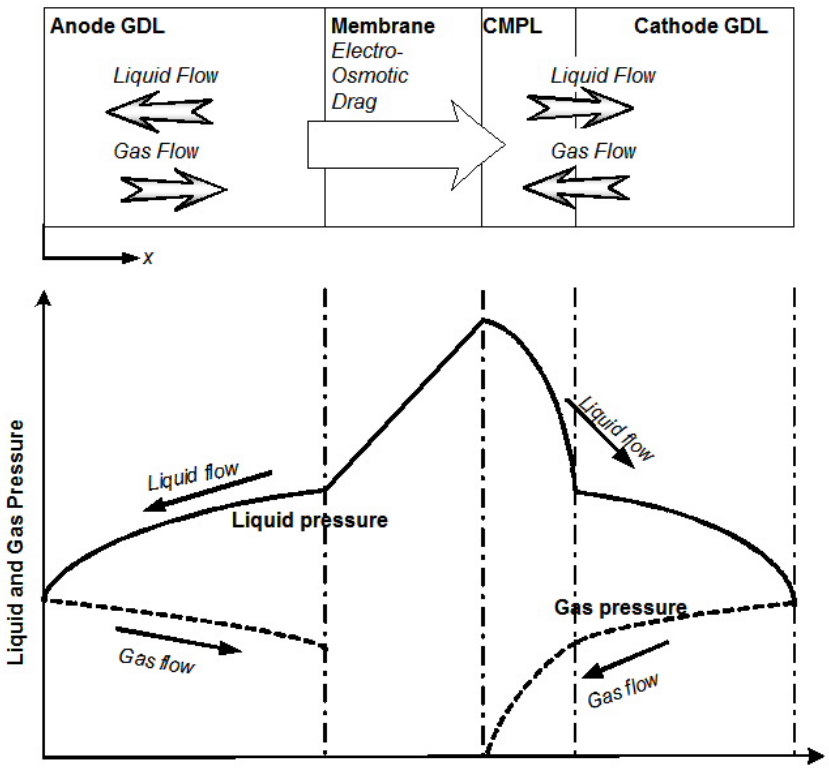

Figure 5.1 Schematics of modeling domain, transport phenomena and individual phase pressure profiles in a PEMFC with micro-porous layer.

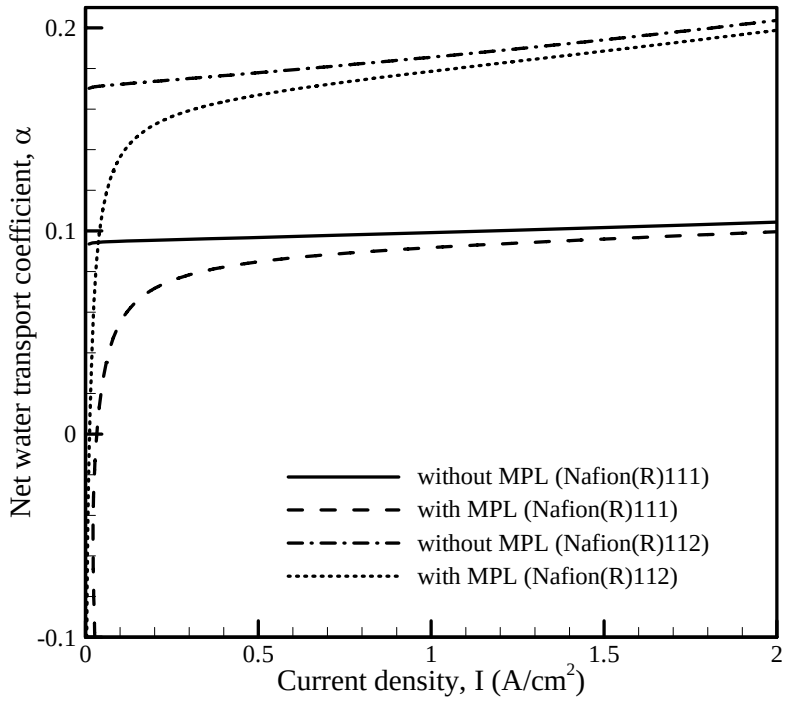

Figure 5.2 Net water transport coefficient, α with and without MPL for two different membrane thicknesses. MPL properties are taken from the baseline-case given in Table 5.2.

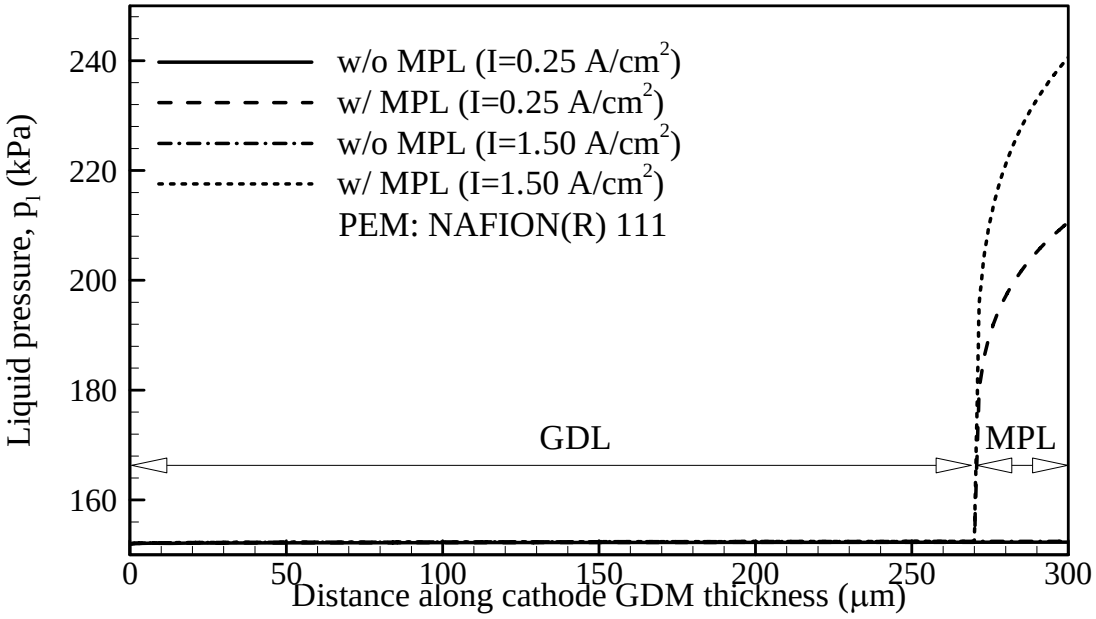

(a)

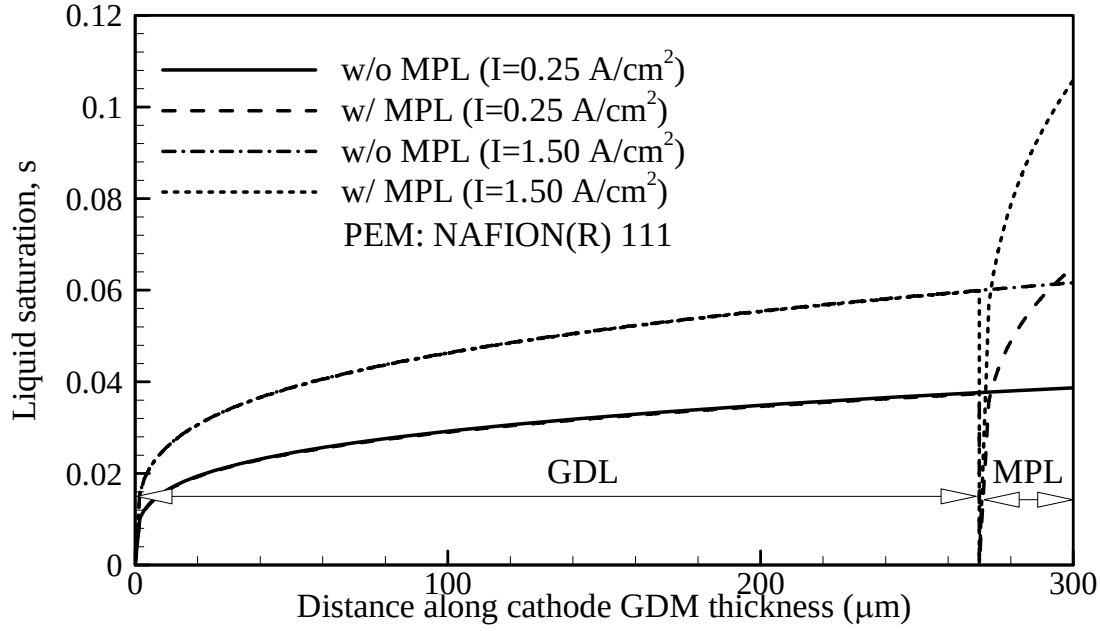

(b)

Figure 5.3 Effect of MPL on (a) liquid pressure, and (b) liquid saturation across the cathode GDM.

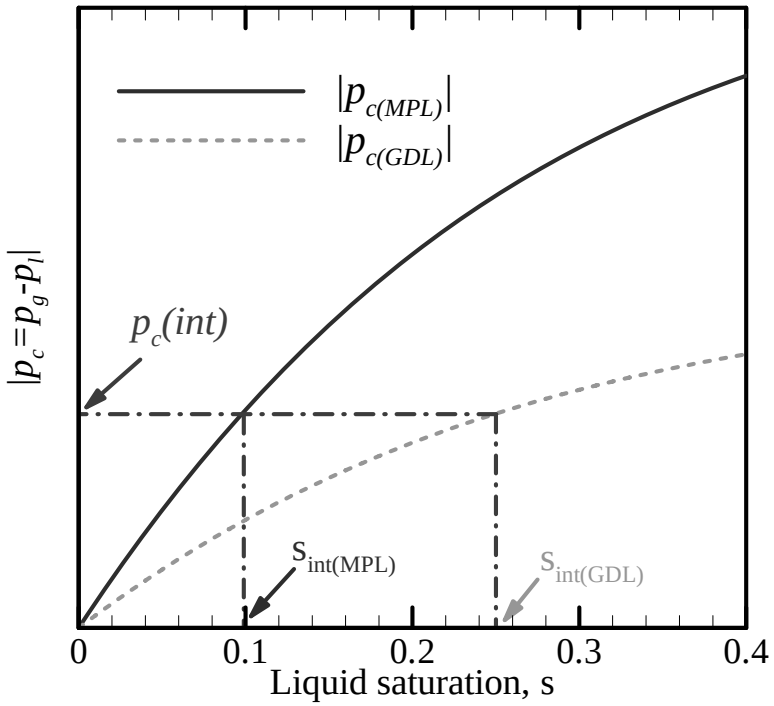

Figure 5.4 Schematics of saturation discontinuity at the GDL-MPL interface

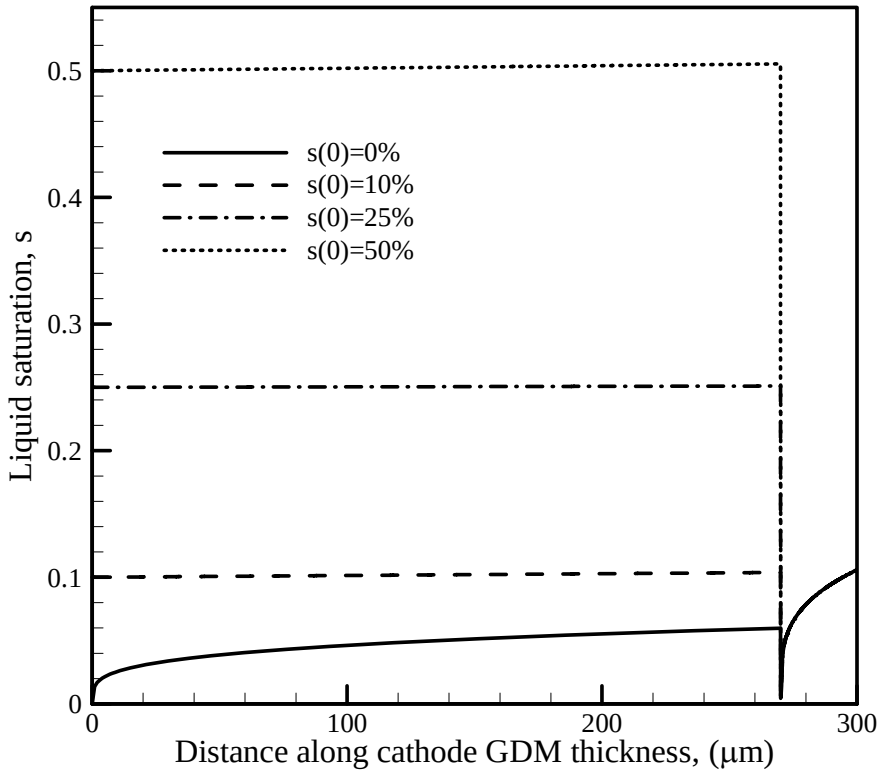

Figure 5.5 Liquid saturation profiles with different boundary conditions at the GDL/channel interface.

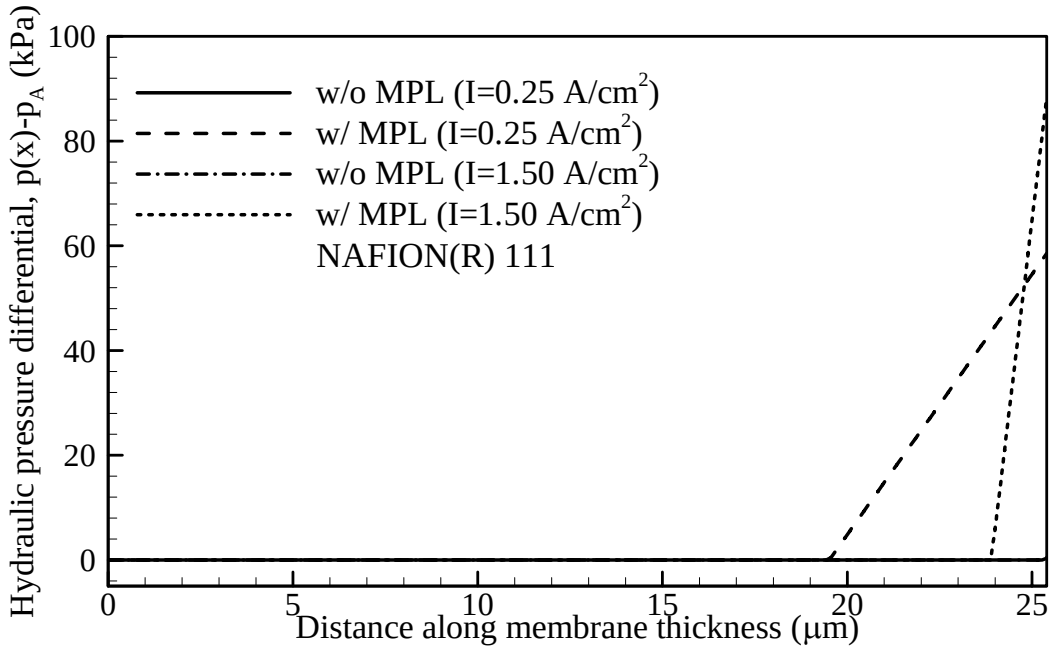

(a)

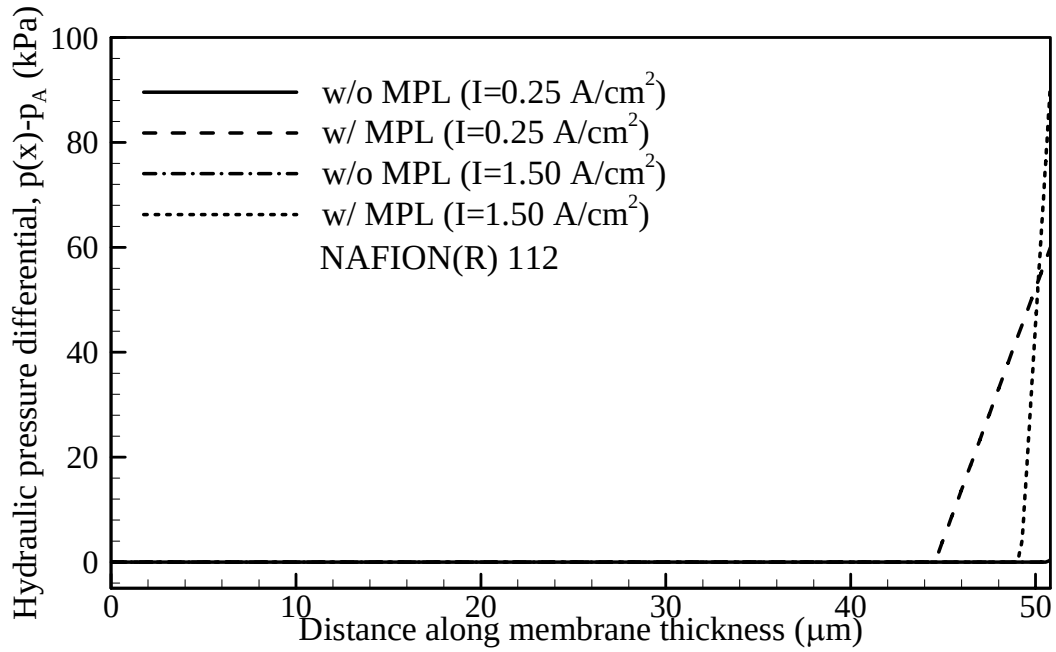

(b)

Figure 5.6 Hydraulic pressure profiles in the membrane for: (a) Nafion® 111 (25.4 μm) and, (b) Nafion® 112 (50.8 μm).

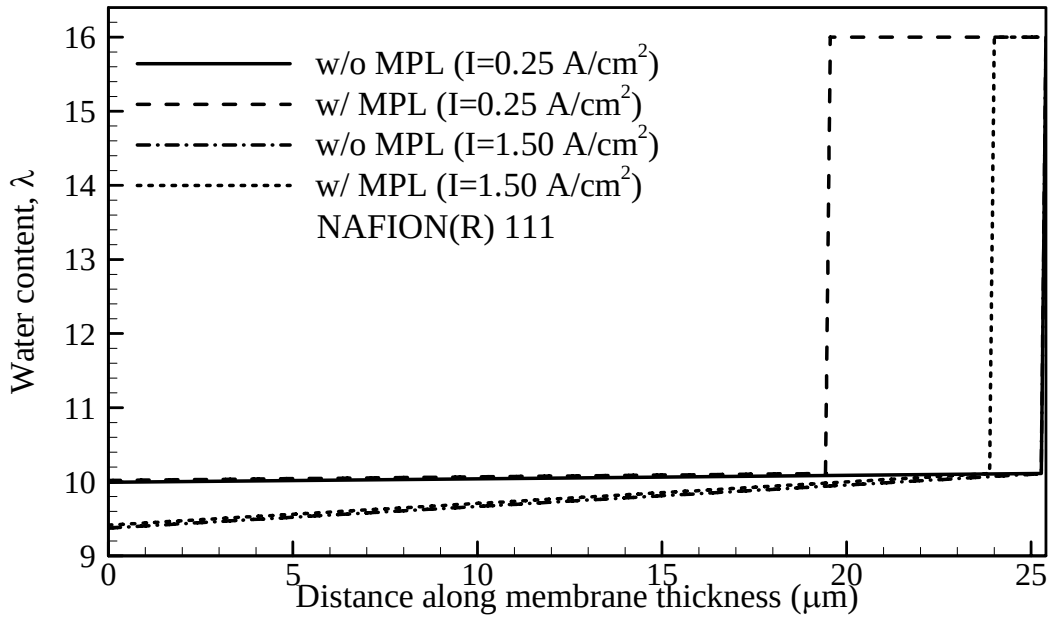

(a)

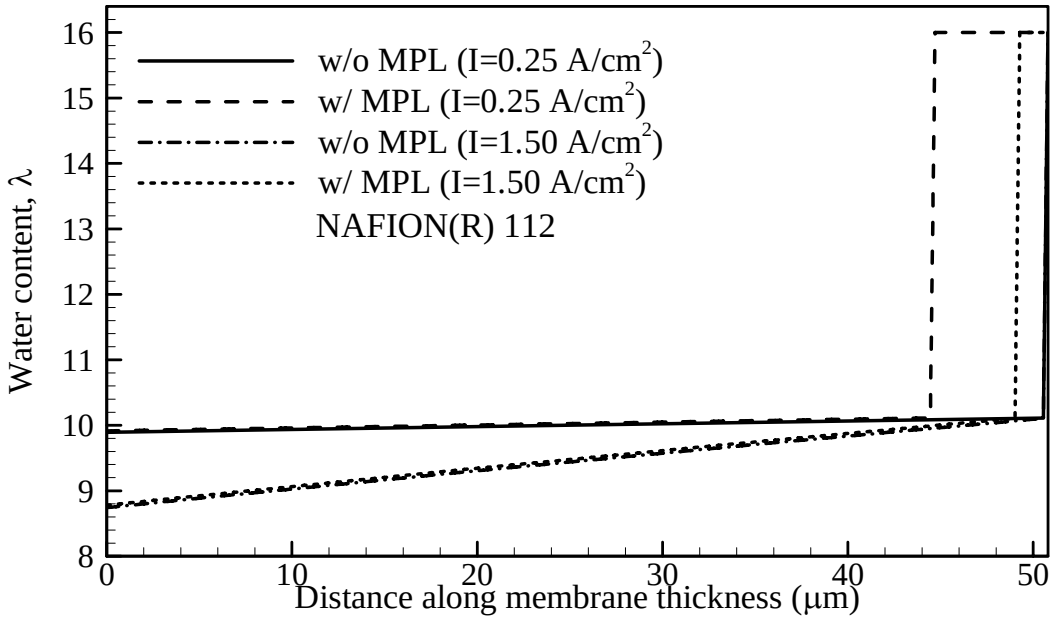

(b)

Figure 5.7 Water content profiles in the membrane for: (a) Nafion® 111 (25.4 μm) and, (b) Nafion® 112 (50.8 μm).

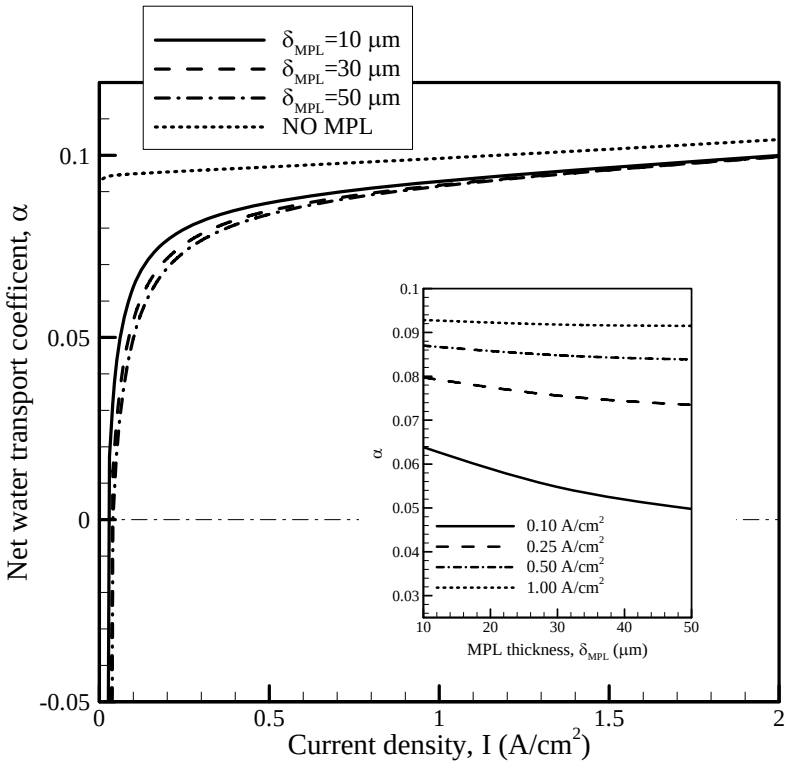

Figure 5.8 Net water transport coefficient, α for different MPL thicknesses. Other MPL properties are taken from baseline-case given in Table 5.2. Inset shows the variation of net water transport coefficient with MPL thickness at different current densities.

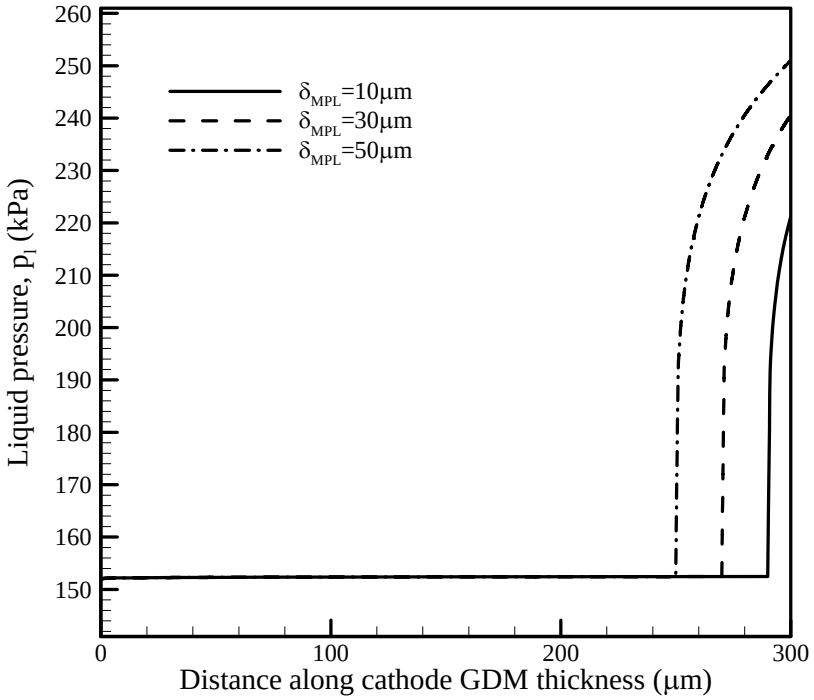

Figure 5.9 Liquid pressure profiles in cathode GDM for different MPL thicknesses at 1.5 A/cm^2. Other MPL properties are taken from baseline-case given in Table 5.2. Inset shows the variation of net water transport coefficient with MPL thickness at different current densities.

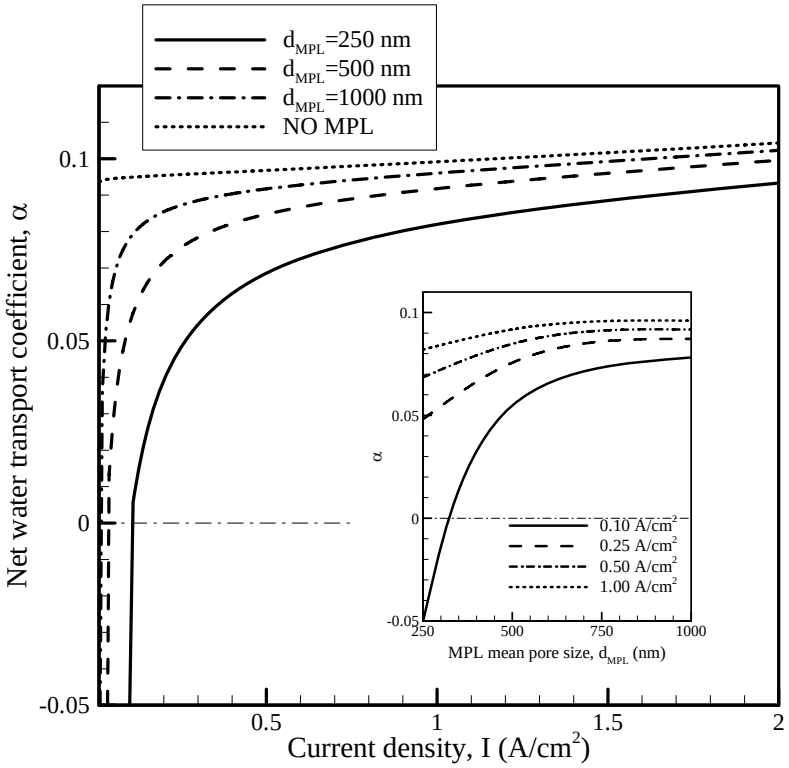

Figure 5.10 Net water transport coefficient, α for different mean pore sizes of MPL. Other MPL properties are taken from baseline-case given in Table 5.2. Inset shows the variation of net water transport coefficient with mean pore size of MPL at different current densities.

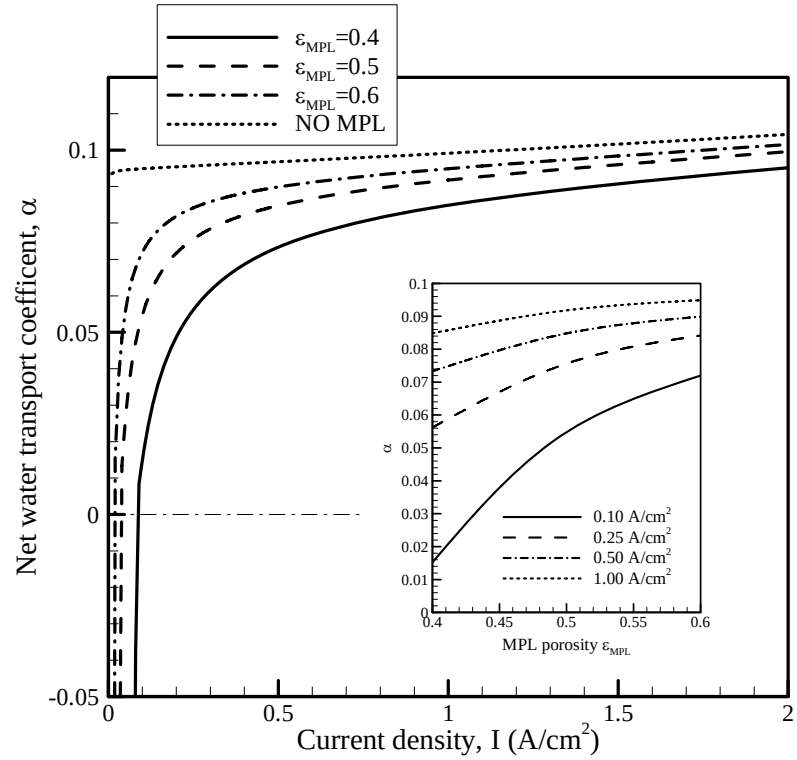

Figure 5.11 Net water transport coefficient, α for different MPL bulk porosities.Other MPL properties are taken from baseline-case given in Table 5.2. Inset shows the variation of net water transport coefficient with MPL bulk porosity at different current densities.

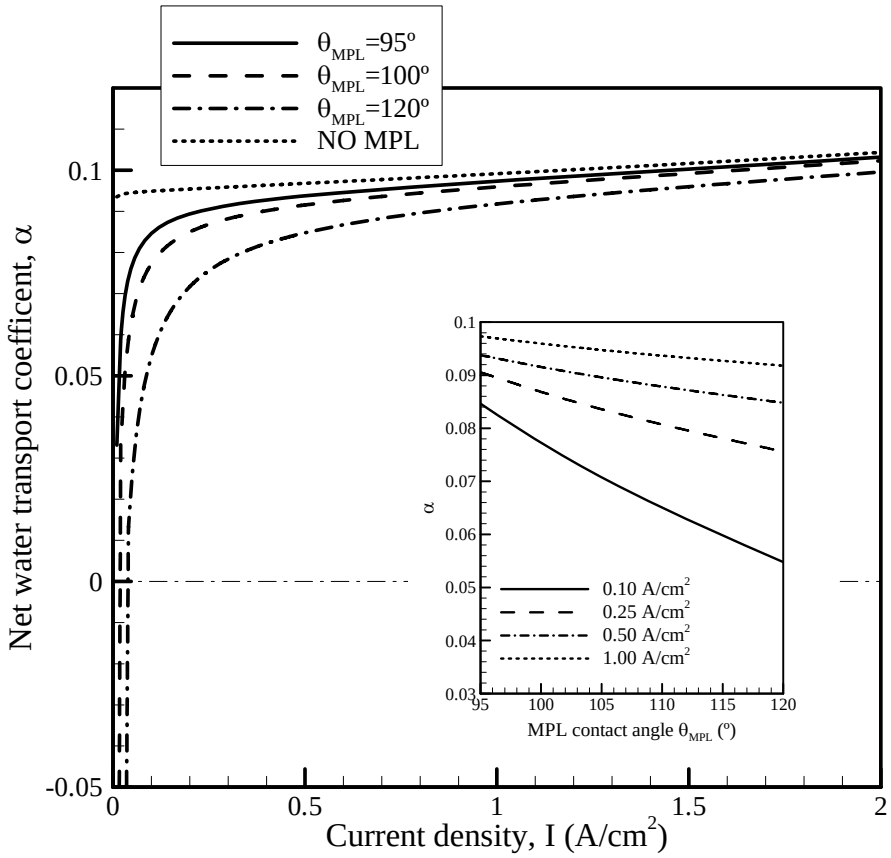

Figure 5.12 Net water transport coefficient, α for different MPL contact angles. Other MPL properties are taken from baseline-case given in Table 5.2. Inset shows the variation of net water transport coefficient with MPL contact angles at different current densities.

6. Modeling Anisotropic Two-Phase Heat and Mass Transfer in Gas Diffusion Layer of PEM Fuel Cells[††]

6.1. Introduction

The proton exchange membrane fuel cells (PEMFCs), owing to their high energy efficiency, low emission and low noise, are widely considered as the most promising alternative power source in the 21st century for automotive, portable and stationary applications. A typical PEMFC consists of several distinct components: the membrane electrode assembly (MEA) comprising a proton conducting electrolyte membrane sandwiched between two catalyst layers (CL), the porous gas diffusion layers (GDL) and the bipolar plates with embedded gas channels. In the anode CL, the hydrogen oxidation reaction (HOR) splits the hydrogen into electrons, which are transmitted via the external circuit, and protons, which migrate through the membrane and participate in the oxygen reduction reaction (ORR) in the cathode CL to recombine with oxygen and producing water and waste heat.

Despite significant progress in recent years in enhancing the overall cell performance, a major limitation arises from the two-phase transport owing to the blockage of the open pore paths due to liquid water in the cathode GDL thus hindering oxygen transport to the active reaction sites in the CL. GDL plays a crucial role in the overall water management, which requires a delicate balance between reactant transport from the gas channels and water removal from the electrochemically active sites. An effective water management prevents flooding while ensuring sufficient membrane hydration to minimize ohmic losses. Along with water management, thermal management is also a key to high performance and longevity of PEMFCs. At an energy-conversion efficiency of roughly 50%, a PEMFC produces nearly the same amount of waste heat as its electric power output. Furthermore, PEMFCs tolerate only a small temperature variation, since the proton conductivity of the polymer electrolyte membrane strongly depends on the degree of its hydration and hence on the membrane temperature since the vapor saturation pressure is a strong function of temperature, as shown in Figure 6.1. It is seen that a 10ºC temperature difference can alter the saturation pressure by 50%. (Water saturation pressure is 0.37 atm. at 75ºC, whereas it is 0.56 atm. at 85ºC.) Additionally, condensation of water vapor releases heat, causing undesirable local hot spots, which could reduce the membrane performance by reducing the degree of hydration and hence accelerate degradation. These concerns require rigorous thermal management in a PEMFC, coupled with precise water management. Thus, fundamental understanding of thermal transport phenomena is of paramount importance and the non-isothermal two-phase PEMFC model presented here

[††] This chapter is based on a manuscript submitted for consideration of journal publication: U. Pasaogullari, P. P. Mukherjee, C. Y. Wang, and K. S. Chen, "Anisotropic two-phase heat and mass transfer in gas diffusion layer of polymer electrolyte fuel cells", submitted to *J. Appl. Phys* on September 22, 2006.

is extremely useful in order to elucidate heat transfer mechanisms and quantify the temperature distribution.

Several studies (Nguyen and White 1993, Fuller and Newman 1993, Yi and Nguyen 1998, Maggio et al. 1996, Shimpalee and Dutta 2000, Um et al. 2000, Zhou and Liu 2001, Bradean et al. 2002) attempted to predict temperature distribution under single-phase (dry) conditions in a PEMFC. Most recently, Wang (2004) and Ju *et al.* (2005) reviewed the single-phase, non-isothermal models of PEMFCs in detail.

Two-phase transport in PEMFCs has been studied by several researchers (Wang et al. 2001, Natarajan and Nguyen 2001, You and Liu 2002, Wang 2003, Weber et al. 2004, Pasaogullari and Wang 2004a, 2004b, 2005; Pasaogullari et al. 2005, Weber and Newman 2005, Meng and Wang 2005) in varied levels of complexities; however, the focus of these studies was primarily on the isothermal investigation of the transport phenomena. The issue of two-phase heat transfer with condensation/evaporation, leading toward a simultaneous description of water and thermal management, has hardly been explored. In their works, Nam and Kaviany (2003), and Rowe and Li (2001) studied both the phenomena using a one-dimensional model. Nam and Kaviany focused on the two-phase transport in the cathode GDL of a PEMFC with particular emphasis on the influence of the GDL structure, in terms of fiber diameter, porosity and capillary pressure, on the water removal rate. On the other hand, the model of Rowe and Li was more rigorous which included a comprehensive description of multi-component species (oxygen, hydrogen and vapor/liquid water) transport as well as proton and electron transport.

Among the multidimensional, nonisothermal, two-phase models for a PEMFC, notable works include Yuan and Sunden (2004), Costamagna (2001), Berning and Djilali (2003), Mazumder and Cole (2003), and Bradean *et al.* (2004). Except Costamagna, all of the afore-mentioned multi-dimensional models considered the phase change effect. Whereas the two-phase model by Berning and Djilali is based on the unsaturated flow theory (UFT) with the assumption of constant gas pressure across the porous medium; Mazumder and Cole adopted the multiphase mixture (M^2) model originally proposed by Wang and Cheng (1997). Birgersson *et al.* (2005) and Senn and Poulikakos (2005) recently presented a two-dimensional, nonisothermal, two-phase model based on the multi-fluid approach, which is in contrast to the M^2 model approach. Birgersson *et al.* further emphasized the importance of thermal contact resistance on the flooding behavior. Most recently, Wang and Wang (2006) developed a full-cell, nonisothermal, two-phase model based on the M^2 approach; and they identified the importance of water transport as well as heat removal via vapor-phase diffusion under the temperature gradient. However, none of the prior models took into account the effect of intrinsic anisotropy in the GDL structure on the two-phase heat transport phenomena.

Unlike the typical porous media often encountered in reservoir simulations or groundwater flows, the GDL structure is characterized by a fibrous porous medium, exhibiting significant anisotropy due to the orientation of the underlying fibers or fiber-bundles as shown in Figures 6.2a and 6.2b for carbon paper and carbon cloth, respectively. Due to the preferential orientation of the constituting fibers, the GDL exhibits strong anisotropy leading to different transport coefficients in the through-plane and in-plane directions. In the present work, two-phase heat transfer and temperature distribution in a PEMFC cathode gas diffusion layer (GDL) is analyzed in detail, with particular emphasis on the effect of GDL anisotropy on the underlying heat and water transport, for the first time. Therefore, the primary objective of the current work is to present a model for predicting two-phase flow and thermal transport and the underlying interactions occurring in the cathode GDL of a PEFC. In the next section, the development of our two-phase, non-isothermal model for a cathode GDL is discussed. Finally, the salient predictions from the current model illustrating the effect of GDL anisotropy on the temperature and water distributions are presented.

6.2. Mathematical Model

In the present study, we focus on two-phase transport of water and heat in the cathode GDL of a PEMFC; accordingly, the modeling domain is limited to the cathode GDL only, and the boundary conditions are specified at the interfaces of GDL with the catalyst layer, gas channel and current collector, as shown schematically in Figure 6.3a. The associated transport fluxes are shown in Figure 6.3b. Taking advantage of the symmetries of the configuration into account, the two-dimensional cross-section of the GDL (Figure 6.3a, the rectangle ABCDE) between the catalyst layer and half of the channel and half of the current-collector land is considered.

6.2.1. Two-phase model and governing equations

Our model is based on the multiphase mixture model (M^2), originally proposed by Wang and Cheng (1997) and used later for two-phase PEMFC modeling by Wang *et al.* (2001), You and Liu (2002), Pasaogullari (2004a, 2004b, 2005), Pasaogullari *et al.* (2005), Meng and Wang (2005), Mazumder and Cole (2003), and Wang and Wang (2006). The multi-phase mixture (M^2) model is an exact re-formulation of the classical two-fluid, two-phase model in a single equation. One salient feature of M^2 model is that it can be conveniently used in a computational domain where single- and two-phase zones co-exist, often the case in a PEMFC. In classical two-fluid models, the interface between single- and two-phase zones has to be tracked explicitly, which substantially increases the numerical complexity.

6.2.1.1 Mass conservation

Mass conservation for the two-phase mixture as given by the M^2 model is:

$$\frac{\partial(\varepsilon\rho)}{\partial t} + \nabla \cdot (\rho \mathbf{u}) = 0 \tag{6.1}$$

In this equation, $\mathbf{u}$ and ρ are the superficial mixture velocity and mixture density, respectively (Wang and Cheng 1997):

$$\rho = \rho_l \cdot s + \rho_g \cdot (1 - s) \tag{6.2}$$

Here, *s* and (1-s) represent the fractions of the open pore space occupied by the liquid and gas phases, respectively.

6.2.1.2. Momentum conservation

The momentum conservation for the two-phase mixture based on the mixture velocity $\mathbf{u}$ is:

$$\frac{1}{\varepsilon}\left[\frac{\partial(\rho \mathbf{u})}{\partial t} + \frac{1}{\varepsilon}\nabla \cdot (\rho \mathbf{u}\mathbf{u})\right] = \nabla \cdot (\mu_B \nabla \mathbf{u}) - \nabla p - \frac{\mu}{K}\mathbf{u} \tag{6.3}$$

where, μ is the mixture viscosity (Wang and Cheng 1997):

$$\mu = \rho\left[\frac{k_{rl}}{\nu_l} + \frac{k_{rg}}{\nu_g}\right]^{-1} \tag{6.4}$$

Equation 6.3 is the Brinkman extension to the Darcy's law using superficial velocities (i.e. based on total volume, rather than the open pore volume); therefore, the predicted velocities are continuous at interfaces.

6.2.1.3. Species conservation

The species conservation equation in the M^2 model, written in terms of molar concentration, is (Pasaogullari and Wang 2004a):

$$\frac{\partial(C^i)}{\partial t} + \nabla \cdot (\gamma_c \mathbf{u} C^i) = \nabla \cdot \left[\mathbf{D}_g^{i,eff} \nabla C_g^i\right] - \nabla \cdot \left[\left(\frac{C_l^i}{\rho_l} - \frac{C_g^i}{\rho_g}\right)\mathbf{j_l}\right] \tag{6.5}$$

Here, C^i is the total concentration of species *i* in liquid and gas phases. The liquid and gas phases have different flow-fields; therefore, the advective transport of species is corrected via an advection correction factor, γ_c.

$$\gamma_c = \begin{cases} \dfrac{\rho}{C^{\mathrm{H_2O}}}\left(\dfrac{\lambda_l}{M^{\mathrm{H_2O}}} + \lambda_g \dfrac{C_g^{\mathrm{H_2O}}}{\rho_g}\right) & \text{for water} \\ \dfrac{\rho\lambda_g}{\rho_g(1-s)} & \text{for other species} \end{cases} \tag{6.6}$$

where λ_l and λ_g are the relative mobility of liquid and gas phases, respectively:

$$\lambda_k = \frac{k_{rk}/\nu_k}{\sum_k k_{rk}/\nu_k} \tag{6.7}$$

Here, k_{rl} and k_{rg} are the relative permeabilities of liquid and gas phases, respectively:

$$k_{rk} = \frac{K_k}{K} \tag{6.8}$$

In this work, we assume the relative permeabilities of individual phases are related to the cube of phase saturations, *i.e.* (cf. Wang et al. 2001):

$$k_{rk} = s_k^{\,3} \tag{6.9}$$

where s_k is the saturation of phase *k*. Phase saturations, s_k are defined as the fraction of the open pore volume occupied by that individual phase; hence the liquid saturation, *s* is defined as:

$$s = \frac{V_l}{V} \tag{6.10}$$

Wang and Cheng (1997) define the mixture mass fraction as:

$$\rho mf^{\,i} = \rho_g mf_g^{\,i}(1-s) + \rho_l mf_l^{\,i} s \tag{6.11}$$

which leads to definition of liquid saturation from the total water concentration, $C^{\mathrm{H_2O}}$ via:

$$s = \frac{\rho mf^{\,\mathrm{H_2O}} - \rho_g mf_g^{\,\mathrm{H_2O}}}{\rho_l mf_l^{\,\mathrm{H_2O}} - \rho_g mf_g^{\,\mathrm{H_2O}}} = \frac{C^{\mathrm{H_2O}} - C_{sat}^{\mathrm{H_2O}}}{C_l^{\mathrm{H_2O}} - C_{sat}^{\mathrm{H_2O}}} \qquad \text{where } C_l^{\mathrm{H_2O}} = \frac{\rho_l}{M^{\mathrm{H_2O}}} \tag{6.12}$$

Since oxygen and nitrogen are assumed to be insoluble in liquid water due to very low solubility (Atkins 1998), liquid phase only includes water *i.e.*, $mf_l^{\mathrm{H_2O}} = 1$.

Accounting for anisotropy of the diffusion media, the effective gas diffusion coefficient, $\mathbf{D}_g$ becomes a second-rank tensor, as the effective diffusivities in the in–plane and through–plane direction are

significantly different due to the fiber orientation of the GDL, as seen in Figure 6.1. The treatment of anisotropic diffusivity in the numerical model is explained in the appendix (Section 6.5). Nam and Kaviany (2003) have investigated the effective gas diffusion coefficients in the GDL, using a pore network model. Their predictions agreed well with the previous correlations of Tomadakis and Sotirchos (1993) on fibrous porous media:

$$\mathbf{D}_g^{i,eff} = f(\varepsilon) D_g^i$$
$$\text{where } f(\varepsilon) = \varepsilon\left(\frac{\varepsilon - \varepsilon_p}{1-\varepsilon_p}\right)^{\alpha} \qquad \alpha = \begin{cases} 0.521 & \text{in - plane direction} \\ 0.785 & \text{through - plane direction} \end{cases} \tag{6.13}$$

This effective diffusion model predicts that in-plane diffusion coefficient is larger than the through-plane counterpart. The structured orientation of fibers in the in-plane direction causes a less tortuous path for gas diffusion than that in the through-plane direction, in which fibers are more randomly oriented resulting in more tortuous gas diffusion path.

The last term in the right hand side of the species conservation equation (Equation 6.5) represents the capillary transport in the porous media. The theory of capillary transport in hydrophobic PEFC GDLs has been explained by Pasaogullari and Wang (2004a). The capillary flux, $\mathbf{j}_l$, is defined as (Wang and Cheng 1997):

$$\mathbf{j_l} = \frac{\lambda_l \lambda_g}{\nu} K\left[\nabla p_c + (\rho_l - \rho_g)\mathbf{g}\right] \tag{6.14}$$

where p_c is the capillary pressure and given by (Wang and Cheng 1997):

$$p_c = \sigma \cos(\theta_c)\left(\frac{\varepsilon}{K}\right)^{1/2} J(s) \tag{6.15}$$

Here, *J(s)* is the Leverett function and, for both hydrophobic and hydrophilic GDL is given as (Pasaogullari and Wang 2004a):

$$J(s) = \begin{cases} 1.417(1-s) - 2.120(1-s)^2 + 1.263(1-s)^3 & \text{if } \theta_c < 90° \\ 1.417s - 2.120s^2 + 1.263s^3 & \text{if } \theta_c > 90° \end{cases} \tag{6.16}$$

The above Leverett function was proposed by Udell (1985) for packed beds, and its applicability to PEMFC GDL requires experimental verification, which is still absent in the literature.

Since the permeability of the GDL differs by up to an order of magnitude in the in-plane and through plane directions, the capillary liquid water flow is no longer isotropic; hence, we also account for the anisotropy in liquid water flow via:

$$j_x = \frac{\lambda_l \lambda_g}{\nu} K_{xx} \left[\frac{\partial p_c}{\partial x} + (\rho_l - \rho_g) g_x \right]$$
$$j_y = \frac{\lambda_l \lambda_g}{\nu} K_{yy} \left[\frac{\partial p_c}{\partial y} + (\rho_l - \rho_g) g_y \right] \quad (6.17)$$

where K_{xx} and K_{yy} denote the permeabilities in the through-plane and in-plane directions, respectively. Through-plane permeability of the PEMFC GDLs has been characterized by Williams *et al.* (2004), and in particular the permeability of Toray carbon paper (TGPH-090) was found to be 8.69×10^{-12} m^2. On the other hand, in-plane permeability of carbon-paper GDLs has been reported to be in the range of 1.9-4.7×10^{-12} m^2 by Bluemle *et al.* (2004).

When applied to water, the species equation, Equation 6.5, implies that the water transport within a two-phase zone is due to gas phase diffusion (i.e. the first term on the right hand side) and capillary action (i.e. second term on the right hand side), in addition to advection. The gas phase diffusion driven by the gradient in saturation concentration vanishes in an isothermal two-phase zone as saturation concentration is only a function of temperature, but can be significant in a non-isothermal, two-phase zone. In the latter case, the gas phase diffusion of water aids in the capillary transport in the through-plane direction (i.e. from catalyst layer towards gas channel) because both fluxes are directed towards outside of the GDL. But, the two are opposed to each other in the in-plane direction where the gas phase diffusive flux of water is pointed from the channel region (hotter) toward the land region (cooler), while the capillary flux of liquid water is from the land (higher liquid saturation) to channel regions.

6.2.1.4. Energy conservation

The energy conservation equation in M^2 model for the GDL is (Wang and Cheng 1997):

$$\frac{\partial}{\partial t} \left\{ \left[(1-\varepsilon)(\rho c_p)_s + \varepsilon \rho c_p \right] T \right\} + \nabla \cdot \left(\gamma_h \rho c_p \mathbf{u} T \right) = \nabla \cdot \left(\mathbf{k}^{eff} \nabla T \right) + S_{T,PC} \quad (6.18)$$

This equation describes the conduction and convection heat transfer in PEMFCs and a heat source/sink due to condensation and evaporation. Since the pore size of the GDL is relatively small (~10μm), and advection within the GDL is negligible, the solid and fluid temperatures are taken to be equal. The terms on the left hand side of Equation 6.18 are the transient and convective terms, respectively. In the transient term, $(1-\varepsilon)(\rho c_p)_s + \varepsilon \rho c_p$ represents the total heat capacitance of the porous medium, consisting of

solid matrix and two-phase mixture occupying the open pores. Again, since the liquid and gas phases have different flow-fields, the advective heat transfer is corrected via (Wang and Cheng 1997):

$$\gamma_h = \frac{\rho\left(\lambda_l c_{p,l} + \lambda_g c_{p,g}\right)}{s\rho_l c_{p,l} + (1-s)\rho_g c_{p,g}} \tag{6.19}$$

The last term on right hand side of Equation 6.18 describes the heat release or adsorption due to phase change (*i.e.* condensation or evaporation) and is given by:

$$S_{T,PC} = h_{fg} \cdot \dot{m}_{fg} \tag{6.20}$$

where h_{fg} is the latent heat of condensation/evaporation and $\dot{m}_{fg}$ the mass rate of phase change that can be readily calculated from the continuity equation of liquid phase, which consists of only water:

$$\dot{m}_{fg} = \varepsilon \frac{\partial(\rho_l s)}{\partial t} + \nabla \cdot \left(\rho_l \mathbf{u}_l\right) \tag{6.21}$$

The liquid phase velocity is calculated using:

$$\rho_l \mathbf{u}_l = \mathbf{j}_l + \lambda_l \rho \mathbf{u} \tag{6.22}$$

Substituting Equation 21 into Equation 22 yields:

$$\dot{m}_{fg} = \varepsilon \frac{\partial(\rho_l s)}{\partial t} + \nabla \cdot \left(\mathbf{j}_l + \lambda_l \rho \mathbf{u}\right) \tag{6.23}$$

Thermal conductivity of the GDL also exhibits anisotropy, and it is found that the in-plane GDL conductivity may be larger by up to 14 times than that of in the through-plane direction (source: Toray Industries, Inc.). Therefore, the anisotropy of the GDL solid matrix is also accounted for heat conduction in the GDL via effective conductivity tensor, $\mathbf{k}^{eff}$ as explained in the appendix (Section 6.5).

6.2.2. Boundary conditions

The water production and heat generation rates are linearly related to current density distribution. However, our modeling domain only includes the cathode GDL; therefore, the following assumptions need to be made in order to predict the current density:

a). Water content in the membrane and catalyst layers is only a function of cathode side water concentration and temperature. This assumption will only hold true if the anode side is also fully saturated and the net water transport across the membrane is small, resulting in small water content gradients across the membrane. Therefore, in addition, net water transport coefficient, α is also assumed to be zero, which is a reasonable assumption for thinner membranes, i.e. <25μm.

b). Concentration overpotential of the anode hydrogen oxidation reaction (HOR) is negligible.

c). Bipolar plates are perfectly electronically conductive, i.e. negligible ohmic losses across the plates.

d). Cathode catalyst layer is a thin interface between the GDL and the membrane.

Using the above assumptions, the current density distribution is calculated as follows:

First, the cell potential is equal to:

$$V_{cell} = U_{oc}(T) - \eta_a - \eta_c - IR_{\Omega} \tag{6.24}$$

where R_{Ω} is the ionic resistance of membrane and catalyst layers:

$$R_{\Omega} = \frac{\delta_{mem}}{\kappa_e} + 2\frac{\delta_{CL}}{\kappa_e \varepsilon_{mc}^{1.5}} \frac{I_{CL}^{ave}}{I} \tag{6.25}$$

The anode activation polarization is described as follows. Using a linear kinetics approximation due to facile anode electrochemical kinetics in PEFCs gives:

$$\eta_a = \frac{I\,RT}{(\alpha_a + \alpha_c) F\, ai_o^{ref,a}} \tag{6.26}$$

The cathode activation polarization is described via Tafel kinetics due to higher overpotentials:

$$\eta_c = \frac{RT}{\alpha_c F} \ln\left(\frac{C_{O_2}^{ref}}{C_{O_2}} \frac{I}{ai_o^{ref,c}} \right) \tag{6.27}$$

Combining Equations 6.24 – 6.27 yields:

$$V_{cell} = U_{oc}(T) - \frac{I\,RT}{(\alpha_a + \alpha_c) F\, ai_o^{ref,a}} - \frac{RT}{\alpha_c F} \ln\left(\frac{C_{O_2}^{ref}}{C_{O_2}} \frac{I}{ai_o^{ref,c}} \right) - IR_{\Omega} \tag{6.28}$$

which is a nonlinear equation with only one unknown, current density, I for a given cell voltage. This non-linear equation is solved at the GDL-CL interface using a bisection method, with an accuracy of up to 10^{-8} A/cm^2.

We note that the prediction of current density is not meant to be thoroughly accurate since it involves certain assumptions; hence it is only used as an input to the model. For accurate prediction of current density, modeling domain needs to be extended to include the anode and the membrane, which is outside the scope of this work. Given the current distribution, the boundary conditions are prescribed as follows.

6.2.2.1. Catalyst-layer-GDL interface (left boundary in Figure 6.3a, line AB):

The total mass flux due to consumption/production of all species is given by:

$$\mathbf{j}_m \cdot \mathbf{n}_{GDL-CL} = \frac{\mathrm{I}}{2\mathrm{F}}\left[(1+2\alpha)M^{\mathrm{H_2O}} - \frac{1}{2}M^{\mathrm{O_2}}\right] \tag{6.29}$$

The water flux due to water production and net water transport from anode can be expressed as:

$$\mathbf{j}_{\mathrm{H_2O}} \cdot \mathbf{n}_{GDL-CL} = \frac{\mathrm{I}}{2\mathrm{F}}(1+2\alpha) \tag{6.30}$$

where α is the net water transport coefficient across the membrane, and in this work it is assumed to be zero, since the membrane is assumed to be very thin (25.4 μm Nafion® 111).

Since the anode and the electrolyte are not included in the modeling domain, we also need to assume the distribution of heat generation rate. It is assumed that all the heat generation associated with cathode ORR and half of the joule heating due to ohmic losses is transported through cathode. The resulting heat flux at the GDL-catalyst layer interface then becomes:

$$q''_{GDL-CL} = \mathrm{I}\left(\eta_{\mathrm{c}} + T\frac{dU_{oc}}{dT} + \frac{1}{2}R_{\Omega}\right) \tag{6.31}$$

The latent heat effects due to condensation/evaporation in the GDL is not included in this term, since it is calculated via continuity of liquid water flow as explained in Equation 6.23, and included as heat source/sink in the energy conservation equation. Here, it is assumed that water enters the GDL in the same phase as in GDL.

6.2.2.2. Current collector – GDL interface (top-right boundary in Figure 6.3a, line CD):

The current collectors, typically graphite or metal, have large thermal conductivities; therefore, the temperature at this interface is taken to be equal to the given cell temperature. Note that, this also includes an inherent assumption of zero contact resistance between the current collector and GDL.

$$T_{GDL-CC} = T_{cell} \tag{6.32}$$

As the current collector is impermeable, a zero-flux boundary condition for species and no-slip velocity boundary condition are prescribed at the current collector-GDL interface.

6.2.2.3. Gas channel – GDL interface (bottom-right boundary in Figure 6.3a, DE):

At this boundary, gas-phase pressure is taken to be equal to the operating pressure of the PEMFC (i.e. 1 atm) whereas capillary pressure is set to zero. A convective heat transfer boundary is utilized and the convective heat transfer coefficient is calculated from correlations for the laminar flow in square cross-section ducts (Incropera and Dewitt 1996) as 25 W/m^2·K and the free-stream temperature is taken equal to

the operating temperature of the cell (i.e. 80ºC). Water concentration is taken to be equal to the saturation water concentration at the cell temperature, typical of an inlet section for a fully humidified cathode.

At the top and bottom boundaries (lines AE and BC in Figure 6.3a), symmetry boundary conditions are applied.

6.2.3. Numerical implementation

The resulting set of equations are discretized using a finite-volume method (Patankar 1980) and solved within the commercially available CFD software, Fluent®, by customizing via user defined functions (Fluent 6.2 User's Guide, Fluent Inc., Lebanon, New Hampshire). Fluent provides the flexibility of solving a generic advection-convection equation (Equation 6.33).

$$\frac{\partial(R\phi)}{\partial t} + \nabla \cdot (\mathbf{J}\phi) = \nabla \cdot (\mathbf{\Gamma} \nabla \phi) + S \tag{6.33}$$

The variables R, $\mathbf{J}$, $\mathbf{\Gamma}$ and S are customized via user-defined functions. The species conservation equations and energy equations are implemented using this generic scalar equation template.

The software utilizes the well-known SIMPLE algorithm for pressure-velocity coupling, and an algebraic multi-grid (AMG) solver to efficiently solve the set of discretized linear equations. For details of the SIMPLE algorithm, the reader is referred to the text by Patankar (1980).

6.2.3.1. Grid Independence

A grid independence study was carried out to determine the required grid resolution. The results are shown in Figure 6.4, and as seen 2400 computational cells (40 computational cells in the through-plane direction, 60 computational cells in the in-plane direction) were found to be adequate and computational time required for the 2D non-isothermal two-phase results shown in this work was around 10 minutes on a single PC (2 GB RAM, 1.66 GHz).

6.3. Results and Discussion

In order to investigate the effects of GDL anisotropy, two different GDLs were simulated at the same operating conditions, at 353.15 K cell temperature and 1 atm operating pressure. The two-dimensional domain employed in the computations corresponds to the inlet region of a PEMFC operated with fully humidified air. The first GDL is isotropic with uniform transport properties in all directions. The properties were taken to be that for Toray TGPH carbon paper (source: Toray Industries, Inc.); and the values for through-plane direction were used for all directions. The second GDL is anisotropic and the principal axes of the porous media (i.e. GDL) coincide with the coordinate axes (i.e. orthotropic). The

properties for this GDL were again taken to be that for Toray TGPH carbon paper. The transport properties are listed in Table 6.1.

Figure 6.5 shows the cathode polarization curves for both isotropic and anisotropic GDLs. Since the boundary conditions on the channel side was taken to be that at the inlet, oxygen concentration is high; therefore polarization curves do not show any mass transfer limitation effects, even at higher current densities. The overall performance at this location is limited by the ionic conductivity of membrane and catalyst layers. Both GDLs show very similar performance at relatively low current densities; however, the performances start to differ at high current densities due to limited electronic conductivity of isotropic GDL in the in-plane direction. As seen in Figure 6.6, due to a lower electronic conductivity in the in-plane direction, electron transport in the in-plane direction requires higher electronic phase potential gradient, resulting in higher electronic potential in the regions underneath the gas channel for the isotropic GDL. As the current flows through the current collector ribs, the distance for current flow is longer for those regions underneath the channel, and in turn it requires higher potential difference. In contrast, the electronic potential profile for the anisotropic GDL shows almost a one-dimensional behavior with very little variation in the in-plane direction due to a relatively large conductivity. Note that, Toray TGPH series carbon paper has almost 15 times higher electronic conductivity in the in-plane direction than that in the through-plane direction.

The effect of GDL anisotropy is clearly pronounced in the current density distributions, as shown in Figure 6.7. In the anisotropic GDL, the current density mainly follows the oxygen concentration, as shown in Figure 6.8, indicating that the reaction is mainly limited by mass transfer effects. On the other hand, the isotropic GDL shows an interesting profile with lower current density values under the gas channel even though the oxygen concentration is higher in those areas; and a higher current density in regions closer to the current collector. This profile indicates that for the isotropic GDL, both oxygen concentration and electronic potential affect the current distribution, each dominating in different parts of the active catalyst layer. Discontinuities in the current density profiles are related to liquid water distribution and resulting effective oxygen diffusivity, and are discussed later in detail with liquid saturation distributions.

Figure 6.9 shows the temperature contours in the GDL for two different cell voltages, 0.6 and 0.4 V, respectively. Perhaps, the most profound effect of the GDL anisotropy is seen in the temperature profiles. The isotropic GDL has equal conductivities in both in-plane and through plane directions, i.e. 1.7 W/m-K. It is seen here that a maximum temperature difference of up to 2ºC in 0.6 V and 5ºC in 0.4 V is observed for the isotropic GDL. Note that the heat generation rate at 0.4 V is roughly 2.5 times of that at 0.6 V. Similar to electronic phase potential, temperature profile also shows a maximum underneath the gas

channel. Since most of the heat generated (up to 99% as predicted by the results here) is transported through current collectors, main conductive heat transfer path is from under the channel towards current collector, where typically coolant channels are located. This requires that the heat generated under the channel has to travel in the in-plane direction; therefore, in-plane conductivity becomes the dominating parameter governing the temperature distribution. When a more realistic in-plane conductivity of 21 W/m-K is used (source: Toray Industries, Inc.), the temperature profile becomes almost one-dimensional, varying mostly in the through-plane direction. However, in the isotropic case with 1.7 W/m-K in-plane thermal conductivity, a highly non-uniform temperature distribution in the GDL is observed. The temperature is higher near the catalyst layer, since the heat flow is mainly by conduction. Furthermore, there is also a strong temperature gradient in the GDL from the region underneath the channel to the region underneath the land. This profile again indicates that the heat transfer from the GDL is mainly through the current collector land, that is, the land acts as a heat sink for the GDL. In anisotropic GDL, it is seen that the temperature distribution in the GDL is more uniform and maximum temperature is lower than the isotropic case. Although, the thermal conductivity in the through-plane direction has the same value for both isotropic and anisotropic cases, the heat transfer in the in-plane direction is much more effective with anisotropic GDLs due to higher conductivity; therefore temperature differences are smaller resulting in a more uniform temperature profile.

When the liquid saturation distributions in Figure 6.10 are examined, it is not surprising to see that most significant effects of GDL anisotropy are seen in the distribution of the liquid water. Liquid water distribution is a result of a combined effect of temperature distribution, oxygen distribution and electronic phase potential distribution, since they govern the water production rate through the current density. Temperature distribution becomes especially important since the saturation concentration, which governs the condensation of water, is a direct function of temperature as indicated in Figure 6.1. As seen in Figure 6.10, the anisotropic GDL predicts a larger portion of GDL being flooded with water compared to the isotropic GDL, since the overall lower temperature of the anisotropic GDL causes total water concentration to reach saturation concentration in a larger portion of the GDL. In the isotropic GDL, liquid water is mostly seen under the current collectors due to lower temperatures in this region, however in the anisotropic GDL liquid water is also seen under the gas channels. However, note that the simulation results presented here represent the near-the-inlet region of a PEMFC with the cathode inlet being fully humidified. In the actual PEMFC system, the channel water concentration would increase along the channel due to water production; therefore, the entire GDL cross-section might become flooded.

It is also seen that the maximum liquid saturation – which occurs underneath the current collectors in both cases – is higher in anisotropic GDLs. This is due to the fact that, in the anisotropic GDL, liquid water

transport in the in-plane direction is less effective due to the permeability being lower. Since the in-plane permeability is lower, it requires larger pressure gradient to drive the same liquid water flow, thereby requiring higher liquid saturation differential. Also note that, the distance between the maximum liquid saturation point and evaporation front is much longer in the anisotropic GDL, which contributes to the requirement of higher liquid pressure differential.

Unlike in an isothermal two-phase zone, there is water transport in vapor diffusion mode in a non-isothermal two-phase zone due to variation in saturation vapor concentration with temperature. This mode of vapor diffusion is from the high temperature regions to low temperature regions, since saturation concentration of water vapor increases with temperature as indicated in Figure 6.1. In the isotropic GDL, there exist temperature variations in both in-plane and through-plane directions, which results in water transport from the higher temperature region (under the middle of gas channel) to the lower temperature region (under the current collector). The water vapor then condenses underneath the current collector due to lower temperature, releasing heat. This mode of heat transfer is referred to as the "heat pipe effect" by Wang and Wang (2006) and found to be in comparable order with heat conduction. In our model predictions we also see similar effects in the isotropic GDL; however in an anisotropic model this effect vanishes since the temperature variation in the in-plane direction is minimal, minimizing any water vapor diffusion due to saturation concentration gradients in the in-plane direction.

To investigate the effect of anisotropy in the overall transport of heat and water vapor diffusion, conductive heat transfer and water vapor diffusion pathlines are plotted in Figure 6.11 for both anisotropic and isotropic GDLs at 0.4V. The conductive heat transfer pathlines were calculated from the conductive heat flux vectors given by:

$$\mathbf{j}^{\text{Heat}} = -\sum k_i \frac{\partial T}{\partial x_i}\mathbf{i}_i \tag{6.34}$$

where k_i is the effective conductivity in direction i. It is seen from Figure 6.11a that the conductive heat flux follows different paths for isotropic and anisotropic GDLs. In the isotropic GDL, a diagonal path from the region under the channel closer to catalyst layer towards the current collector is observed. As can be deduced from the temperature contours in Figure 6.9b, in the anisotropic GDL, the heat transfer is almost one-dimensional in the through-plane direction, and most of the lateral (in the in-plane direction) heat transfer occurs in regions very close to the channel-GDL interface.

Figure 6.11b shows the water vapor diffusion pathlines, which were calculated similar to heat conduction pathlines by the following equation:

$$\mathbf{j}^{\mathrm{H_2O}} = -\sum D_i^{\mathrm{H_2O,eff}} \frac{\partial C_{\mathrm{H_2O}}^{g}}{\partial x_i} \mathbf{i}_i \tag{6.35}$$

It is seen that the principal direction for water vapor diffusion is the through-plane direction in both the anisotropic and isotropic GDLs. However, it is seen that water vapor diffusion follows the temperature contour shown in Figure 6.9b in the two-phase region as water vapor concentration is equivalent to saturation concentration. Therefore, water vapor diffusion in two-phase region can be written as:

$$\mathbf{j}_{\mathrm{H_2O}}^{\mathrm{eff}} = -\sum D_i^{\mathrm{H_2O,eff}} \frac{\partial C_{\mathrm{H_2O}}^{sat}}{\partial x_i} \mathbf{i}_i = -\sum D_i^{\mathrm{H_2O,eff}} \frac{dC_{\mathrm{H_2O}}^{sat}}{dT} \frac{\partial T}{\partial x_i} \mathbf{i}_i = \frac{dC_{\mathrm{H_2O}}^{sat}}{dT} \sum \frac{D_i^{\mathrm{H_2O,eff}}}{k_i} j_i^{Heat} \tag{6.36},$$

and it becomes a function of temperature gradient. Therefore, vapor diffusion follows similar pathlines to conductive heat transfer flux in the two-phase region. Another interesting feature shown in Figure 6.11b is that the vapor diffusion changes direction at the condensation front, both visible at isotropic and anisotropic GDLs. As seen in Figure 6.12, vapor concentration has a peak at the condensation front and vapor diffusion is from condensation front towards the current collector in the two-phase region and it is from condensation front to GDL-channel interface in the single-phase region.

Figures 6.13 and 6.14 show the liquid and gas-phase flow fields, respectively. As seen in Figure 6.13, liquid pressure has a maximum co-located with the highest liquid saturation as shown in Figure 6.10, and liquid water flow is from higher liquid saturation to lower liquid saturation. Note that there is no liquid water flow in single-phase regions. In contrast, gas phase pressure is higher at the GDL-channel interface and gas flow is from high gas pressure locations to low gas pressure locations. It is also seen that gas velocity is significantly higher in two-phase regions than it is in single-phase regions. The reason for this is that the velocities plotted here are mass averaged: In a single-phase zone the gas velocity can be approximated as:

$$\rho_{gas} \mathbf{u}_{gas} = \mathbf{j}_{\mathrm{H_2O}} M_{\mathrm{H_2O}} + \mathbf{j}_{\mathrm{O_2}} M_{\mathrm{O_2}} = \frac{I}{2F}(1+2\alpha) M_{\mathrm{H_2O}} - \frac{I}{4F} M_{\mathrm{O_2}} \tag{6.37}$$

Assuming α is zero:

$$\rho_{gas} \mathbf{u}_{gas} = \frac{I}{4F}\left(2M_{\mathrm{H_2O}} - M_{\mathrm{O_2}}\right) = \frac{I}{2F} M_{\mathrm{H_2}} \tag{6.38}$$

Since water and oxygen fluxes are in different directions, the resulting velocity becomes small. However in a two-phase region, the phase velocities can be approximated as:

$$\rho_{gas} \mathbf{u}_{gas} = \mathbf{j}_{\mathrm{O_2}} M_{\mathrm{O_2}} = -\frac{I}{4F} M_{\mathrm{O_2}} \tag{6.39}$$

$$\rho_{liq}\mathbf{u}_{liq} = \mathbf{j}_{H_2O} M_{H_2O} = \frac{I}{2F}(1+2\alpha) M_{H_2O} \tag{6.40}$$

Since water and oxygen do not share the same velocity field anymore, the phases are separated and the gas velocity is significantly higher in the two-phase regions.

Figures 6.13 and 6.14 clearly show that the M^2 model is not a homogenous mixture model, rather a reformulation of the two-fluid model, capable of resolving the flow-fields for both phases individually.

6.4. Conclusions

A multi-dimensional model for predicting the two-phase transport of heat and water was developed and applied to investigate the temperature and water distributions in the cross-section of the cathode GDL in a PEMFC. The main focus has been to assess the effects of anisotropy of the gas diffusion layer on the coupled heat and mass transport in the cathode. A few observations can be made from this study:

i) Depending on the anisotropy of the GDL and the cell voltage, a temperature differential of up to 5ºC is predicted by the model. The fibrous structure of the GDL results in inherently higher conductivities along the fiber directions (i.e. usually the in-plane direction), and this anisotropy strongly affects the temperature distribution. The assumption of the isotropic conductivity for GDL fails to predict the temperature distribution accurately.

ii) The temperature distribution strongly affects the two-phase transport of water. Different temperature profiles are predicted for anisotropic and isotropic GDLs as a result of different thermal conductivities in the in-plane direction. This strongly affects the water transport and results in significantly different liquid saturation distributions. Due to overall lower temperature predicted, average liquid saturation is higher in the anisotropic GDL.

iii) In the non-isothermal two-phase zone, water removal is by both capillary transport of liquid water and gas phase diffusion of water vapor. The two transport mechanisms aid each other in the through-plane direction across the GDL thickness, but opposing each other in the in-plane direction, i.e. from channel to land.

iv) GDL anisotropy also affects the electron transport similar to heat conduction. Due to limited electronic conductivity in the in-plane direction for an isotropic GDL, the reaction is rather limited by electron transport and higher current densities are predicted in regions closer to current collectors due to shorter distance.

The present study demonstrates a strong need for coupled, anisotropic two-phase heat and water transport modeling of PEMFCs. Work is ongoing to incorporate the present anisotropic, non-isothermal, two-phase GDL sub-model into a full-cell PEMFC model in order to capture more profound effects of the

temperature distribution on other physicochemical processes in PEMFCs, such as the electrochemical kinetics in catalyst layers and hydration of the membrane.

6.5. Appendix: Orthotropic Diffusion

In an anisotropic media, the diffusion flux of a scalar ϕ in direction *i* depends not only the gradient of scalar ϕ in direction *i*, but in other directions, *j* via:

$$-\frac{\partial \phi}{\partial x_i} = \sum_j \frac{1}{\Gamma_{ij}} j_j^{\phi} \tag{A1}$$

where Γ_{ij} is the diffusion coefficient tensor and j_j^{ϕ} is the diffusive flux of scalar ϕ in *j* direction. This equation can be re-written for diffusive fluxes as:

$$j_i = -\sum_j \Gamma_{ij} \frac{\partial \phi}{\partial x_j} \tag{A2}$$

In an isotropic media, the diffusion tensor contains only diagonal elements (i.e. $\Gamma_{ij}=0$ when $i \neq j$), therefore the diffusive flux becomes:

$$j_i = -\Gamma_i \frac{\partial \phi}{\partial x_i} \tag{A3}$$

For a pure diffusion problem, in the absence of generation or consumption of scalar ϕ, it can be shown that (Bejan 1997):

$$\sum_i \frac{\partial j_i}{\partial x_i} = \sum_i \frac{\partial}{\partial x_i} \left[\sum_j \Gamma_{ij} \frac{\partial \phi}{\partial x_j} \right] = 0 \tag{A4}$$

Through a suitable transformation, Equation A4 is reduced to the canonical form:

$$\sum_i \frac{\partial}{\partial \zeta_i} \left[\Gamma_i \frac{\partial \phi}{\partial \zeta_i} \right] = 0 \tag{A5}$$

The transformed coordinates that satisfy Equation A5 is called the principal directions of the diffusion media. Consequently, if the principal directions of diffusion media (i.e. directions of the fiber orientation) coincide with the coordinate axes (i.e. *orthotropic diffusion*), then the diffusive flux of scalar ϕ can be written as:

$$j_i = -\Gamma_i \frac{\partial \phi}{\partial x_i} \tag{A6}$$

where $\Gamma_i = \Gamma_{ii.}$ The diffusion coefficient tensor, then, reduces to a diagonal tensor:

$$\Gamma = \begin{bmatrix} \Gamma_{xx} & 0 & 0 \\ 0 & \Gamma_{yy} & 0 \\ 0 & 0 & \Gamma_{zz} \end{bmatrix} \tag{A7}$$

Nomenclature

C^i	Molar concentration of species *i* [mol/m^3]
c_p	Specific heat [J/kg·K]
D^i	Diffusion coefficient of species *i* [m^2/s]
F	Faraday's constant [96487 C/mol]
h_{fg}	Latent heat of evaporation of water [kJ/kg]
I	Current density [A/m^2]
$\vec{j}_k$	Mass flux of phase *k* [kg/m^2·s]
K	Absolute permeability [m^2]
k	Thermal conductivity [W/m·K]
mf_k^i	Mass fraction of species *i* in phase *k*
M^i	Molecular weight of species *i* [kg/mol]
p	Pressure [Pa]
R	Universal gas constant [8.314 J/mol·K]
s	Liquid saturation
U_{oc}	Open circuit potential [V]
$\vec{u}$	Velocity [m/s]
V_{cell}	Cell voltage [V]

Greek Letters

ε	Bulk porosity
γ_c	Advection coefficient
η	Overpotential {V]
μ	Dynamic viscosity, [Pa.s]
ν	Kinematic viscosity, [m^2/s]
ρ	Density [kg/m^3]
τ	Bruggman correction factor

subscripts

g	gas
l	liquid
sat	saturation

superscript

H_2O	water

Table 6.1 Physical parameters and properties

Parameters/Properties	Value
Modeling Domain Dimensions and GDL Properties	
Cathode GDL thickness	300 μm
Half channel width	500 μm
Half current collector rib width	250 μm
GDL porosity, ε	0.7
Through-plane GDL permeability, K_{in}	$8.69\cdot10^{-12}$ m^2 (Williams et al. 2004)
In-plane GDL permeability, K_{th}	$3.00\cdot10^{-12}$ m^2 (Bluemle et al. 2004)
GDL contact angle, θ_c	110º
Fluid Properties	
Thermal cond. of liquid water*	$\left(0.621529+6.05\cdot10^{-4}\,\theta\right)\mathrm{W/m\cdot K}$
Viscosity of liquid water*	$\left(7.0968-0.0444\theta\right)\cdot10^{-4}\,\mathrm{Pa\cdot s}$
Density of liquid water*	$\left(1021.516-0.622\theta\right)\mathrm{kg/m^3}$
Gas mixture viscosity [43]	$\mu_g=\sum_{i=1}^{N}\frac{x_i\mu_i^g}{\sum_{k=1}^{N}\left[8\left(1+MW_i/MW_k\right)\right]^{-0.5}\cdot\left[1+\sqrt{\mu_i^g/\mu_k^g}\left(MW_k/MW_i\right)^{\frac{1}{4}}\right]^2}$
Water vapor viscosity*	$\left(0.8918+0.003344\theta\right)\cdot10^{-5}\,\mathrm{Pa\cdot s}$
Nitrogen viscosity*	$\left(1.6824+0.004294\theta\right)\cdot10^{-5}\,\mathrm{Pa\cdot s}$
Oxygen viscosity*	$\left(1.9267+0.005159\theta\right)\cdot10^{-5}\,\mathrm{Pa\cdot s}$
Gas density	$\rho_g=\sum_{i=1}^{N}C_i^gMW_i$ where $C_{\mathrm{N_2}}^{\mathrm{g}}=p_g/RT-C_{\mathrm{H_2O}}^{\mathrm{g}}-C_{\mathrm{O_2}}^{\mathrm{g}}$
Gas mixture thermal conductivity (Wilke 1950)	$k_g=\sum_{i=1}^{N}\frac{x_ik_i^g}{\sum_{k=1}^{N}\left[8\left(1+MW_i/MW_k\right)\right]^{-0.5}\cdot\left[1+\sqrt{\mu_i^g/\mu_k^g}\left(MW_k/MW_i\right)^{\frac{1}{4}}\right]^2}$
Thermal cond. of water vapor*	$\left(0.0152084+9.757\cdot10^{-5}\,\theta\right)\mathrm{W/m\cdot K}$
Thermal cond. of oxygen*	$\left(0.024508+8.021\cdot10^{-5}\,\theta\right)\mathrm{W/m\cdot K}$
Thermal cond. of nitrogen*	$\left(0.024255+6.313\cdot10^{-5}\,\theta\right)\mathrm{W/m\cdot K}$
Binary gas diffusion coefficient (Bird et al. 2002)	$D_{AB}=\frac{1}{p}a\left(\frac{T}{\sqrt{T_{cA}T_{cB}}}\right)^b\left(p_{cA}p_{cB}\right)^{1/3}\left(T_{cA}T_{cB}\right)^{5/12}\left(\frac{1}{M_A}+\frac{1}{M_B}\right)^{1/2}$
Surface tension*	$\left(7.7331-0.0183\theta\right)10^{-2}$ N/m
Water saturation pressure	$10^{2.826317+0.02953\theta-9.1837\cdot10^{-5}\theta^2+1.4454\cdot10^{-7}\theta^3}$ Pa

$\theta=\frac{\left(T-273.15\mathrm{K}\right)}{\mathrm{K}}$ where T is local temperature in K.

* Data is obtained by curve-fitting NIST Chemistry Webbook (http://webbook.nist.gov) data in relevant temperature range.

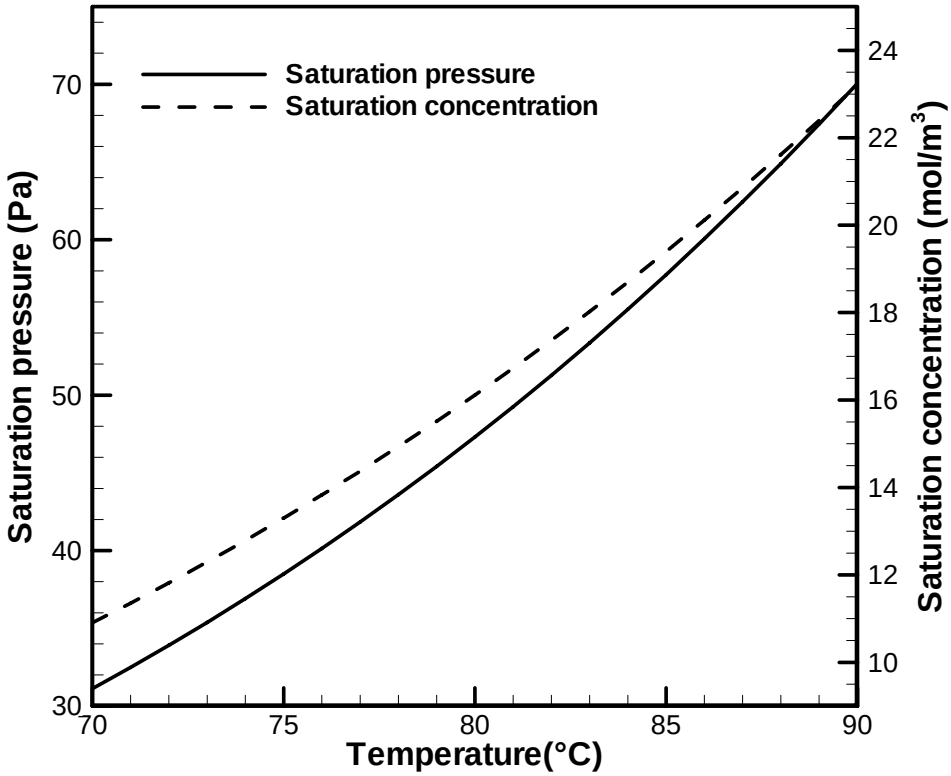

Figure 6.1. Dependence of the water saturation pressure on temperature in the operation temperature range of PEFCs

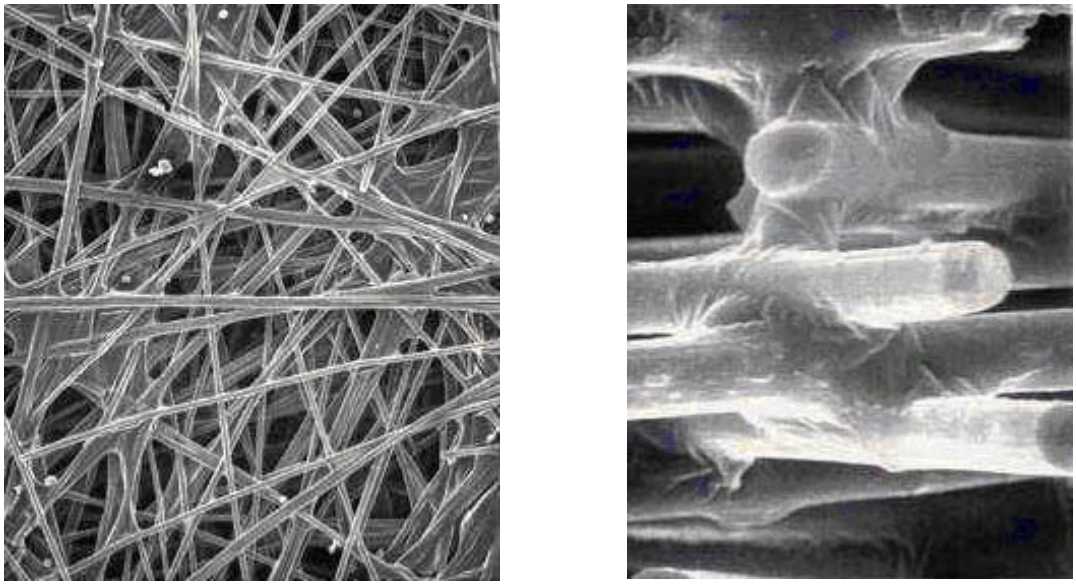

(a) (b)

Figure 6.2. Scanning Electron Microscopy (SEM) images of a Toray TGPH series carbon paper GDL. (a) Surface (b) Cross-section (Source: Toray Industries, Inc.).

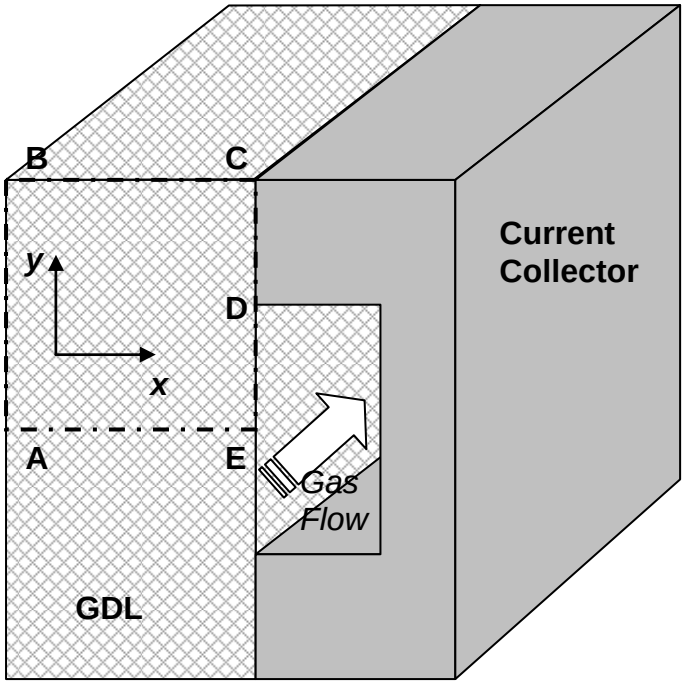

(a)

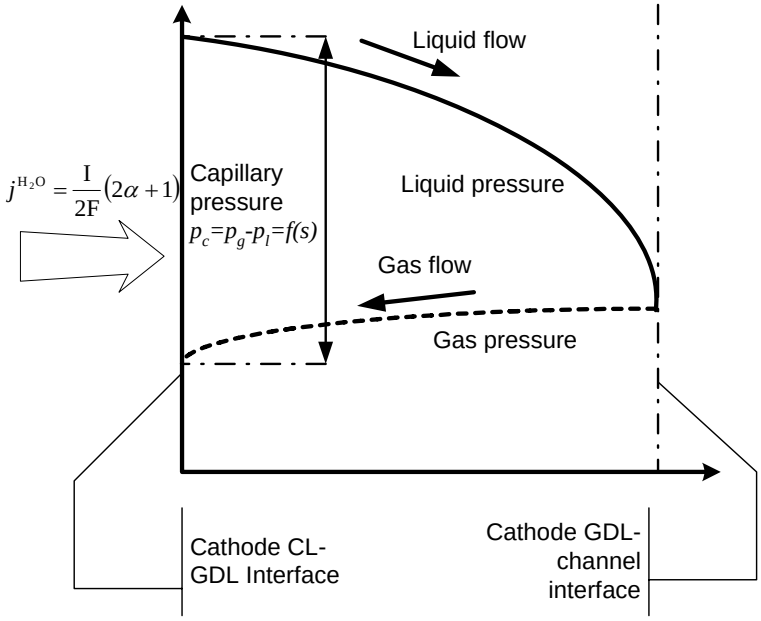

(b)

Figure 6.3. (a) Modeling domain, and (b) transport processes and phase pressures in GDL.

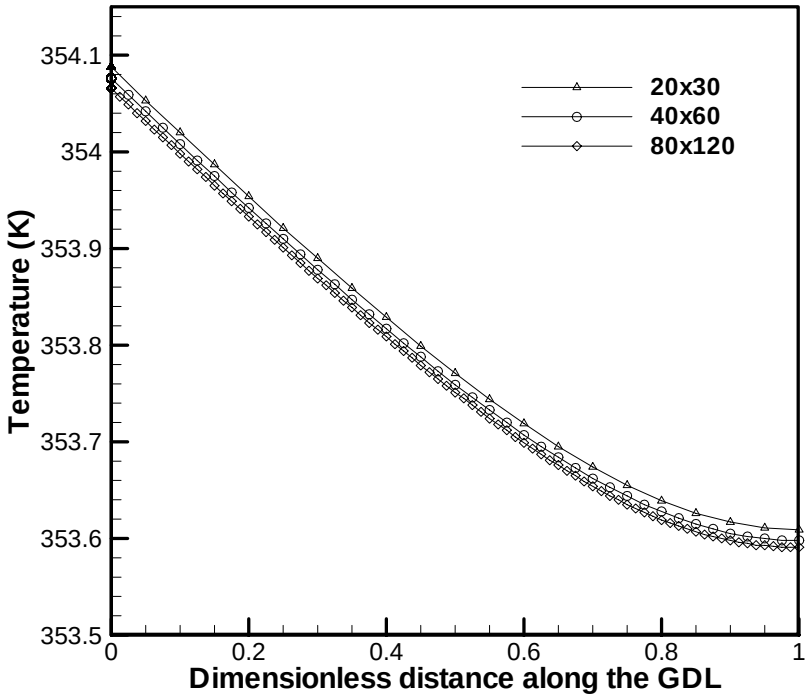

Figure 6.4. Grid independence of the simulations: Temperature profile across the GDL under the gas channel.

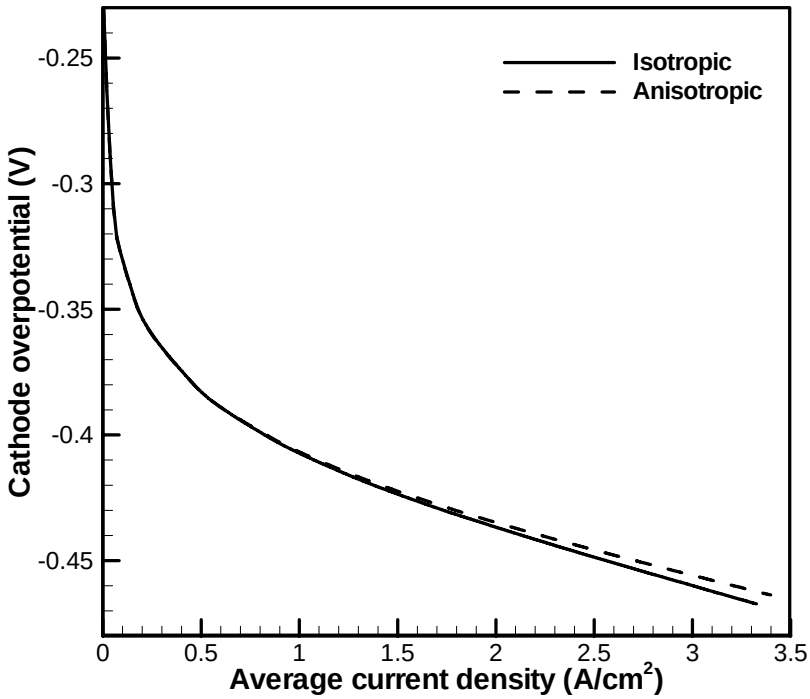

Figure 6.**5.** Cathode polarization curves for isotropic and anisotropic GDLs.

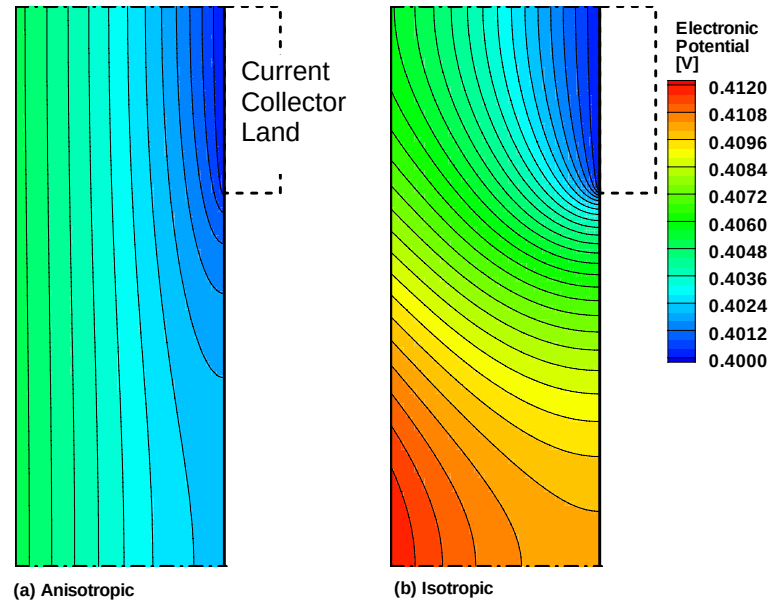

Figure 6.6. Electronic phase potential distribution in GDL at 0.4 V cell voltage (a) Anisotropic; (b) Isotropic.

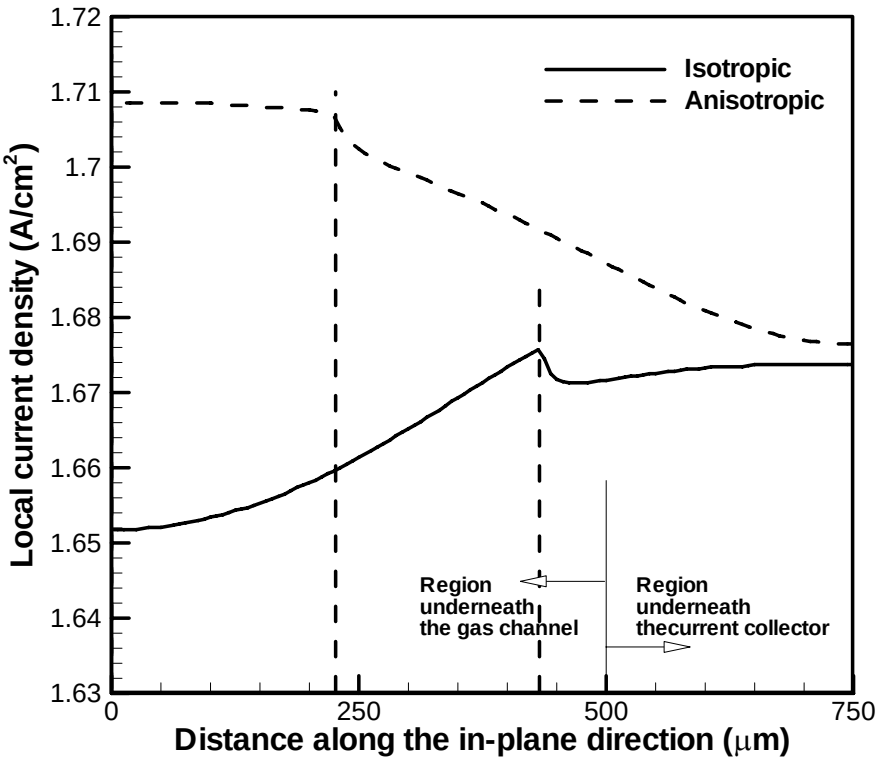

Figure 6.7. Current density distribution at 0.4 V.

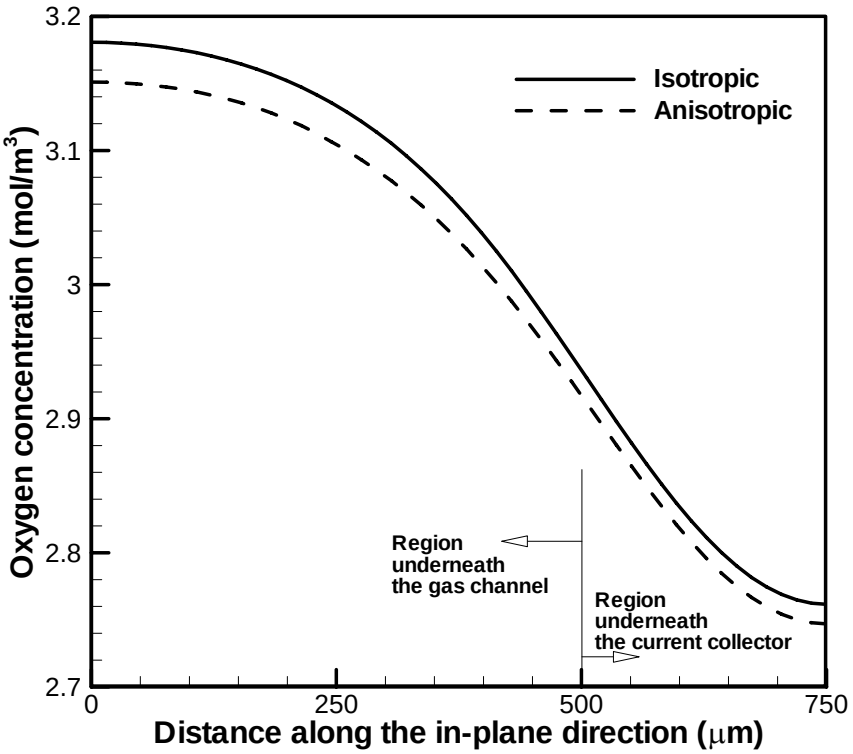

Figure 6.8. Oxygen concentration at the catalyst layer-GDL interface at 0.4 V

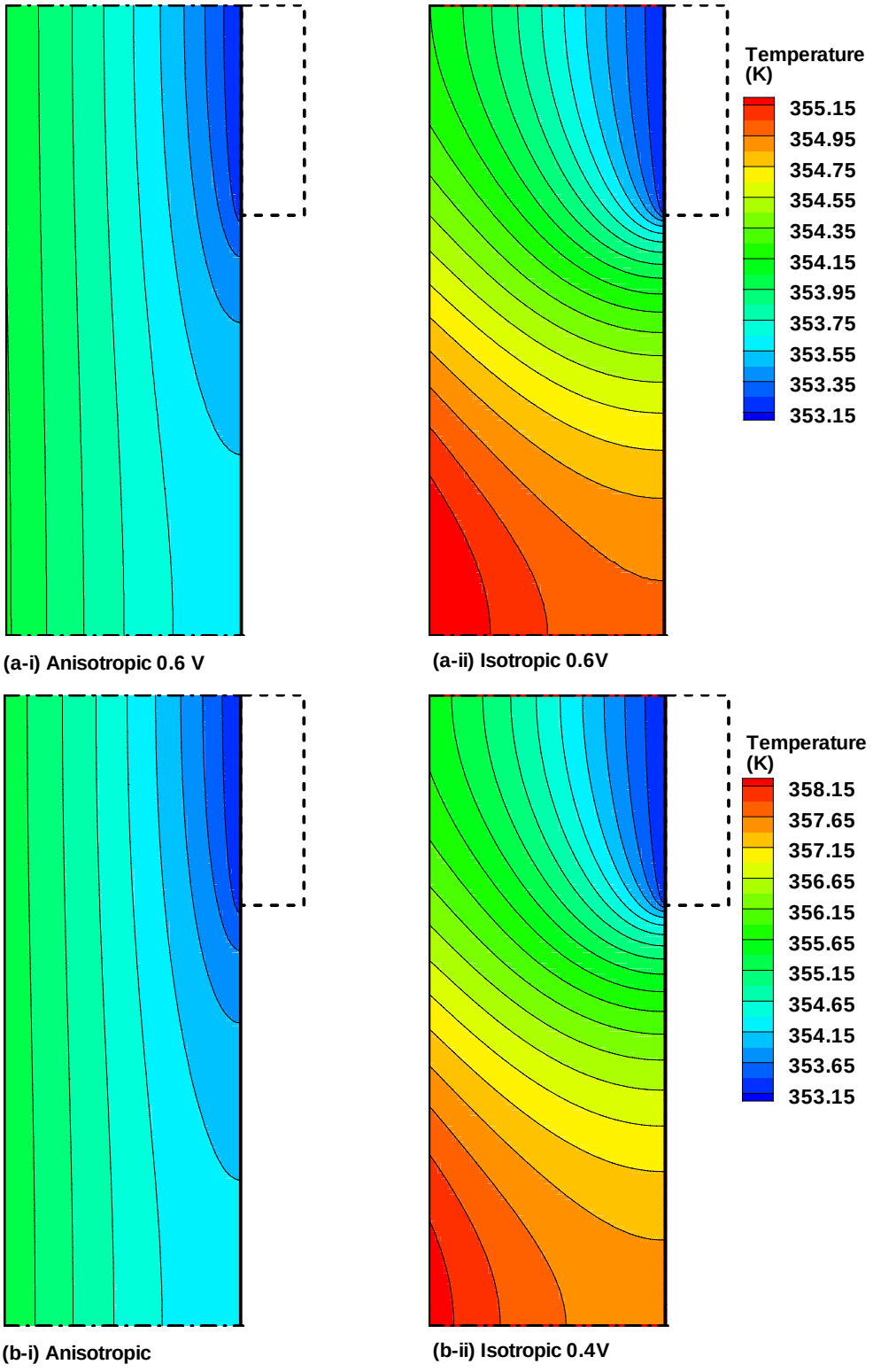

Figure 6.9. Temperature contours: (a) 0.6V (b) 0.4V; i – anisotropic, ii – isotropic .

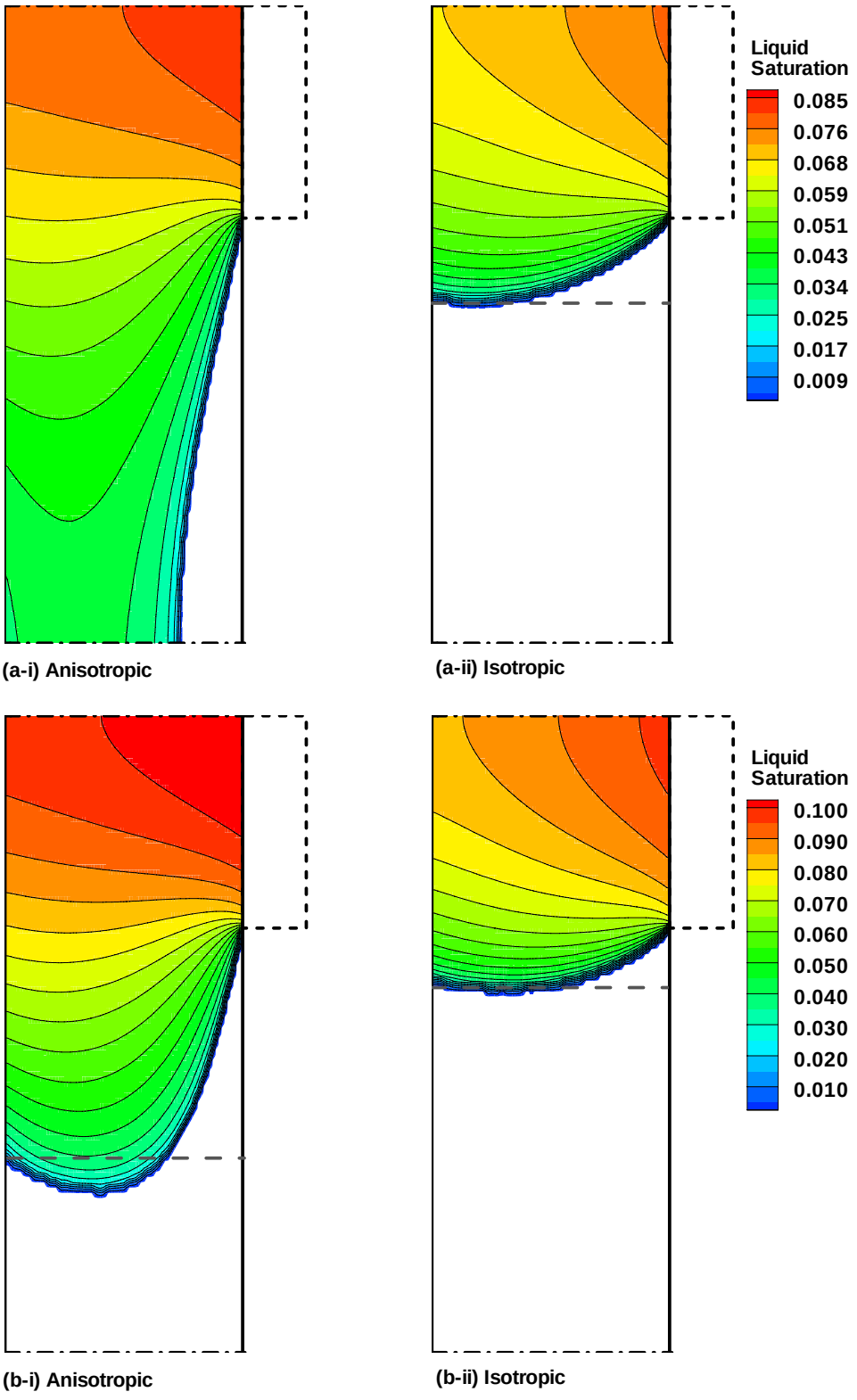

Figure 6.10. Liquid saturation contours: (a) 0.6V (b) 0.4V; i – anisotropic, ii – isotropic .

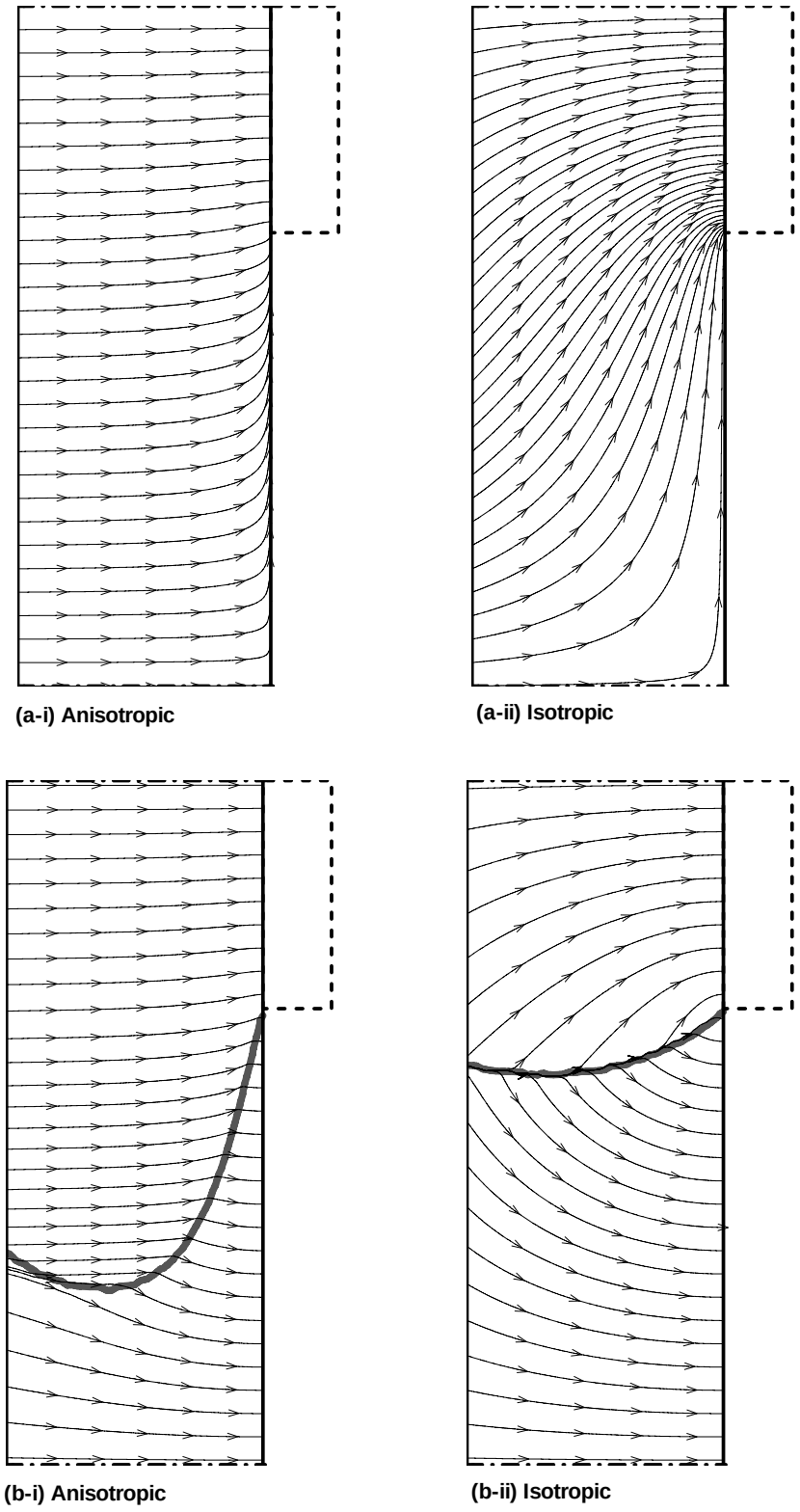

Figure 6.11. (a) Conductive heat flux pathlines (b) Vapor diffusion flux pathlines at 0.4V: thick gray lines represent the predicted condensation front.
(i) – anisotropic (ii) – isotropic .

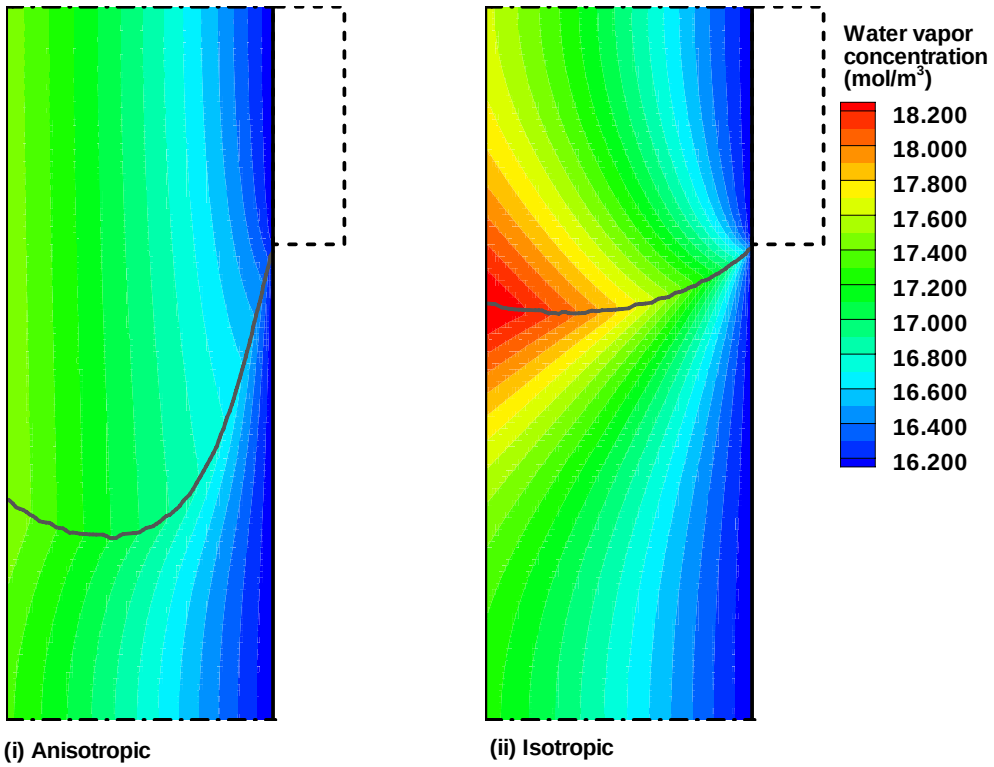

Figure 6.12. Water vapor concentration contours at 0.4 V:
(i) – anisotropic (ii) – isotropic.
Thick gray lines represent the predicted condensation front.

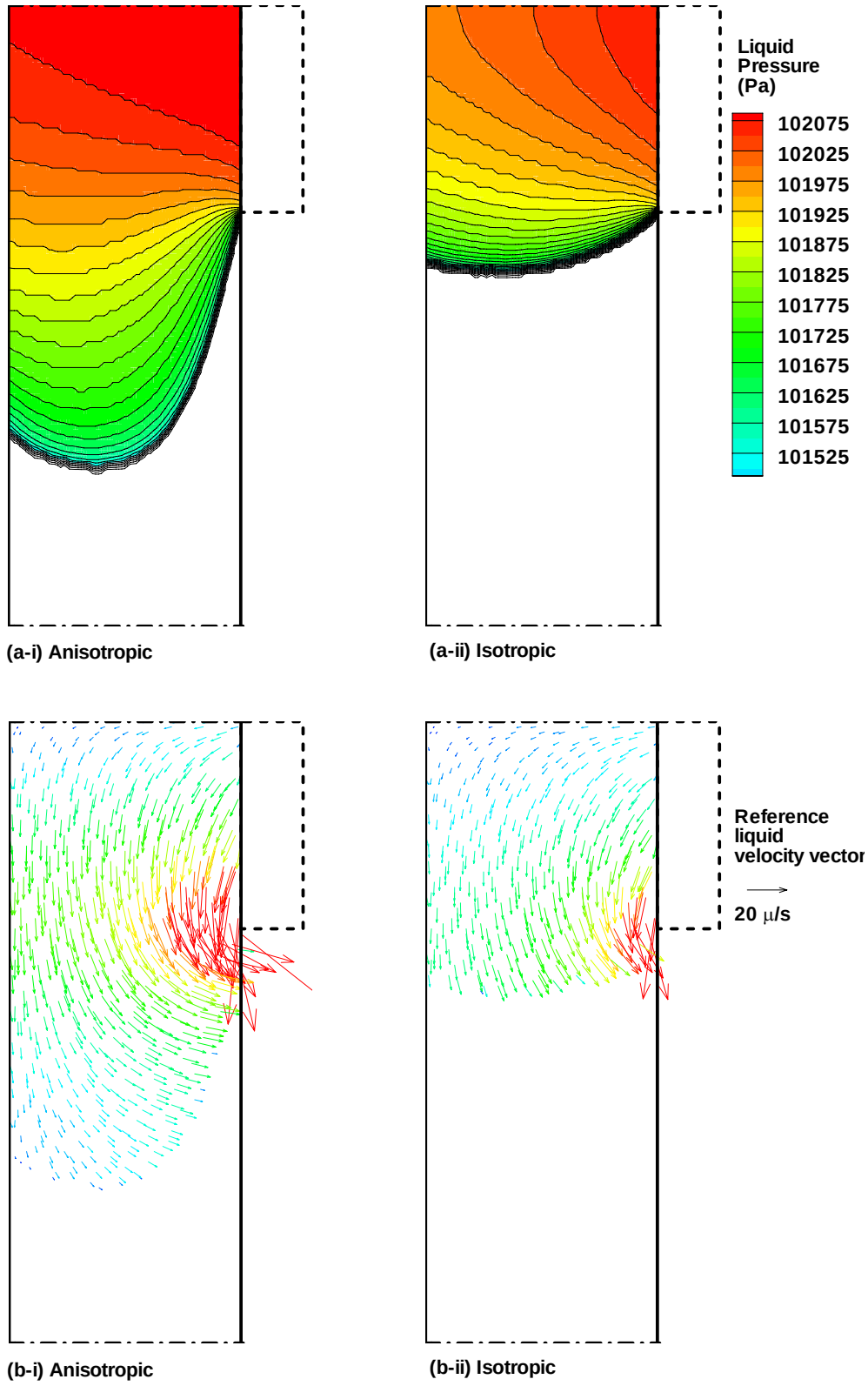

Figure 6.13. Liquid flow-field (a) Pressure (b) Velocity vectors at 0.4V:
(i) – anisotropic (ii) – isotropic.

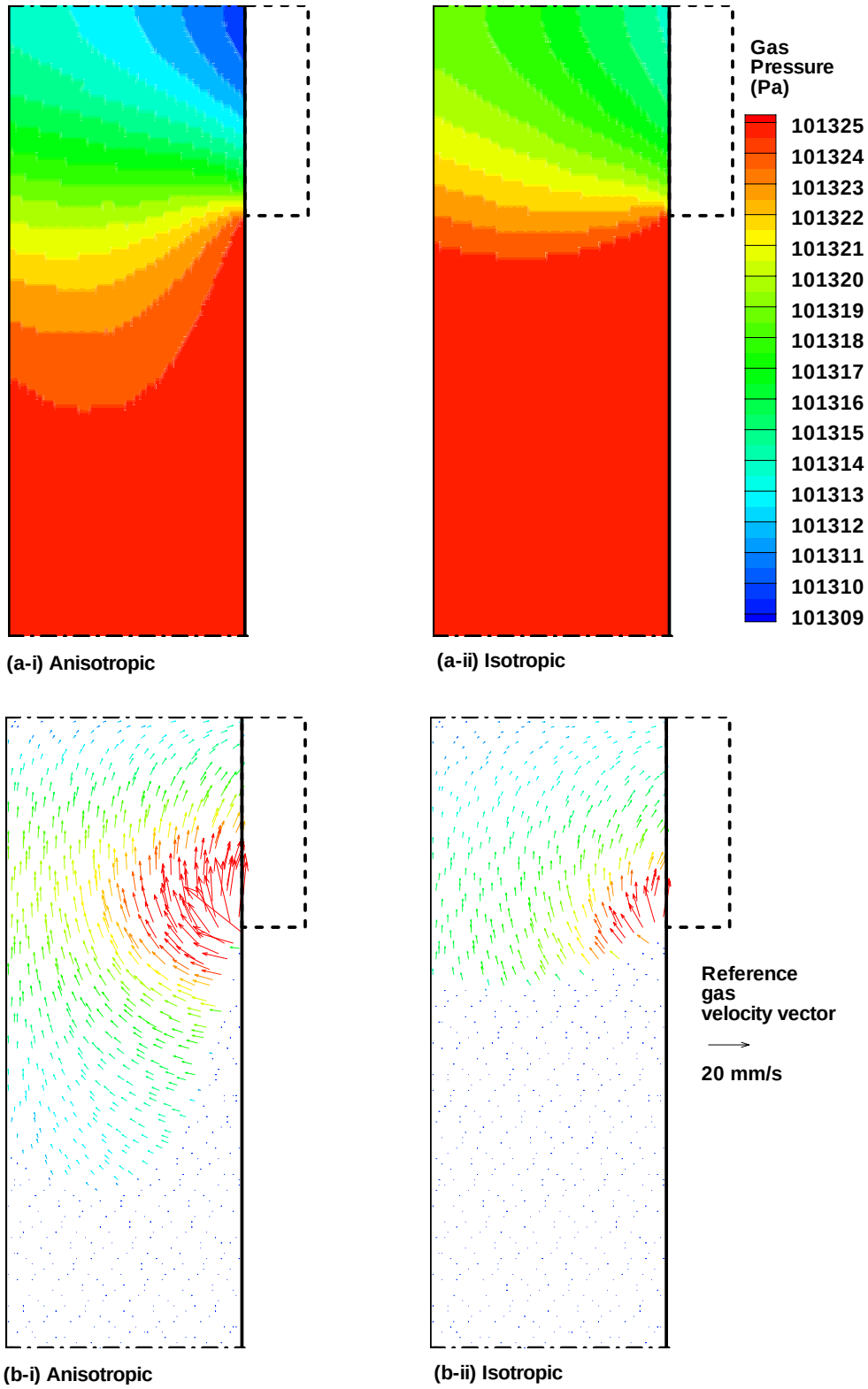

Figure 6.14. Gas flow-field (a) Pressure (b) Velocity vectors at 0.4V:
(i) – anisotropic (ii) – isotropic .

7. Modeling Liquid-Water Transport and Flooding in PEM Fuel Cell Flow Channels[⌗⌗]

7.1. Introduction

Channel flooding refers to a situation where a substantial fraction of liquid water accumulates in gas channels, thus causing two-phase flow and pressure drop fluctuations. Channel flooding is most severe at low current densities where gas velocity is low and insufficient to drain liquid water out of the fuel cell channels. Thus, channel flooding is a main cause of the mass transport loss and operational instability in the low current density and low flowrate operation. This operational regime is exceptionally important for PEMFCs due to its potential of high energy conversion efficiency. Another detrimental consequence of channel flooding is the mal-distribution of flow in parallel channels, leading to profound performance and durability implications, such as (1) loss of active areas; (2) fuel starvation and hence oxygen reduction reaction on the anode side thus leading to carbon corrosion on the cathode side; and (3) O_2 starvation and hence H_2 evolution on the cathode side and furthermore H_2/O_2 combustion thus leading to hot spot formation. Directly, less flow means less reactant and hence reaction rate is non-uniform in the catalyst layer. The indirect problem is that less flow would mean less momentum and hence more susceptible to blockage due to water vapor condensation. This leads to a serious loss of efficiency of the fuel cell as the whole channel is lost due to blockage. The reason is the cycle of liquid clogging and subsequent flush out in the flooded channel. Hence for a stable fuel cell, flooding of the channels must be avoided.

Maharudrayya et al. (2005) proposed an analytical solution for pressure drop in single-phase flow in the channels of PEM fuel cell. Two-phase flow characteristics in the PEM fuel cell channels were investigated experimentally by Lee et al. (2005). They proposed a friction factor closely resembling the friction factor for laminar flow in a circular channel. But their investigation considered a single point injection of the liquid, which is not the case for a fuel cell channel. The channel flooding or flow instability was not investigated. The results were validated based on gas phase Reynolds number even in the case of multiphase flow.

Barreras et al. (2005) investigated the mal-distribution of flow in parallel microchannels of fuel cells experimentally and numerically. The inlet flow enters the channels preferentially. This non-homogeneity is attributed partly to the formation of the recirculation bubbles at the inlet. Making the angle of the inlet header more than right angle to the parallel channels alleviates mal-distribution.

To date, no model existed in the literature can treat channel flooding. While mist flow model and film flow model has been developed for the extreme cases of high gas velocity (liquid volume fraction < 0.1%) and low gas velocity/highly hydrophilic channel wall (liquid volume fraction < 10%), respectively, a general model covering a wide range of liquid fraction and capable of capturing flow mal-distribution

[⌗⌗] This chapter was based on a manuscript being prepared for publication: S. Basu, Y. Wang, C.-Y. Wang, and K. S. Chen, “Prediction of two-phase flow maldistribution in PEM fuel cell channels”, in preparation for publication.

has been absent. The most urgent need in PEMFC modeling has been to develop a two-phase flow and flooding model for fuel cell channels, allowing the liquid water saturation to be predicted at levels as high as 20-30%. The liquid saturation of 20-30% from a channel-only model is sufficient to characterize the channel flooding once it is integrated with other component models of a fuel cell. For the similar reason, channel clogging as represented by the liquid saturation close to 100% will arise in a fuel cell environment where there are multiple channels and electrochemical reaction rate in each channel area is coupled with the flooding situation inside the gas channel. Thus, such a model will enable channel flooding, two-phase flow maldistribution in multiple, parallel channels, and the flowfield effect on liquid water removal to be captured. In the future, when this channel model is integrated with other component models such as MEA and GDL, it then becomes possible to predict channel clogging which arises from the strong interactions between GDL and channel flow behaviors.

We propose a novel approach to treat fuel cell channels as a *structured porous medium* with straight capillary pores. The pore size is proportional to the channel dimension and is sufficiently small that the Reynolds number is small to warrant the laminar flow regime. The porous medium permeability can then be determined by hydraulic conductance of laminar flow through a flow channel of various cross sections. The geometrical analogy between capillary channels and porous media was long recognized in scientific research. Indeed, this is the way the single-phase flow through porous media is "understood" – by using a model such as flow through a capillary bundle to establish the pressure drop-flow rate relationship for porous medium flow. For complex channel geometries, such as serpentine flowfields, the single-phase permeability can still be computed with reasonable accuracy by CFD codes as long as the flow is laminar.

The two-phase nature makes it difficult to theoretically prove the exact analogy between a capillary channel and a porous medium. However, this approach was successfully applied to develop a two-phase flow model in micro heat pipes by Wang et al. (1994); was reviewed extensively by Olbricht (1996); and was most recently applied to simulate micro-channel heat exchangers in electronics cooling (Imke, 2004). In this approach, all two-phase flow features such as the liquid-gas interface and two-phase flow patterns are lumped into capillary pressure and relative permeability. Thus, one must "calibrate" these two-phase flow properties before one can apply M^2 model to the channel region and simulate the liquid saturation distribution along the channel.

Note that the only difference between a random porous medium such as GDL and a regularly structured porous medium such as gas channels lies in the pore morphology. The pore structure is random in the former case whereas it is regular in the latter case. However, the porous medium flow theory is applicable to both types of porous media. Indeed, a future GDL may well be a structured porous layer featuring micro-fabricated regular patterns. In this case, the same porous medium theory will continue to work in the global sense (i.e. the overall pressure drop versus the flowrate). Thus, in the global sense, the governing equations for porous medium flow remain the same, whether the pore morphology is random

or structured. In fact, in all porous medium flow equations, the pore morphology information does not directly enter the governing equations, but indirectly through the porosity and permeability. In the M^2 model for two-phase flow, similarly the pore morphology affects neither the governing equations nor the two-phase flow properties such as the capillary pressure and relative permeability. They are only functions of the liquid saturation in a representative elementary volume of a porous medium.

7.2. Numerical Model

This section describes the M^2 governing equations and supplemental relationships for a two-phase flow in PEMFC channels. The M^2 model consists of the mixture continuity, momentum and species transport equations. One major species equation solves for the total water amount. The liquid saturation (i.e. liquid volume fraction) is defined in Equation 7.4. The coefficients are calculated according to M^2 model (Olbricht 1996, Imke 2004), as shown in Equations 7.5 – 7.9.

Continuity equation: $$\varepsilon \frac{\partial \rho}{\partial t} + \nabla \cdot (\rho \vec{u}) = 0 \tag{7.1}$$

Momentum conservation: $$\rho \vec{u} = -\frac{K}{\nu}(\nabla P - \gamma_\rho \rho \vec{g}) \tag{7.2}$$

Species conservation:

$$\varepsilon \frac{\partial}{\partial t}(C^k) + \nabla \cdot (\gamma_c \vec{u} C^k) = \nabla \cdot (D_g^{k,eff} \nabla C_g^k) - \nabla \cdot [(\frac{mf_l^k}{M^k} - \frac{C_g^k}{\rho_g}) \vec{j}_l] \tag{7.3}$$

$$s = \frac{C^{H2O} - C_{sat}}{\rho_l / M^{H2O} - C_{sat}} \tag{7.4}$$

$$\lambda_l = \frac{k_{rl} / \nu_l}{k_{rl} / \nu_l + k_{rg} / \nu_g} \quad \text{and} \quad \lambda_g = 1 - \lambda_l \tag{7.5}$$

$$\gamma_c = \begin{cases} \frac{\rho}{C^{H2O}} (\frac{\lambda_l}{M^{H2O}} + \frac{\lambda_g}{\rho_g} C_{sat}) & \text{for water} \\ \frac{\rho \lambda_g}{\rho_g (1-s)} & \text{for other species} \end{cases} \tag{7.6}$$

$$\vec{j}_l = \frac{\lambda_l \lambda_g}{\nu} K[\nabla P_c + (\rho_l - \rho_g)\vec{g}]$$

(7.7)

where $P_c = \sigma \cos(\theta_c)\left(\frac{\varepsilon}{K}\right)^{1/2} J(s)$

$$J(s) = \begin{cases} 1.417(1-s) - 2.120(1-s)^2 + 1.263(1-s)^3 & \text{for } \theta_c > 90^o \\ 1.417s - 2.120s^2 + 1.263s^3 & \text{for } \theta_c < 90^o \end{cases} \quad (7.8)$$

$$\gamma_\rho = \frac{\rho_l \lambda_l + \rho_g \lambda_g}{s\rho_l + (1-s)\rho_g} \quad (7.9)$$

$$k_{rl} = \left(\frac{s - s_{ir}}{1 - s_{ir}}\right)^n ; \quad k_{rg} = (1-s)^n \quad (7.10)$$

$$s_{ir} = \frac{1}{22} Bo - 0.264 \quad \text{(Brown 1950)} \quad (7.11)$$

$$s_{ir} = \frac{1}{(20 + 0.9Bo)} \quad \text{(Saez and Carbonell 1985)} \quad (7.12)$$

$$Bo = \frac{\rho_l g d_h^2}{\sigma \cos\theta} \quad \text{for channel wall contact angle < 90°} \quad (7.13)$$

$$K = c\frac{d_h^2}{32} \quad (7.14)$$

$$d_h = 4\frac{\text{cross - section area}}{\text{channel perimeter}} \quad (7.15)$$

Note that two parameters have been introduced in the relative permeability correlation. One is the irreducible liquid saturation, s_{ir}, below which the liquid water is immobile or disconnected. In a microchannel, a certain amount of water once accumulated could never be flushed out due to wall adhesion at the angles. This is called irreducible liquid saturation (S_{ir}). The relative conductivity of liquid is defined with respect to this as in Equation 7.10. The irreducible liquid saturation can be calculated from the empirical relations by Brown (1950), Saez and Carbonell (1985); see Equations 7.11 and 7.12, respectively. The irreducible liquid saturation depends on the Bond number (Bo), which is the ratio of body-force due to gravity in a channel to the surface tension force (Equation 7.13). The conductivity of

the channel is calculated according to Equation 7.14 while the hydraulic diameter is defined in Equation 7.15.

The second key parameter is the exponent 'n' in Equation 7.10, which can be determined by numerical experiments as suggested by Dullien (1992). So is the flow conductivity '*K*' of Equation 7.14. The reason for this is that the value of shape factor 'c' is analytically available only for a few cross-sectional geometries of single channels.

The model equations are solved numerically using the commercial flow solver, Fluent. Figure 7.1 shows two computational domains for a five-channel and a seven-channel flowfield, respectively. A straight manifold feeding five parallel channels are considered. Channels are 1 *mm* wide and 20 *mm* in length. The pitch of the channels or the width of the land separating two channels is 2 *mm*. With GDL intrusion, the c/s area of the two end channels are taken as 20% less than the other channels (a representative condition). The manifold is 5mm in width. The Reynolds number of the flow, based on inlet width, is 250, which is a representative number about the middle of the Reynolds number range in the practical applications. The pressure drop in the channels is used to determine the flow conductivity for the system.

Computations are carried out for various current densities and flow stoichiometric ratios under the isothermal condition. The water addition is assumed to be equal and uniform along all the channels, with and without GDL intrusion. Due to channel flooding and water condensation, oxygen transport through the GDL may be hindered and therefore less reaction takes place. This eventually decreases the amount of water added to the channels. For this reason the liquid saturation does not lead to cell death promptly. At present the transient behavior of the liquid water transport in the channels is not studied.

7.3. Results and Discussion

7.3.1. Determination the value of exponent 'n'

Extensive parametric study has been performed on a single channel to match the two phase pressure drop coefficient obtained experimentally in order to determine a proper value of exponent '*n*'. The two phase pressure drop coefficient is defined as the ratio of the two phase pressure drop to the pressure drop for a single phase flow.

$$\Phi = \frac{\Delta P_{2\Phi}}{\Delta P_{1\Phi}} \quad \text{where} \quad \Delta P = P_{inlet} - P_{outlet} \tag{7.16}$$

Two representative cases are shown here (Fig. 7.2a and 7.2b): I_{avg} = 0.8 A/cm^2, Stoichiometry = 2.0 and 4.0. The value of exponent n = 5.0 results in the pressure drops closest to the experimental measurements. Therefore n = 5.0 is used in the present study.

In Figure 7.3 the liquid saturation profiles are shown for the case with I_{avg} = 0.8A/cm^2 and stoichiometry = 2.0, with n = 4.0, 4.5, 5.0. The model predicts an increased level of saturation as the exponent is increased, although the trend of the profile remains the same. At dew point of 80^{o}C the liquid water saturation starts to grow immediately from the inlet. At lower dew point (70^{o}C), a dry-to-wet transition could be captured; see Figure 7.4. The saturation level increases with the exponent in liquid relative permeability.

7.3.2. Single phase flow

The velocity contour shows the flow mal-distribution clearly in the case of 20% area mal-distribution as presented in Figure 7.5. The standard deviation (SD) of the normalized flow through the channels is 0.315. The performance of this design for the perfectly formed channels is investigated as well. The velocity contour for perfect parallel channels shows almost uniform flow in the channels (Figure 7.6) with the SD of normalized flow 0.129. The velocity contours indicate that the area maldistribution can have a severe effect on the flow distribution.

7.3.3. Two phase flow – five channel results

Low current density is the prime operating range for PEMFCs and its efficiency is maximal under such conditions. Channel flooding is predominant in these conditions. Therefore the two-phase flow in the channels is numerically studied for current density of 0.2 A/cm^2 and stoichiometry of 4.0 and 2.0. As expected, the liquid saturation decreases with stoichiometry. At the low current density and low stoichiometry, the maximum liquid saturation reaches 27% (Figure 7.7). The pressure contour shows a few interesting features. Near the liquid front the pressure decreases sharply (Figure 7.8). Most probably, this occurs due to the condensation process. The two-phase pressure drop coefficient for this case is calculated to be 3.6 while the experimental result is 4.0.

At high stoichiometry (i.e. St = 4.0) the liquid saturation is lower. Although the maximum liquid saturation is not significantly lower, it is found that liquid water could be flushed out of a few channels (Figure 7.10). This trend matches qualitatively with the experimental observations. The pressure contour (Figure 7.11) displays a similar feature to the case of stoichiometry 2.0. A sharp pressure drop could be found near all the condensation fronts. The two-phase pressure drop coefficient is 2.5 while the experimental result is 2.6. In the earlier computations with a single channel the pressure drop coefficient at low stoichiometry was lower. But in the present computations the results are much closer. We conjecture that the presence of the exit manifold is responsible for this.

The maldistribution of flow in the channels is clear from the velocity contour as displayed in Figure 7.12. In Figure 7.13 the relative stoichiometry plots clearly show that at the end channels stoichiometry is much lower due increased resistance resulting from GDL intrusion. At higher stoichiometry this maldistribution effect is more prominent. The predicted liquid saturation contours clearly indicate that the channels are

flooded and the present model is capable of capturing channel flooding. At such high liquid saturation oxygen transport will be seriously hindered, resulting in a substantial mass transport loss and ultimately to cell shutdown.

7.3.4. Two phase flow – seven channel results

The cathode channel flooding experiments are conducted using a test cell consisting of seven parallel channels. Computations are carried out for a seven channel case without the GDL intrusion. As is expected, at low current density and low stoichiometry the channels are almost totally flooded (Figure 7.14). Interestingly in this case, the pressure surge observed at the phase boundaries are much smaller (Figure 7.15). The velocity contours (Figure 7.16) shows a maldistribution in the channels. The flow is highest at the far channel. The maldistribution increases as the number of channel increases. At high stoichiometry and high current density many channels are completely dry (Figure 7.17). The liquid front is pushed much downstream in all the channels.

The pressure contour (Figure 7.18) does show a very small pressure surge at the phase boundaries. As the velocity is higher, the gradient of liquid water near the liquid front is expected to be smaller. With a smaller saturation gradient the pressure gradient is expected to be smaller too. The velocity contour (Figure 7.19) shows less maldistribution in the present case than low stoichiometry and low current density case. The two phase pressure drop coefficients (defined in Equation 7.16) for this case is compared with the experimental results.

The maldistribution of flow increases significantly in the case of seven channels (Figure 7.20), when compared with the case of five channels (Figure 7.13). But interestingly, the maldistribution decreases significantly between low current density low stoichiometry case to high current density high stoichiometry case.

Computations were carried out for a single channel to calibrate the model constants. The results for the single channel and final multi-channel cases are plotted with respect to the experimental results (Figure 7.21). As shown in Figure 7.21a, at high current density and high stoichiometry the model seems to over predict the pressure drop. At medium stoichiometry the model predicts the pressure drop well. But it seems the effect of stoichiometry on the model is less than what is observed in the experiments.

From Figure 7.21, it can be seen that at low stoichiometry the single channel case shows a large deviation from the experimental result. For the multi-channel case, due to the presence of the manifold, the two phase pressure drop coefficient shows better agreement with the experimental result. From the comparison of experimental and numerical pressure drop coefficients it is clear that the present model can predict the two phase pressure drop, although some finer adjustments might be added to improve its sensitivity to the stoichiometry variation and performance at low current density operating conditions.

7.4. Conclusions

It is important to have a two-phase model that can estimate the liquid saturation and pressure drop across the cathode channels. The two-phase flow field in the channels is computed by a M^2 model for the first time. The two-phase pressure drop coefficient predicted by the M^2 model is found to be in good agreement with experimental measurements. Flow maldistribution between parallel channels is clearly captured by the present model, and effects of GDL intrusion at the edge channels are assessed. The predicted liquid saturation contours show qualitative agreement with experimental observations via optical visualization.

In future work, this steady-state model can be further extended to unsteady analysis. In addition, this channel two-phase model could be integrated into a full PEMFC model. Two-phase flow behavior and their mutual interactions in different kind of channel geometries could be studied and analyzed theoretically using the results of this code.

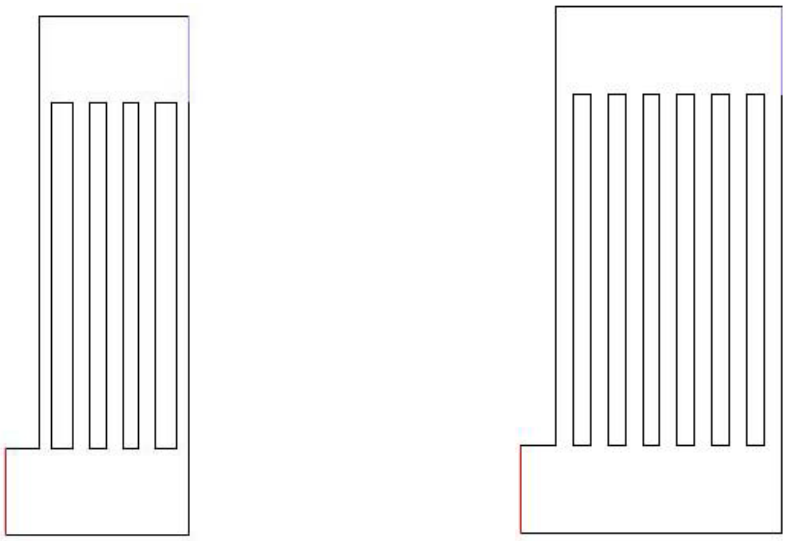

Figure 7.1: Computational domains for five and seven channel geometries.

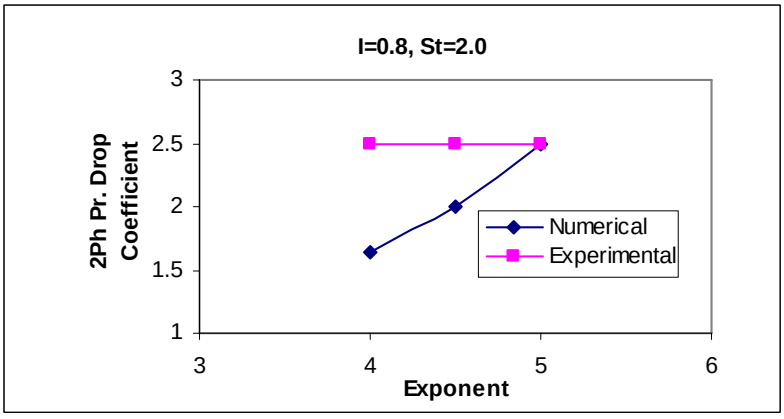

(a)

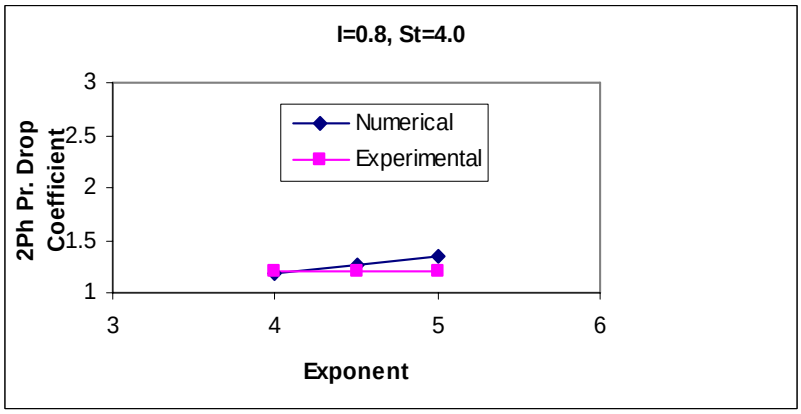

(b)

Figure 7.2. Two-phase pressure drop coefficient as a function of exponent
(a) I = 0.8, St = 2.0; (b) I = 0.8, St = 4.0.

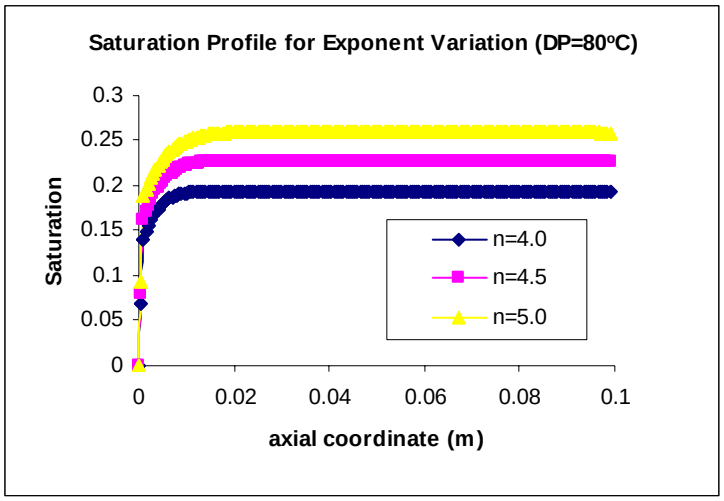

Figure 7.3. Axial profiles of the cross-section averaged liquid saturation at dew point 80°C.

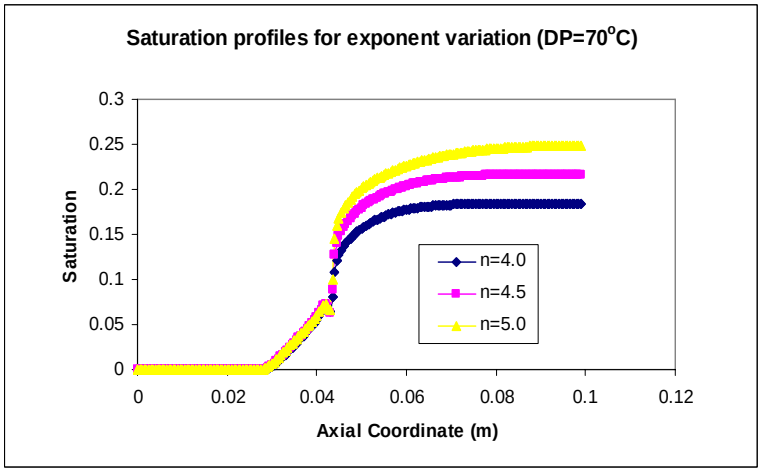

Figure 7.4. Axial profiles of the cross-section averaged liquid saturation at dew point 70°C.

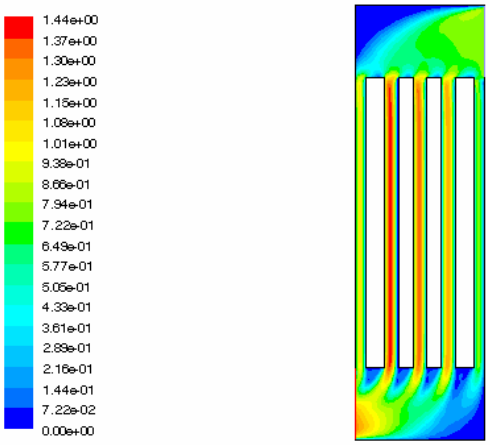

Figure 7.5. Velocity (m/s) contours for channels with area mal-distribution due to GDL intrusion in the two edge channels

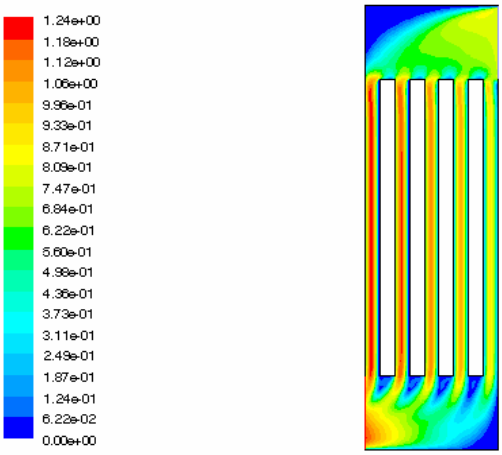

Figure 7.6. Velocity (m/s) contours for perfect parallel channels with uniform cross-sectional area.

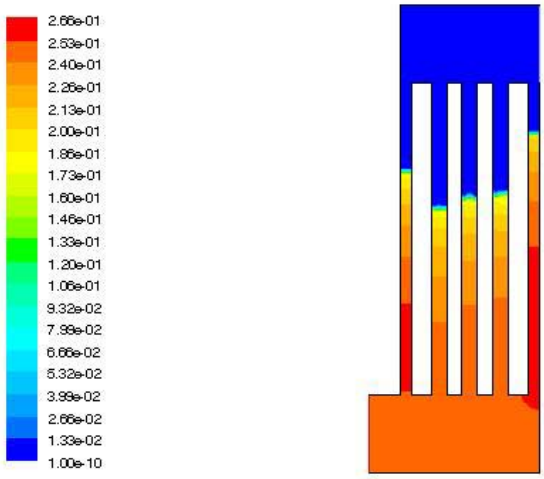

Figure 7.7. Saturation contours in 5-channel flowfield (20% intrusion, I=0.2A/cm^2, St=2.0)

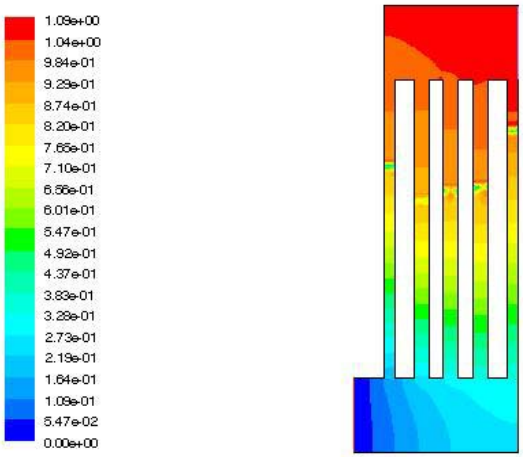

Figure 7.8. Pressure (Pa) contours in 5-channel flowfield (20% intrusion, I=0.2A/cm^2, St=2.0)

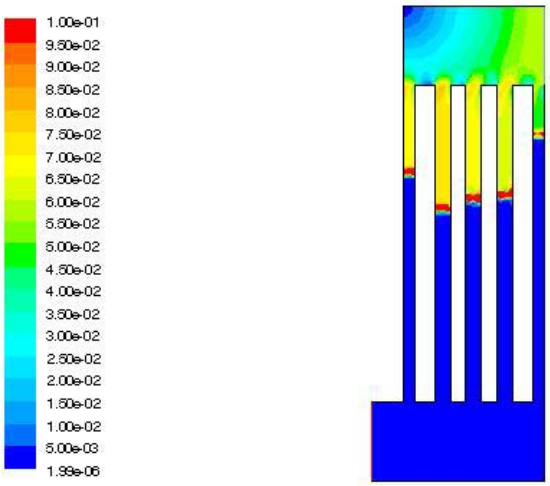

Figure 7.9. Velocity (m/s) contours in 5-channel flowfield (20% intrusion, I=0.2A/cm^2, St=2.0)

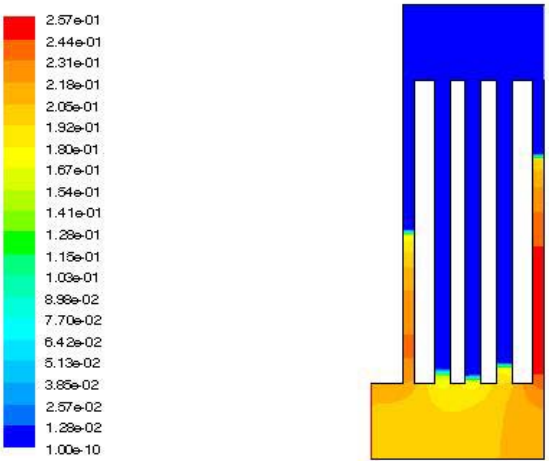

Figure 7.10. Saturation contours in 5-channel flowfield (20% intrusion, I=0.2A/cm^2, St=4.0)

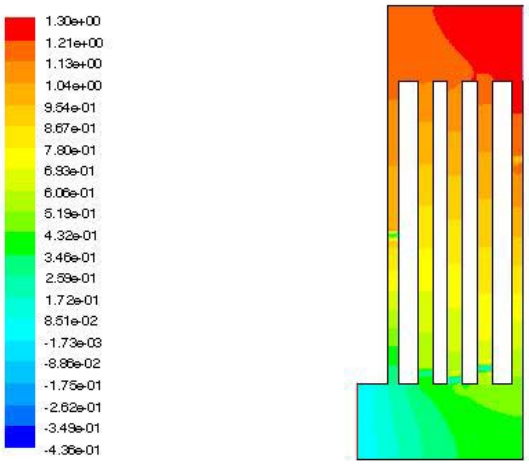

Figure 7.11. Pressure (Pa) contours in 5-channel flowfield (20% intrusion, I=0.2A/cm^2, St=4.0).

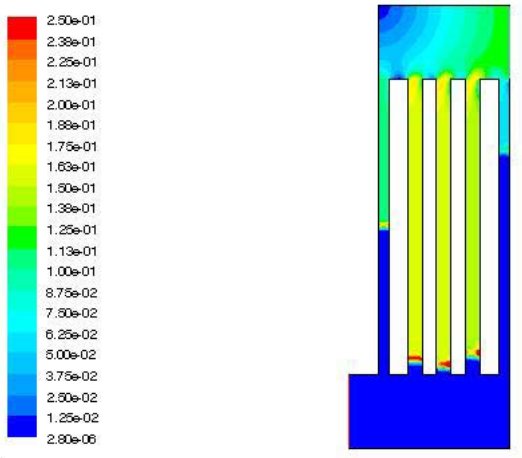

Figure 7.12. Velocity (m/s) contours in 5-channel flowfield (20% intrusion, I=0.2A/cm^2, St=4.0).

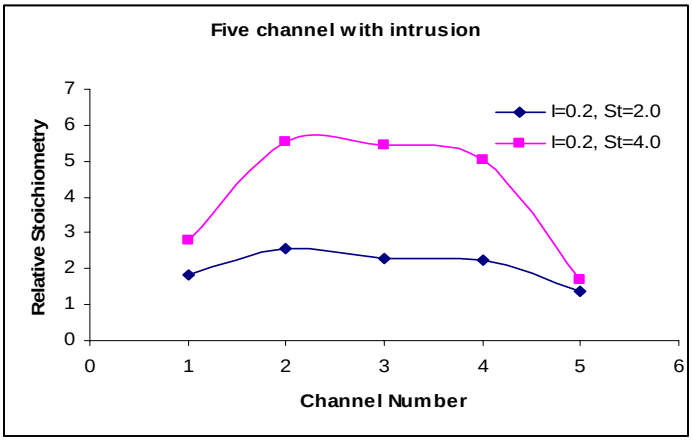

Figure 7.13. Maldistribution of flow in the channels.

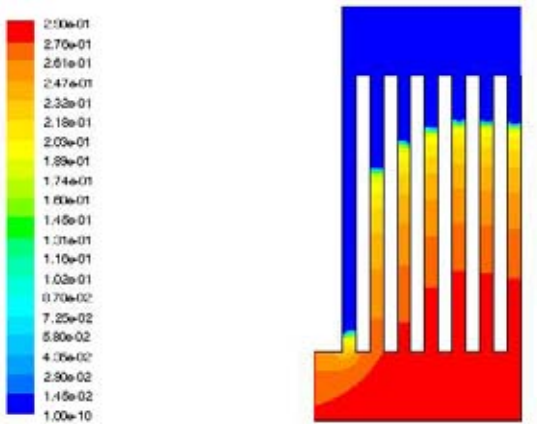

Figure 7.14. Saturation contours in 7-channel flow field (no intrusion, I=0.2A/cm^2, St=2.0).

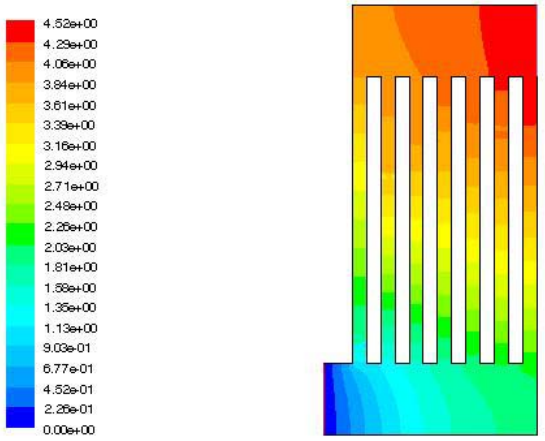

Figure 7.15. Pressure (Pa) contours in 7-channel flow field (no intrusion, I=0.2A/cm^2, St=2.0).

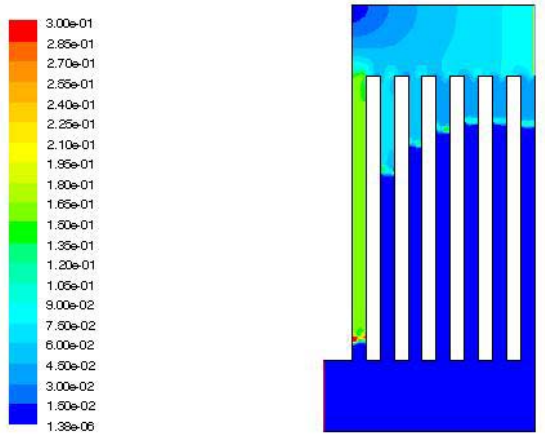

Figure 7.16. Velocity (m/s) contours in 7-channel flow field (no intrusion, I=0.2A/cm^2, St=2.0).

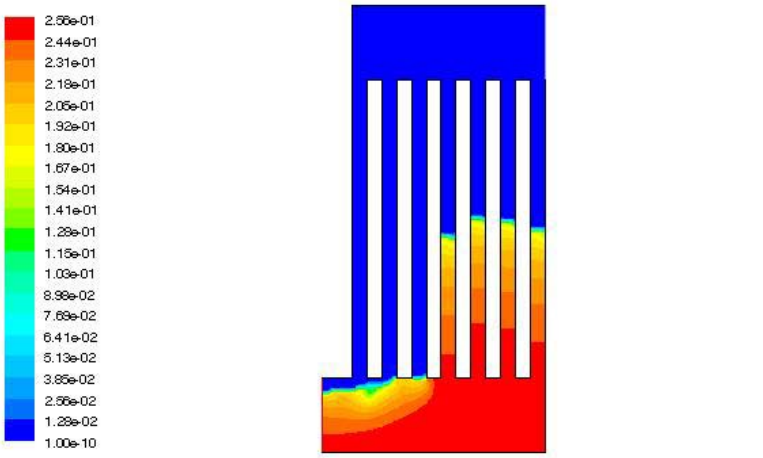

Figure 7.17. Saturation contours in 7-channel flow field (no intrusion, I=0.8A/cm^2, St=4.0).

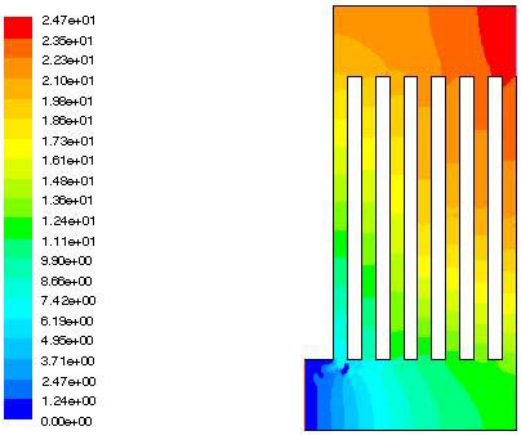

Figure 7.18. Pressure (Pa) contours in 7-channel flow field (no intrusion, I=0.8A/cm^2, St=4.0).

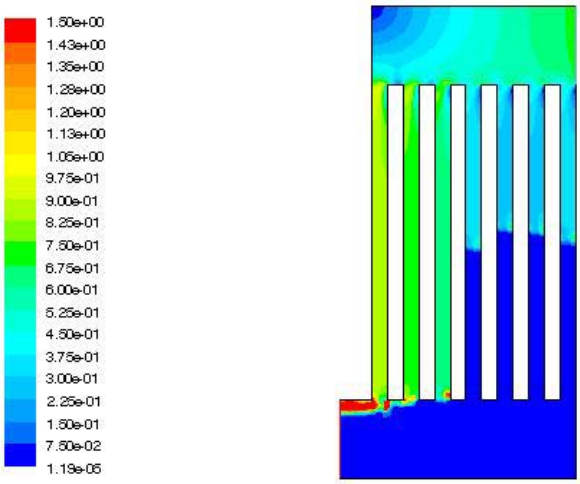

Figure 7.19. Velocity (m/s) contours in 7-channel flow field (no intrusion, I=0.8A/cm^2, St=4.0).

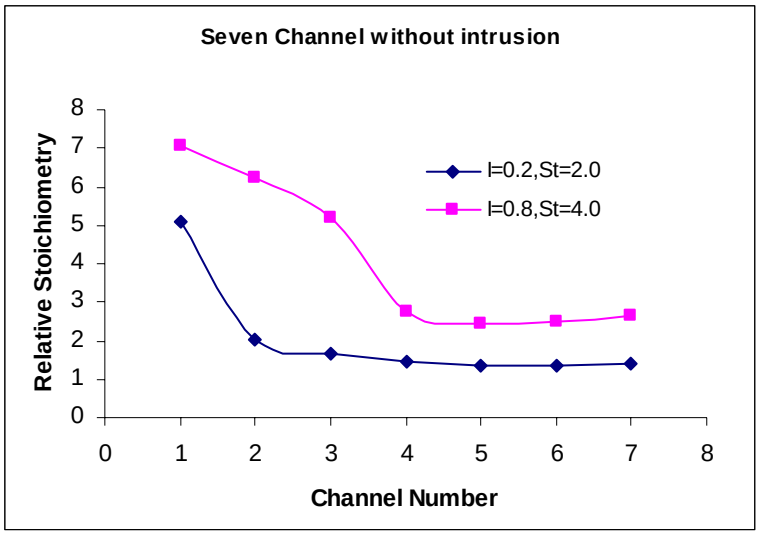

Figure 7.20. Maldistribution of flow in the channels.

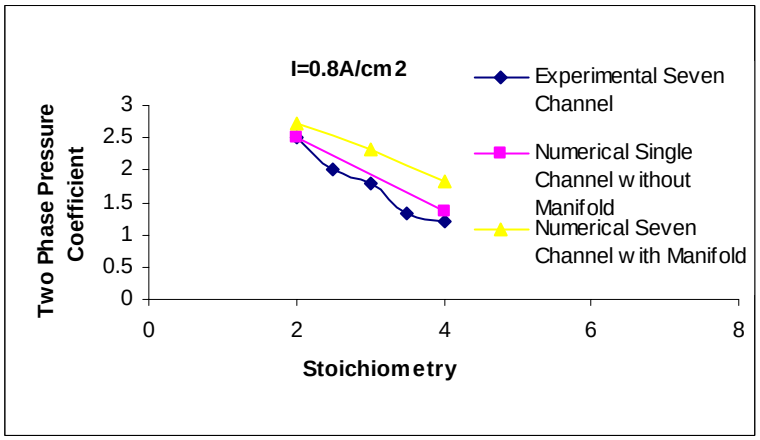

Figure 7.21a. Comparison of two phase pressure drop coefficient for I = 0.8A/cm^2.

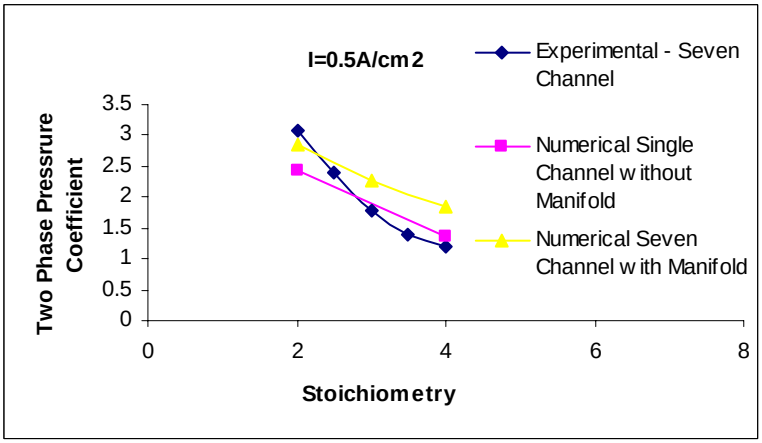

Figure 7.21b. Comparison of two phase pressure drop coefficient I=0.5A/cm^2.

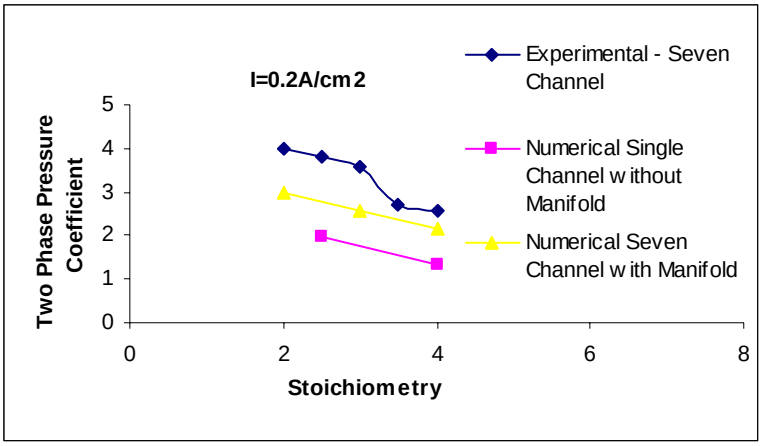

Figure 7.21c. Comparison of two phase pressure drop coefficient I=0.2A/cm^2.

8. A New Constitutive Model for Predicting Proton Conductivity in Polymer Electrolyte Membrane[§§]

8.1. Introduction

One of the key technical challenges in predicting the performance of a polymer-electrolyte-membrane fuel cell (PEMFC) is the ability to accurately compute the potential drop across the polymer electrolyte or membrane. With Ohm's law being customarily taken as valid in relating current density to electrolyte-potential gradient, the accuracy in computing potential drop across the membrane depends on the ability to accurately estimate the proton conductivity in the polymer electrolyte. One of the most prevalently used proton-conductivity models is the following empirical correlation developed by Springer et al. (1991) for the Nafion 117 membrane (for $\lambda > 1$ where λ is membrane water content as defined below):

$$\kappa_{30} = 0.005193\,\lambda - 0.00326 \tag{8.1}$$

In Equation 8.1, λ is the membrane's water content, defined as the number of moles of water per mole of acid sites attached to the membrane (namely, SO_3H), and κ_{30} is proton conductivity at 30° C in units of $\Omega^{-1}\,cm^{-1}$ or S/cm. Springer et al.'s empirical correlation (Equation 8.1) was based on the experimental data of Zawodzinski et al. (1991 & 1993). To account for the temperature dependence of proton conductivity, Springer et al. (1991) then used a standard Arrhenius relationship and an activation energy of 2.52 kcal/mole (obtained using data from Zawodzinski et al. 1991 & 1993) to arrive at the following empirical correlation that relates conductivity to membrane water content and cell temperature:

$$\kappa = \exp\left[1268\left(\frac{1}{303} - \frac{1}{273 + T_{cell}}\right)\right]\kappa_{30} \tag{8.2}$$

The above correlation is simple and easy to implement in a full fuel-cell computer model but only valid for the conditions under which the fitted data was collected. For each new membrane, a whole new set of data must be generated at the conditions of interest.

Hsu et al. (1980) first proposed the following power-law model, which is based on the heuristic percolation theory, to describe proton conductivity in Nafion:

$$\kappa = \kappa_0 (f_v - f_{v0})^q \tag{8.3}$$

where f_{v0} is the threshold value for the volume fraction (f_v) of the aqueous phase (i.e., water) in the polymer, q is the critical exponent, and κ_0 is the prefactor. f_v can be expressed explicitly in terms of water content as follows:

[§§] Portion of this chapter has been published in a proceeding paper: K. S. Chen and M. A. Hickner, "A new constitutive model for predicting proton conductivity in polymer electrolytes", in *ASME Proceedings of IMECE'04*, paper # 60848 (2004).

$$f_v = \frac{\lambda \overline{V}_w}{\overline{V}_m + \lambda \overline{V}_w} = \frac{\alpha\lambda}{1+\alpha\lambda} \tag{8.4}$$

where $\overline{V}_w$ is the molar volume of water, $\overline{V}_m$ is the molar volume of dry membrane, and $\alpha \equiv \overline{V}_w / \overline{V}_m$. Using an AC impedance technique with frequencies between 10^0 and 10^7 Hz and a constant measuring current density of 1.25 mA/cm^2, Hsu et al. obtained limited conductivity data using a range of equivalent weights (1050, 1100, 1350, and 1500) of Nafion (Na^+ form) for small aqueous-phase volume fractions (from about 0.1 to about 0.2) to obtain values for the three constants: q = 1.5, f_{v0} = 0.10, κ_0 = 0.16 S/cm. Hsu et al.'s power-law conductivity model with these constants significantly under-estimates the conductivity of Nafion membrane as compared with the experimental data of Zawodzinski et al. (1991 & 1993). For example, at λ = 10, conductivity estimated by Hsu et al.'s model is 0.0091 S/cm whereas Zawodzinski et al. (1991 & 1993) reported a measured value of 0.0484 S/cm. Morris and Sun (1993) used data they obtained for Nafion 117 (H^+ form) to obtain the following power-law conductivity model:

$$\kappa = 0.125(f_v - 0.06)^{1.95} \tag{8.5}$$

Similarly, Morris and Sun's model under-estimates the conductivity of Nafion by almost an order of magnitude – for λ = 10, conductivity estimated by Morris and Sun's model is 0.0048 S/cm as compared to 0.0484 S/cm reported by Zawodzinski et al. (1991 & 1993).

More recently, Weber and Newman (2004) presented the following semi-empirical conductivity model that is based on heuristic percolation theory and similar to that of Hsu et al. (1980) and Morris and Sun (1993):

$$\kappa = 0.5\left(f_v - 0.06\right)^{1.5} \tag{8.6}$$

Though Weber and Newman claim that their model fits well the majority of the Nafion-conductivity data in the literature, conductivity from their power-law model increases with water content without any upper limit – this is not born out by the data presented by Gottesfeld and Zawodzinski (1997), which shows a peak conductivity at a water content around 22. Springer et al's correlation (Equation 8.1) suffers from the same drawback.

Thampan et al. (2000) developed a constitutive conductivity model for Nafion or like membranes based on the dusty-fluid model for transport and the percolation model for structural aspects. Their model also includes the thermodynamics of dissociation of the acid group in the presence of polar solvents such as water. Though the constitutive model of Thampan et al. is relatively comprehensive, it requires four adjustable parameters, which may explain why this model has not received much attention from other researchers as compared with empirical correlation of Springer et al. (1991). For comparison, Thampan et al.'s model is presented in Equation 8.7:

$$\kappa = \frac{F^2}{RT}\frac{D^e_{12}}{(1+\delta)}\frac{1}{\lambda \bar{V}_w}\bar{\alpha}\left(f_v - f_{v0}\right)^{1.5} \tag{8.7}$$

where D^e_{12} is the effective mutual diffusion coefficient of hydronium ion (H_3O^+) and water; δ ($\equiv D^e_{12}/D^e_{1m}$) is the ratio of the effective diffusivity of H_3O^+ interaction with water to that with membrane, which is considered to be an adjustable parameter; and $\bar{\alpha}$ is the degree of acid-group dissociation given by:

$$\bar{\alpha} = \frac{(\lambda+1) - \sqrt{(\lambda+1)^2 - 4\lambda(1-1/K_{A,C})}}{2(1-1/K_{A,C})} \tag{8.8}$$

with $K_{A,C}$ being the acid dissociation constant, which in turn depends on temperature:

$$K_{A,C} = K_{A,C,298}\exp\left[-\frac{\Delta H_0}{RT}\left(\frac{1}{T}-\frac{1}{298}\right)\right] \tag{8.9}$$

Moreover in Equation 8.7, the percolation threshold volume fraction, f_{v0}, is considered to be a fitted parameter whereas D^e_{12} is taken to be the diffusion coefficient of H_3O^+ at infinite dilution in water. In short, the model of Thampan et al. (2000) requires four adjustable parameters: f_{v0}, $K_{A,C,298}$, ΔH_0, and δ.

In this work, we adopted a constitutive model approach in developing a new model relating proton conductivity to water content. Our objective was to develop a relatively simple conductivity model that covers a sufficiently wide range of water content and can be easily incorporated into a full fuel-cell computer model. The value of λ was measured to be approximately 22 by Zawodzinski et al. (1991 & 1993) when the membrane is equilibrated with liquid water. To enable the fundamental understanding of the transport processes (e.g., by modeling) when the cathode is flooded with liquid water, it would be desirable to have a constitutive model that can predict proton conductivity for λ > 22. By employing volume of the hydrated membrane to determine the molar concentration of protons, a conductivity model depending on the molar volumes of dry membrane and water but otherwise requiring no adjustable parameters is developed in a relatively simple derivation. We then show that the same constitutive model can be derived by using an approach similar to that taken by Thampan et al. (2000); in this approach, the volume of the pore solution is used to determine the molar concentration of protons, and the proton interactions with water and membrane is taken into account to estimate the continuum diffusion coefficient for protons. In Thampan et al.'s model, the ratio of the effective diffusivity for proton interaction with membrane to that for proton interaction with water is taken to be a constant adjustable parameter. We show that by taking this ratio to be inversely proportional to membrane water content and properly choosing the proportionality constant, the same constitutive model requiring no adjustable parameters can be derived. To help validate our new constitutive model, the proton conductivity of Nafion 117 was measured in our laboratory using a 4-point probe.

8.2. Experimental

Proton conductivity of Nafion 117 was measured by four-probe electrochemical impedance spectroscopy (EIS) using a Solartron 1260 frequency response analyzer coupled with a Solartron 1287 potentiostat. A schematic diagram of the membrane- conductivity measuring cell is shown in Figure 8.1. The outer electrodes of the cell are connected to the working and counter electrodes on the 1287 potentiostat, and the two inner electrodes are connected to the reference electrodes. We chose to measure the conductivity of Nafion membranes in the in-plane direction due to the dominant impedance response of the membrane sample in this geometry. Through-plane measurements are much more difficult and susceptible to interfacial phenomena interfering with the measurement of the true membrane properties. While our measurements do not reflect the orientation of the membrane in a working fuel cell, the measurements with our cell compare well to literature data taken using a through-plane measurement (e.g., Alberti et al. 2001).

EIS was performed on water-immersed samples by imposing a relatively small (10 mV amplitude) sinusoidal (AC signal) voltage across the membrane sample at frequencies between 100 kHz and 100 Hz (scanning from high to low frequencies); and the resultant current response was measured. From the amplitude and phase lag of the current response, a complex number, the impedance, was computed, which is composed of a real component, Z', and an imaginary component, Z". An example of the raw impedance data plotted on a complex plane is shown in Figure 8.2.

To compute the membrane proton conductivity from the complex impedance response, the impedance line is extrapolated to the x-axis. The extrapolated value of the real impedance where the imaginary response is zero is then taken as the resistance of the membrane and the membrane proton conductivity is computed from the following equation:

$$\kappa = \frac{L}{Z'A} \tag{8.10}$$

where L is the length between the reference electrodes, Z' is the real part of the impedance response (extrapolated to Z" = 0), and A is the area available for proton conduction (width x thickness).

8.3. Constitutive Model

Current density is generally related to the species molar flux using Faraday's law (cf. Newman 1991):

$$\vec{i} = F\sum_{i=1}^{n}[z_i(\vec{J}_i + c_i\vec{v})] \tag{8.11}$$

where F is Faraday's constant (≡ 96487 C/mole), z_i, c_i and $\vec{J}_i$ are, respectively, the charge number, molar concentration and molar migration/diffusive flux of species i, and $\vec{v}$ is mixture-fluid velocity due to convection. Due to electro-neutrality (i.e., $\sum z_i c_i = 0$), the second term at the right side (i.e., the

convective term) drops out from Equation 8.11. Also, at current density of practical fuel-cell operations (e.g., for automotive and stationary power applications), migration flux dominates over diffusive flux, we have from Equation 8.11 (cf. Newman 1991):

$$\vec{i} = F\sum_{i=1}^{n} z_i \vec{J}_i = -F^2 \sum_{i=1}^{n} z_i^{\,2} u_i c_i \nabla\Phi \tag{8.12}$$

where u_i is species mobility and Φ is electrolyte potential. Using the Nernst-Einstein equation to relate species mobility to diffusivity and considering that proton is the only mobile and charged species in the membrane, we have by setting $z_{H^+} = 1$:

$$\vec{i} = -\left(\frac{F^2 D_{H^+,eff} c_{H^+}}{RT} \right) \nabla\Phi = -\kappa \nabla\Phi \tag{8.13}$$

where κ is the proton conductivity given by

$$\kappa = \frac{F^2 D_{H^+,eff} c_{H^+}}{RT} \tag{8.14}$$

with R being the universal gas constant, T temperature, $D_{H^+,eff}$ the effective diffusivity, and c_{H^+} the molar concentration, respectively, of protons. Next, we need to express c_{H^+} and $D_{H^+,eff}$ as functions of water content (λ). It turns out that there are two different ways of deriving the same constitutive model, depending on how c_{H^+} is determined. We shall present the simpler way first and then derive the same constitutive model using an approach similar to that taken by Thampan et al. (2000).

To determine c_{H^+}, we can assume that the membrane swells freely and that the molar volume of the hydrated membrane, V, changes based on the assumption of constant additive molar volumes of water and the dry membrane (cf. Weber and Newman 2004):

$$V = \overline{V}_m + \lambda \overline{V}_w \tag{8.15}.$$

Then, the molar concentration of protons is simply given by:

$$c_{H^+} = \frac{1}{\overline{V}_m + \lambda \overline{V}_w} = \frac{1}{\overline{V}_m (1 + \alpha\lambda)} \tag{8.16}.$$

Now, the effective diffusivity of protons can be related to the continuum diffusion coefficient, D_{H^+}, by employing a Bruggeman correction exponent of q and adopting a percolation threshold of f_{v0} (cf. Weber and Newman 2004):

$$D_{H^+,eff} = D_{H^+} (f_v - f_{v0})^q \tag{8.17}.$$

The above equation shows that $D_{H^+,eff}$ approaches D_{H^+} as $f_v \to 1$ (that is, as water content is sufficiently high per Equation 8.4), indicating that D_{H^+} can be taken as the proton diffusivity at infinite dilution in water, $D^0{}_{H^+,w}$. Substituting Equations 8.16 and 8.17 into Equation 8.14 and replacing D_{H^+} by $D^0{}_{H^+,w}$ yields:

$$\kappa = \frac{F^2}{RT}\frac{D^0{}_{H^+,w}}{\overline{V}_m(1+\alpha\lambda)}\left(f_v - f_{v0}\right)^q \tag{8.18}.$$

The value of proton diffusivity at infinite dilution in water is well documented in the open literature and text books; for example, Newman (1991) reports a value of $9.312\cdot10^{-5}$ cm^2/s for $D^0{}_{H^+,w}$ at 25°C.

Now, we shall show how Equation 8.18 can be derived by an approach similar to that taken by Thampan et al. (2000). In this approach, the molar concentration of protons in Equation 8.14 can be evaluated using the volume of pore solution, that is:

$$c_{H^+} = \frac{1}{\lambda\overline{V}_w} \tag{8.19}.$$

Because c_{H^+} is now defined on the basis of per unit volume of pore solution, we need to evaluate D_{H^+} accordingly by taking into account the proton interactions with water and membrane when migrating through the pores (cf. Thampan et al. 2000):

$$\frac{1}{D_{H^+}} = \frac{1}{D_{H^+,w}} + \frac{1}{D_{H^+,m}} \tag{8.20}$$

where $D_{H^+,w}$ and $D_{H^+,m}$ are diffusivities for proton interactions, respectively, with water and membrane matrix. Re-writing Equation 8.20, we have:

$$\frac{1}{D_{H^+}} = \frac{1}{D_{H^+,w}}\left(1 + \frac{D_{H^+,w}}{D_{H_+,m}}\right) \tag{8.21}.$$

Now, taking $D_{H^+,w}/D_{H_+,m}$ to be inversely proportional to water content with $\overline{V}_m/\overline{V}_w = \alpha^{-1}$ as the proportionality constant, we have:

$$\frac{D_{H^+,w}}{D_{H_+,m}} = \frac{1}{\alpha\lambda} \tag{8.22}.$$

Substituting Equation 8.22 into Equation 8.21 yields an expression for D_{H^+}:

$$D_{H^+} = \frac{\alpha\lambda}{1+\alpha\lambda}D_{H^+,w} \tag{8.23}.$$

It is interesting to note from Equation 8.23 that D_{H^+} approaches $D_{H^+,w}$ as λ becomes sufficiently large (that is, $\lambda >> 1/\alpha$), which implies that $D_{H^+,w}$ represents the value of proton diffusivity at infinite dilution in water, $D^0{}_{H^+,w}$. Substituting Equation 8.23 into Equation 8.17 gives:

$$D_{H^+,eff} = D_{H^+,w}\frac{\alpha\lambda}{1+\alpha\lambda}(f_v - f_{v0})^q \tag{8.24}$$

Substituting Equations 8.19 and 8.24 into Equation 8.14 yields:

$$\kappa = \frac{F^2}{RT}\frac{\alpha}{\bar{V}_w}\frac{D_{H^+,w}}{(1+\alpha\lambda)}(f_v - f_{v0})^q \tag{8.25}.$$

But

$$\frac{\alpha}{\bar{V}_w} = \frac{\bar{V}_w}{\bar{V}_m\bar{V}_w} = \frac{1}{\bar{V}_m} \tag{8.26}.$$

Upon substituting Equation 8.26 into Equation 8.25 and replacing $D_{H^+,w}$ by $D^0{}_{H^+,w}$, we have:

$$\kappa = \frac{F^2}{RT}\frac{D^0{}_{H^+,w}}{\bar{V}_m(1+\alpha\lambda)}(f_v - f_{v0})^q \tag{8.27}$$

which is the same as Equation 8.18. In essence, we have derived the same constitutive model in two different ways.

It should be pointed out that a key difference between the derivation presented above and the model of Thampan et al. (2000) lies in the treatment of $D_{H^+,w}/D_{H_+,m}$: Thampan et al. has considered it to be a constant parameter (though they do expect it to increase as the water content of the membrane decreases); in the derivation presented above, it is taken to be inversely proportional to water content such that D_{H^+} recovers the upper limiting value of proton diffusion at infinite dilution in water and reasonably represents the lower limiting values at vanishingly small water content.

Setting f_{v0} to 0.06 and q to 1.5 and substituting Equation 8.4 in Equation 8.18 or Equation 8.27 yields a new constitutive model for proton conductivity in membrane, which depends on the molar volumes of dry membrane and water content but otherwise requires no adjustable parameters:

$$\kappa_{30} = \frac{F^2}{RT}\frac{D^0{}_{H^+,w}}{\bar{V}_m(1+\alpha\lambda)}\left(\frac{\alpha\lambda}{1+\alpha\lambda} - 0.06\right)^{1.5} \tag{8.28}$$

where the subscript 30 indicates that conductivity computed from this model are those at 30°C; and $D^0{}_{H^+,w}$ again refers to the value of proton diffusivity at infinite dilution in water. To account for

temperature effects, we follow Springer et al. (1991) and use a standard Arrhenius relationship and an activation energy of 2.26 kcal/mole (which is the average of the value used by Springer et al. and that obtained from our measurements; this average value is used here in order to make use of wider range of experimental data) to arrive at the following constitutive model that relates conductivity to membrane water content and temperature:

$$\kappa = \exp\left[1137\left(\frac{1}{303} - \frac{1}{T+273}\right)\right]\kappa_{30} \tag{8.29}$$

where T is membrane temperature in centigrade (or °C) and κ_{30} (conductivity at 30 °C) is given by Equation 8.28.

8.4. Results and Discussion

Measurements were conducted on Nafion 117 (H^+ form) membranes immersed in liquid water for temperatures between 30°C and 80°C. The method of Zawodzinski et al. (see, Zawodzinski et al. 1991 & 1993, and Gottesfeld and Zawodzinski 1997) was used to generate Nafion 117 membranes with high lambda values whereby the membranes were swollen in hot glycerol solutions. After swelling in hot glycerol, the membranes were rinsed well and soaked in de-ionized water for at least 48 hours to remove all glycerol from the membrane.

The water content or λ values were determined by gravimetric analysis, in which the membrane samples were weighed when wet at 30°C, dried for at least 72 hours at 150°C, and then reweighed. The λ of each membrane sample was then calculated as follows:

$$\lambda = \frac{\frac{m_w}{M_w}}{m_{m,0} \cdot IEC} \tag{8.30}$$

where m_w is the mass of water absorbed (mass of the wet membrane minus the mass of the dry membrane), M_w is the molecular weight of water, $m_{m,0}$ is the mass of the dry membrane, and IEC is the ion exchange capacity of the PEM (usually expressed in units of milli-equivalents of acid per gram of dry polymer). IEC and equivalent weight (EW) are inversely proportional to each other:

$$IEC = \frac{1000}{EW} \tag{8.31}$$

with IEC in milli-equivalents per gram and EW in grams of polymer containing one equivalent of acid group or SO_3H. It should be noted that the λ values of the membrane samples equilibrated in liquid water did not change between 30°C and 80°C.

To study temperature effects, conductivities of the membrane samples were measured in liquid water between 30°C and 80°C. For each data point, the dimensions of the membrane were measured to ensure an accurate measure of the swollen membrane's conductivity. Figure 8.3 shows proton conductivity of Nafion 117 (as measured in our laboratory using a 4-point probe) as a function of water content; the error bars in Figure 8.3 indicate uncertainties in our measurements. For comparison, experimental data reported by Zawodzinski et al. (1991) and Gottesfeld and Zawodzinski (1997) at 30°C are also included in Figure 8.3.

The conductivity of all membrane samples increases with temperature as expected. The average activation energy for proton conduction was found to be 2.0 kcal/mole, with the unswollen Nafion 117 membrane showing an activation energy of 2.3 kcal/mole and the highly swollen Nafion 117 membranes (swollen in 200°C glycerol) having an activation energy of 1.9 kcal/mole. A maximum conductivity at all temperatures was observed for samples with a λ value around 39. These swollen membranes with λ = 38.7 had conductivities about 7% higher on average than non-swollen Nafion 117 membranes with a λ value around 22. This increase in conductivity for slightly swollen membranes is a result of increased water mobility within the pores, which results in slightly higher proton conductivities for these samples. For λ-values greater than 39, the conductivity of the swollen membranes steadily decreases with increasing λ due to increased dilution of the acid groups, which occurs with large membrane swelling.

Overall, conductivity values measured in our laboratory lie close to those reported by Gottesfeld and Zawodzinski (1997). Differences in the two data sets could arise from preparation and swelling methods for the membranes or differences in conductivity cell design.

Figure 8.4 compares conductivity of Nafion membrane at 30^{o}C as predicted by the present constitutive model and other representative correlation and models with experimental data of Gottesfeld and Zawodzinski (1997), Zawodzinski et al. (1991 & 1993) and those obtained from the present work. The parameter values used in computing conductivity from the present constitutive model (Equation 8.27) are: $D^0_{H^+,w}$ =10.571·10^{-5} cm^2/s (diffusivity of proton at infinite dilution in water at 30^{o}C), $\overline{V}_m$ = 550 cm^3/mole, $\overline{V}_w$ = 18.0783 cm^3/mole, and α = 0.03287. Values for the four adjustable parameters used in Thampan et al.'s model are: $K_{A,C,298}$ = 6.2 , $\Delta H_0 = -$ 52.3 kJ/mole, f_{v0} = 0.06, δ_- = 0.7 and 1.5, respectively. As can be seen from Figure 8.4, conductivity predicted by the present constitutive model (Equation 8.27) agrees very well with experimental data for water content from 1.5 to about 45, covering a wide range of water contents. In contrast, conductivities predicted by Springer et al. (1991)'s and Weber and Newman (2004)'s model agree with experimental data for water content up to about 22, but then they diverge from each other as water content increases beyond. As for conductivity predicted by Thampan et al. (2000)'s model, with δ = 0.7 good agreement is achieved for water content up to about 10 whereas with δ = 1.5 the model significantly over-predicts conductivity for water contents below about 22; in

short, good agreement can not be achieved using Thampan et al's model for a wide range of water contents when a single value of δ is used – this is actually recognized by Thampan et al. themselves. Although some of the models give good agreement with the experimental data over a limited range of λ values, conditions and membrane water content can vary widely within an operating fuel cell. Large down-channel gradients in gas humidity and high frequency resistance (a measure of membrane conductivity) have been reported, respectively, by Mench et al. (2003) and Bender et al. (2003). It is desirable that a proton conductivity model describes the membrane proton conductivity accurately over a sufficiently wide range of conditions which may occur in a fuel cell. Moreover, a membrane-conductivity model that can describe the membrane's behavior over a wide range of water contents can enable a more fundamental understanding of the transport processes within the membrane as alluded to previously.

8.5. Summary and Conclusions

A new constitutive model for predicting proton conductivity in polymer electrolyte or membrane was developed. Our conductivity model depends on the molar volumes of dry membrane and water but otherwise requires no adjustable parameter. Prediction computed from the present conductivity model yields good agreement with experimental data from the literature and those from our own measurements for a wide range of water contents: from 1.5 to about 45. In contrast, no other conductivity model from the literature can yield good agreement with experimental data for such a wide range of water content.

1. Securing screws
2. Teflon blocks
3. Stainless steel electrodes
4. Equilibration windows
5. Membrane sample

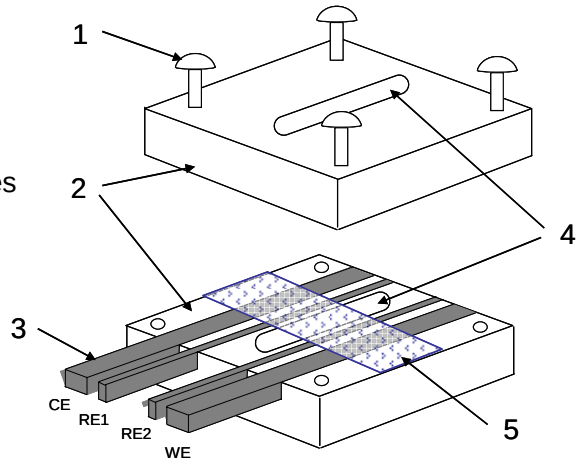

Figure 8.1 Schematic of four-point membrane-conductivity measuring cell used in present work

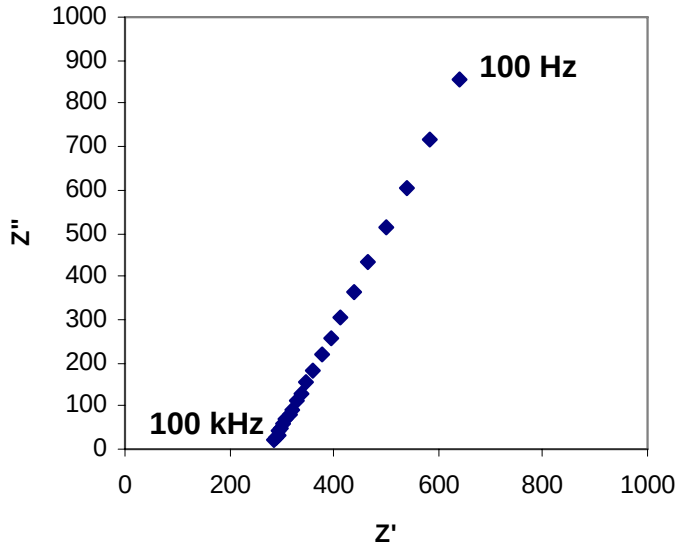

Figure 8.2. Impedance response of a typical proton-conducting membrane between 100kHz and 100 Hz

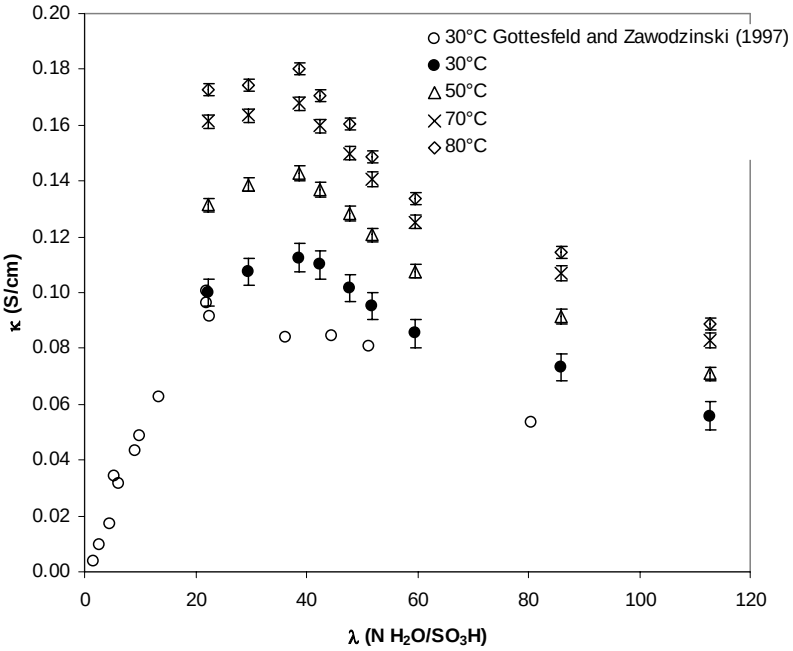

Figure 8.3. Proton conductivity (κ) of Nafion 117 as a function of water content (λ). Open circles are data at 30°C from Gottesfeld and Zawodzinski (1997).

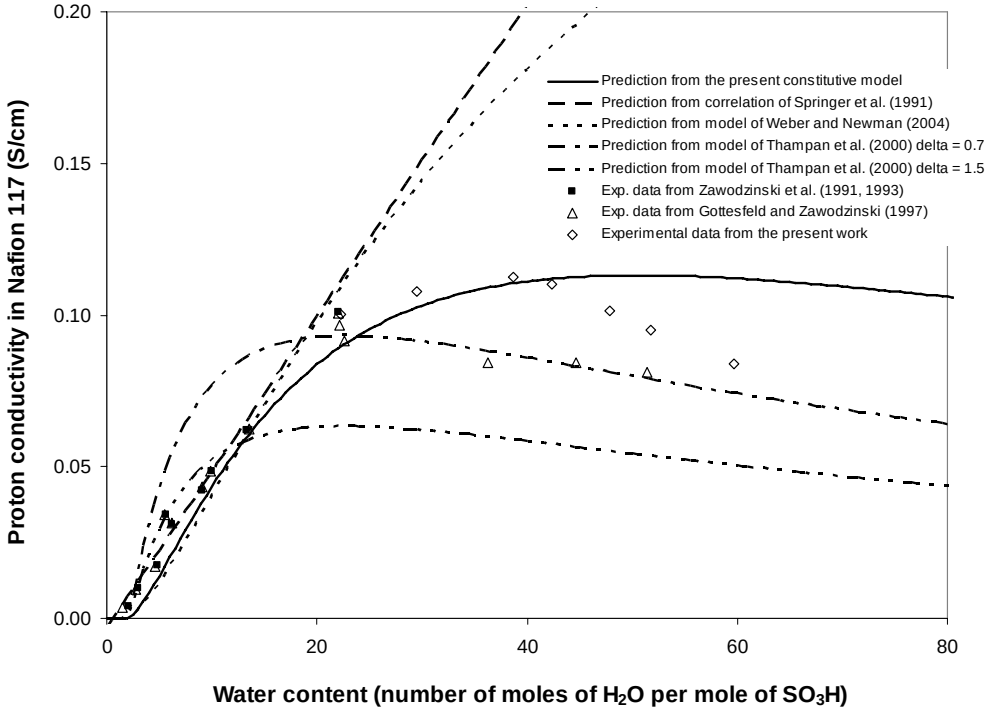

Figure 8.4. Proton conductivity in Nafion membrane at 30°C as a function of water content: comparison between predictions computed by various models and experimental data.

9. Analytical and Numerical Models for Predicting Performance of PEM Fuel Cells[***]

9.1. A 1-D Analytical Model for Predicting Performance of an Idealized PEM Fuel Cell

9.1.1. Introduction

In this section, we present the derivation of a one-dimensional or 1-D analytical model for predicting performance of an idealized PEM fuel cell, which is, more specifically, an explicit expression relating cell voltage to current density. Figure 9.1 shows a schematic of an idealized PEM fuel cell which consists of only the MEA components (i.e., the anode, membrane and cathode) – this idealization can be realized when the current density is so small that transport resistances and species consumption/generation rates are negligibly small such that species concentrations remain constant; moreover, in such an idealized PEM fuel cell, over-potentials are so small that the Butler-Volmer equations can be linearized. In practice, of course, transport resistances across the GDLs and down the flow channels and the rates of species consumption and generation are appreciable and the oxygen reduction reaction (ORR) in the cathode is so slow that the Butler-Volmer equation for ORR can not be linearized. Nevertheless, an explicit expression relating the cell voltage to current density for an idealized PEM fuel cell is useful in the verification of multi-dimensional numerical performance models and in the estimation of certain model parameters, e.g., Butler-Volmer kinetic parameters, particularly for the hydrogen oxidation reaction (HOR) in the anode. Parameter estimation for PEMFC models were recently demonstrated by Carnes and Djilali (2005) using a 1-D PEMFC model for transport in the principal direction of current flow. After its derivation, we illustrate utility of our 1-D analytical performance model by computing sample polarization curves.

9.1.2. Governing equations

9.1.2.1. Anode and cathode electrode regions

Here, both electrode and electrolyte phases are present. From the law of charge conservation, we have with one-dimensional approximation (i.e., assume that gradients exist only along y-axis that is normal to the anode and cathode current collectors),

$$\frac{d(i_1 + i_2)}{dy} = 0 \qquad \text{or} \qquad -\frac{di_1}{dy} = \frac{di_2}{dy} \tag{9.1}$$

where i_1 and i_2 are the current densities along the y-axis in electrode and electrolyte phases, respectively. The gradients of current densities (which are the rates of current density generation per unit volume or volumetric sources of current density) can be related to the electrode potential (Φ_1) and electrolyte potential (Φ_2) and open-circuit potential (U_0) via the Butler-Volmer equation:

[***] Portion of this chapter has been published in a proceeding paper: K. S. Chen and M. A. Hickner, "Modeling PEM fuel cell performance using the finite-element method and a fully-coupled implicit solution scheme via Newton's technique", in ASME Proceedings of FUELCELL2006, paper # 97032 (2006).

$$-\frac{di_1}{dy}=\frac{di_2}{dy}=ai_0\left[e^{\frac{\alpha_a F}{RT}(\Phi_1-\Phi_2-U_0)}-e^{-\frac{\alpha_c F}{RT}(\Phi_1-\Phi_2-U_0)}\right] \quad (9.2).$$

Current densities i_1 and i_2 are related to their respective potential gradients via Ohm's law:

$$i_1=-\sigma\frac{d\Phi_1}{dy} \qquad \text{and} \qquad i_2=-\kappa\frac{d\Phi_2}{dy} \quad (9.3)$$

where σ and κ are respectively, the electrode and electrolyte conductivities. Substituting Equation 9.3 into Equation 9.2 yields a pair of one-dimensional or 1-D equations that govern charge transport in the electrodes:

$$\frac{d}{dy}\left(-\sigma\frac{d\Phi_1}{dy}\right)+ai_0\left[e^{\frac{\alpha_a F}{RT}(\Phi_1-\Phi_2-U_0)}-e^{-\frac{\alpha_c F}{RT}(\Phi_1-\Phi_2-U_0)}\right]=0 \quad (9.4),$$

and

$$\frac{d}{dy}\left(-\kappa\frac{d\Phi_2}{dy}\right)-ai_0\left[e^{\frac{\alpha_a F}{RT}(\Phi_1-\Phi_2-U_0)}-e^{-\frac{\alpha_c F}{RT}(\Phi_1-\Phi_2-U_0)}\right]=0 \quad (9.5).$$

9.1.2.2 Membrane region

In the membrane region, which is sandwiched between the anode and cathode electrode regions, solid electrode phase is absent; consequently, no electrochemical reaction takes place and only i_2 is active (and i_1 is undefined), and we have:

$$\frac{d}{dy}\left(-\kappa\frac{d\Phi_2}{dy}\right)=0 \quad (9.6).$$

9.1.3. Boundary conditions

At the anode current collector (y = 0), $\Phi_1=0$, and $i_2=0$. At the cathode current collector (y = L), $\Phi_1=V$ and $i_2=0$ where V is the cell voltage. At the anode/membrane interface (y = L_a) and at the membrane/cathode interface (y = L – L_c), $i_1=0$, and Φ_2 is continuous.

9.1.4. Analytical solutions in the asymptotic regimes of small surface over-potentials

When the surface over-potential, η ($\equiv\Phi_1-\Phi_2-U_0$), is sufficiently small, the Butler-Volmer equations can be linearized such that Equations 9.4 and 9.5 reduce to, respectively, after setting $\alpha_a=\alpha_c=½$:

$$\frac{d}{dy}\left(\sigma\frac{d\Phi_1}{dy}\right)=\frac{ai_0F}{RT}(\Phi_1-\Phi_2-U_0) \quad (9.7),$$

and

$$\frac{d}{dy}\left(-\kappa\frac{d\Phi_2}{dy}\right)=\frac{ai_0F}{RT}(\Phi_1-\Phi_2-U_0) \quad (9.8).$$

Taking both σ and κ to be uniform throughout the cell, Equations 9.7 and 9.8 can be combined to arrive at a single equation in terms of the surface over-potential:

$$\frac{d^2\eta}{dy^2} = \beta\eta \tag{9.9},$$

where $\beta = \frac{ai_0F}{RT}\frac{\sigma+\kappa}{\sigma\kappa}$ is a parameter having the units of length^{-2} (e.g., cm^{-2}). Solving Equation 9.9 with the boundary conditions for Φ_1 and Φ_2 as described previously yields solutions to Φ_1 & Φ_2 as presented below.

9.1.4.1. Anode region ($0 \le y \le L_a$):

$$\eta(y) = \frac{i}{\sigma_a\sqrt{\beta_a}}\left\{\left[\frac{\sigma_a+\kappa\cosh(\sqrt{\beta_a}L_a)}{\kappa\sinh(\sqrt{\beta_a}L_a)}\right]\cosh(\sqrt{\beta_a}y) - \sinh(\sqrt{\beta_a}y)\right\} \tag{9.10},$$

$$\Phi_1(y) = \frac{1}{\sigma_a+\kappa}\left\{\kappa\eta - iy - \frac{i[\sigma_a+\kappa\cosh(\sqrt{\beta_a}L_a)]}{\sigma_a\sqrt{\beta_a}\sinh(\sqrt{\beta_a}L_a)}\right\} \tag{9.11},$$

$$\Phi_2(y) = -U_{0,a} - \frac{i[\sigma_a+\kappa\cosh(\sqrt{\beta_a}L_a)]}{\sigma_a\kappa\sqrt{\beta_a}\sinh(\sqrt{\beta_a}L_a)} - \frac{i}{\kappa}y - \frac{\sigma_a}{\kappa}\Phi_1(y) \tag{9.12},$$

where $i = i_1 + i_2$, and $\beta_a = \frac{(ai_0)_aF}{RT}\frac{\sigma_a+\kappa}{\sigma_a\kappa}$ with subscript *a* denoting the anode.

9.1.4.2. Cathode region ($L - L_c \le y \le L$):

$$\eta(y) = -\frac{i}{\sigma_c\sqrt{\beta_c}}\left\{\left[\frac{\sigma_c+\kappa\cosh(\sqrt{\beta_c}L_c)}{\kappa\sinh(\sqrt{\beta_c}L_c)}\right]\cosh[\sqrt{\beta_c}(L-y)] - \sinh[\sqrt{\beta_c}(L-y)]\right\} \tag{9.13}$$

$$\Phi_1(y) = V + \frac{1}{\sigma_c+\kappa}\left\{\kappa\eta + i(L-y) + \frac{i[\sigma_c+\kappa\cosh(\sqrt{\beta_c}L_c)]}{\sigma_c\sqrt{\beta_c}\sinh(\sqrt{\beta_c}L_c)}\right\} \tag{9.14}$$

$$\Phi_2(y) = V - U_{0,c} + \frac{i[\sigma_c+\kappa\cosh(\sqrt{\beta_c}L_c)]}{\sigma_c\kappa\sqrt{\beta_c}\sinh(\sqrt{\beta_c}L_c)} + \frac{i}{\kappa}(L-y) + \frac{\sigma_c}{\kappa}[V - \Phi_1(y)] \tag{9.15}$$

where $\beta_c = \frac{(ai_0)_cF}{RT}\frac{\sigma_c+\kappa}{\sigma_c\kappa}$ with subscript *c* denoting the cathode.

9.1.4.3. Membrane region ($L_a \le y \le L - L_c$):

$$\Phi_2(y) = -\frac{i}{\kappa}y - U_{0,a} - \frac{i[\sigma_a+\kappa\cosh(\sqrt{\beta_a}L_a)]}{\sigma_a\kappa\sqrt{\beta_a}\sinh(\sqrt{\beta_a}L_a)} \tag{9.16}$$

$$-\frac{i}{\sigma_a+\kappa}\left\{\frac{[\sigma_a+\kappa\cosh(\sqrt{\beta_a}L_a)][\cosh(\sqrt{\beta_a}L_a)-1]}{\kappa\sqrt{\beta_a}\sinh(\sqrt{\beta_a}L_a)} - \frac{\sinh(\sqrt{\beta_a}L_a)}{\sqrt{\beta_a}} - \frac{\sigma_a}{\kappa}L_a\right\}$$

In the membrane region, i_1 and Φ_1, and η are undefined.

Lastly, making use of the boundary condition that Φ_2 is continuous at the anode/membrane and cathode/membrane interfaces yields an explicit equation relating the cell voltage to the current density:

$$V = (U_{0,c} - U_{0,a}) - \frac{iL}{\kappa}\left[1 + \frac{1}{\sqrt{\beta_a}L}\left(\csc h(\sqrt{\beta_a}L) + \frac{\kappa}{\sigma_a}\coth(\sqrt{\beta_a}L)\right) + \frac{1}{\sqrt{\beta_c}L}\left(\csc h(\sqrt{\beta_c}L) + \frac{\kappa}{\sigma_c}\coth(\sqrt{\beta_c}L)\right)\right]$$
$$- \frac{i}{(\sigma_a+\kappa)\sqrt{\beta_a}}\left[\left(\frac{\sigma_a}{\kappa} + \cosh(\sqrt{\beta_a}L_a)\right)\left(\coth(\sqrt{\beta_a}L_a) - \csc h(\sqrt{\beta_a}L_a)\right) - \sinh(\sqrt{\beta_a}L_a) - \frac{\sigma_a}{\kappa}\sqrt{\beta_a}L_a\right] \quad (9.17).$$
$$- \frac{i}{(\sigma_c+\kappa)\sqrt{\beta_c}}\left[\left(\frac{\sigma_c}{\kappa} + \cosh(\sqrt{\beta_c}L_c)\right)\left(\coth(\sqrt{\beta_c}L_c) - \csc h(\sqrt{\beta_c}L_c)\right) - \sinh(\sqrt{\beta_c}L_c) - \frac{\sigma_c}{\kappa}\sqrt{\beta_c}L_c\right]$$

It is helpful to note that the second term on the right hand side of Equation 9.17 represents the potential or voltage loss across the membrane region whereas the third and fourth terms reflect, respectively, the voltage loss across the anode and cathode regions. In other words, the cell voltage is equal to the open circuit potential difference between the anode and cathode minus the voltage losses across the anode, membrane and cathode regions.

9.1.5. Sample polarization curves predicted by the analytical performance model

Figure 9.2 shows sample polarization curves computed using the analytical performance model for five different electrolyte conductivities: 0.02, 0.04, 0.06, 0.08, and 0.1 S/cm. Relevant model parameters are: L_a = 0.003 *cm*, L_m = 0.03 *cm*, L_c = 0.003 *cm*, $\alpha_a = \alpha_c = 1$, $(ai_0)_a$ = 10000 A/cm^3, $(ai_0)_c$ = 100 A/cm^3, $\sigma_a = \sigma_c$ = 5000 S/cm, $U_{0,a} = 0$, $U_{0,c}$ = 1.18 V, $U_0 = U_{0,c} - U_{0,a}$ = 1.18 V, T = 80 °*C*. As can be seen from Figure 9.2, cell voltage decreases with increasing current density due to higher voltage losses across the cell. Moreover, electrolyte conductivity has tremendous effect on cell voltage, which drops dramatically as electrolyte conductivity is lowered.

9.2. A Multi-dimensional Finite-Element Model for Simulating Performance of PEM Fuel Cells

9.2.1. Introduction

Many numerical PEMFC models have been reported in the literature as documented recently by Weber and Newman (2004), and Wang (2004) in two extensive review articles. Many of these models are 1-D (consider spatial variations only in the direction normal to the membrane and GDLs); see, for example, Spring et al. (1991), and Bernardi and Verbrugge (1991). The multi-dimensional models reported in the literature almost uniformly employ the finite-volume or control-volume approach using finite-difference approximation (that is, cast the governing equations in finite-difference form) – which is the conventional computational fluid dynamics (CFD) approach; see, for example, Gurau et al. (1998), Um et al. (2000), Dutta et al. (2000), Mazumder and Cole (2003), and Li and Becker (2004) and Li et al. (2005), and Sivertsen and Djilali (2005). One notable exception is the Ph.D. thesis research work of Nathan Siegel

(see, Siegel 2003, Siegel et al. 2003 & 2004) who solved the PEMFC governing equations using CFDesign^{TM}, which is a commercial CFD solver based on the finite-element method. The CFD approach usually requires many (ranging from many hundreds to several thousands) iterations for achieving convergence, which in part is due to the segregated or sequential solution scheme employed. Numerical instability due to finite-difference approximation can also arise. To be fair, the key benefit of the segregated solution method should be recognized: memory requirement is greatly reduced compared with the simultaneous solution scheme used in the present work.

In the present work, we employ a computational approach that differs from the conventional CFD approach in a couple aspects. First, we apply Galerkin's method of weighted residuals with finite-element basis functions to reduce the set of governing partial differential equations (PDEs) to a set of nonlinear ordinary differential equations or ODEs (in the case of transient operations) or algebraic equations (in the case of steady-state operations), as versus using control volumes with finite-difference approximation in the CFD approach. Second, we use a fully-coupled implicit solution scheme via Newton's technique to solve the resultant set of nonlinear ODEs or algebraic equations simultaneously, as compared to the segregated or sequential solution method employed in previous studies. The simultaneous solution scheme coupled with the use of Newton's method with an analytical Jacobian enables us to achieve quadratic convergence in our solution procedure. We illustrate our computational approach in a two-dimensional case study of a simplified PEM fuel cell. We compare predictions computed from our PEMFC model with experimental data (current distribution and polarization curve) obtained using the segmented cell technique in our laboratory as well as that reported by Mench et al (2003).

9.2.2. Governing equations

9.2.2.1. Gas flow channels

Velocity, pressure, and species concentrations in the GFCs are governed, respectively, by the laws of conservation of momentum, mass and species:

$$\frac{\partial \rho \mathbf{u}}{\partial t} + \nabla \cdot \rho \mathbf{u}\mathbf{u} = -\nabla p + \nabla \cdot \mu \nabla \mathbf{u} \tag{9.18}$$

$$\frac{\partial \rho}{\partial t} + \nabla \cdot \rho \mathbf{u} = 0 \tag{9.19}$$

$$\frac{\partial (c_i)}{\partial t} + \nabla \cdot (\mathbf{u} c_i) + \nabla \cdot \mathbf{J}_i = 0 \tag{9.20}.$$

In Equations 9.18 and 9.19, gas-mixture density, ρ, is taken to obey the ideal gas law with M_i and x_i being, respectively, the molecular weight and mole fraction of species *i*:

$$\rho = \frac{(P+p)}{RT} \sum_{i=1}^{n} M_i x_i \approx \frac{P}{RT} \sum_{i=1}^{n} M_i x_i = c \sum_{i=1}^{n} M_i x_i \tag{9.21}.$$

where P is the reference or base pressure of the gaseous mixture, which is orders of magnitude larger than its gauge hydrodynamic pressure, p; n is the total number of species present; and c is the total molar concentration of the mixture.

9.2.2.2. Gas diffusion layers

Similar to that in the GFCs, velocity, pressure, and species concentrations in the GDLs are governed by the laws of conservation of momentum, mass and species. However, since the GDLs are porous, the governing equations accordingly are those that describe transport through porous media:

$$\frac{\partial}{\partial t}\left(\frac{\rho \mathbf{u}}{\varepsilon}\right)+\nabla\cdot\left(\frac{\rho \mathbf{u}\mathbf{u}}{\varepsilon^2}\right)=-\nabla p+\nabla\cdot(\mu_B\nabla\mathbf{u})-\frac{\mu}{k}\mathbf{u} \tag{9.22}$$

$$\frac{\partial \varepsilon\rho}{\partial t}+\nabla\cdot(\rho\mathbf{u})=0 \tag{9.23}$$

$$\frac{\partial\left(\varepsilon c_i\right)}{\partial t}+\nabla\cdot\left(\mathbf{u}c_i\right)+\nabla\cdot\mathbf{J}_i=0 \tag{9.24}$$

Gas-mixture density in Equations 9.22 and 9.23 are similarly given by the ideal gas law, Equation 9.21.

9.2.2.3. Catalyst layers

Since the catalyst layers are also porous, velocity and pressure in these regions are similarly given by Equations 9.22 and 9.23. But the species consumption/generation associated with the HOR in the anode and the ORR in the cathode need to be taken into account in the species conservation equation. Accordingly, we have:

$$\frac{\partial}{\partial t}\left(\frac{\rho \mathbf{u}}{\varepsilon}\right)+\nabla\cdot\left(\frac{\rho \mathbf{u}\mathbf{u}}{\varepsilon^2}\right)=-\nabla p+\nabla\cdot(\mu_B\nabla\mathbf{u})-\frac{\mu}{k}\mathbf{u} \tag{9.22}$$

$$\frac{\partial \varepsilon\rho}{\partial t}+\nabla\cdot(\rho\mathbf{u})=0 \tag{9.23}$$

$$\frac{\partial\left(\varepsilon c_i\right)}{\partial t}+\nabla\cdot\left(\mathbf{u}c_i\right)+\nabla\cdot\mathbf{J}_i=r_i \tag{9.25}$$

where r_i denotes the rate of species consumption or generation. For the H_2 and O_2 species, we employ the Butler-Volmer kinetic model to describe the rate of species consumption due to the HOR and ORR:

$$r_i=\frac{ai_0}{nF}\left(\frac{c_i}{c_{i,ref}}\right)^{\beta}\left[\exp\left(\frac{\alpha_a F}{RT}(\Phi_1-\Phi_2-U_0)\right)-\exp\left(-\frac{\alpha_c F}{RT}(\Phi_1-\Phi_2-U_0)\right)\right] \tag{9.26}$$

in which n = 2, β = ½, and U_0 = 0 for r_{H_2} associated with the HOR; and n = 4, β = 1, and U_0 = 1.23 – 0.0009 (T – 298.15) with T being in Kelvin and U_0 being in Volt for r_{O_2} associated with the ORR.

In Equation 9.26, Φ_1 (electrode potential) and Φ_2 (electrolyte potential) are given by the charge conservation equations:

$$\nabla \cdot (-\sigma \nabla \Phi_1) = -ai \tag{9.27}$$

$$\nabla \cdot (-\kappa \nabla \Phi_2) = ai \tag{9.28}.$$

In Equations 9.27 and 9.28, *ai* is the volumetric current source and is given by: $ai = 2Fr_{H_2}$ in the anode and $ai = 4Fr_{O_2}$ in the cathode with *F* being Faraday's constant (≡ 96487 C/mole) and r_{H_2} & r_{O_2} given by Equation 9.26. In Equation 9.28, κ is the electrolyte conductivity and it depends on water content and temperature (see, e.g., Equation 8.29).

In the present work, the diffusive fluxes, $\mathbf{J}_i$, in Equations 9.20, 9.24 and 9.25 are simply taken to be given by the Fick's first law of diffusion (Bird et al. 2002):

$$\mathbf{J}_i = -D_i \nabla c_i \tag{9.29}.$$

Alternatively, $\mathbf{J}_i$, can be taken to be given by the Stefan-Maxwell flux equations (as some have reported in the literature), which may be more accurate but definitely are more difficult to solve and implement numerically based on our past experience in modeling thermal batteries (Chen et al. 2000).

9.2.2.4. Membrane

Electrolyte potential in the membrane region is again governed by the law of charge conservation. Since no current generation or consumption occurs here, we have:

$$\nabla \cdot (-\kappa \nabla \Phi_2) = 0 \tag{9.30}$$

Water (considered present only as vapor in the current version of our model) transport in the membrane is due to diffusion and electro-osmotic drag, and H_2O species balance gives:

$$\nabla \cdot (-D_{H_2O} \nabla c_{H_2O} + n_d \frac{i}{F}) = 0 \tag{9.31}.$$

9.2.3. Boundary condions

9.2.3.1. Gas flow channel walls

The GFC walls are assumed to be impermeable and no-slip. Accordingly, the boundary conditions along GFC walls are:

$$\mathbf{u} = \mathbf{0} \tag{9.32},$$

$$\mathbf{n} \cdot \mathbf{J}_i = 0 \quad (\mathbf{n} \text{ is a normal unit vector}) \qquad \text{or} \qquad \nabla c_i = 0 \tag{9.33}.$$

9.2.3.2. Gas flow channel inflow planes

At the anode and cathode inflow planes or inlets, flows are taken to be plug and velocity components are:

$$u = 0 \tag{9.34}$$

$$v = v_{in} \quad \text{with} \qquad v_{in,a} = \frac{\xi_a I_{ref} A}{2Fc^a_{H_2} A_a} \quad \text{and} \qquad v_{in,c} = \frac{\xi_c I_{ref} A}{4Fc^c_{O_2} A_c} \tag{9.35}$$

where *u* and v are, the velocity components, respectively, normal to and along the gas flow channels; here, the subscripts and superscripts *a* and *c* denote, respectively, anode and cathode; ξ represents stoichiometric flow ratio; *I* is reference current density; *A* is the active electrode surface area; A_a and A_c are the flow cross-sectional areas of the anode and cathode gas flow channels, respectively. At these boundaries, the species concentrations are also specified:

$$c_i = c_{i,in} \tag{9.36}$$

9.2.3.3. Gas flow channel outflow planes

Pressures at the anode and cathode GFC outflow planes are specified, respectively, to be the desired back pressures:

$p = P_{anode,outflow}$ at the anode GFC outlet (9.37),

$p = P_{cathode,outflow}$ at the cathode GFC outlet (9.38)

where $P_{anode,\ outflow}$ and $P_{cathode,\ outflow}$ are the back pressures, respectively, at the anode and cathode sides.

9.2.3.3. Current collectors

In the present work, the current collectors are taken to be at the GDL/catalyst-layer interfaces. Moreover, the anode current collector is specified to be the reference potential. Accordingly, boundary conditions at these boundaries are:

$\Phi_1 = 0$ at the anode current collector (9.39),

$\Phi_1 = V$ at the cathode current collector (9.40),

$\mathbf{n} \cdot \mathbf{i}_2 = 0$ (**n** is a normal unit vector) or $\nabla \Phi_2 = 0$ at anode & cathode current collectors (9.41).

In Equation 9.40, *V* is the cell voltage.

Lastly, at the GFC/GDL, GDL/catalyst-layer, and membrane/catalyst-layer interfaces, velocity, pressure, and species concentrations are taken be continuous.

9.2.4. Numerical method of solution

The discretized set of the governing equations (Equations 9.18 – 9.20, 9.22 – 9.25, 9.27 – 28, and 9.30 – 9.31) along with boundary conditions (Equations 9.32 – 9.36) are solved simultaneously using Galerkin's method of weighted residuals with finite-element basis functions and a fully-coupled implicit solution scheme via Newton's technique. Only a brief description of the solution method is given here (readers who are interested in further details are referred to Schunk et al. 1997). First, unknowns of velocity, pressure, species concentrations, electrode potential, and electrolyte potential are expressed in terms of piecewise quadratic polynomial basis functions (ψ_j) and pressure is represented by piecewise linear basis functions (ϕ_j) as follow:

$$\mathbf{u} = \sum_{j=1}^{9} \mathbf{u}_j \psi_j \tag{9.42}$$

$$p = \sum_{j=1}^{4} p_j \phi_j \tag{9.43}$$

$$c_i = \sum_{j=1}^{9} c_{i,j} \psi_j \tag{9.44}$$

$$\Phi_1 = \sum_{j=1}^{9} \Phi_{1,j} \psi_j \tag{9.45}$$

$$\Phi_2 = \sum_{j=1}^{9} \Phi_{2,j} \psi_j \tag{9.46}$$

where $\mathbf{u}_j$, $c_{i,j}$, $\Phi_{1,j}$, $\Phi_{2,j}$, p_j are the respective local nodal unknowns to be solved for. Next, Galerkin's method of weighted residuals is applied to reduce the set of governing partial differential equations (PDEs) to a set of nonlinear ordinary differential equations (ODEs) or algebraic equations for the nodal unknowns of velocity, pressure, species concentrations, electrode potential, and electrolyte potential. For steady-state operation that is considered in the present work, we have:

$$\mathbf{R}^{M,Channel}{}_k = \iint \left[-\nabla \cdot \rho \mathbf{u}\mathbf{u} - \nabla p + \nabla \cdot (\mu \nabla \mathbf{u}) \right] \psi_k \, dA = \mathbf{0} \tag{9.47}$$

$$\mathbf{R}^{M,GDL}{}_k = \iint \left[-\nabla \cdot \left(\frac{\rho \mathbf{u}\mathbf{u}}{\varepsilon^2} \right) - \nabla p + \nabla \cdot (\mu_B \nabla \mathbf{u}) - \frac{\mu}{k} \mathbf{u} \right] \psi_k \, dA = \mathbf{0} \tag{9.48}$$

$$\mathbf{R}^{C}{}_k = \iint \left[\nabla \cdot (\rho \mathbf{u}) \right] \phi_k \, dA = 0 \tag{9.49}$$

$$\mathbf{R}^{S,i}{}_k = \iint \left[\nabla \cdot \left(\mathbf{u} c_i \right) + \nabla \cdot \mathbf{J}_i \right] \psi_k \, dA = 0 \tag{9.50}$$

$$\mathbf{R}^{\Phi_1}{}_k = \iint \left[\nabla \cdot (-\sigma \nabla \Phi_1) + ai \right] \psi_k \, dA = 0 \tag{9.51}$$

$$\mathbf{R}^{\Phi_2}{}_k = \iint \left[\nabla \cdot (-\kappa \nabla \Phi_2) - ai \right] \psi_k \, dA = 0 \tag{9.52}$$

$$\mathbf{R}^{W}{}_k = \iint \left[\nabla \cdot (-D_{H_2O} \nabla c_{H_2O} + n_d \frac{i}{F}) \right] \psi_k \, dA = 0 \tag{9.53}.$$

Equations 9.47 – 9.53, are further reduced by performing the integration by parts and applying the boundary conditions where appropriate to arrive at a set of nonlinear algebraic equations, which are then solved using Newton's method as follow:

$$\mathbf{U}^{k+1} = \mathbf{U}^k - \mathbf{J}^{-1}(\mathbf{U}^k)\mathbf{R}(\mathbf{U}^k) \tag{9.54}$$

where **J** is the Jacobian matrix of partial derivatives of R_i with respect to the unknown coefficients $\mathbf{U}_j$ and the non-zero entries of the Jacobian matrix $J_{ij} = \partial R_i / \partial U_j$ are calculated analytically from Equations 9.47 – 9.53. In the present work, the use of analytical Jacobian is the key to achieving quadratic convergence. Lastly, the matrix equations are solved using UMFPACK, which is a set of routines for solving unsymetric sparse linear systems, Ax = b, using the Unsymmetric MultiFrontal method (see, http://www.cise.ufl.edu/research/sparse/umfpack). The multi-dimensional, multi-physics finite-element code, GOMA, were used as the basic platform for solving the equations; details regarding GOMA are documented elsewhere by Schunk et al. (1997).

For the case study carried out in the present work, it took around 10 minutes of CPU time on a 3.6 GHz HP Workstation xw8200 running with a single processor to converge (when the maximum residual tolerance was around 10^{-8}) in 4 iterations with 127,590 unknowns.

9.2.5. Experimental

Current density distribution measurements were performed using an experimental cell with segmented anode and cathode electrodes as shown in Figure 9.3. The segmented electrodes were held in place by a supporting, non-conductive Lexan block and the segments were maintained in electrical isolation. The electrodes themselves were gold-plated aluminum blocks with seven-channel parallel gas flow channel geometry. Electrical connections were made to the segments through the gas sampling tubes welded onto the back of the segment blocks which remained capped and were not used in this study. Each segment had an area of 1.23 cm^2 and eight segments were utilized in this study to yield a total cell area of 9.84 cm^2. The cell temperature, gas flow rates, inlet humidity, and cell pressure was controlled by a Fuel Cell Technologies (Albuquerque, NM) test stand. The cell potential and current for each segment was controlled and recorded with an Arbin (College Station, TX) BT2000 multichannel potentiostat. Membrane electrode assemblies composed of Nafion 112 membranes with anode and cathode loadings of 0.3 mg Pt/cm^2 were purchased from Ion Power, Inc. Carbon paper gas diffusion layers (approximately 300 μm thick) with an integral microporous layer were segmented to match the electrode segments. Potentiostatic polarization curves were gathered simultaneously (all segments at the same potential) for each segment with a 5 minute equilibration time at each potential and a 3 minute data acquisition time with the current density measured every 10 seconds. The average current density during the 3 minute measurement is what is reported. Data was gathered simultaneously for each segment then simply summed for all segments at a given potential to construct a full-cell polarization curve.

9.2.5. Results and discussion

A two-dimensional base case study of a simplified PEM fuel cell having a straight channel and operating under steady state was performed. Table 9.1 lists relevant cell geometry, operating conditions, and

transport and electrochemical properties. The inlet flowrates were set to be equivalent to 1.5 atm, 2.5 stoic at 0.75 A/cm^2 for anode and 1.5 atm, 2.0 stoic at 0.75 A/cm^2 for cathode with the relative humidity being 100% for both inlets – the corresponding inlet velocities (along channel component) are: 10.02 cm/s for anode, and 15.54 cm/s for cathode; inlet species concentrations are: $c_{H_2} = 2.79 \cdot 10^{-5}$ moles/cm^3, $c_{O_2} = 0$, and $c_{H_2O} = 2.39 \cdot 10^{-5}$ moles/cm^3 for the anode, and $c_{H_2} = 0$, $c_{O_2} = 0.75 \cdot 10^{-5}$ moles/cm^3 and $c_{H_2O} = 1.61 \cdot 10^{-5}$ moles/cm^3 for the cathode.

Figure 9.4a shows the finite-element mesh used in the base case study, which has 5,610 elements and a total of 127,590 unknowns. The mesh is scaled toward the inlet and outlet as well as the walls and interfaces for better solution accuracy. With the mesh as shown in Figure 9.4a, it took around 10 minutes of CPU time on a 3.6 GHz HP Workstation xw8200 running with a single processor to converge (the maximum residual tolerance was below 10^{-8}) in 5 iterations with 127,590 unknowns. Figure 9.4b displays the absolute error (L_2 and L_∞ norms) as a function of the number of iterations required. Clearly, quadratic convergence was achieved.

Figure 9.5a shows the computed velocity field whereas Figure 9.5b displays pressure contour for the base case study. Figure 9.6 further presents plots of velocity and pressure along centerlines of GFCs. Velocities along centerline of GFCs rapidly rise and reach the maximum values due to the plug flow velocity conditions specified at the inlets. As expected, the pressure drops along the anode and cathode GFCs; the pressure in the anode GFC is seen to be consistently higher than that in the cathode GFC for the chosen operating conditions.

Figure 9.7 shows contour plots of computed species molar concentrations for H_2, O_2, and H_2O, respectively. As shown, H_2 concentration decreases along anode GFC due to the HOR, which consumes hydrogen. Similarly, O_2 concentration decreases along cathode GFC due to ORR, which consumes oxygen. Lastly, H_2O concentration drops along anode GFC due to electro-osmotic drag of water from anode to cathode. In contrast, H_2O concentration rises along cathode GFC due to the ORR, which generates water..

Figures 9.8 and 9.9 present comparisons between computed predictions and experimental data in order to help assess the validity of our PEMFC model. Figure 9.8 compares computed and measured current density along the cathode current collector. Besides data obtained in our laboratory using a segmented PEMFC test cell with a total cell area of 9.84 cm^2, current density along the cathode current collector measured by Mench et al. (2003) using a 50 cm^2 test cell is also included for comparison. Here, the fractional distance from the cathode inlet is defined as the distance from the cathode inlet divided by the total flow channel length. Figure 8.9 further compares the computed overall polarization curve with that measured in our laboratory as well as that reported by Mench et al. (2003). Here, a contact resistance of 300mΩ cm^2 was prescribed in computing the cell voltage to account for the interfacial resistances within

the fuel cell (the contact resistance value used here is comparable to the 150mΩ cm^2 used by Ju et al. 2005 in their validation study). Reasonably good agreements between computed predictions and experimental data are seen in Figures 9.8 and 9.9 but discrepancies do exist. In the case of current density distribution, visible discrepancies are seen near the entrance and exit of the cathode inlet and outlet whereas in the case of overall polarization curve, discrepancy is appreciable at high current densities. Discrepancies are expected since two important aspects are not accounted for in our current PEMFC model: 1) effects of liquid water; and 2) energy transport – this can have significant effects since localized evaporation can occur due to non-uniform temperature distribution. Moreover, our current model is two-dimensional, which prevents it to capture the three-dimensional effects as present in Mench et al.'s experiments with a serpentine flow field; velocity and species concentration in the in-plane direction (perpendicular to the flow direction) can vary significantly due to the presence of the alternative land/channel patterns.

9.2.6. Summary and concluding remarks

A numerical model for simulating PEMFC performance is presented; our model employs the finite-element method and a fully-coupled implicit solution scheme via Newton's technique. With our numerical approach, equations that govern flow, species and charge transport, and electrochemical reactions are solved simultaneously and quadratic convergence is ensured due to the use of Newton's method with an analytical Jacobian. The utility of our computational approach is illustrated by computing predictions of velocity, pressure, species concentrations, electrode potential, and electrolyte potential in a two-dimensional case study of a simplified PEM fuel cell. Comparisons between computed predictions and experimental data obtained in our laboratory and from the literature are presented in order to help assess the validity of our PEMFC model.

To be useful as a tool for PEMFC process design and optimization, the following additional phenomena need to be incorporated in the present model: 1) the presence and transport of liquid water, particularly the efficient removal of liquid water; 2) energy transport and temperature effects, particularly local heating due to non-uniform temperature distribution; and 3) three-dimensional effects, particularly the effects due to the presence of the alternative land/channel patterns as in serpentine flow fields. Lastly, it would be helpful to have direct comparison of computational performance and accuracy between the present approach and the conventional CFD approach. It should be pointed out that the present numerical method is much more memory intensive as compared with the segregated or sequential solution scheme often employed in the CFD approach. It should also be pointed out that we do not claim the present approach to be superior in any way as compared to the CFD approach; rather, we present an alternative numerical method for solving the nonlinear, highly coupled equations that govern the various complex phenomena involved in a PEM fuel cell.

Nomenclature

u	Superficial mass average velocity (cm/s)
p	Hydrodynamic pressure (dyne/cm^2)
T	Temperature (K)
F	Faraday's constant (96487 C/mole)
R	Universal gas constant (8.314 J/mole-K)
ρ	Density of gaseous mixture (g/cm^3)
μ	Viscosity of gaseous mixture (g/cm-s)
μ_B	Brinkman viscosity (g/cm-s)
ε	Porosity
K	Permeability (cm^2)
c_i	Molar concentration of species i (moles/cm^3)
$C_{i,ref}$	Ref. concentration of species i (moles/cm^3)
D_i	Diffusion coefficient of species i (cm^2/s)
κ	Electrolyte conductivity (Ω^{-1}cm^{-1})
Φ_1	Electrode potential (V)
Φ_2	Electrolyte potential (V)
$U_{0,a}$	Anodic open circuit potential (V)
$U_{0,c}$	Cathodic open circuit potential (V)
i	Current density (A/cm^2)
a	Interfacial surface area per unit volume (cm^{-1})
t	Time (s)
r_i	Rate of production/consumption for species i
α_a	Anodic transfer coefficient
α_c	Cathodic transfer coefficient
n_d	Electro-osmotic drag coefficient

Table 9.1. Cell geometry, operating conditions, and transport and electrochemical properties in the base case study

PARAMETER	VALUE
Cell length	7.112 cm
Gas channel width	0.254 cm
GDL thickness	0.03 cm
Membrane thickness	0.0051 cm
Catalyst layer thickness	0.001 cm
Cell voltage	0.7 V
Cell temperature	80°C
Relative humidity at inlet	100%
Anode outlet or back pressure	1.5 atm
Cathode outlet or back pressure	1.5 atm
Velocity at anode inlet	10.02 cm/s
Velocity at cathode inlet	14.54 cm/s
Transfer coefficients, α_a and α_c	1
Anode exchange current density $(ai_0)_{anode}$	1000 A/cm^3
Cathode exchange current density $(ai_0)_{cathode}$	0.0025 A/cm^3
GDL porosity	0.17
GDL permeability	1.12x10^{-10} cm^2
H_2 diffusivity in anode GFC	1.1 cm^2/s
H_2O diffusivity in anode GFC	1.1 cm^2/s
O_2 diffusivity in cathode GFC	0.0324 cm^2/s
H_2O diffusivity in cathode GFC	0.074 cm^2/s
Electro-osmotic drag coefficient, n_d	0.2

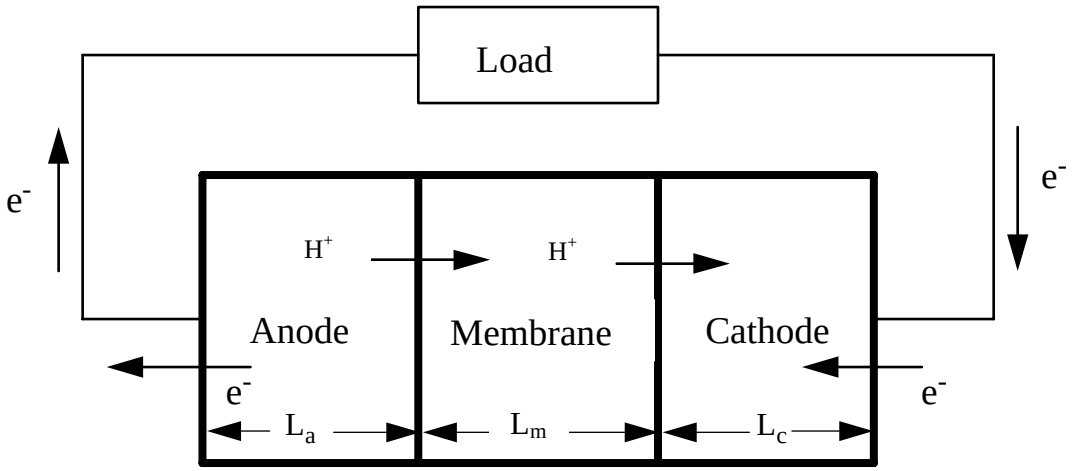

Figure 9.1. Schematic of an idealized PEM fuel cell

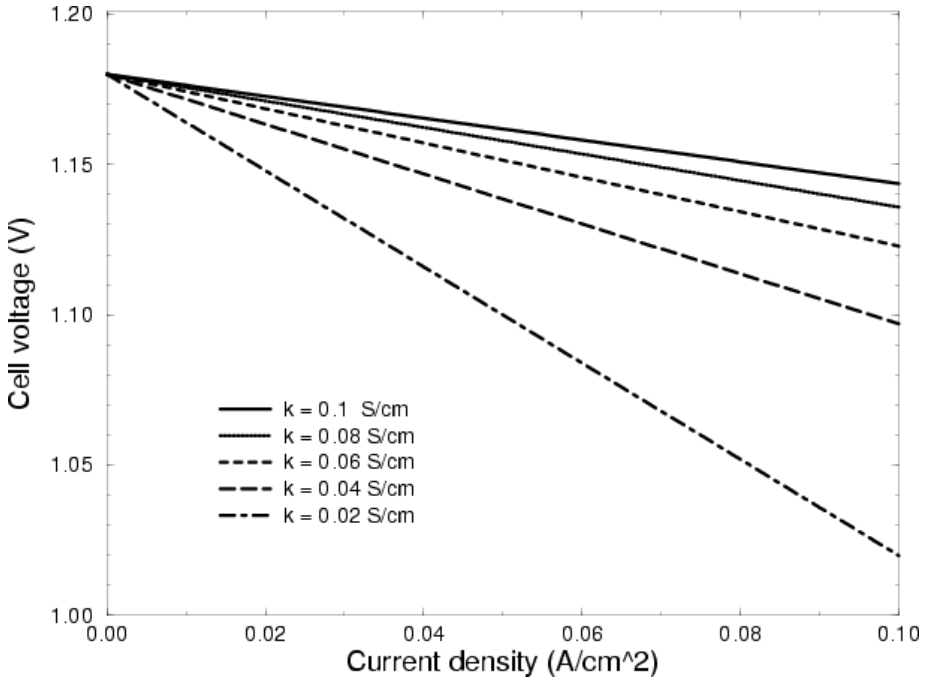

Figure 9.2. Sample polarization curves predicted by the analytical performance model – Effect of electrolyte conductivity.

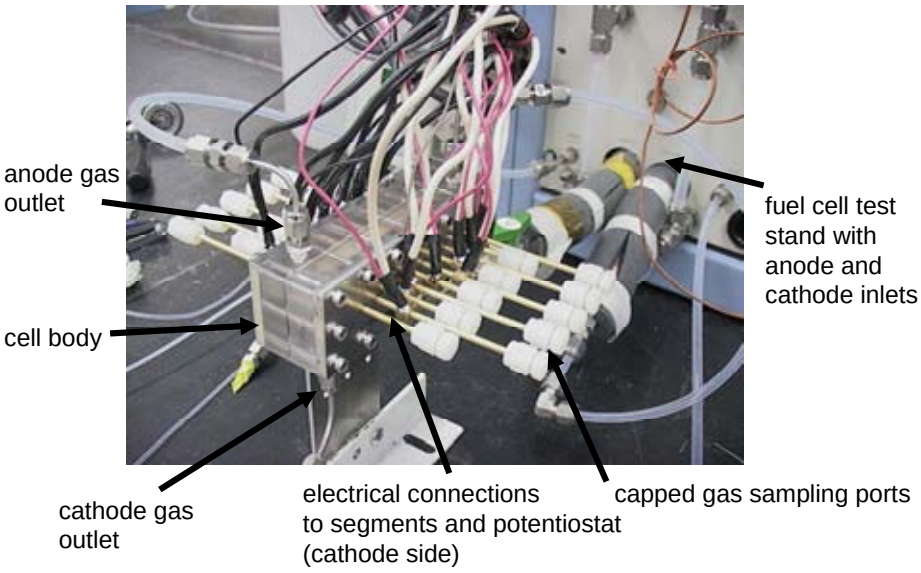

Figure 9.3. Segmented cell used for current distribution and polarization curve measurements in the present work.

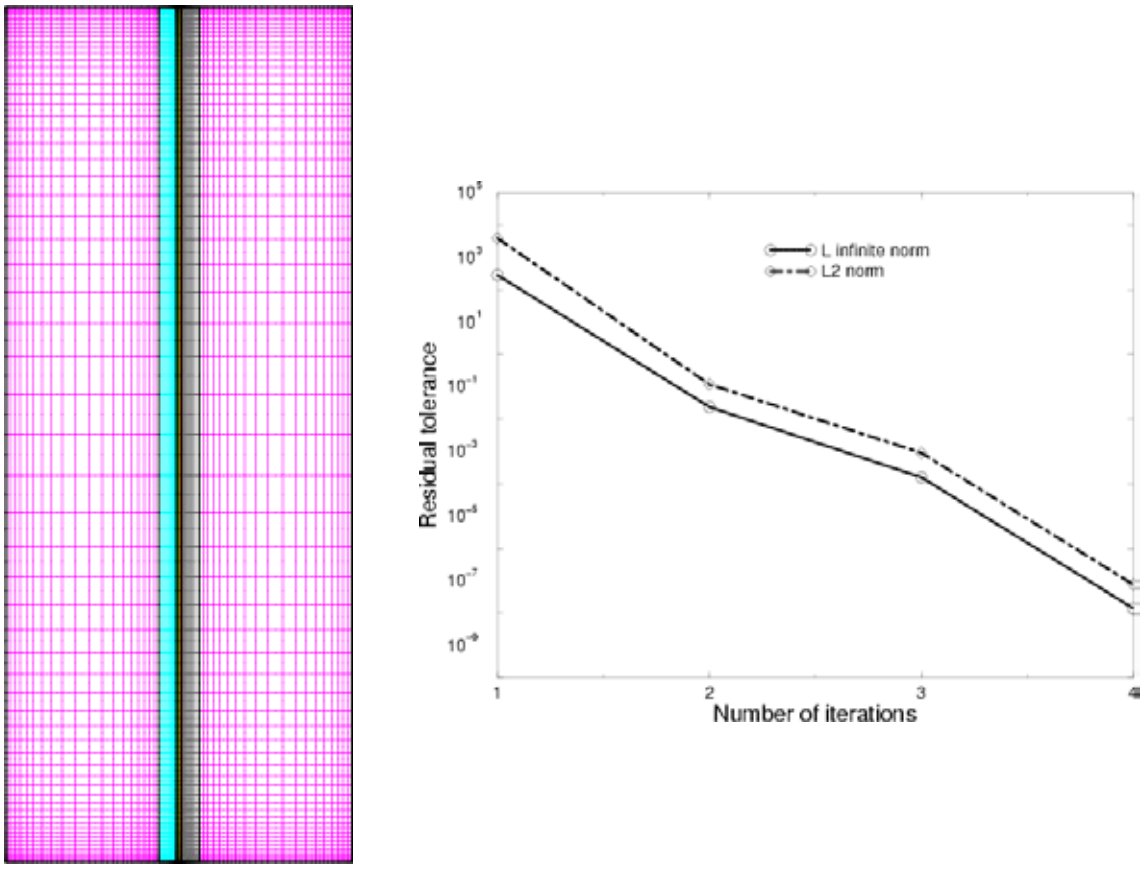

(a) (b)

Figure 9.4. Finite-element mesh used in the present study and sample convergence history: (a) finite-element mesh with 5,610 elements and 127,590 unknowns; (b) L_2 and L_∞ norms versus number of iterations.

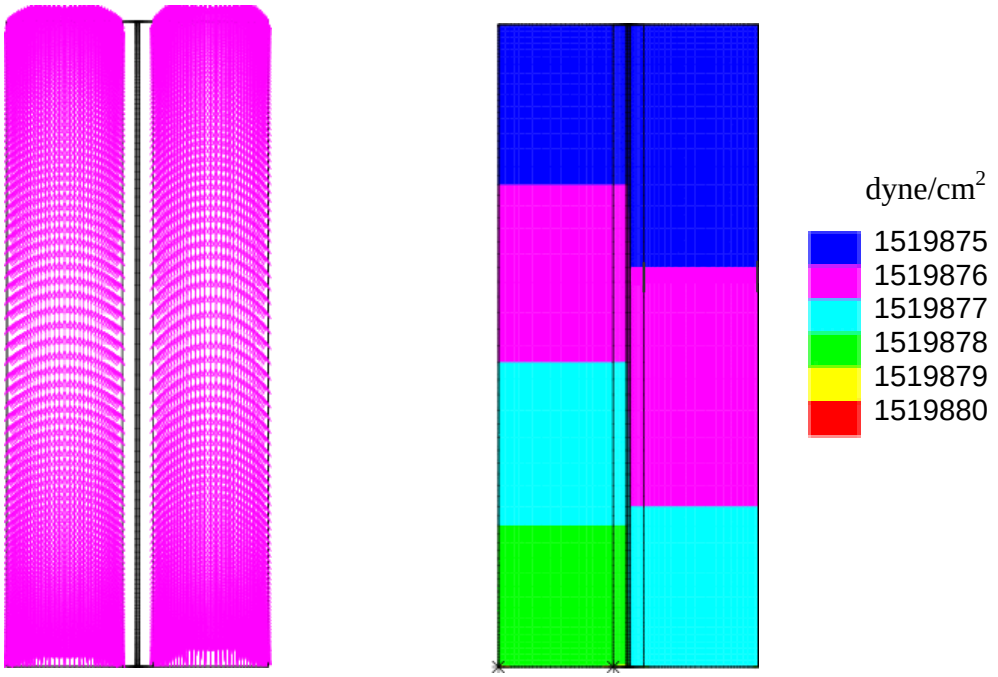

(a) (b)

Figure 9.5. Sample computed predictions: (a) velocity vector field; and (b) pressure contour.

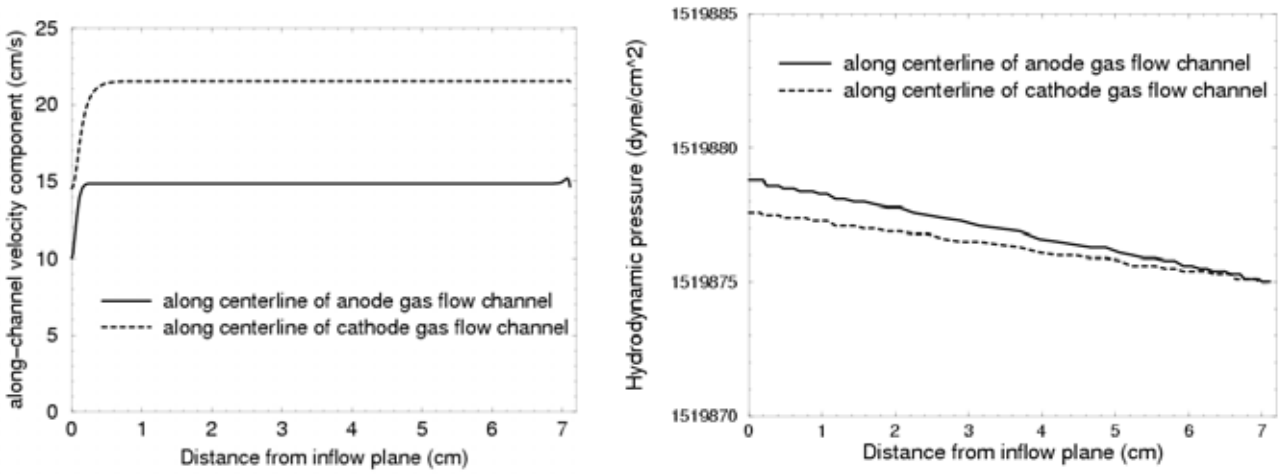

(a) (b)

Figure 9.6. Computed velocity and hydrodynamic pressure along centerlines of gas flow channels: (a) velocity; (b) hydrodynamic pressure.

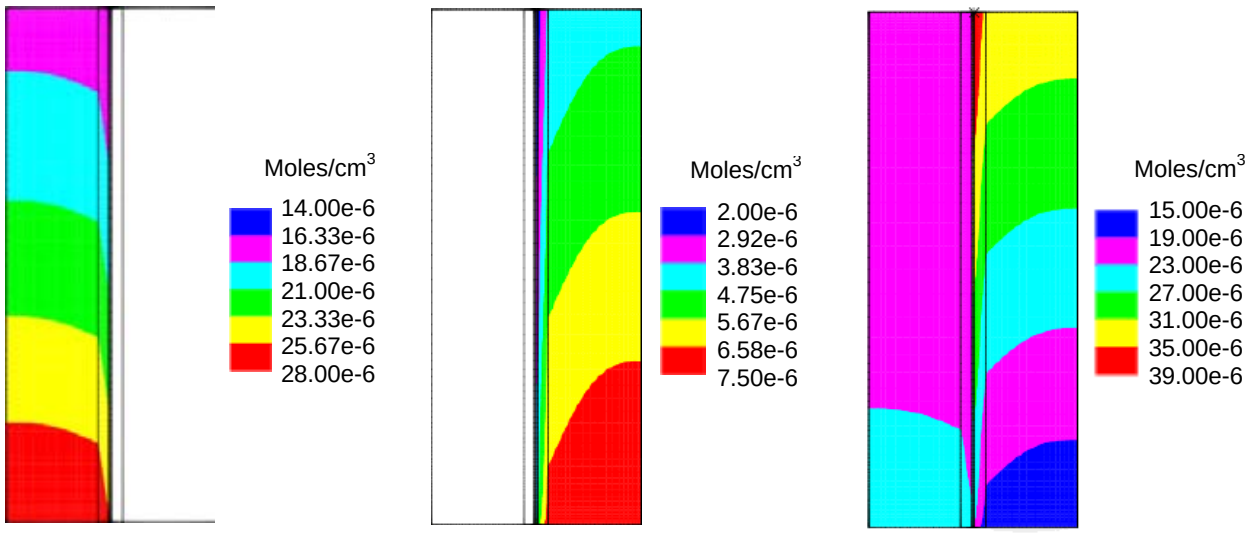

(a) (b) (c)

Figure 9.7. Computed prediction of species concentrations: (a) H_2, (b) O_2, and (c) H_2O.

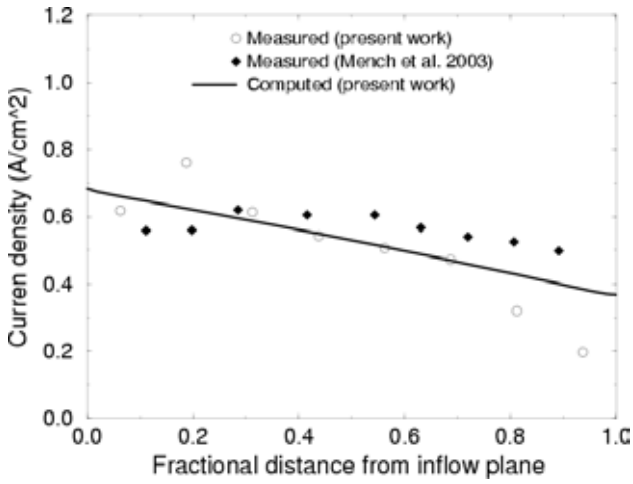

Figure 9.8. Model validation – comparison of computed and measured current distributions along the cathode current collector.

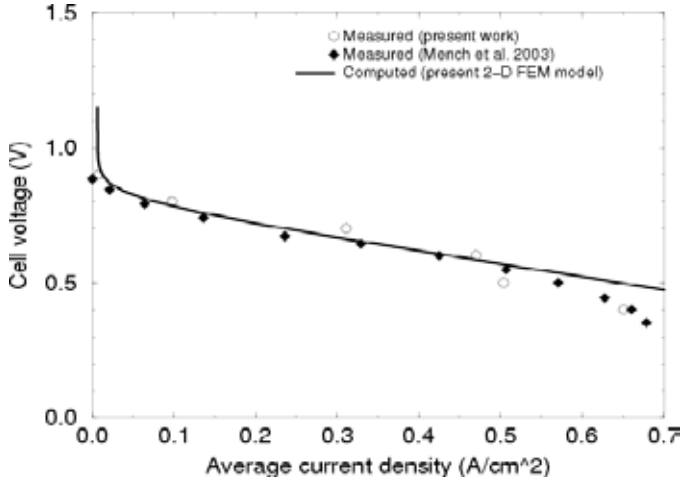

Figure 9.9. Model validation – comparison of computed and measured overall polarization curves.

10. An Exploratory Study on Membrane Electrode Assembly Degradation

10.1. Introduction

Degradation of PEMFCs is becoming a major research topic as fuel cells are being pushed to the brink of commercialization. Degradation can occur in the proton exchange membrane, in the catalyst layers, at the interfaces of the MEA components or in the porous media or cell hardware. It is thought that the membrane degrades primarily by chemical degradation when peroxides are formed in the cell. The other components of the cell including the platinum electrocatalyst and carbon catalyst support are thought to degrade primarily by electrochemical corrosion at high potentials. Durability in automotive applications are especially challenging due to the load cycling of the system and high potentials encountered during system rest. At high potentials above 0.9-1.0V in the acidic environment of a PEMFC, both the platinum catalyst and carbon support corrosion in the electrode can occur. Corrosion of these components can cause a decrease in electrochemically active surface area (EASA) of the platinum catalyst which would have a detrimental effect on the polarization performance of the cell and electrode thinning could occur which may impact the interfacial resistances within the MEA. Various accelerated corrosion protocols have been proposed, and we have chosen two, a potential cycling test and a static potential hold, to explore some of the key phenomena associated with PEMFC degradation with our primary focus being the catalyst layer. In this Chapter, we present an exploratory experimental study that focuses on MEA degradation.

10.2. Experimental

In order to obtain a durability baseline and begin to understand some of the phenomena occurring during aging of standard PEMFC materials, MEAs composed of commercial components were aged using two accelerated protocols. Ion Power (New Castle, DE) catalyst coated membranes were based on N112 (i.e., Nafion 112) membranes with anode and cathode loadings of 0.3 mg Pt/cm^2. The gas diffusion layers were carbon paper with integral microporous layers and testing was performed in Fuel Cell Technologies (Albuquerque, NM) 5 cm^2 hardware. The potential profiles for each test are shown in Figure 10.1. Potential cycling was conducted from 0.1 to 1.2V at 50 mV/s with hydrogen on the anode and nitrogen on the cathode at 80°C and 80°C gas dewpoints at ambient outlet pressure. This protocol has been shown to slowly corrode the Pt nanoparticle catalyst on the fuel cell cathode (Borup 2005). After each round of potential cycling, the fuel cell's polarization curve performance was interrogated and the electrochemically active surface area (EASA) of the cathode was measured. Polarization curves were taken at 80°C under hydrogen and air at 20 psig outlet pressure with flow rates of 200 and 500 std. cm^3/min., respectively. Cyclic voltammagrams for EASA measurement were recorded at the same conditions as the cyclic potential aging experiments.

A constant potential hold at 1.2V with the anode under hydrogen and the cathode under nitrogen was also performed at 80°C with the inlet gases humidified to 80°C dewpoints and ambient outlet pressure.

Periodically during this test, the cell's polarization performance was measured. In each test series, MEAs were aged and then cross-sectioned for scanning electron microscopy to measure the catalyst layer thickness as a function of degradation stress.

10.3. Results and Discussion

Shown in Figure 10.2 are cyclic voltammagrams recorded on a fresh MEA, 0 cycles, and MEAs aged for 1000, 5000, and 10,000 cycles respectively. The decrease in the area of the low voltage peak between 0.1 and 0.45 V indicates that the EASA of the cathode catalyst is decreasing with increasing potential cycles. The platinum surface area was plotted versus number of cycles in Figure 10.3. The EASA decreased rapidly between 0 and 500 cycles and continued to decrease until just 8% of the original EASA was measured after 10,000 potential cycles. The change in polarization curve performance with cycling is correlated to the loss in EASA. Shown in Figure 10.4 are polarization curves under hydrogen and air conditions as noted in the experimental section. It is somewhat surprising that the polarization curve performance did not decline as dramatically as one might expect given the drastic loss in EASA. A loss of 150-200 mV is observed even though more than 90% of the EASA was lost. This may be an indication of the low utilization of the platinum catalyst during fuel cell operation which has been observed previously.

Scanning electron microscopy was performed on the cycled MEAs to measure the electrode thinning during electrochemical aging. Figure 10.5 shows SEM micrographs of the aged MEAs. During potential cycling a band of platinum is observed just inside the membrane on the cathode side (the bottom electrode in each of the micrographs). This band has been attributed to platinum dissolving and reprecipitating in response to the potential cycling. As the number of cycles is increased, the cathode becomes noticeably thinner from about 17 microns at 0 cycles to 14 microns at 10,000 cycles. The decrease in electrode thickness was plotted as a function of potential cycles in Figure 10.6. The change in thickness with number of cycles is similar to the loss of EASA where a rapid decrease occurs up to 5000 cycles then levels off however, the electrode thinned only about 20% as opposed to a greater than 90% loss in EASA. Potential cycling certainly has an impact on the cathode thickness, but it is also thought to greatly impact the size of the platinum nanoparticles. Transmission electron microscopy is currently in progress to image the change in size of the nanoparticles during cycling.

Static potential holds at 1.2V with hydrogen on the anode and nitrogen on the cathode were performed in order to measure the catalyst layer thinning for this type of accelerated aging test. The catalyst layer thinned quite dramatically from about 17.5 microns to 8.5 microns after 40 hours of potential hold. This thinning is much more severe than in the potential cycling case as shown in Figure 10.7. The polarization curve performance was measured at 10 hour intervals during the potential holds and is shown in Figure 10.8. Along with the dramatic catalyst layer thinning, the polarization performance of the cell declines steeply with aging at a constant potential. This exploratory study shows that potential holds are much

more damaging to the cathode catalyst layer than potential cycling. However, any excursions of cell potential up to 1.2V are shown to degrade fuel cell performance. It is though that the main degradation mechanism at these high potentials is platinum and carbon corrosion in the catalyst layer.

10.4. Conclusions

Both potential cycling and potential hold accelerated corrosion tests had an impact on the polarization performance of the fuel cell. Electrode thinning was observed in each case, and the decline in performance was most likely attributable to a decrease in the platinum surface area of the electrocatalyst. Potential cycling did not have as detrimental an effect on electrode performance as constant potential holds. This could be due to the time spent above 1.0 V. For 10,000 potential cycles, the time spend above 1.0 V was 80,000 s, which is about 22 hours. Further work will need to be performed to correlate changes upon cycled potential or potential hold.

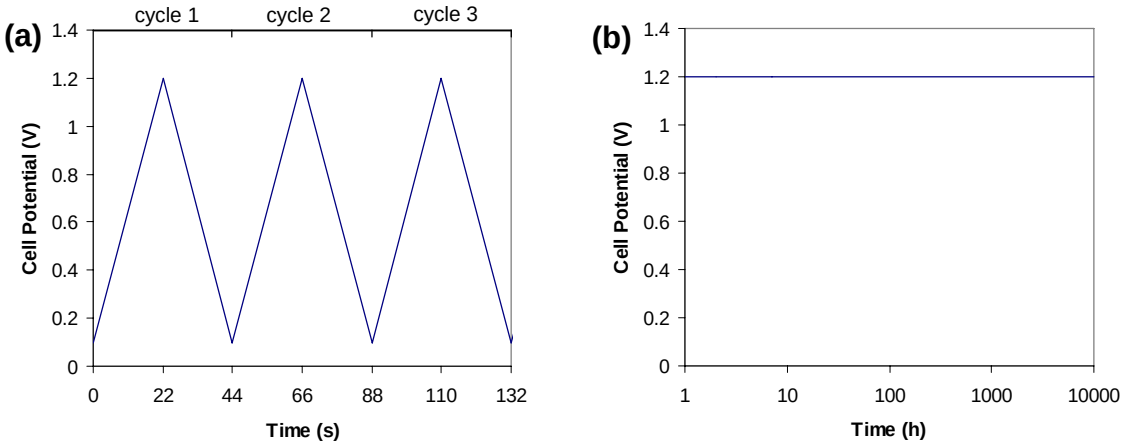

Figure 10.1. Potential profiles for (a) cycling from 0.1 to 1.2V at 50 mV/s and (b) constant potential hold at 1.2V.

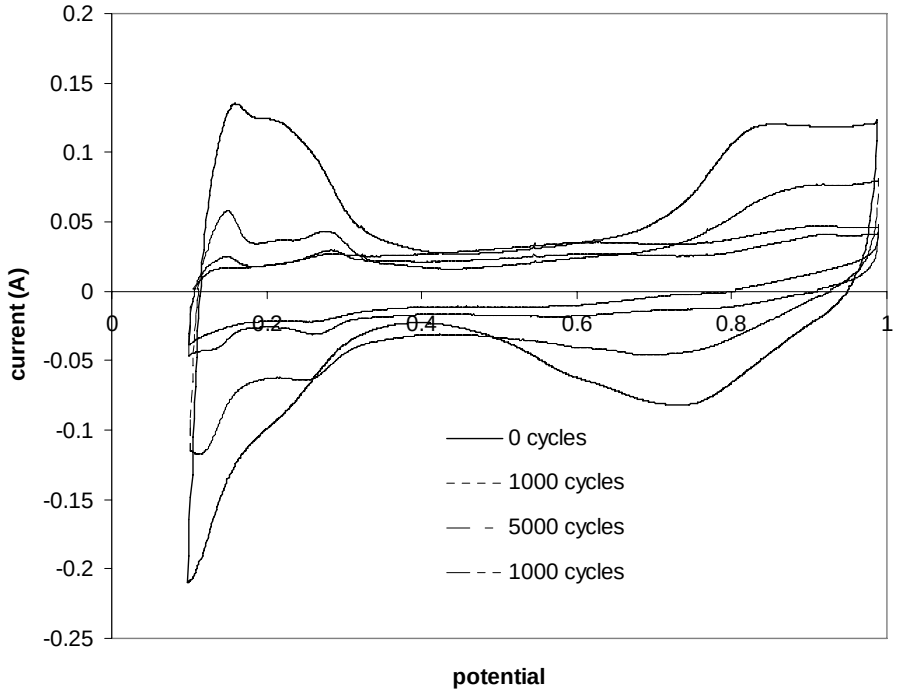

Figure 10.2. Cyclic voltammagrams on a fresh MEA (0 cycles), 1000, 5000, and 10000 cycles.

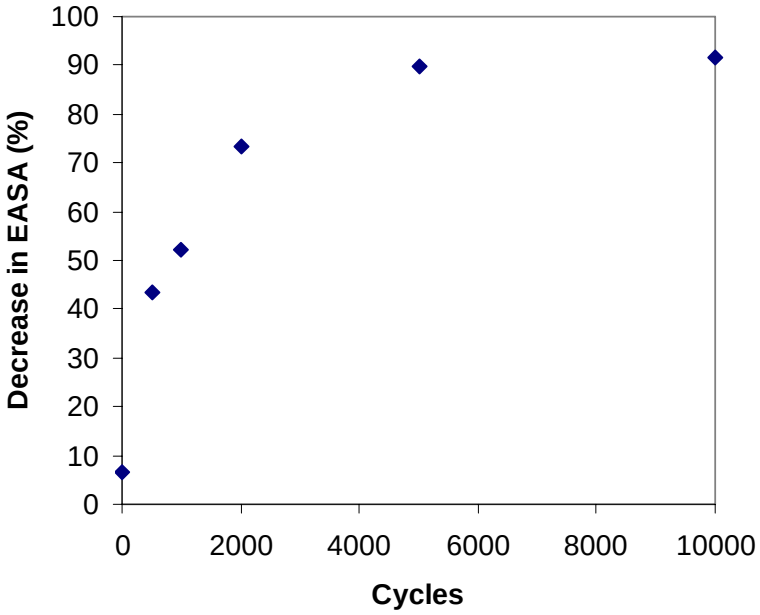

Figure 10.3. EASA as a function of potential cycles from 0.1 to 1.2V.

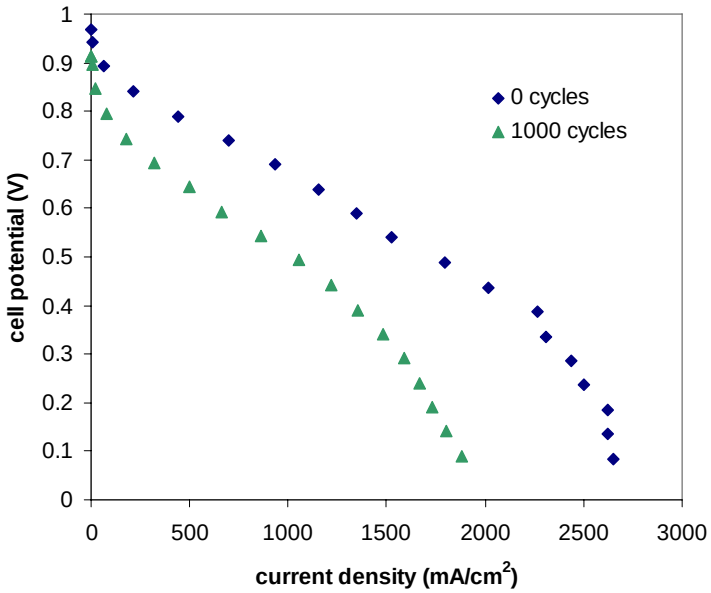

Figure 10.4. Polarization curves of a fresh MEA (0 cycles) and after 1.2V potential cycles.

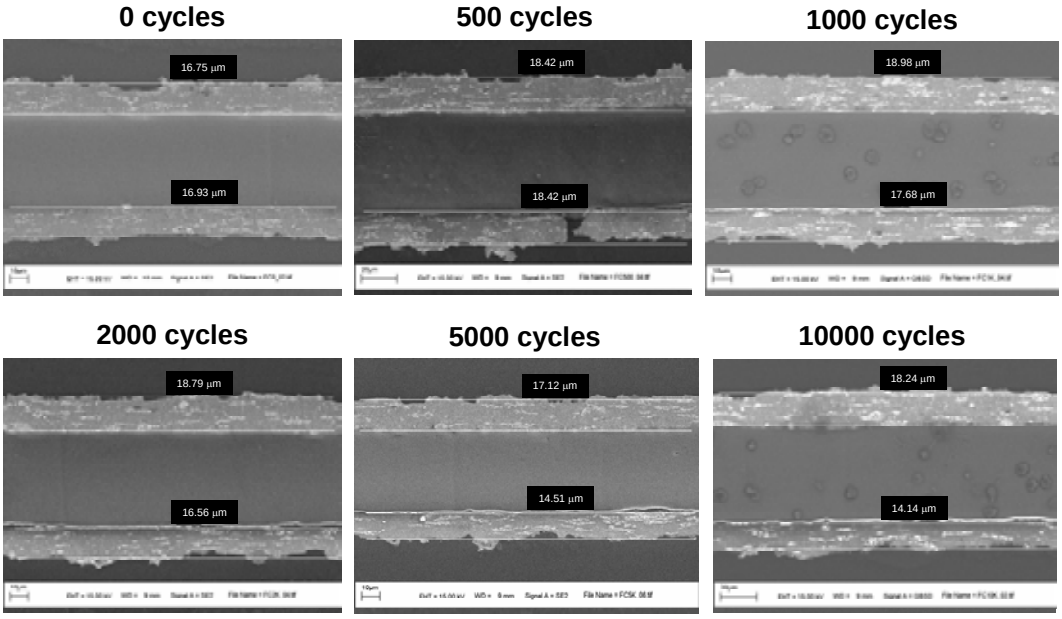

Figure 10.5. SEM micrographs of aged MEAs in potential cycling from 0.1 to 1.2V. Cathode shown on the bottom in each image.

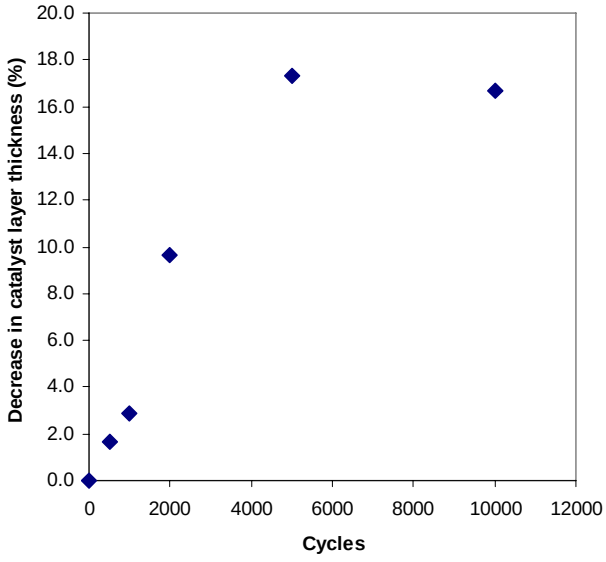

Figure 10.6. Decrease in catalyst layer thickness with number of potential cycles from 0.1 to 1.2 V.

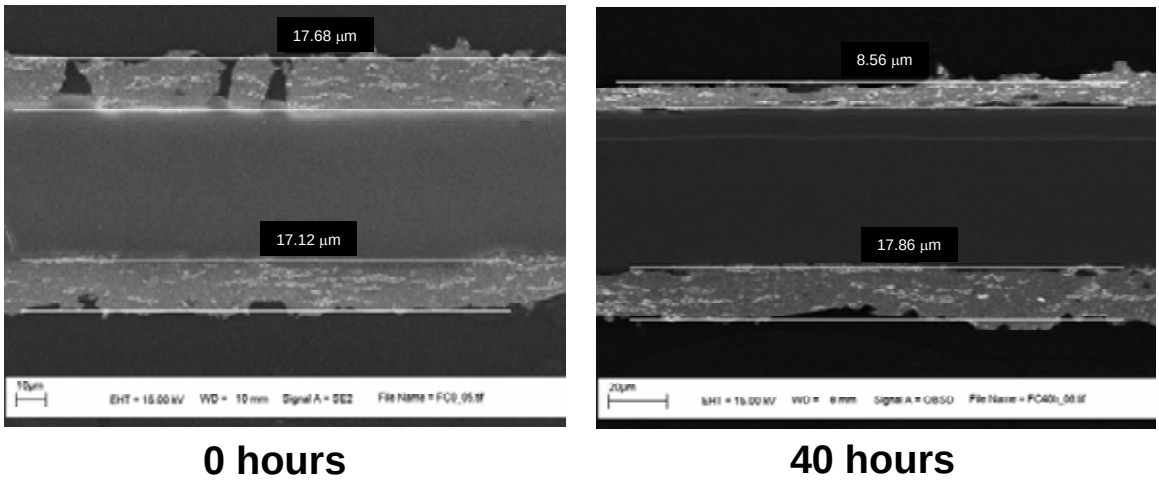

Figure 10.7. SEM micrographs of electrodes held at 1.2V under hydrogen on the anode and nitrogen on the cathode, which is shown on top in each image.

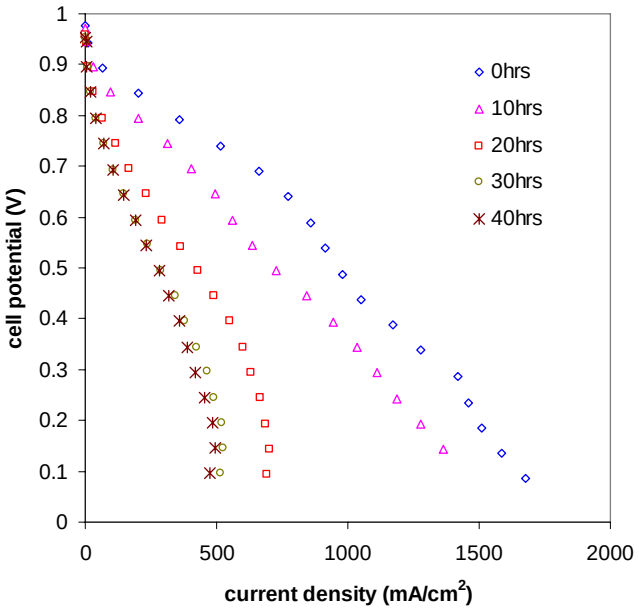

Figure 10.8. Polarization curve performance at 80°C and 100 % RH gas feeds at 10h intervals during 1.2V potential hold.

11. Summary and Concluding Remarks

In the LDRD project documented in this report, we employed a technical approach of combining experiments with computational modeling and analyses to elucidate the performance of hydrogen-fed PEMFCs. Our efforts have focused on understanding water transport in and removal from a hydrogen-fed PEMFC. Using a transparent operating cell and a specially-designed apparatus that simulates the cathode operation of a PEMFC, we directly visualized the formation, growth, and instability of liquid-water droplets at the GDL/GFC interface and recorded shapes of droplets in their observable states under various conditions. Based on our experimental observation and data, we developed a simplified model for predicting the onset of water-droplet instability at the GDL/GFC interface; we also compared the measured and computed water-droplet instability diagrams, and assessed validity of our model by verifying it using a full-flow finite-element analysis. Using a state-of-the-art neutron imaging instrument available at NIST, we probed liquid-water distribution inside an operating PEMFC under a variety of operating conditions and investigated effects of evaporation due to local heating by waste heat on water removal. Moreover, we developed computational models and demonstrated their utilities in case studies for analyzing the effects of micro-porous layer on net water transport across the membrane and GDL anisotropy on the temperature and water distributions in the cathode of a PEMFC, and predicting the liquid saturation, pressure drop, and flow maldistribution across the PEMFC cathode channels.

In addition to our focused work on elucidating water transport and removal, we developed constitutive, analytical, and numerical models for predicting and simulating the electrochemical performance of PEMFCs. Specifically, we developed a constitutive model for computing proton conductivity in polymer electrolyte membranes and a one-dimensional or 1-D analytical model for predicting electrochemical performance of an idealized PEMFC with relatively small surface over-potentials. Furthermore, we developed a multi-dimensional computer model, which is based on the finite-element method and a fully-coupled implicit solution scheme via Newton's technique, for simulating performance of PEMFCs. We demonstrated utility of our finite-element model by comparing the computed current density distribution and overall polarization curve with those measured using a segmented cell in a two-dimensional or 2-D case study. Lastly, we conducted an exploratory experimental study on MEA degradation. A list of refereed and proceeding publications produced in this LDRD project is attached as an appendix, which shows that i) three journal publications and six proceeding papers have been published; ii) one proceeding paper has been accepted for publication; iii) two manuscripts have been submitted to refereed journals; and iv) two manuscripts are being prepared for journal publication.

Though we've made significant progress toward elucidating PEMFC performance and durability in our LDRD project as evidenced by the number of papers published, accepted, submitted, and being prepared as listed in the appendix, much more remains to be done. In the area of water-droplet removal, we've considered only a single droplet emerging from the GDL/GFC interface. In reality, multiple droplets may

form at the GDL/GFC interface and the detached droplets may merge to form bigger droplets, which can in turn form water "slug" in the channel and thus cause "flooding" in the GFC. In the area of probing liquid-water distribution inside an operating PEMFC, we've done so by using neutron radiography via a normal view (i.e., the viewing direction is normal to the GFC, GDL and membrane) such that it is not feasible to identify liquid water in the GFC, GDL and membrane separately. One possible solution for this is to employ neutron radiography via a side view (i.e., the viewing direction is in parallel with the GFc, GDL and membrane) and via tomography (obtaining three-dimensional images by rotating the object).

In the area of electrochemical performance modeling, the finite-element model developed in the present work needs improvement in several aspects. Specifically, to be useful as a tool for PEMFC process design and optimization the following additional phenomena need to be incorporated: 1) the formation, transport, and removal of liquid water, particularly liquid-water removal via droplet shearing and evaporation due to local heating by waste heat; 2) energy transport and temperature effects, particularly local heating that gives rise to non-uniform temperature distribution; and 3) three-dimensional or 3-D effects, particularly that due to the presence of the alternative land/channel patterns as in serpentine flow fields; we can most effectively simulate the 3-D effects using a quasi-3-D approach – that is, 2-D detailed transport models (including accounting for HOR and ORR) in the plane normal to the GFC coupled with 1-D flow models along the GFC. Lastly, it would be helpful to have direct comparisons of computational accuracy and efficiency between the present approach (which employs the finite-element method and a fully-coupled implicit solution scheme via Newton's technique) and the conventional CFD approach (which is based on the finite-difference approximation and segregated solution scheme).

Due to limited time and resources available in our LDRD project, we have conducted only an exploratory experimental study of MEA degradation. Much more needs to be done. Understanding membrane degradation due to chemical attack or decomposition is one challenge and predicting membrane failure resulted from stress (which can be caused by membrane hydration and de-hydration during load cycling) is another. Yet another challenge is elucidating mechanisms underlying catalyst-layer disintegration due to carbon corrosion and Pt-particle ripening and migration. Developing computational models for analyzing these key phenomena will be extremely useful in improving MEA and thus PEMFC durability.

Lastly, it is critically important to characterize the non-uniform hydrophilic/hydrophobic nature of the cathode GDL and quantify its effects on oxygen and water transport and thus on electrochemical performance – the local capillary pressure that controls liquid-water transport strongly depends on the local hydrophilic/hydrophobic nature of the cathode GDL. This has not been carried out due to the limited time and resources available in this project. Being able to determine (experimentally or computationally) the local capillary pressure throughout the cathode GDL will be an important step toward developing accurate pore-level models for simulating oxygen and water transport in the cathode GDL.

Appendix: List of Refereed & Proceeding Publications, and DOE Proposals Produced in the LDRD project

Refereed publications

Chen, K. S., Hickner, M. A., and Noble D. R., "Simplified Models for Predicting the Onset of Liquid Water Droplet Instability at the Gas Diffusion Layer/Gas Flow Channel Interface", *Int. J. Energy Res.*, **29**(12), p.1113 – 1132 (2005).

Pasaogullari, U., Wang, C.-Y., and Chen, K. S., "Two-phase transport in polymer electrolyte fuel cells with bilayer cathode diffusion media", *J. Electrochem. Soc*., **152**, p. A1574 (2005).

Hickner, M. A., Siegel, N. P., Chen, K. S., McBrayer, D. N., Hussey, D. S., Jacobson, D. L, and Arif, M., "Real-time Imaging of Liquid Water in an Operating Proton Exchange Membrane Fuel Cell", *J. Electrochem. Soc.*, **153** (5), A902 (2006).

U. Pasaogullari, P. P. Mukherjee, C. Y. Wang, and K. S. Chen, "Anisotropic Two-Phase Heat and Mass Transfer in Gas Diffusion Layers of Polymer Electrolyte Fuel Cells", manuscript submitted to *J. Appl. Phys*., September, 2006.

Wang, Y., Wang, C. Y., and Chen, K. S., "Elucidating differences between carbon paper and carbon cloth in polymer electrolyte fuel cells", submitted to *Electrochimica Acta,* July , 2006.

Hickner, M. A., Siegel, N. P., Chen, K. S., Hussey, D. S., Jacobson, D. L, and Arif, M., "Neutron imaging studies of water and heat transport in an operating PEM fuel cell", manuscript in preparation.

Basu, S., Wang, Y., Wang, C. Y., and Chen, K. S., "Prediction of two-phase flow maldistribution in PEM fuel cell channels", manuscript in preparation for journal publication.

Proceeding papers

Chen, K. S. and Hickner, M. A., "A new constitutive model for predicting proton conductivity in polymer electrolytes", in *ASME Proceedings of IMECE'04*, paper # 60848 (2004).

Noble, D. R. and Chen, K. S., "Elucidating water-droplet removal in polymer electrolyte fuel cells", in *ASME Proceedings of IMECE'04*, paper # 62129 (2004).

Pasaogullari, U., Wang, C.-Y., and Chen, K. S., "Liquid water transport in polymer electrolyte fuel cells with multi-layer diffusion media", in *Proceedings of IMECE'04*, paper # 59283 (2004).

Hickner, M. A. and Chen, K. S., "Experimental studies of liquid water droplet growth and instability at the gas diffusion layer/gas flow channel interface", in *ASME Proceedings of FUELCELL2005*, paper # 74118 (2005).

Chen, K. S. and Hickner, M. A., "Modeling PEM fuel cell performance using the finite-element method and a fully-coupled implicit solution scheme via Newton's technique", in *ASME Proceedings of FUELCELL2006*, paper # 97032 (2006).

Hickner, M. A., Siegel, N. P., Chen, K. S., Hussey, D. S., Jacobson, D. L, and Arif, M., "Neutron imaging studies of water and heat transport in PEM fuel cells", accepted for publication in the *2006 Fuel Cell Seminar Conference Proceeding* (2006).

Pasaogullari, U., Mukherjee, P. P., Wang, C. Y., and Chen, K. S., "Effect of anisotropy of gas diffusion layers on two-phase heat and mass transport in polymer electrolyte fuel cells", in *ECS Transaction* (2006).

DOE Proposals

K. S. Chen and M. A. Hickner, "Elucidating water transport and removal in PEM fuel cell MEAs via experimental characterization/diagnostics and computational modeling", a full proposal submitted to DOE's EERE Office, Hydrogen, Fuel Cells and Infrastructure Technologies Program, in response to DOE's Laboratory Call for Research and Development for Fuel Cell Technologies, April 6, 2006.

K. S. Chen and T. E. Springer, “Modeling and mechanistic studies”, part of a full proposal submitted to DOE by Los Alamos National Laboratory and titled “Water transport exploratory studies”, April 6, 2006.

K. S. Chen, “Modeling stress development in Nafion membrane during PEM fuel cell operation via elasto-viscoplastic approach”, part of a full proposal submitted to DOE by Ballard Power Systems and titled “Understanding of Water Management on MEA/Component Structure for Automotive Fuel Cells”, April 6, 2006.

R. Masel, R. Alkire, R. Braatz, S. Ha, M. Hickner, M. Shannon, C.-Y. Wang, and A. Wieckowski, "Models and in-situ measurements of water transport in PEM fuel cells”, a full proposal submitted to DOE’s EERE Office, Hydrogen, Fuel Cells and Infrastructure Technologies Program, in response to DOE’s Laboratory Call for Research and Development for Fuel Cell Technologies, April 6, 2006.

K. S. Chen and M. A. Hickner, “Elucidating and improving MEA performance and durability via experiments and modeling”, a task proposal in Sandia’s FY07 AOP submitted to DOE’s EERE Office, Hydrogen, Fuel Cells, and Infrastructure Technologies Program, June 30, 2006.

References

Adamson, A.W., Physical Chemistry of Surfaces, 5th ed., John Wiley & Sons, New York (1990).

Adler, S. B., "Fuel cells: current status and future challenges", in Frontiers of Engineering: Reports on Leading-Edge Engineering from the 2005 Symposium, p. 143 – 150, National Academy of Sciences, Washington D. C. (2005).

Atkins, P.W., Physical Chemistry, 6th ed., Oxford University Press (1998).

Basu, S., Wang, C.-Y., and K. S. Chen, "Prediction of two-phase flow maldistribution in PEM fuel cell channels", manuscript in preparation for journal publication.

Beattie, P.D., Basura, V.I., and Holdcroft, S., "Temperature and pressure dependence of O_2 reduction at Pt|Nafion® 117 and Pt|BAM® 407 interfaces", *J. Electroanal. Chem*., **468**, 180 (1999).

Bejan, A., Advanced Engineering Thermodynamics, 2nd ed. Wiley, New York (1997).

Bellows, R.J., et al., "Neutron imaging technique for in situ measurement of water transport gradients within Nafion in polymer electrolyte fuel cells," *J. Electrochem. Soc.* **146**(3), 1099-1103, (1999).

Bernardi, D. M. and Verbrugge, M. W. , "Mathematical model of a gas diffusion electrode bonded to a polymer electrolyte", *AIChE J*., **37**, p. 1151 (1991).

Bernardi, D.M. and Verbrugge, M.W., "A mathematical model of the solid-polymer-electrolyte fuel cell", *J. Electrochem. Soc.*, **139**, 2477 (1992).

Berning, T. and Djilali, N., "A 3D, multiphase, multicomponent model of the cathode and anode of a PEM fuel cell", *J. Electrochem. Soc.*, **150**, A1589-A1598 (2003).

Bird, R. B., Stewart, W. E., and Lightfoot, E. N., Transport Phenomena, 2nd edition, John Wiley & Sons, Inc.: New York (2002).

Birgersson, E., Noponen, M., and Vynnycky, M., "Analysis of a two-phase non-isothermal model for a PEFC", *J. Electrochem. Soc.* **152**, A1021 (2005).

Bluemle, M. J., Gurau, V., Mann Jr., J. A., and Zawodzinski Jr., T. A., *206th Meeting of the Electrochemical Society*, October 2-8, Honolulu, HI (2004).

Borup, R., Davey, J.R., Wood, D.L., Garzon, F.H., and Inbody, M., "Durability of PEM electrocatalysts and gas diffusion media," in The 1st Fuel Cells Durability Symposium, Knowledge Foundation, Brookline, MA (2005).

Bradean, R., Promislow, K., and Wetton, B., "Transport phenomena in the porous cathode of a proton exchange membrane fuel cell", *Numerical Heat Transfer, Part A: Applications* **42**, 121 (2002).

Bradean, R., Promislow, K., and Wetton, B., Proceedings of IMECE04, Nov. 13-20, Anaheim, California, USA, IMECE 2004-61347 (2004).

Cabasso, I., Yuan, Y., and Xu, X., US Patent #5783325 (1998).

Carnes, B. and Djilali, N., "Systematic parameter estimation for PEM fuel cell models", *J. Power Sources*, **144**, p. 83-93 (2005).

Chen, E., "History", in Fuel Cell Technology Handbook, Chapter 2, p. 2.1-2.40, Hoogers, G., editor, CRC Press, New York (2003).

Chen, K. S., Evans, G. H., Larson, R. S., Noble, D. R., and Houf, W. G., "Final report on LDRD project: a phenomenological model for multicomponent transport with simultaneous electrochemical reactions in concentrated solutions", *Sandia Technical Report*, SAND2000-0207 (2000).

Chen, K. S. and Hickner, M. A., "A new constitutive model for predicting proton conductivity in polymer electrolytes", in *ASME Proceedings of IMECE'04*, paper # 60848 (2004).

Chen, K. S. and Hickner, M. A., "Modeling PEM fuel cell performance using the finite-element method and a fully-coupled implicit solution scheme via Newton's technique", in *ASME Proceedings of FUELCELL2006*, paper # 97032 (2006).

Chen, K. S., Hickner, M. A., and Noble D. R., "Simplified models for predicting the onset of liquid water droplet instability at the gas diffusion layer/gas flow channel interface", *Int. J. Energy Res.*, **29**(12), p.1113 – 1132 (2005).

Chen, W., Fadeev, A. Y., Hsieh, M. C., Öner, D., Youngblood, J. and McCarthy, T. J., "Ultrahydrophobic and ultralyophobic surfaces: some comments and examples", *Langmuir*, **15** (10), p. 3395-3399 (1999).

Costamagna, P., "Transport phenomena in polymeric membrane fuel cells", *Chemical Engineering Science* **56**, 323 (2001).

Dimitrakopoulos, P. and Higdon, J. J. L., "Displacement of fluid droplets from solid surfaces in low-Reynolds-number shear flows", *J. Fluid Mech*., **336**, 351-378 (1997).

Dimitrakopoulos, P. and Higdon, J. J. L., "On the displacement of three-dimensional fluid droplets from solid surfaces in low-Reynolds-number shear flows", *J. Fluid Mech*., **377**, 189-222 (1998).

Dimitrakopoulos, P. and Higdon, J. J. L., "On the displacement of three-dimensional fluid droplets adhering to a plane wall in viscous pressure-driven flows", *J. Fluid Mech*., **435**, 327-350 (2001).

Du, B., Guo, Q., Pollard, R., Rodriguez, D., Smith, C., and Elter, J., "PEM fuel cells: status and challenges for commercial stationary power applications", *JOM*, 2006 August issue, p. 45 – 49 (2006).

Dussan, V. E. B and Chow, R. T. P., "On the ability of drops or bubbles to stick to non-horizontal surfaces of solids", *J. Fluid Mech*., **137**, 1-29 (1983).

Dussan, V. E. B., "On the ability of drops or bubbles to stick to non-horizontal surfaces of solids. Part 2. small drops or bubbles having contact angles of arbitrary size", *J. Fluid Mech*., **151**, 1-20 (1985).

Dussan, V. E. B., "On the ability of drops to stick to surfaces of solids. Part 3. the influence of the motion of the surrounding fluid on dislodging drops", *J. Fluid Mech*., **174**, 381-397 (1987).

Dutta, S., Shimpalee, S., and Van Zee, J. W., "Three-dimensional numerical simulation of straight channel PEM fuel cells", *J. Appl. Electrochem*., **30**, p. 135 (2000).

Fuller, T.F. and Newman, J., "Water and thermal management in solid-polymer-electrolyte fuel cells", *J. Electrochem. Soc*. **140**, 1218 (1993).

Gasteiger, H. A. and Mathias, M. F., "Fundamental research and development challenges in polymer electrolyte fuel cell technology", paper presented at the *Workshop on High Temperature PEM Fuel Cells*, Pennsylvania State University, December (2003).

Giorgi, L., Antolini, E., Pozio, A., and Passalacqua, E., "Influence of the PTFE content in the diffusion layer of low-Pt loading electrodes for polymer electrolyte fuel cells", *Electrochim. Acta*, **43**, 3675 (1998).

Gurau, V., Liu, H., and Kakac, S**., "**Two-dimensional model for proton exchange membrane fuel cells", *AIChE J*., **44**, p. 2410 (1998).

Hara, N., Tsurumi, K., and Watanabe, M., "An advanced gas diffusion electrode for high performance phosphoric acid fuel cells", *J. Electroanal. Chem.*, **413**, p. 81 (1996).

He, W., Yi, J. S, and Nguyen, T. V., "Two-phase flow model of the cathode of PEM fuel cells using interdigitated flow fields", *AIChE J.*, **46**(10), 2053-2064 (2000).

Hickner, M. A. and Chen, K. S., "Experimental studies of liquid water droplet growth and instability at the gas diffusion layer/gas flow channel interface", in *ASME Proceedings of FUELCELL2005*, paper # 74118 (2005).

Hickner, M. A., Siegel, N. P., Chen, K. S., Hussey, D. S., Jacobson, D. L, and Arif, M., "Neutron imaging studies of water and heat transport in PEM fuel cells", accepted for publication in the *2006 Fuel Cell Seminar Conference Proceeding* (2006).

Hickner, M. A., Siegel, N. P., Chen, K. S., McBrayer, D. N., Hussey, D. S., Jacobson, D. L, and Arif, M., "Real-time Imaging of Liquid Water in an Operating Proton Exchange Membrane Fuel Cell", *J. Electrochem. Soc.*, **153** (5), A902 (2006).

Incropera, F. P. and DeWitt, D.P., Fundamentals of Heat and Mass Transfer, Wiley, New York (1996).

Jacobson, D. L., Hussey, D. N., and Arif, M., personal communication (2003).

Jannsen, G.J.M. and Overvelde, M.L.J., "Water transport in the proton-exchange-membrane fuel cell: measurements of the effective drag coefficient", *J. Power Sources,* **101**, 117 (2001).

Johnson, R. E., and Dettre, R. H.,"Contact angle hysteresis: IV. Contact angle measurements on heterogeneous surfaces", *J. Phys. Chem.* **69**, p.1507-1515 (1965).

Jordan, L. R., Shukla, A. K., Behrsing, T., Avery, N.R., Muddle, B.C., and Forsyth, M., *J. Appl. Electrochem.* **30**, 641 (2000).

Ju, H., Meng, H., and Wang, C. Y., "A single-phase, non-isothermal model for PEM fuel cells", *Int. J. Heat Mass Transfer* **48**, 1303 (2005).

Ju, H., Wang, C. Y., Cleghorn, S., and Beuscher, U., "Nonisothermal modeling of polymer electrolyte fuel cells. I. Experimental Validation", *J. Electrochem. Soc.*, **152** (8), p. A1645-A1653 (2005).

Kaviany, M., Principles of Heat Transfer in Porous Media, Springer, New York (1999).

Kong, C. S., Kim, D.-Y., Lee, H.-K., Shul, Y.-G., and Lee, T-H., " Influence of pore-size distribution of diffusion layer on mass-transport problems of proton exchange membrane fuel cells", *J. Power Sources,* **108**, 185 (2002).

Lander, L.M., Siewierski, L.M., Brittain, W.J., and Vogler, E.A., "A systematic comparison of contact angle methods," *Langmuir*, **9**, p. 2237 – 2239 (1993).

Larminie, J. and Dicks, A., Fuel Cells Explained, 2nd ed., John Wiley & Sons, Ltd., West Sussex, England (2003).

Lee, S. J., Mukarjee, S., McBreen, J., Rho, Y.W., Kho, Y.T., and Lee, T.H., "Anode water removal: A water management and diagnostic technique for solid polymer fuel cells", *Electrochim. Acta*, **40**, 321 (1995).

Li, S. and Becker, U., "A three dimensional CFD model for PEMFC", in 2nd *ASME Fuel Cell Conference Proceedings* (2004).

Li, S., Cao, J., Wangard, W., and Becker, U., "Modeling PEMFC with Fluent: numerical performance and validations with experimental data", in *ASME Proceedings of FUELCELL2005*, paper # 74058 (2005).

Maggio, G., Recupero, V., and Mantegazza, C., "Modelling of temperature distribution in a solid polymer electrolyte fuel cell stack", *J. Power Sources* **62**, 167 (1996).

Mazumder, S. and Cole, J. V., "Rigorous 3-D mathematical modeling of PEM fuel cells. II. Model predictions with liquid water transport", *J. Electrochem. Soc.*, 150, A1510-A1517 (2003).

Meier, F. and Eigenberger, G., "Transport parameters for the modelling of water transport in ionomer membranes for PEM-fuel cells", *Electrochim. Acta,* **49**, 1731 (2004).

Mench, M. M., Wang, C. Y., and Ishikawa, M., "In situ current distribution measurements in polymer electrolyte fuel cells", *J. Electrochem. Soc.*, **150 (8)**, A1052-A1059, (2003).

Mench, M. M., Dong, Q. L, and Wang, C. Y., "In situ water distribution measurements in a polymer electrolyte fuel cell", *J. Power Sources*, **124**, 90-98 (2003).

Meng, H. and Wang, C.Y., "Model of two-phase flow and flooding dynamics in polymer electrolyte fuel cells", *J. Electrochem. Soc.* **152**, 1733 (2005).

Meredith, R.E., Tobias, C.W., in: C.W. Tobias (Ed.), Advances in Electrochemical Science and Engineering, 2nd ed., Interscience, New York (1962).

Motupally, S., Becker, J.A., and Weidner, J.W., "Diffusion of water in Nafion 115 membranes", *J. Electrochem. Soc.* **147**, 3171 (2000).

Nam, J.H. and Kaviany, M., "Effective diffusivity and water-saturation distribution in single- and two-layer PEMFC diffusion medium", *Int. J. Heat and Mass Transfer*, **46**, 4595 (2003).

Natarajan, D. and Nguyen, T. V., "A two-dimensional, two-phase, multicomponent, transient model for the cathode of a proton exchange membrane fuel cell using conventional gas distributors", *J. Electrochem. Soc.*, **148**, A1324-A1335 (2001).

Natarajan, D. and Nguyen, T. V., "Three-dimensional effects of liquid water flooding in the cathode of a PEM fuel cell", *J. Power Sources*, **115**, 66-88 (2003).

J. S. Newman, Electrochemical Systems, 2nd ed., Prentice Hall, Englewood Cliffs, NJ (1991).

Nguyen, T.V. and White, R.E., "A water and heat management model for proton-exchange-membrane fuel cells", *J. Electrochem. Soc.* **140**, 2178 (1993).

Noble, D. R. and Chen, K. S., "Elucidating water-droplet removal in polymer electrolyte fuel cells", in Proceedings of IMECE '04, paper # 62129 (2004).

Öner, D. and McCarthy, T. J., "Ultrahydrophobic surfaces: effects of topography length scales on wettability," *Langmuir*, **16** (20), p. 7777 – 7782 (2000).

Paganin, V., A., Ticianelli, E. A., and Gonzalez, E. R., "Development and electrochemical studies of gas diffusion electrodes for polymer electrolyte fuel cells", *J. Appl. Electrochem.*, **26**, 297 (1996).

Pasaogullari, U., Mukherjee, P. P., Wang, C. Y., and Chen, K. S., "Effect of anisotropy on two-phase heat and mass transfer of cathode gas diffusion layers of polymer electrolyte fuel cells", manuscript submitted to *J. Appl. Phys.*, September, 2006.

Pasaogullari, U. and Wang, C.Y.. Abstract No. 1190, 203th Electrochemical Society Meeting, April 27-May 2, Paris, France (2003).

Pasaogullari, U. and Wang, C.Y., Abstract No. 1103 204th Electrochemical Society Meeting, October 12-16, Orlando, Florida (2003).

Pasaogullari, U. and Wang, C.Y., "Two-phase transport and the role of micro-porous layer in polymer electrolyte fuel cells", *Electrochim. Acta*, **49**, 4359 (2004).

Pasaogullari, U. and Wang, C. Y., "Liquid water transport in gas diffusion layer of polymer electrolyte fuel cells", *J. Electrochem. Soc.*, **151**, A399-A406 (2004).

Pasaogullari, U. and Wang, C. Y., "Two-phase modeling and flooding prediction of polymer electrolyte fuel cells", *J. Electrochem. Soc.*, **152**, A380 (2005).

Pasaogullari, U., Wang, C.-Y., and Chen, K. S., "Liquid water transport in polymer electrolyte fuel cells with multi-layer diffusion media", in *Proceedings of IMECE'04*, paper # 59283 (2004).

Pasaogullari, U., Wang, C.-Y., and Chen, K. S., "Two-phase transport in polymer electrolyte fuel cells with bilayer cathode diffusion media", *J. Electrochem. Soc.*, **152**, p. A1574 (2005).

Passalacqua, E., Lufrano, F., Squadrito, G., Patti, A., and Giorgi, L., "Influence of the structure in low-Pt loading electrodes for polymer electrolyte fuel cells", *Electrochim. Acta*, **43**, 3665 (1998).

Passalacqua, E., Squandrito, G., Lufrano, F., Patti, A., and Giorgi, L., "Effects of the Diffusion Layer Characteristics on the Performance of Polymer Electrolyte Fuel Cell Electrodes", *J. Appl. Electrochem.*, **31**, 449 (2001).

Patankar, S.V., Numerical Heat Transfer and Fluid Flow, Hemisphere, Washington, DC (1980).

Qi, Z. and Kaufman, A., "Improvement of water management by a microporous sublayer for PEM fuel cells", *J. Power Sources*, **109**, 38 (2002).

Raistrick, I. D., "Modified gas diffusion electrode for proton exchange membrane fuel cells", in Proceedings of the Symposium on Diaphragms, Separation, and Ion-Exchange Membranes", Van. Zee, J. W., White, R. E., Kinoshita, K., and Barney, H. S., Eds., Proceedings Volume PV-86, Electrochemical Society, Ponnington, NJ, p. 172 (1986).

Rowe, A. and Li, X., "Mathematical modeling of proton exchange membrane fuel cells", *J. Power Sources* **102**, 82 (2001).

Sackinger, P. A., Schunk, P. R, and Rao, R. R., "A Newton-Raphson pseudo-solid domain mapping technique for free and moving boundary problems: a finite-element implementation", *J. Comput. Phys.*, **125**, 83-103 (1995).

Sandstede, G., Cairns, E. J., Bagotsky, V. S., and Wiesener, K., "History of low temperature fuel cells", in Handbook of Fuel Cells: Fundamentals, Technology and Applications, Chapter 4, Vol. 1, p. 143-218, John Wiley & Sons Ltd., West Sussex, England (2003).

Satija, R., Jacobson, D. L., and Arif, M., and Werner, S. A., "In situ neutron imaging technique for evaluation of water management systems in operating PEM fuel cells", *J. Power Sources*, **129**, 238-245 (2004).

Schunk, P. R, Sackinger, P. A, Rao, R. R, Chen, K. S., Cairncross, R. A., Baer, T. A., and Labreche D. A., "GOMA 2.0 – a full-Newton finite element program for free and moving boundary problems with coupled fluid/solid momentum, energy, mass, and chemical species transport: user's guide", *Sandia Technical Report* SAND97-2404, Sandia National Laboratories, Albuquerque, New Mexico (1997).

Senn, S.M. and Poulikakos, D., **"**Multiphase transport phenomena in the diffusion zone of a PEM fuel cell", *J. Heat Transfer* **127**, 1245 (2005).

Shimpalee, S. and Dutta, S., "Numerical prediction of temperature distribution in PEM fuel cells", *Numerical Heat Transfer, Part A*, **38**, 111 (2000).

Siegel, N. P., *Development and Validation of A Computational Model for A Proton Exchange Membrane Fuel Cell*, Ph. D. Thesis, Virginia Polytechnic Institute and State University, Blacksburg, VA (2003).

Siegel, N. P., Ellis, M. W., Nelson, D. J., and von Spakovsky, M. R., "Single domain PEMFC model based on agglomerate catalyst geometry", *J. Power Sources*, **115**, 81-89 (2004).

Siegel, N. P., Ellis, M. W., Nelson, D. J., and von Spakovsky, M. R., "A two-dimensional computational model of a PEMFC with liquid water transport", *J. Power Sources*, **124**, 403-414 (2004).

Sivertsen, B. R. and Djilali, N., "CFD-based modelling of proton exchange membrane fuel cells", *J. Power Sources*, **141**, p. 65 (2005).

Springer, T.E., Zawodzinski, T.A., and Gottesfeld, S., "Polymer Electrolyte Fuel Cell Model", *J. ELectrochem. Soc.* **138**, 2334 (1991).

Tomadakis, M.M. and Sotirchos, S.V., "Ordinary and transition regime diffusion in random fiber structures", *AIChE J.* **39**, 397 (1993).

Tuber, K., Pocza, D., and Hebling, C., "Visualization of water buildup in the cathode of a transparent PEM fuel cell", *J. Power Sources*, **124**, 403-414 (2003).

Tucker, M., Odgaard, M., Yde-Andersen, S., and Thomas, J., "Electrode porosity considera-tions for DMFCs", paper presented at the 203rd Meeting of the Electrochemical Society, April 27th–May 2nd, Paris, France (2004).

Udell, K.S., "Heat transfer in porous media considering phase change and capillarity—the heat pipe effect", *Int. J. Heat Mass Transfer* **28**, 485 (1985).

Um, S., Wang, C. Y. Wang, and Chen, K. S., "Computational fluid dynamics modeling of proton exchange membrane fuel cells", *J. Electrochem. Soc.*, **147**, p. 4485 – 4493 (2000).

Wang, C. Y., in Handbook of Fuel Cells – Fundamentals, Technology and Applications W. Lietsich, A. Lamm and H.A. Gasteiger, Editors, Vol.3, Part 3, 337 John Wiley & Sons, Chicester (2003).

Wang, C. Y., "Fundamental models for fuel cell engineering", *Chem. Rev.* **104**(10), 4727-4766 (2004).

Wang, C.Y. and Cheng, P., "Multiphase flow and heat transfer in porous media", in *Advances in Heat Transfer*, eds. by J.P. Hartnett et al., Jr., **30**, p.93 – 196, Academic Press (1997).

Wang, Y. and Wang, C.Y., "A nonisothermal, two-phase model for polymer electrolyte fuel cells", *J. Electrochem. Soc.* **153**, A1193 (2006).

Wang, Z. H., Wang, C. Y., and Chen, K. S., "Two-phase flow and transport in the air cathode of proton exchange membrane fuel cells", *J. Power Sources*, **94**, 40-50 (2001).

Weber, A. Z., Darling, R.M., and Newman, J., "Modeling two-phase behavior in PEFCs", *J. Electrochem. Soc*, **151**, A1715 (2004).

Weber, A. and Newman, J., Abstract No. 1038 204th Electrochemical Society Meeting, October 12-16, Orlando, Florida (2003).

Weber, A. and Newman, J., "Modeling transport in polymer-electrolyte fuel cells", *Chem. Rev.* **104**, 4679 (2004).

Weber, A.Z. and Newman, J., "Effects of microporous layers in polymer electrolyte fuel cells", *J. Electrochem. Soc.*, **152**, A677 (2005).

Wilkinson, D. P. and Vanderleeden, O., "Serpentine flow field design," Handbook of Fuel Cells – Fundamentals, Technology, and Applications, W. Vielstichm, H.A. Gasteiger,and A. Lamm, eds., John Wiley & Sons, New York, Vol. 3, p. 315-324 (2003).

Williams, M.V., Kunz, H.R., and Fenton, J.M., "Influence of Convection Through Gas-Diffusion Layers on Limiting Current in PEM FCs Using a Serpentine Flow Field", *J. Electrochem. Soc.*, **151**, A1617 (2004).

Williams, M.V., Begg, E., Bonville, L., Kunz, H.R., and Fenton, J.M., "Characterization of gas diffusion layers for PEMFC", *J. Electrochem. Soc.*, **151**, A1173 (2004).

Wilke, C.R., *J. Chem. Phys.* **18**, 517 (1950).

Wilson, M. S., Valerio, J. A., and Gottesfeld, S**., "**Low platinum loading electrodes for polymer electrolyte fuel cells fabricated using thermoplastic ionomers", *Electrochim. Acta*, **40**, p. 355 (1995).

Yang, X. G., Zhang, F. Y., Lubawy, A. L., and Wang, C. Y., "Visualization of liquid water transport in a PEFC", *Electrochem. Solid-State Lett.*, **7** (11), A408-A411 (2004).

Yi, J.S. and Nguyen, T.V., "An along-the-channel model for proton exchange membrane fuel cells", *J. Electrochem. Soc.*, **145**, 1149 (1998).

You, L. and Liu, H., "A two-phase flow and transport model for the cathode of PEM fuel cells", *Int. J. Heat Mass Transfer*, **45**, 2277-2287 (2002).

Yuan, J., and Sunden, B., "Two-phase flow analysis in a cathode duct of PEFCs", *Electrochim. Acta*, **50**, 677 (2004).

Zawodzinski, T.A., Springer, T.E., Uribe, F., and Gottesfeld, S., "Characterization of polymer electrolytes for fuel cell applications", *Solid State Ionics*, **60**, 199 (1993).

Zawodzinski, T.A., Davey, J., Valerio, J., and Gottesfeld, S., "The water content dependence of electro-osmotic drag in proton-conducting polymer electrolytes", *Electrochim. Acta*, **40**, 297 (1995).

Zhou, T. and Liu, H., "A general three-dimensional model for proton exchange membrane fuel cells", *Int. J. Transport Phenomena* **3**, 177 (2001).

Distribution

1	MS 0384	A. C. Ratzel	1500
1	MS 0834	W. L. Hermina	1510
1	MS 0834	A. M. Grillet	1513
1	MS 0836	J. S. Lash	1514
6	MS 0836	K. S. Chen	1514
1	MS 0836	H. K. Moffat	1514
1	MS 0836	D. R. Noble	1514
1	MS 0836	R. R. Rao	1514
1	MS 0836	P. R. Schunk	1514
1	MS 0836	B. Carnes	1543
1	MS 1082	W. K. Schubert	1723
1	MS 1082	C. A. Apblett	1723
1	MS 0614	D. Ingersoll	2521
1	MS 1104	M. L. Tatro	6200
1	MS 1104	R. D. Robinett	6330
1	MS 0734	J. B. Kelley	6334
1	MS 1110	J. S. Nelson	6337
1	MS 1127	N. P. Siegel	6337
1	MS 0734	E. B. Stechel	6338
2	MS 0734	M. A. Hickner	6338
1	MS 0734	C. J. Cornelius	6338
1	MS 0734	C. H. Fujimoto	6338
1	MS 9054	D. R. Hardesty	8360
1	MS 9052	J. O. Keller	8367
1	MS 9409	C. D. Moen	8757
2	MS 9018	Central Technical Files	8944
2	MS 0899	Technical Library	4536
1	MS 0123	LDRD Office	1011

1 Prof. Chao-Yang Wang
Director of Electrochemical Engine Center
Mechanical and Nuclear Engineering Dept
The Pennsylvania State University
338A Reber Building
University Park, PA 16802

1 Prof. Ugur Pasaogullari
Connecticut Global Fuel Cell Center, and
Department of Mechanical Engineering
University of Connecticut
Storrs, CT 06269-5233

1 Dr. Daniel S. Hussey
NIST
100 Bureau Dr., MS-8461
Gaithersburg, MD 20899-8461

1 Dr. David S. Jacobson
NIST
100 Bureau Dr., MS-8461
Gaithersburg, MD 20899-8461

1 Dr. Bryan S. Pivovar
Fuel Cell Team Leader
P. O. Box 1663, M. S. D429
Los Alamos National Laboratory
Los Alamos, NM 87545

1 Dr. Rod Borup
Team Leader
Institute for Hydrogen and Fuel Cell Research MST-11
P. O. Box 1663, MST-11, MS J579
Los Alamos National Laboratory
Los Alamos, NM 87545

1 Dr. Silvia Wessel
Manager, Plate and Electrode Materials
Ballard Power Systems
4343 North Fraser Way
Burnaby BC V5J 5J9, Canada

1 Dr. Colleen Legzdins
Senior Research Engineer
Ballard Power Systems
4343 North Fraser Way
Burnaby BC V5J 5J9, Canada

1 Dr. Sanjiv Kumar
Senior CFD Engineer
Ballard Power Systems
4343 North Fraser Way
Burnaby BC V5J 5J9, Canada

1 Dr. Radu Bradean
Senior Applied Scientist/Engineer
Ballard Power Systems
9000 Glenlyon Parkway
Burnaby BC V5J 5J9, Canada

1 Dr. Jay Sui
Senior Research Engineer
University of Victoria
Institute for Integrated Energy Systems
PO Box 3055, STN CSC
Victoria BC V8W 3P6, Canada

1 Prof. Ned Djilali
University of Victoria
Institute for Integrated Energy Systems
PO Box 3055, STN CSC
Victoria BC V8W 3P6, Canada

1 Dr. Haijiang Wang
Senior Research Officer, Project Leader
National Research Council/Institute for Fuel Cell Innovation
3250 East Mall
Vancouver BC V6T 1W5, Canada

1 Dr. Shaoping Li
Lead Development Engineer/Fuel Cell Group Manager
Fluent Inc.
10 Cavendish Court
Centerra Resource Park
Lebanon, NH 03766-1442

1 Dr. Richard Pollard
Manager, Fundamentals Center of Excellence
Plug Power
968 Albany-Shaker Road
Latham, NY 12110

1 Dr. Zhigang Qi
Fellow
Plug Power
968 Albany-Shaker Road
Latham, NY 12110

1 Dr. Bin Du
Research Scientist
Plug Power
968 Albany-Shaker Road
Latham, NY 12110

1 Dr. Guoqing Wang
Senior Mechanical Engineer
Plug Power
968 Albany-Shaker Road
Latham, NY 12110

1 Dr. Tom Trabold
GM Fuel Cell Actitivies
Mail Code 144-001-101
10 Carriage Street
P.O. Box 603
Honeoye Falls, NY14472-0603

1 Dr. Wenbin Gu
GM Fuel Cell Actitivies
Mail Code 144-001-101
10 Carriage Street
P.O. Box 603
Honeoye Falls, NY14472-0603

1 Dr. Craig S. Gittleman
GM Fuel Cell Actitivies
Mail Code 144-001-101
10 Carriage Street
P.O. Box 603
Honeoye Falls, NY14472-0603

1 Dr. Yeh-Hung Lai
GM Fuel Cell Actitivies
Mail Code 144-001-101
10 Carriage Street
P.O. Box 603
Honeoye Falls, NY14472-0603

1 Prof. Jeffery S. Allen
815 R. L. Smith Building
Department of Mechanical Engineering
Michigan Technological University
1400 Townsend Drive
Houghton, MI 49931

1 Prof. Brian Dennis
Mechanical & Aerospace Engineering
Box 19018 Woolf Hall, Room 316C
University of Texas at Arlington
Arlington, TX 76019-0018